# Modeling of Material-Environment Interactions for Hypersonic Thermal Protection Systems

by

Samuel Y. Chen

A dissertation submitted in partial fulfillment
of the requirements for the degree of
Doctor of Philosophy
(Aerospace Engineering)
in the University of Michigan
2020

Doctoral Committee:

       Associate Professor Krzysztof Fidkowski, Chair
       Adjunct Professor Iain D. Boyd
       Associate Professor Eric Johnsen
       Associate Professor Veera Sundararaghavan

*"So long, and thanks for all the fish."*

Douglas Adams, The Hitchhiker's Guide to the Galaxy

Samuel Y. Chen

samuelyc@umich.edu

ORCID iD: 0000-0001-7740-006X

If there is any to be had, to God be all the glory.

# ACKNOWLEDGEMENTS

First of all, I want to thank my advisor, Prof. Iain Boyd, for mentoring me during my time at the University of Michigan. Under your guidance, I've been provided more opportunities and learned more than I could have imagined only five short years ago. I also thank my other committee members, Profs. Krzysztof Fidkowski, Veera Sundararaghavan, and Eric Johnsen for serving on my committee and reviewing this dissertation. I'd especially like to thank Prof. Krzysztof Fidkowski for assuming the duties of Chair, and for offering valuable assistance and advice.

Outside of Michigan, I'd like to thank the researchers at NASA Ames, in particular Dr. David Hash, for providing formative opportunities and experiences there. From my undergraduate days, I would also like to express my gratitude towards my undergraduate mentor at The College of New Jersey, Dr. Lisa Grega. You helped me realize that pursuing my dreams was possible.

I thank my NGPDL labmates and those in the UM Aerospace department, particularly Dr. Andrew Lee, who has been a steadfast friend. I also thank my friends in Ann Arbor and back in NJ – you made it all bearable and even joyful at times, and these past five years were the best I've ever had.

Finally, I would like to recognize my family for their constant support and encouragement, no matter how small or large.

# TABLE OF CONTENTS

**Chapter**

# LIST OF FIGURES

**FIGURE**

# LIST OF TABLES

**TABLE**

# LIST OF APPENDICES

**APPENDIX**

# LIST OF ABBREVIATIONS

**TPS** Thermal Protection System

**SiC** Silicon Carbide

**ZrB$_2$** Zirconium Diboride

**HfB$_2$** Hafnium Diboride

**ICP** Inductively-Coupled Plasma

**UVM** University of Vermont

**LTE** Local Thermodynamic Equilibrium

**FWHM** Full Width at Half Maximum

**UHTC** Ultra-High Temperature Ceramic

**SEB** Surface Energy Balance

**CFD** Computational Fluid Dynamics

**A-P** Active-to-Passive

**P-A** Passive-to-Active

**ACE** Aerotherm Chemical Equilibrium

**TGA** Thermo-gravimetric Analysis

**CEA** Chemical Equilibrium with Applications

**QSS** Quasi-Steady State

**LOS** line-of-sight

**LeMANS** "Le" Michigan Aerothermodynamic Navier-Stokes Solver

**NEQAIR** Nonequilibrium and Equilibrium Radiative Transport Spectra

# ABSTRACT

Hypersonic vehicles operate in extreme conditions, experiencing high heating loads, gas temperatures often exceeding 10,000 K in the shock layer, and oxidizing environments. Thermal protection systems (TPS) are thus a vital component to the design of a hypersonic flight vehicle. The overarching goal of this work is to characterize and model the material-environment interactions between TPS materials and the hypersonic flowfield – these dictate the thermal and chemical behavior of the TPS. Two materials are investigated: *ablative* materials, which degrade during exposure to flight conditions, and *ultra-high temperature ceramics* (UHTCs), which exhibit refractory and oxidation-resistant properties. A coupled framework involving computational fluid dynamics (CFD), material response, surface chemistry, and radiation is used to simulate experiments and evaluate the material models.

This work is divided into three main parts. The first part of this dissertation demonstrates how radiative emission can be used in simulations to investigate the chemical kinetics of ablative materials. CFD–radiation simulations are performed in collaboration with high-temperature plasma experiments, using radiative emission measurements in the reacting boundary layer to validate the chemical models.

The second part focuses on the development of a thermodynamic model describing oxidation of silicon carbide (SiC), a UHTC material. The model is validated against experimental data in the literature, and coupled CFD simulations of SiC oxidation are performed using the model. Predicted surface temperatures and simulated emission spectra are shown to be in good agreement with experimental data.

The third part details the development and evaluation of a thermodynamic model for zirconium diboride ($ZrB_2$) and $ZrB_2$-SiC oxidation, a UHTC composite. Overall, thermodynamic modeling approaches are sufficient to describe the equilibrium oxidation behavior of these TPS materials. However, limitations of the proposed models are also discussed, motivating the need for higher-fidelity finite-rate models and additional experimental data.

# CHAPTER 1

# Introduction

*"When an object flies really fast, it gets really hot."*

## 1.1 Background

### 1.1.1 Hypersonic Flight

The hypersonic flight regime is generally defined to be at speeds above Mach 5. Physically, this is when ideal gas assumptions begin to break down and nonequilibrium effects dominate flow phenomena [1]. There are important military, national security, commercial, and space applications for hypersonic flight. Notably, re-entry environments encountered by spacecraft are in the hypersonic regime, including the Space Shuttle which reached speeds of nearly Mach 25 during re-entry into the Earth's atmosphere [2].

Hypersonic vehicles experience "extreme" conditions with high heating loads and high-temperature, reacting environments. Figure 1.1 illustrates a representative hypersonic vehicle and associated physical phenomena. A central challenge when designing and operating hypersonic vehicles is to withstand these conditions over the

1

expected flight trajectory and duration. Consequently, the Thermal Protection System (TPS) is a vital component for any hypersonic vehicle. Before considering the TPS, it is important to first understand the magnitude of the heating loads a hypersonic vehicle experiences.
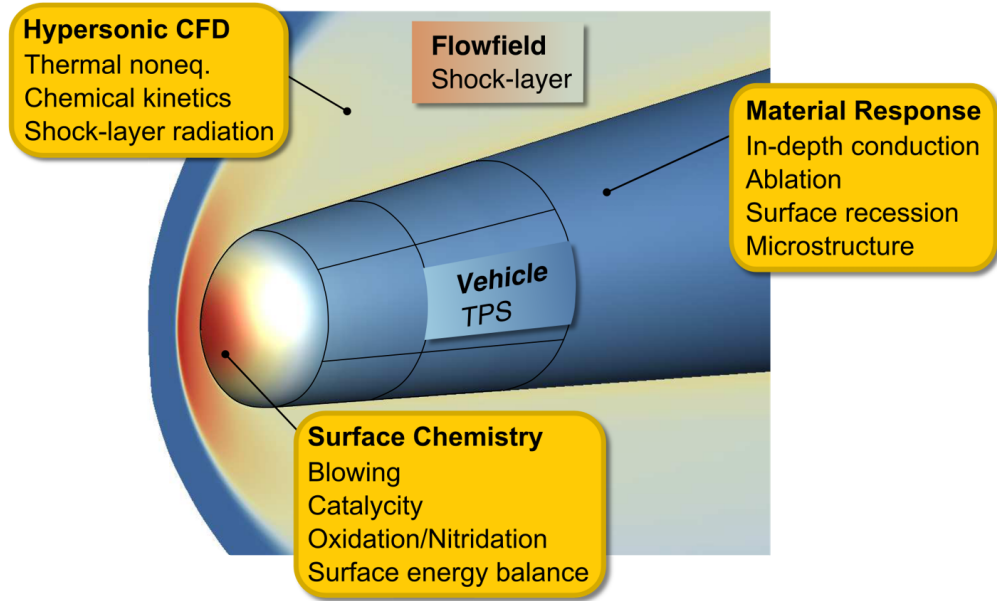


Figure 1.1: Different domains and physical processes for hypersonic vehicles.

On a basic level, the temperatures and energies involved in hypersonic flight come from the dissipation of the vehicle's kinetic energy into the gas environment. In the shock layer, gas temperatures may reach upwards of 10,000 K. Although most of this energy is convected away with the flow, a fraction of this energy is transferred to the vehicle in the form of convective and radiative heating. Researchers have investigated the *stagnation point* heating over various axisymmetric geometries. Physically, the convective heating is dependent on the vehicle geometry, flow conditions, boundary layer chemistry, and even the TPS material itself. Early efforts utilized correlations to

predict convective heating rates, such as the work of Fay and Riddell [3]. Sutton and Graves generalized these correlations for different planetary atmospheres and surface catalycities [4]. For a fully-catalytic (but otherwise non-reacting) surface in an Earth entry environment, Eq. (1.1) gives the approximate cold-wall stagnation point heat flux [4]:

$$\dot{q}_{\text{stag}} = k_{\text{env}} \sqrt{\frac{\rho}{R_n}} V^3 \quad \left[ \frac{\text{W}}{\text{m}^2} \right], \quad k_{\text{env}} = 1.7415 \times 10^{-4} \tag{1.1}$$

Importantly, this result illustrates that peak stagnation point heating is *inversely* related to the square root of the effective nose radius, $R_n$.

For some hypersonic applications, blunt bodies with a large effective nose radius are utilized in the vehicle design, e.g. space re-entry capsules. From Eq. (1.1), this results in lower peak heating, due in large part to increasing the shock stand-off distance relative to the vehicle. Blunt bodies also have a larger drag coefficient than slender geometries, which is usually desired for re-entry applications. However, for sustained atmospheric hypersonic flight, aerodynamic constraints preclude the use of blunt bodies. Instead, slender bodies and sharp leading edges are utilized in vehicles designed for sustained hypersonic flight, minimizing the drag. As a result, the peak heating experienced by these vehicles may be more severe, imposing additional requirements on the TPS materials and design.

As mentioned, the TPS must be able to handle these intense external heat loads generated during hypersonic flight, ranging from $10^2$ to $10^5$ W/cm$^2$. However, chemical interactions between the high-temperature, reacting environment and the TPS

material present an additional challenge. These chemical interactions are commonly referred to as surface chemistry, gas-surface interactions, and more generally *material-environment* interactions. In most cases, uncontrolled material degradation is the limiting factor in TPS design, either from thermal, mechanical, or chemical mechanisms. Some TPS materials, such as *ablative* materials, are designed to degrade in hypersonic environments, but at the cost of reusability. The choice of TPS material depends entirely on the application, and requires trade-offs between reusability and performance.
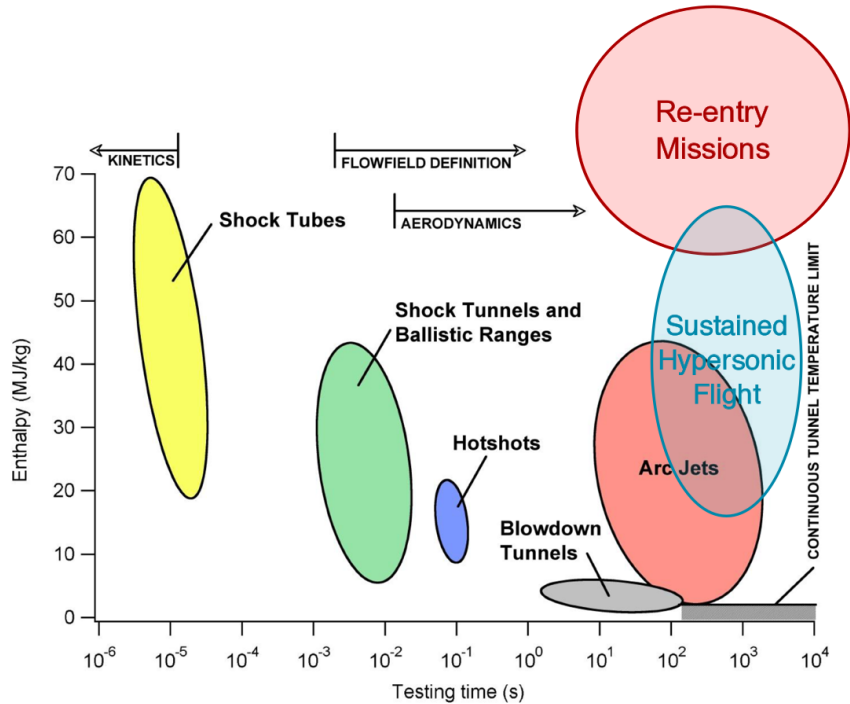


Figure 1.2: Capabilities of various hypersonic ground test facilities. Image adapted from Ref. [5].

Another challenge in the design of a hypersonic vehicle is the experimental testing capability. Experimental ground test facilities designed to investigate hypersonic flight conditions are limited by either the freestream enthalpy or the testing time,

shown in Fig. 1.2. There are gaps in the freestream enthalpy and test time capabilities with respect to flight-realistic conditions for both re-entry and sustained hypersonic flight applications. Robust simulations are thus needed for the design and validation of hypersonic vehicles, to fill in these gaps and provide truly predictive capabilities.

In large part, simulation capabilities are limited by the development of accurate physical models. For aerothermal analysis of hypersonic vehicles, three "domains" are considered to model the material-environment interactions between the vehicle TPS and the flowfield, illustrated in Fig. 1.1. In general, Computational Fluid Dynamics (CFD) tools simulate the hypersonic flowfield. Material Response models analyze the thermal and chemical behavior of the vehicle TPS, including any changes in material microstructure. At the interface of the flowfield and the material, surface chemistry models account for material-environment interaction. Physically, these processes are all coupled, and there is a need for high-fidelity methods and models that account for the coupled nature.

### 1.1.2 Ablative Thermal Protection Systems

Ablative TPS have a long history of use in re-entry applications and in rocket nozzles, well before even the development of the Space Shuttle [6]. *Ablation* refers to the combined thermal, chemical, and mechanical degradation of a material. Typically, these are oxidation processes, although in certain cases nitridation may also be a factor. Ablation results in loss of material over time, and this must be taken into account when designing ablative TPS. Ablative TPS are used in applications

where heating loads exceed the capabilities of reusable TPS materials. Figure 1.3 illustrates the re-entry trajectories for several NASA missions. Reusable TPS systems are feasible only at "low" velocities and moderate entry trajectories.
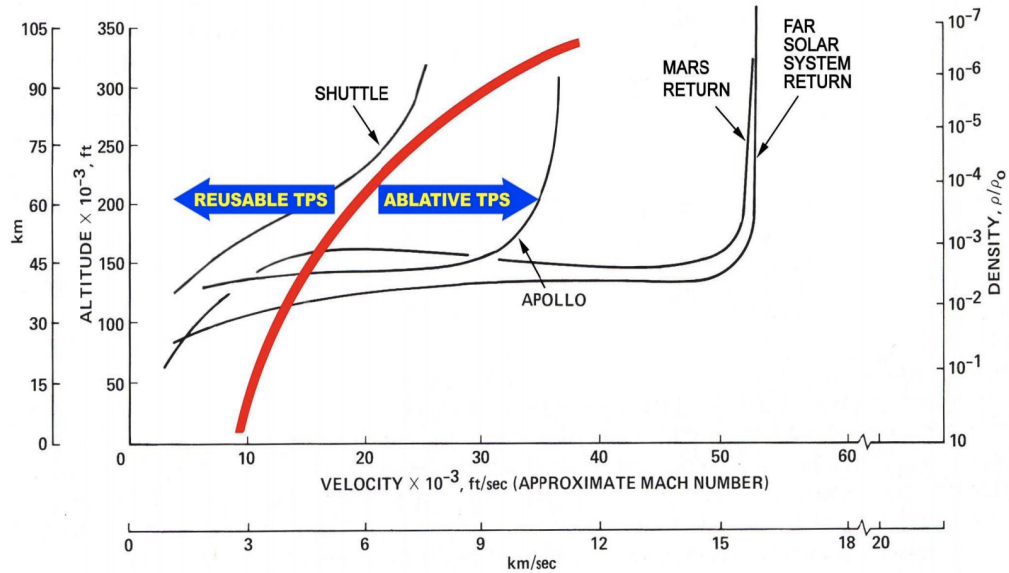


Figure 1.3: Limitations of reusable TPS materials. Image reproduced from Ref. [7].

*Pyrolyzing* ablators are important for modern ablative TPS, such as the Phenolic-Impregnated Carbon Ablator (PICA). Pyrolysis involves *internal* material decomposition. In contrast, non-pyrolyzing ablators involve only surface ablation. The PICA ablator consists of a carbon fiber mesh embedded in a matrix of phenolic resin, illustrated in Fig. 1.4. During pyrolysis, the phenolic resin is volatilized through endothermic phase transformations, exposing a porous char-layer consisting of carbon fibers. These fibers oxidize, and both ablation processes occur simultaneously. The combination of fiber ablation and pyrolysis gases thickens the boundary layer, reducing the convective heating experienced by the vehicle [8].
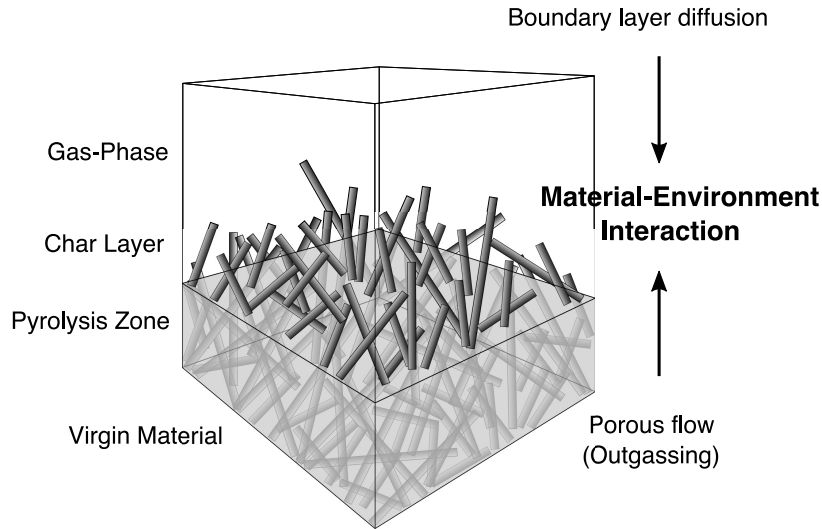
Figure 1.4: Surface of a pyrolyzing ablator (e.g. PICA).

Chemical ablation processes include internal decomposition, surface chemistry, and gas-phase chemistry, shown in Fig. 1.4. Material-environment interactions are the result of boundary layer diffusion and outgassing of the ablative and pyrolysis gases. In the gas phase, the chemical kinetics of pyrolysis gas products and air are still not well understood, often relying on heritage chemical mechanisms that may have limited experimental validation [9].

### 1.1.3 Ultra-High Temperature Ceramics

Ultra-High Temperature Ceramic (UHTC) materials are a class of TPS that have been proposed for use in hypersonic sharp leading edge applications, where ablative materials may be detrimental due to the shape change from surface recession. UHTCs demonstrate high melting temperatures (refractory) and oxidation-resistant properties. These materials include Silicon Carbide (SiC), Zirconium Diboride (ZrB$_2$), Hafnium Diboride (HfB$_2$), and their composites. Refractory properties are important

in non-ablating TPS materials, since radiation is a primary cooling mechanism. Figure 1.5 plots the melting temperatures for various UHTC compounds. In particular, $ZrB_2$ and $HfB_2$ are materials of interest due to the *combination* of refractory and oxidation-resistant properties [10].
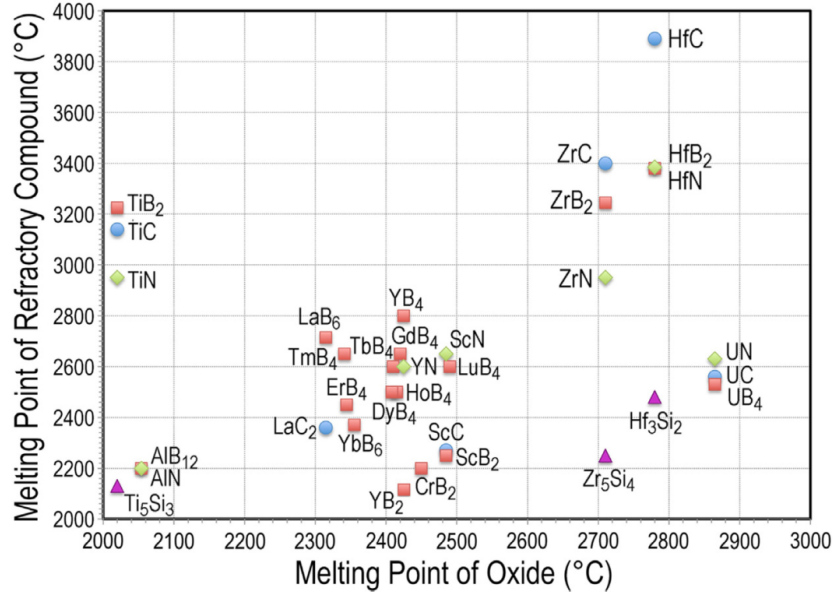


Figure 1.5: Melting points for various refractory materials. Image reproduced from Ref. [10].

UHTCs demonstrate additional desirable properties such as low density, low thermal expansion, and high thermal conductivity [11]. Depending on the application, a high or low thermal conductivity may be desired. For sharp leading edges, a high thermal conductivity allows heat to be conducted into cooler parts of the vehicle, effectively acting as a heat sink. In hypersonic applications, using UHTCs often involves trade-offs between refractory performance and oxidation-resistance. In most cases, the limiting factor is the oxidation resistance of these materials, not the refractory temperature [11].

8

Generally, the oxidation behavior of UHTC materials such as SiC, $ZrB_2$, and $HfB_2$ can be characterized as either "passive" or "active," illustrated in Fig. 1.6. Passive oxidation occurs at moderate temperatures, where a condensed oxide layer "passivates" onto the surface. The condensed oxide limits the diffusion of gaseous oxidants onto the material surface, providing oxidation resistance. At elevated temperatures, active oxidation occurs, where the condensed oxide is volatilized through evaporation and/or chemical processes. Gaseous oxides are then produced from reactions with the base UHTC material. The transition from passive-to-active oxidation is of particular interest in this work, since it is often the limiting factor for these UHTC materials in practical hypersonic flight applications.
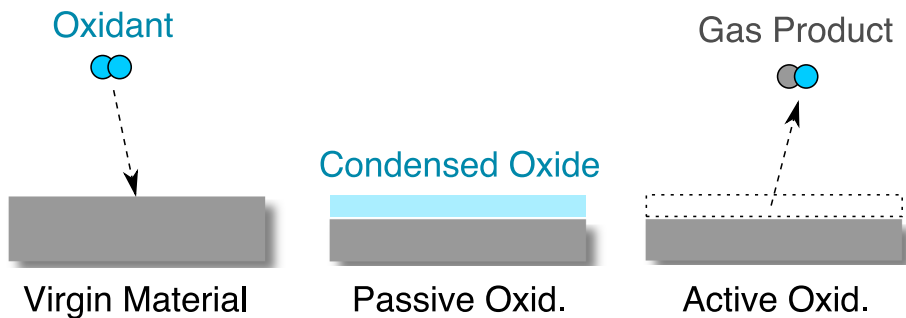


Figure 1.6: Passive and active oxidation for UHTC materials.

## 1.2  Motivation and Scope

The overall motivation for this dissertation is to support the development of hypersonic flight vehicles, including new TPS materials that enable higher performance, allowing hypersonic vehicles to fly faster, at lower altitudes, and for longer durations.

There are two classes of TPS materials that are investigated in this work: pyrolyzing ablators and UHTCs. Pyrolyzing ablators have been investigated by other researchers extensively in the literature, but less data are available on the material-environment interactions. There is a larger emphasis on SiC and $ZrB_2$ UHTC materials, since limited modeling work has been performed by other researchers.

The focus of this dissertation is to characterize and model the material-environment interactions between TPS materials and hypersonic environments, specifically the physical processes that occur in the reacting boundary layer of hypersonic flight vehicles. A coupled simulation framework is proposed, combining CFD flowfield analyses, material response models, and detailed surface chemistry models for TPS materials. The techniques and analyses used to investigate each TPS material are generalized, and used throughout this work.

A major theme throughout this dissertation is the use of first-principle thermodynamic analysis techniques to examine the complex physical and chemical processes involved in material-environment interactions. The thermodynamic approach is motivated by the *lack* of experimental data in the literature for material-specific gas-surface reactions. Models for TPS materials based on these analyses provide insight into material-environment interactions using relatively simple thermodynamic principles. These models are then used as part of the larger high-fidelity, multi-physics framework involving flowfield, materials, and radiation. In addition, thermodynamic models establish a baseline to evaluate the need for higher-fidelity models. A central question that is addressed throughout this dissertation is *"What level of fidelity is needed?"*

Much of this work is also motivated by collaborative experiments and simulations. The simulations performed in this dissertation address two seemingly disparate tasks: model development and characterization of experimental facilities. Hypersonic facilities are vital to any real-world development, and significant effort is spent to better characterize these facilities. Simulations of the facilities and experiments themselves aid in the characterization, providing data that augment the experimental diagnostics. In turn, this provides higher-quality data to validate the development of new models. Ultimately, the goal of this work is to simulate, analyze, and predict the thermal and chemical behavior of hypersonic vehicles.

## 1.3    Dissertation Outline

The dissertation consists of eight chapters, and related work is discussed in the context of each chapter. This first chapter provides an introduction to the different types of TPS, the physcial processes involved, and the challenges in modeling them. The second chapter provides the physical and numerical foundations used throughout this dissertation, including physical models, CFD, and material response calculations.

The main body of the dissertation consists of five chapters (Chapters 3 to 7), each covering one or more aspects of the coupled framework, illustrated in Fig. 1.7. The third chapter involves characterization of the flowfield environment, detailing a collaborative experiment–simulation effort to investigate the chemical kinetics of pyrolysis gases using radiative emission spectroscopy. Chapter four covers the development and validation of a surface chemistry model for SiC oxidation and nitridation.
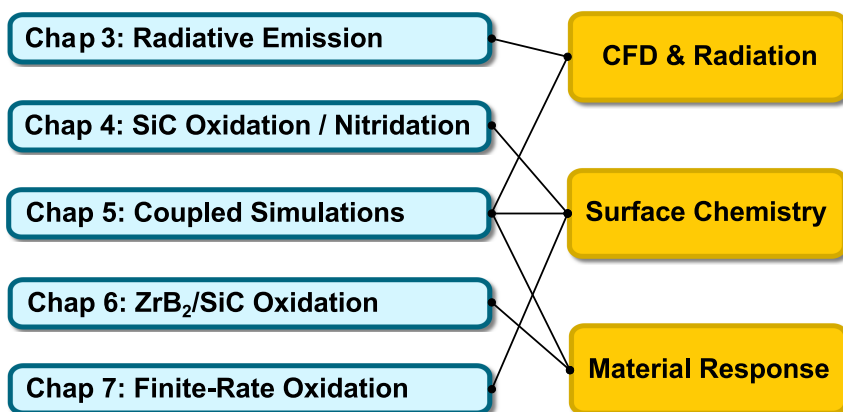
Figure 1.7: Overview of dissertation work in relation to the coupled framework.

The fifth chapter describes simulations using the SiC oxidation model, coupling the surface chemistry model to both CFD and material response analyses. The sixth chapter discusses the development and evaluation of a material response model for $ZrB_2$ and $ZrB_2$-SiC oxidation. Chapter seven presents a higher-fidelity approach to surface chemistry modeling, discussing the limitations of the models developed in Chapters four and six, and proposes finite-rate parameters for both SiC and $ZrB_2$-SiC oxidation. The eighth and final chapter summarizes the results from each preceding chapter, the primary research contributions, and recommendations for future work.

# CHAPTER 2

# Numerical Modeling and Simulation

This chapter describes various models and techniques that will be employed throughout this dissertation to simulate the relevant physical and chemical phenomena. First, a physical description is provided for multiphase systems in thermodynamic equilibrium. Next, CFD calculations are briefly described for hypersonic flowfields. Finally, material response and boundary layer analyses are discussed.

## 2.1   Thermal Equilibrium

A detailed understanding of the physical structure of atoms and molecules is fundamental to any discussion of thermodynamics and equilibrium. For a general gas "particle" governed by the ideal gas law, there are several energy modes that arise from the physical structure. In the gas phase, particles interact via collisions, and collisions serve to transfer energy between particles and between the individual energy modes [12]. From quantum theory, the energy levels of each mode are *quantized*, although a classical/continuum treatment may be appropriate for certain modes. For diatomic molecules, a brief description of each energy mode is provided below:

- **Translational:** From kinetic theory, the translational energy mode describes the kinetic energy of a particle. Classically, the translational energy of a particle is simply $\varepsilon_{\mathrm{tr}} = \frac{1}{2}mv^2$. The translational energy mode is inherently related to the velocity distribution function (VDF) [12]. In general, three degrees of freedom are allowed in physical space (e.g. x, y, z), and translational energy levels are treated as a continuum due to infinitesimally small spacing between energy levels (on the order of $10^{-38}$ J [12]).

- **Rotational:** The rotational energy may be described with a rigid-rotor model [12]. Two degrees of freedom are allowed for diatomic molecules, although three are possible for triatomic or larger molecules. The rotational energy levels are still quantized, but a classical treatment is typically utilized due to the relatively small spacing between quantized energy levels. There are certain exceptions to this, such as in spectroscopy where discrete rotational energy levels contribute to the radiative absorption and emission.

- **Vibrational:** The vibrational energy describes the oscillations between individual atoms in diatomic molecules. The vibrational energy levels are quantized, and the spacing is relatively large. Between one and two degrees of freedom are allowed in diatomic molecules, limited by the degree of activation. A triatomic or larger molecule may have additional vibrational degrees of freedom, depending on the symmetry. In general, the vibrational energy mode is never fully activated due to the tendency of molecules to dissociate at higher vibrational energy levels.

- **Bound Electrons:** The electrons "bound" to an atom/molecule may occupy several quantized energy levels, and the discrete energy levels generally have very large spacing. The ground level is denoted by "X", the first excited level by "A", the second excited level by "B", and so on. Typically, the ground level is the most heavily populated, but excited levels are important for determining the radiative emission and absorption from atoms and molecules.

- **Free Electrons:** "Free" electrons also have an energy mode attributed to their translational motion, and are distinct from the bound electrons. Classically, these electrons have very small mass but high velocities, and their energy is treated as a continuum. Free electrons are usually considered a separate chemical species, along with ionized versions of the base species (e.g. $O^+$ vs. O).

Often, the translational energy mode is considered separately from the other internal energy modes. Monatomic gas particles have only translational and electronic energy modes available. Depending on the species and energy mode, multiple states may occupy the same energy level, so *degeneracy* is the number of states that may occupy the same energy level.

From statistical mechanics, collisions and the transfer of energy between modes and particles *equilibrate* the distribution of energy. The Boltzmann relation describes the distribution of internal energy for a gas in *thermal equilibrium. Within* each

internal energy model, the Boltzmann relation is expresed in Eq. (2.1):

$$\frac{n_j/g_j}{n_i/g_i} = \exp\left(-\frac{\Delta\varepsilon_{ij}}{k_B T}\right) \tag{2.1}$$

$$\Delta\varepsilon_{ij} = \varepsilon_j - \varepsilon_i \tag{2.2}$$

$\varepsilon$ is the energy level of a *single particle*, and $g_i$ is the degeneracy of level $i$. A *partition function $Q$* is related to the sum of all energy levels and their degeneracies [12], defined in Eq. (2.3):

$$Q = \sum_i g_i \exp\left(-\frac{\varepsilon_i}{k_B T}\right) \tag{2.3}$$

The partition function is species and temperature-dependent. In terms of the partition function, the Boltzmann distribution may also be expressed in Eq. (2.4) [12]:

$$\frac{n_i}{\sum_i n_i} = \frac{g_i \exp\left(-\frac{\varepsilon_i}{k_B T}\right)}{\sum_i g_i \exp\left(-\frac{\varepsilon_i}{k_B T}\right)} = \frac{g_i \exp\left(-\frac{\varepsilon_i}{k_B T}\right)}{Q} \tag{2.4}$$

It can be shown that this distribution maximizes the entropy of the system [12]. The partition function relates to the equilibrium partition of energy *between* modes. Individual partition functions are defined for each energy mode, and the overall partition function is obtained by taking the product of all the partition functions for the energy modes in Eq. (2.5).

$$Q(T) = Q_{\mathrm{tr}} Q_{\mathrm{rot}} Q_{\mathrm{vib}} Q_{\mathrm{el}} \tag{2.5}$$

Macroscopic thermodynamic properties may also be determined from the partition function. For example, the total internal energy (including the translational energy) is a function of the temperature and overall partition function in Eq. (2.6) [12]:

$$e_k = nk_BT^2 \frac{\partial}{\partial T} \ln Q_k \qquad (2.6)$$

More simply, the temperature $T$ also describes the distribution of energy in thermal equilibrium, using the Boltzmann relationship between energy levels and populations. In terms of temperature, the thermal equilibrium condition is expressed simply as:

$$T_{\text{tran}} = T_{\text{rot}} = T_{\text{vib}} = T_{\text{elec}} = T_{e^-} \qquad (2.7)$$

For gases in thermal nonequilibrium, a *multi-temperature* approximation assumes different temperatures for each internal energy mode. A prominent example is the two-temperature model [13]:

$$T_{\text{tr}} \rightarrow T_{\text{tran}} = T_{\text{rot}} \qquad (2.8)$$

$$T_{\text{ve}} \rightarrow T_{\text{vib}} = T_{\text{elec}} = T_{e^-} \qquad (2.9)$$

$$T_{\text{tr}} \neq T_{\text{ve}} \qquad (2.10)$$

Free electrons are assumed to be in equilibrium with either the translational-rotational mode, or the vibrational-electronic mode.

In general, species in a solid or liquid state are always assumed to be in thermal equilibrium. Physically, intermolecular forces dominate the interactions between par-

17

ticles, and these interactions serve to equilibrate the various internal energy modes.

## 2.2 Chemical Equilibrium

### 2.2.1 Relating Thermodynamics and Chemistry

From the previous discussion, thermal equilibrium relates to the distribution of internal energy. For a single chemical species, thermal equilibrium implies that the internal energy modes are in mutual equilibrium. For multi-species mixtures, thermal equilibrium implies that these internal energy modes are additionally in equilibrium *between* species, i.e. that their internal energy distributions are described by the *same* temperature.

In contrast, *chemical* equilibrium refers to the population distribution of individual species in multi-species mixtures, e.g. the ratio of $O_2$ to O. Thermal and chemical equilibrium are not mutually exclusive. For this work, *thermodynamic* equilibrium refers to a state exhibiting both thermal and chemical equilibrium. While thermal equilibrium is governed by the Boltzmann relation in Eq. (2.1) and maximization of entropy, chemical equilibria is governed by the principle of *free energy minimization.*

Gibbs free energy is a thermodynamic property describing the maximum amount of reversible work that can be done, mechanical or otherwise at constant temperature and pressure [14]. This is analogous to Helmholtz free energy for constant temperature and volume. The Gibbs and Helmholtz free energy properties are classically defined

in Eqs. (2.11) and (2.12):

$$G(P, T) = H - TS \tag{2.11}$$

$$F(V, T) = E - TS \tag{2.12}$$

From these expressions, minimizing the free energy of the system is equivalent to *maximizing the entropy*, which is consistent with the second law of thermodynamics. For closed systems with constant temperature and volume, the chemical equilibrium state is determined by minimizing the Helmholtz free energy. For open systems with constant temperature and pressure, the chemical equilibrium state is determined by minimizing the Gibbs free energy. In general, Gibbs free energy is more appropriate to describe the thermodynamics of the open systems considered in hypersonic flowfields.

It is critical to point out that for species participating in chemical reactions, the total enthalpy $H$ is actually a combination of the sensible enthalpy, $\Delta H$ and the enthalpy of formation $\Delta H_f$ in Eq. (2.13):

$$H = \Delta H + \Delta H_f^o \tag{2.13}$$

The sensible enthalpy portion is temperature dependent. For a calorically-perfect substance, the sensible enthalpy may be evaluated using Eq. (2.14):

$$\Delta H = C_p(T - T_{\text{ref}}) \tag{2.14}$$

Note that $\Delta H_f$ is relatively temperature-independent, and is typically defined at a "standard" state ($T^o = 298$ K, $P^o = 1$ bar) [14].

For reacting systems, multiple chemical species must be present, so the mixture Gibbs free energy is evaluated instead. Reactions involve a change in the composition of a mixture. The mixture composition can be quantified in terms of the chemical *activity*. For gas-phase species, the activity $a$ is the partial pressure normalized by a reference, or *standard* pressure

$$a_i = \frac{P_i}{P^o} \tag{2.15}$$

Standard pressure is typically defined at 1 bar = 100,000 Pa. In older literature, the standard state ($^o$) referred to a partial pressure of 1 atm = 101,325 Pa [14]. More recently, the standard pressure was changed to 1 bar. This difference is not insignificant depending on the application. For surface species, the activity may be defined similarly in terms of surface coverages (e.g. sites/m$^2$).

$$a_s = \frac{n_s}{n_{\mathrm{ref}}} \tag{2.16}$$

At standard conditions, gases are typically 3–4 orders of magnitude *less dense* compared to solid or liquid phases. Chemically, changes in the activity of gases (related to the partial pressure) have proportionally small effects on the activity of solid and liquid phases in heterogeneous reactions. Thus, *unit* activity is generally assumed for pure solid and liquid species.

An *activity-based* equilibrium reaction constant may now be defined for reactions in Eq. (2.17), describing the chemical activity of species in equilibrium. The equilibrium constant is the ratio of the chemical activities of products to reactants, and is temperature-dependent.

$$K_p(T) = \left( \frac{\prod a_{\text{prod}}}{\prod a_{\text{react}}} \right)^{\text{eq}} = \exp\left( \frac{-\Delta G^o}{RT} \right) \tag{2.17}$$

$$\Delta G^o = \sum G^o_{\text{prod}} - \sum G^o_{\text{react}} \tag{2.18}$$

This ratio is determined from the change in standard Gibbs free energy of the reaction, $\Delta G^o$. It can be shown that the latter expression in Eq. (2.17) minimizes the Gibbs free energy for a reacting system (to be proved later). There are obvious similarities between Eq. (2.17) and the Boltzmann relation in Eq. (2.1), as both seek to maximize the entropy of the system. The key idea is that the chemical state is inherently linked to the thermodynamic state for reacting systems.

Typically, reaction energies involve macroscopic collective quantities in terms of J/mol rather than J/particle, so the denominator of the exponential in Eq. (2.17) involves the universal gas constant $R$, rather than the Boltzmann constant $k_B$ as in Eq. (2.1). The Boltzmann constant $k_B$ is related to the universal gas constant $R$ by Avogadro's number $N_A = 6.022 \times 10^{23} \text{ mol}^{-1}$.

$$k_B = \frac{R}{N_A} \tag{2.19}$$

The change in Gibbs free energy for a reaction is evaluated with Eq. (2.18), and the

Gibbs free energy of each specie is determined at the standard pressure, but at the *specified* temperature.

## 2.2.2 Evaluating Equilibrium Constants

Consider the representative reaction in Eq. (2.20), where $a$, $b$, $c$ denote the stoichiometric coefficients for species $A$, $B$, and $C$:

$$aA + bB \leftrightarrow cC \tag{2.20}$$

The Gibbs free energy of each specie is evaluated at non-standard states using Eq. (2.21) [14]

$$G_A(T, P) = G_A^o + RT \ln P_A \tag{2.21}$$

Computing the change in Gibbs free energy due to the reaction results in:

$$\Delta G = c(G_C^o + RT \ln P_C) - a(G_A^o + RT \ln P_A) - b(G_B^o + RT \ln P_B) \tag{2.22}$$

$$\Delta G^o = cG_C^o - aG_A^o - bG_B^o \tag{2.23}$$

$$\Delta G = \Delta G^o + RT \ln \left( \frac{P_C^c}{P_A^a P_B^b} \right) \tag{2.24}$$

Equation (2.24) is the change in the Gibbs free energy of the system for unit quantities of each reactant as the reaction proceeds isothermally in the forward direction. Recall that the equilibrium composition is determined by minimizing the free energy of the

system. The minimum is obtained when $\Delta G = 0$, corresponding to the *chemical equilibrium* state:

$$0 = \Delta G^o + RT \ln \left( \frac{P_C^c}{P_A^a P_B^b} \right)^{\text{eq}} = \Delta G^o + RT \ln K_p \tag{2.25}$$

$$\ln K_p = -\frac{\Delta G^o}{RT} \tag{2.26}$$

$$K_p = \exp \left( \frac{-\Delta G^o}{RT} \right) \tag{2.27}$$

For a reaction, the magnitude and sign of $\Delta G^o$ indicates how far out of equilibrium the system is, given a stoichiometric ratio of products and reactants, and in what direction it must proceed to equilibrate.

The result in Eq. (2.24) implies that only *changes* in the Gibbs free energy are important for reaction equilibria. In practice, $\Delta G^o$ can be evaluated with Eq. (2.28) as the change in enthalpies and entropies of the reaction at standard pressure, but at the specified temperature $T$:

$$\Delta G^o = \Delta H^o - T\Delta S^o \tag{2.28}$$

For heterogeneous reactions, recall from the earlier discussion that unit activity is generally assumed for pure solid and liquid phases [14]. This implies that the activity of a condensed phase is *independent* of the reaction, and simplifies the thermodynamic calculations for heterogeneous reactions. In many applications, it is also more convenient to express the chemical composition in terms of concentrations (e.g. moles/m$^3$). A *concentration-based* equilibrium constant is related to the activity-based equilib-

rium constant in Eq. (2.29):

$$K_c = K_p \left( \frac{P^o}{RT} \right)^{\Delta n_{\text{gas}}} \tag{2.29}$$

$\Delta n_{\text{gas}}$ is the stoichiometric difference between the number of moles of *gaseous* products and *gaseous* reactants. For example from Eq. (2.20), assuming $A$, $B$, are $C$ are gaseous species, $n_{\text{gas}} = c - a - b$.

### 2.2.3 Multiphase Equilibrium

The general method of computing chemical equilibrium via free energy minimization can be extended to account for arbitrary heterogeneous *multiphase* mixtures involving any number of gas, solid, and liquid species. The formation of each specie $i$ included in the analysis can be written as the sum of gaseous constitutive species $k$, where each element corresponds to a constituent. Equation (2.30) generalizes this procedure:

$$\sum_k \nu_{k \to i} k \longrightarrow i \tag{2.30}$$

$\nu_{k \to i}$ is the stoichiometric coefficient to form species $i$ from $k$. Note that $\nu_{k \to i}$ can be either positive, corresponding to a reactant, or negative, corresponding to a reaction product.

Chemical equilibrium for each reaction is obtained with the equilibrium constant approach in Eq. (2.27), using species thermochemical data from NIST-JANAF [15]

or NASA polynomials [16], and is a function only of temperature at standard pressure. Equation (2.31) defines the partial pressure of gaseous species, and Eq. (2.32) states the necessary condition for condensed species in equilibrium with the gas-phase (assuming unit activities for the condensed species).

$$\ln K_{p,i}(T) = \ln P_i - \sum_k \nu_{k \to i} \ln P_k \tag{2.31}$$

$$\ln K_{p,i}(T) \geq - \sum_k \nu_{k \to i} \ln P_k \quad \begin{cases} \text{if} \quad = \quad \text{then } i \text{ is present as a condensed species;} \\ \text{if} \quad > \quad \text{then } i \text{ is not present in equilibrium.} \end{cases}$$

$$\tag{2.32}$$

To close the system of reaction equations, the total pressure must also be specified, and conservation of elements and total pressure are enforced.

These methods, or variants of these methods, are conveniently generalized in computational programs such as the Aerotherm Chemical Equilibrium (ACE) [17], NASA Chemical Equilibrium with Applications (CEA) [18, 19], and Cantera [20] codes. These programs employ iterative approaches to compute complex multiphase mixtures following the principle of Gibbs free energy minimization [18]. However, a complete discussion of these techniques are outside the scope of this dissertation, and the reader is encouraged to refer to the references for additional details.

## 2.3 LeMANS: Hypersonic Navier-Stokes Solver

For the applications examined throughout this work, the flowfield in hypersonic environments exhibit more complex physical and chemical phenomena than the materials. "Le" Michigan Aerothermodynamic Navier-Stokes Solver (LeMANS) is a Navier-Stokes solver developed at the University of Michigan specifically for hypersonic and subsonic flow applications with thermal and chemical nonequilibrium. It can handle unstructured three-dimensional meshes, and the governing equations are solved using the finite volume method. LeMANS has been benchmarked (DPLR, LAURA), verified, and validated (Apollo, Fire II, RAM-C) [21–23]. A brief overview of LeMANS is provided in this section, along with models for thermal and chemical nonequilibrium in hypersonic flowfields. No significant modifications were made to these capabilities, so the interested reader may refer to prior works for more detailed information on the implementation of specific features in the LeMANS code. [24]

### 2.3.1 Navier-Stokes Equations

LeMANS solves the compressible Navier-Stokes equations in Eqs. (2.33) to (2.37) that account for an arbitrary number of species $n$, as well as thermal and chemical nonequilibrium. The inviscid and viscous fluxes are split into vectors $\boldsymbol{F}$ and $\boldsymbol{F_v}$, with conserved variables $\boldsymbol{Q}$ and source terms $\boldsymbol{S}_{cv}$.

$$\frac{\partial \boldsymbol{Q}}{\partial t} + \nabla \cdot (\boldsymbol{F} - \boldsymbol{F_v}) = \boldsymbol{S}_{cv} \tag{2.33}$$

$$
\boldsymbol{Q} = \left\{ \begin{array}{c} \rho_1 \\ \vdots \\ \rho_{ns} \\ \rho u_i \\ \rho u_j \\ E \\ E_{ve} \end{array} \right\} \tag{2.34}
$$

$$
\boldsymbol{F_i} = \left\{ \begin{array}{c} \rho_1 u_i \\ \vdots \\ \rho_{ns} u_i \\ \rho u_i^2 + p \\ \rho u_i u_j \\ (E + p) u_i \\ E_{ve} u_i \end{array} \right\} \tag{2.35}
$$

$$
\boldsymbol{F_{v,i}} = \left\{ \begin{array}{c} -J_{i,1} \\ \vdots \\ -J_{i,ns} \\ \tau_{ii} \\ \tau_{ij} \\ \tau_{ii} u_i + \tau_{ij} u_j - (q_{tr,i} + q_{ve,i}) - \Sigma_s(J_{i,s} h_s) \\ -q_{ve,i} - \Sigma_s(J_{i,s} e_{ve,s}) \end{array} \right\} \tag{2.36}
$$

$$
\boldsymbol{S_{cv}} = \left\{ \begin{array}{c} \dot{\omega}_1 \\ \vdots \\ \dot{\omega}_{ns} \\ 0 \\ 0 \\ 0 \\ \dot{\omega}_{ve} \end{array} \right\} \tag{2.37}
$$

Spatial integration is performed over the inviscid and viscous fluxes using the finite-volume method, and the time integration is performed implicitly using the Backward Euler scheme. Temporal integration is first-order accurate, and spatial integration is second-order accurate [24]. The code is massively parallelized using

the OpenMPI software library, and mesh partitioning is performed with the METIS
software library [25].

## 2.3.2 Nonequilibrium Effects

**Thermal Nonequilibrium**

Thermal nonequilibrium is modeled using Park's two-temperature model [13]:

$$T_{\mathrm{tr}} \to T_{\mathrm{tran}} = T_{\mathrm{rot}} \tag{2.38}$$

$$T_{\mathrm{ve}} \to T_{\mathrm{vib}} = T_{\mathrm{elec}} = T_{e^-} \tag{2.39}$$

Energy levels within the respective partitions are assumed to follow the Boltzmann
relation at the partition temperature ($T_{\mathrm{tr}}$ or $T_{\mathrm{ve}}$).

The source term for the vibrational energy equation $\dot{\omega}_{ve}$ in Eq. (2.37) consists of
several components that model the relaxation and energy transfer processes between
internal energy modes:

$$\dot{\omega}_{ve} = \dot{\omega}_{t-v} + \dot{\omega}_{\mathrm{diss}} + \dot{\omega}_{h-e} + \dot{\omega}_{e-i} \tag{2.40}$$

Vibrational relaxation is modeled using the Landau-Teller equation [12] in Eq. (2.41).
Relaxation times for gaseous species can be approximated from the functional rela-
tionship of Millikan and White [26] in Eq. (2.42), where the parameters $a$ and $b$ are
typically fit from experimental data [26].

$$\dot{\omega}_{t-v} = \sum_s \rho_s \frac{e^*_{v,s} - e_{v,s}}{\tau_s} \tag{2.41}$$

$$\tau_s = \frac{1}{P_{\text{atm}}} \exp\left\{ \left[ a(T^{-1/3} - b) - 18.42 \right] \right\} \tag{2.42}$$

The remaining terms in Eq. (2.40) model the energy transfer from different chemical reactions. $\dot{\omega}_{\text{diss}}$ models the effect of dissociation reactions. A *non-preferential* dissociation model is utilized for this work, where molecules are created or destroyed at the average vibrational energy [24, 27]. Reactions between heavy particles and electrons can also transfer energy from the translational mode into the free electrons, described by $\dot{\omega}_{h-e}$. Electron-impact reactions remove energy from free electrons to ionize species, described by $\dot{\omega}_{e-i}$.

**Chemical Nonequilibrium**

The finite-rate chemistry model in LeMANS is evaluated using a modified Arrhenius rate coefficient:

$$k_f(T_c) = C_f T_c^{\eta_f} \exp\left( -\frac{\Theta}{T_c} \right) \tag{2.43}$$

The forward reaction parameters $C_f$, $\eta_f$, and $\Theta$ are provided as part of the chemical kinetic mechanism reaction set (see Appendix A). The rates are evaluated at a "control" temperature $T_c$, which may be $T_{\text{tr}}$, $T_{\text{ve}}$, or $\sqrt{T_{\text{tr}} T_{\text{ve}}}$ depending on the specific reaction.

A generic reaction may be specified as:

$$\sum \alpha_s A \leftrightarrow \sum \beta_s B \tag{2.44}$$
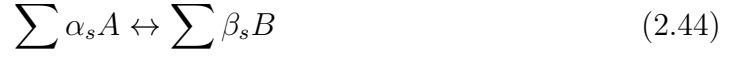
Backward reaction rates are evaluated using the *detailed balance* principle. For a system consisting of multiple "elementary" processes (i.e. individual reactions) in equilibrium, each individual step is in equilibrium with respect to its reverse process. Thus, forward and backward rates are related by the concentration-based equilibrium constant computed using the Gibbs free energy approach in Eq. (2.29):

$$k_b(T_c) = \frac{k_f(T_c)}{K_c(T_c)} \tag{2.45}$$

Gas concentrations are expressed in terms of partial species densities (kg/m$^3$), so a conversion is required to utilize the rates, which are generally specified in CGS units of cm$^3$/mol-s. The source term for species $s$ in reaction $k$ are then given by Eq. (2.47) [24]:

$$\dot{\omega}_{sk} = (\beta_{sk} - \alpha_{sk}) \left[ 10^3 k_{f,k} \prod_j \left( 10^{-3} \frac{\rho_j}{\mathcal{M}_j} \right)^{\alpha_{jk}} - 10^3 k_{b,k} \prod_j \left( 10^{-3} \frac{\rho_j}{\mathcal{M}_j} \right)^{\beta_{jk}} \right] \tag{2.46}$$

$$\dot{\omega}_s = \mathcal{M}_s \sum_k \dot{\omega}_{sk} \tag{2.47}$$

### 2.3.3 Thermodynamic and Transport Processes

In addition to the complex physical and chemical phenomena, diffusive transport effects need to be considered as well. Species-diffusion fluxes are modeled using

modified Fick's law:

$$J_i = -\rho D_i \nabla Y_i + Y_i \sum_{k=1}^{ns} J_k \tag{2.48}$$

Momentum fluxes and shear stresses are calculated assuming a Newtonian fluid with Stoke's hypothesis:

$$\tau_{ij} = \mu \left( \frac{\partial u_i}{\partial x_i} + \frac{\partial u_i}{\partial x_j} \right) + \delta_{ij} \lambda \nabla \bar{u} \tag{2.49}$$

$$\lambda = -\frac{2}{3} \mu \tag{2.50}$$

Conduction heat fluxes are calculated using Fourier's law for both translational-rotational and vibrational-electronic energy partitions:

$$q_{tr} = -\kappa_{tr} \nabla T_{tr} \tag{2.51}$$

$$q_{ve} = -\kappa_{ve} \nabla T_{ve} \tag{2.52}$$

LeMANS uses species thermodynamic data from NASA-9 polynomial fits [16]. The polynomials provide normalized enthalpy and entropy curve fits for each species:

$$\frac{h^o}{RT_{tr}} = -a_0 \frac{1}{T_{tr}^2} + a_1 \frac{\ln T_{tr}}{T_{tr}} + a_2 + a_3 \frac{T_{tr}}{2} + a_4 \frac{T_{tr}^2}{3} + a_5 \frac{T_{tr}^3}{4} + a_6 \frac{T_{tr}^4}{5} + a_7 \frac{1}{T_{tr}} \tag{2.53}$$

$$\frac{s^o}{R} = -\frac{a_0}{2} \frac{1}{T_{tr}^2} - a_1 \frac{1}{T_{tr}} + a_2 \ln T_{tr} + a_3 T_{tr} + a_4 \frac{T_{tr}^2}{2} + a_5 \frac{T_{tr}^3}{3} + a_6 \frac{T_{tr}^4}{4} + a_8 \tag{2.54}$$

Thermodynamic data from NIST-JANAF tables [15] and the NASA polynomials are

in good agreement for all relevant species. Transport properties (species diffusion, viscosity, thermal conductivity) are calculated using Wilke's semi-empirical mixing rule, with Blottner fits for viscosity and Eucken's relation for the thermal conductivity [28]. Charged species are treated with a single-fluid approach (since flows are usually "weakly" ionized [22]), and ambipolar diffusion of electrons enforces local quasi-neutrality [28].

The diffusion coefficients themselves are specie-dependent, and two models are employed to compute the species-dependent diffusion coefficients. In the simplest case, an average Lewis number-based diffusion coefficient is computed with Eq. (2.55). This method assumes *equal* diffusion coefficients for all species.

$$D_s = \frac{\kappa Le}{\rho C_p} \tag{2.55}$$

For cases when an average Lewis number is not known, the *bifurcation* model from Bartlett et al. [29] may be utilized. This method assumes *unequal* diffusion coefficients for each specie based on its molecular weight, and the correlation is accurate to within 15% for species differing up to an order of magnitude in molecular weight [29].

$$D_{ij} = \frac{D_{N_2}}{F_i F_j}, \quad F_i = \left( \frac{\mathcal{M}_i}{\mathcal{M}_{N_2}} \right)^{0.461} \tag{2.56}$$

$$D_s = \frac{D_{N_2}}{F_s F_{mix}} \tag{2.57}$$

## 2.3.4    Boundary Conditions

Implementation of supersonic inlet and outlet boundary conditions for the flow-field are described by Scalabrin [24]. Subsonic inlet and outlet boundary conditions were previously developed and validated by Anna and Boyd based on zeroth-order extrapolation [30].

Several wall boundary conditions are implemented as part of the work presented in this dissertation. A non-catalytic wall boundary conditions enforces zero-gradient in species mass fractions at the wall using 2nd-order accurate extrapolation, corresponding to a catalytic efficiency $\gamma = 0$. A fully-catalytic wall boundary condition enforces that all ions recombine with free electrons into their neutral counterparts (e.g. $\mathrm{Ar}^+ + \mathrm{e}^- \rightarrow \mathrm{Ar}$), and atomic species recombine into their molecular counterparts (e.g. $\mathrm{O} + \mathrm{O} \rightarrow \mathrm{O}_2$), corresponding to a catalytic efficiency of $\gamma = 1$. Blowing and reacting boundary conditions are also implemented, described in Chapters 3 and 5 respectively.

Convective wall heating is evaluated as the sum of three components: translational-rotational, vibrational-electronic, and species diffusion fluxes. With the two-temperature approach, translational-rotational and vibrational-electronic heat fluxes are each evaluated with Fourier's law, with separate thermal conductivities for each energy partition based on Eucken's relation [28] in Eq. (2.59). Modified Fick's law is used to

evaluate the species diffusion flux to the surface in Eq. (2.60):

$$Q_{\text{conv}} = Q_{\text{tr}} + Q_{\text{ve}} + Q_{\text{diff}} \tag{2.58}$$

$$Q_{\text{tr}} = -\kappa_{\text{tr}}\nabla T_{\text{tr}}, \quad Q_{\text{ve}} = -\kappa_{\text{ve}}\nabla T_{\text{ve}} \tag{2.59}$$

$$J_{w,i} = -\rho_w D_i \nabla Y_{w,i} + Y_{w,i} \sum_{k=1}^{\text{ns}} J_{w,k}, \quad Q_{\text{diff}} = \sum_{i=1}^{\text{ns}} J_{w,i} h_{w,i} \tag{2.60}$$

## 2.4   Material Response

There are limitations to using isothermal, steady-state wall assumptions to simulate hypersonic flowfields and their interactions with materials. Material response analyses arise from the need to evaluate in-depth, transient conduction effects. The effects of surface chemistry are also discussed in the context of materials, but are relevant to the flowfield in the near-wall boundary layer.

Generally, material response analyses involve solving a multi-dimensional transient heat conduction problem in Eq. (2.61) over a material domain. This material domain is separate from the CFD flowfield domain, but may exchange information with the flowfield at the aerothermal interface, which is typically posed as a boundary condition to the material domain.

$$\frac{\partial T}{\partial t} = \frac{\kappa}{\rho C_p}\nabla^2 T \tag{2.61}$$

## 2.4.1 B' Tables

B' thermochemical tables were developed to model ablation-type surface chemistry problems [17]. In this work, the B' approach is generalized to account for different TPS materials, including UHTCs. The non-dimensional B' parameter in Eq. (2.62) describes the ablating fluxes blowing from the surface in cases with surface chemistry and ablation. The B' parameter can be computed from the surface chemistry model, discussed later in Chapter 4.

$$B' = \frac{\dot{m}_w}{\rho_e u_e C_M} \tag{2.62}$$

The denominator is typically evaluated from CFD or boundary analysis of the surface fluxes. These B' values are tabulated as functions of ambient pressure and temperature and interpolated for a *fixed* chemical gas composition. Different gas compositions require new B' tables to be constructed. For pyrolyzing ablators, the effects of pyrolysis can also be included with a separate B'$_g$ that describes the production of pyrolysis gases [17, 31, 32], but are not relevant for the applications examined in this dissertation (B'$_g$ = 0).

## 2.4.2 Surface Mass and Energy Balance

At the interface of the flowfield and the material, the evaluation of surface fluxes in Eqs. (2.58) to (2.60) should be consistent between the flowfield and material domains, particularly when coupling the domains together [33]. The Surface Energy Balance (SEB) equation in Eq. (2.63) is relevant to *both* domains, and is illustrated
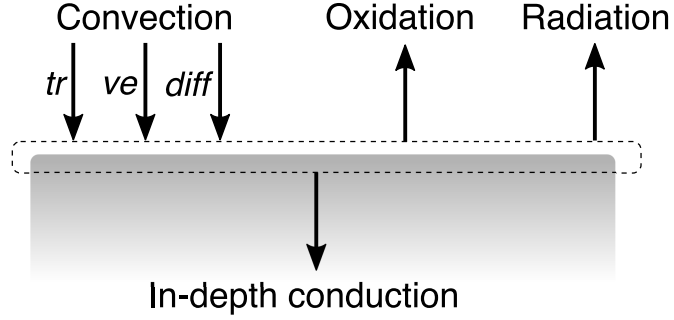
Figure 2.1: Surface energy balance.

in Fig. 2.1. The in-depth conduction term is evaluated from solving the thermal response of the material in Eq. (2.61), where Eq. (2.63) is imposed as a boundary condition and solved iteratively. In steady-state solutions, this term is often neglected, such as in radiative equilibrium CFD wall boundary conditions.

$$
\underbrace{-\kappa \nabla T \Big|_w \cdot \hat{n}}_{\text{Conduction}} = \underbrace{\rho_e u_e C_H (h_e - h_w)}_{\text{Convection}} - \underbrace{\epsilon \sigma (T_w^4 - T_\infty^4)}_{\text{Radiation}} - \underbrace{\dot{m}_w h_w}_{\text{Oxidation}} + \underbrace{\rho_w \dot{s} h_w}_{\text{Grid Convection}}
$$

$$(2.63)$$

In the full surface energy balance equation (Eq. 2.63), the oxidation term alone does not capture the effect of gas-surface reactions on the energy balance. Gaseous oxidation products blowing from the surface thicken the thermal boundary layer, reducing temperature gradients. The gas composition at the surface can also differ radically from the freestream composition due to consumption of oxygen and introduction of oxidation products. This directly affects the chemical species diffusion calculations and mixture enthalpy. These effects are implicitly captured in the evaluation of the convective heating $Q_w$, requiring a coupled approach. Grid convection

36

accounts for the non-stationary surface due to surface recession, and the surface re-
cession rate may be evaluated using B' tables with Eq. (2.64).

$$\dot{s} = \frac{\dot{m}_w}{\rho_s} = B' \frac{\rho_e u_e C_M}{\rho_s} \qquad (2.64)$$

To parameterize complex boundary layer transport phenomena, surface fluxes can
be expressed in terms of dimensionless heat and mass transfer *coefficients.* Consider
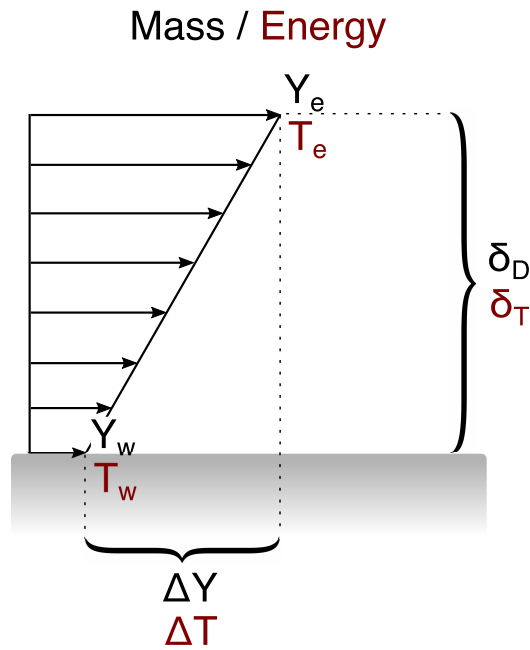


Figure 2.2: One-dimensional boundary layer approximation.

the one-dimensional boundary layer approximation in Fig. 2.2, with *linear* gradients
$\Delta Y = Y_e - Y_w$ and $\Delta h = h_e - h_w$. The mass and heat flux to the surface can
be expressed with Fick's law and Fourier's law respectively, over the boundary layer

height $\delta$:

$$J_w = -\rho_w D \nabla Y_w = -\rho_w D \frac{\Delta Y}{\delta_D} \tag{2.65}$$

$$Q_w = -\kappa \nabla T_w = -\kappa \frac{\Delta T}{\delta_T} \tag{2.66}$$

In this form, the mass and energy transport equations exhibit *similarity*. Note that in some media, the thermal boundary layer height, $\delta_T$, may differ from the diffusive boundary layer height, $\delta_D$. Dropping the negative sign for convention, the mass transfer coefficient is defined as:

$$J_w = \rho_w D \frac{\Delta Y}{\delta_D} = \rho_e u_e C_M \Delta Y \tag{2.67}$$

$$\boxed{C_M = \frac{\rho_w D}{\rho_e u_e \delta_D}} \tag{2.68}$$

The heat transfer coefficient is defined similarly, assuming a calorically perfect gas ($\Delta h = C_p \Delta T$) over the temperature range of $T_w$ to $T_e$:

$$Q_w = \kappa \frac{\Delta T}{\delta_T} = \kappa \frac{\Delta h}{C_p \delta_T} = \rho_e u_e C_H \Delta h \tag{2.69}$$

$$\boxed{C_H = \frac{\kappa}{\rho_e u_e C_p \delta_T}} \tag{2.70}$$

Conventionally, the Lewis number, $Le$, is defined as the ratio of the Schmidt to

Prandtl numbers [34]:

$$Le = \frac{Sc}{Pr} = \frac{\left(\frac{\mu}{\rho D}\right)}{\left(\frac{C_p \mu}{\kappa}\right)} = \frac{\kappa}{\rho C_p D} \tag{2.71}$$

The Lewis number can also be defined in terms of the mass and heat transfer coefficients from Eqs. (2.68) and (2.70):

$$Le = \frac{C_H}{C_M} = \left(\frac{\delta_D}{\delta_T}\right)\frac{\kappa}{\rho_w C_p D} \tag{2.72}$$

Thus, these definitions of $Le$ are functionally equivalent *at the wall*, assuming that the diffusive and thermal boundary layer heights are equal ($\delta_D = \delta_T$).

In two or three-dimensional reacting boundary layers, the explicit forms of $C_M$ and $C_H$ in Eqs. (2.68) and (2.70) are generally not valid, but it is still useful to express surface fluxes in terms of the coefficients. In practice, the heat transfer coefficient $C_H$ is computed from Eq. (2.73), where $Q_w$ is the total convective wall heating from Section 2.3.4.

$$\rho_e u_e C_H = \frac{Q_w}{h_r - h_w} \tag{2.73}$$

The recovery enthalpy at the boundary layer edge $h_r$ is typically assumed to be the stagnation enthalpy of the freestream. For inert, non-oxidizing surfaces, the mixture wall enthalpy is simply a function of the local wall temperature and pressure. For reacting surfaces, the mixture wall enthalpy is a function of the blowing and ambient gas compositions (usually in terms of the B' parameter). For cases with surface

chemistry, the oxidation/ablation term is evaluated from both the blowing mass flux $\dot{m}_w$ and mixture wall enthalpy $h_w$, which depend on the surface chemistry model, discussed later in Chapter 4. The mass transfer coefficient, $C_M$, is evaluated from $C_H$ using the Lewis number.

## 2.5    Chapter Summary

Overall, this chapter provided a description of the concepts, terms, and tools that will be utilized later throughout this work. General modeling approaches were described for various physical processes relevant to hypersonic flight and thermal protection systems. Thermal and chemical equilibria for multiphase reacting systems were discussed in the context of thermodynamic calculations. The CFD code LeMANS was described including models for thermal and chemical nonequilibria in hypersonic flows, as well as the calculation of transport phenomena. Lastly, the treatment of the material thermal response and surface fluxes were discussed, accounting for ablation and/or oxidation effects.

# CHAPTER 3

# Radiative Emission in Plasma Flows

An effective method to understand the response of a TPS material to a high-enthalpy environment is through the study of the gas-phase chemistry in the flow adjacent to the material surface. Investigation of the high-enthalpy environment is made possible by high-fidelity CFD analysis techniques. This provides a detailed understanding of the gas-phase chemical processes that occur in reacting boundary layers. Ablation experiments in plasma test facilities are often conducted to investigate the gas-phase reactions in the boundary layer, in collaboration with modeling and simulation work to evaluate chemical kinetic mechanisms. There are many uncertainties associated with the pyrolysis process regarding both the rate at which it occurs, and the composition of pyrolysis products. Thus, the experiments are designed to control both the rate and composition of the blowing gas [35, 36].

Near-surface optical emission spectroscopy allows the detailed chemical kinetics in the boundary layer to be examined. As a diagnostic tool, optical emission spectroscopy has also been used to determine the presence of certain species in flows [37]. It is not trivial to extract fundamental quantities such as species number density and temperature from these measured spectra, often relying on assumptions of Local

Thermodynamic Equilibrium (LTE) or a detailed description of nonequilibrium [38]. As a result, emission spectroscopy is often limited to qualitative comparisons.

There is extensive work in using collisional-radiative models in a CFD framework to predict emission and radiation [39]. These works often rely upon CFD finite-rate chemistry and collisional-radiative mechanisms to predict populations of species and excited states. Furthermore, there has been an increased ability to model these spectra with codes such as NEQAIR [40]. The improved experimental design provides spatially-resolved, absolute intensity measurements, and allow direct quantitative comparisons between spectra.

There are two main goals for the work described in this chapter: (1) investigate the gas-phase interactions between pyrolysis products and boundary layer, and (2) model these gas-phase chemical kinetics using a CFD-radiation framework. The experiments, measurements, and numerical approach are described. Then, comparisons are made between experimental and numerical results to evaluate the chemical rate mechanisms used to model the chemical kinetics.

## 3.1    Experimental Test Facility

High-enthalpy ground test facilities enable the testing and evaluation of TPS materials in controlled environments. These include both hypersonic (e.g. arcjet) and subsonic, high-enthalpy facilities (e.g. plasma torch). The 30 kW Inductively-Coupled Plasma (ICP) torch at the University of Vermont (UVM) provides subsonic, high-enthalpy flow using a range of gas mixtures to simulate post-shock conditions [41].

Experimental conditions can be extrapolated to flight conditions by matching the enthalpy, stagnation pressure, and velocity gradient at the boundary layer edge. [42]. The facility is shown in Figs. 3.1 and 3.2, and flow exiting the torch is ionized and electronically excited.
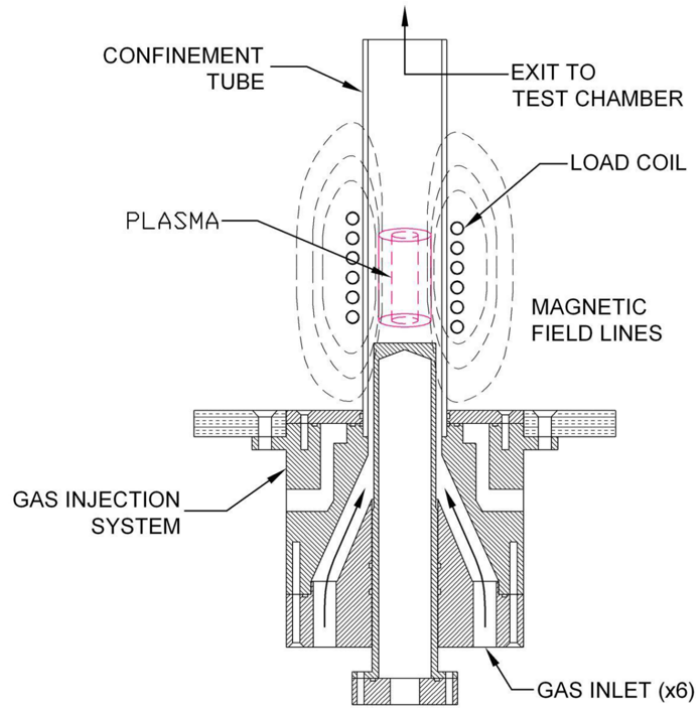


Figure 3.1: Schematic of ICP torch. Image reproduced from Ref. [43].

A 25.0 mm diameter gas-injection probe delivers $CO_2$, $H_2$, or a mixture into the boundary layer of the impinging plasma jet. The injected gas composition mimics the pyrolysis gas products of PICA. The probe consists of a water-cooled copper holder and a porous graphite plug, with a porosity consistent with that of PICA. The diameter of the plug is 11.0 mm. The injection gas is blown through the porous graphite plug, mimicking the char layer of a pyrolyzing TPS.
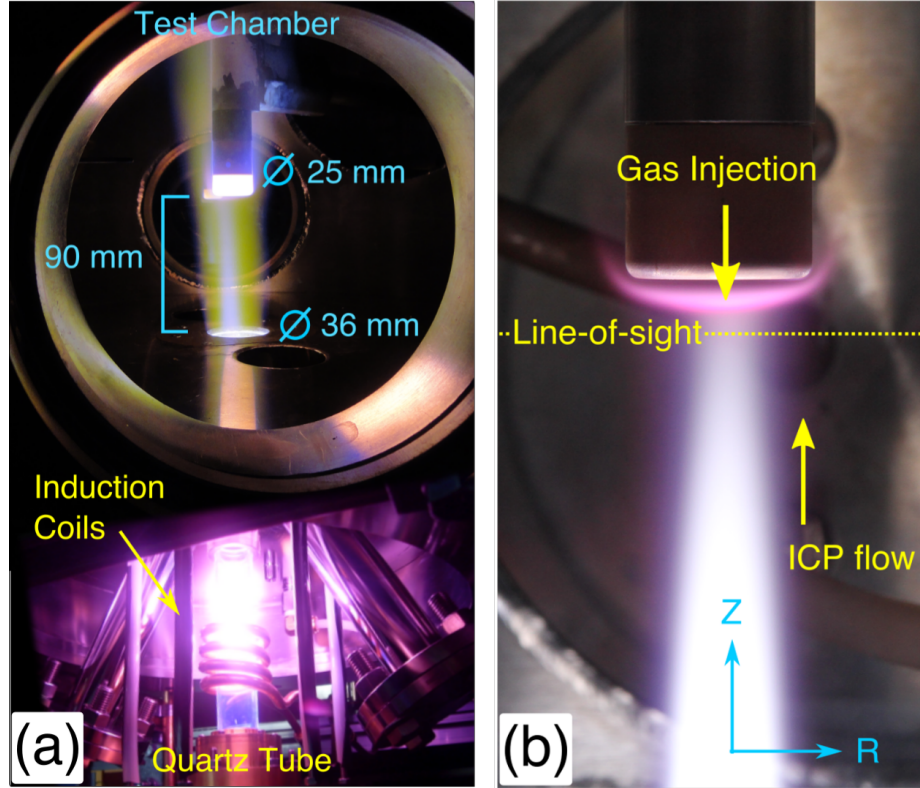
Figure 3.2: UVM's 30 kW ICP torch facility and experiments, (a) composite image of ICP torch facility, and (b) probe and spectroscopy setup.

### 3.1.1 Diagnostics

Optical emission spectroscopy is used to examine the boundary layer gas composition. The spectra are primarily dependent on the species number densities and temperatures along the spectrometer line-of-sight (LOS). These are strongly affected by the chemical interactions between the freestream plasma and the injected gas, where thermal and chemical nonequilibrium effects are important. The spectroscopic measurement schematic is shown in Fig. 3.2(b), where the spectrometer LOS is taken radially near the probe face, perpendicular to the plasma jet. Spatially- and spectrally-resolved radiative emission measurements are taken in-situ at various axial locations, from 0.0 to 4.0 mm, when the flow has reached "steady-state" as deter-

mined from the emission measurements. These measurements are compared directly with the numerical simulations in this chapter.

The spectrometer is an Ocean Optics HR4000CG-UV-NIR high resolution grating spectrometer, with a slit width of $5\mu$m, a line function Full Width at Half Maximum (FWHM) of 1.65 nm, and a spectral range of 200 - 1100 nm. LTE analysis is performed on calibrated, experimentally measured argon spectral lines to estimate the plasma electronic temperature in the probe boundary layer. Laser-Induced Fluorescence (LIF) can also provide an independent measurement of the translational temperature by resolving the Doppler width of the absorbing transitions for plasma compositions with significant populations of N or O atoms [44]. The LTE method was previously tested and found to provide good agreement with LIF temperatures for a plasma composition with 8 SLPM $O_2$ and 30 SLPM Ar [45]. If the plasma is in thermal equilibrium, the translational temperature given by LIF and the electronic temperature assuming LTE will be equal, so the measured spectra can also provide estimates of the overall plasma temperature. Assuming fully dissociated $N_2$ and $O_2$, flow enthalpies at the estimated temperatures also agreed with chemical equilibrium values within 3%.

However, it should be noted that argon spectroscopy can be unreliable with respect to LTE analysis. Kruger, Owano, and Gordon [38, 46–48] demonstrated deviation from LTE assumptions in argon plasmas with trace amounts of molecular diluent, and strong nonequilibrium in the bound and free electrons. They observed that LTE assumptions overpredict the radiative source strength at lower plasma densities. The plasma compositions used in this work utilize significantly less molecular diluents

than the plasma used to validate the LTE method, and this may increase the level of electronic nonequilibrium in the ICP facility, which is not well characterized over the limited number of transitions observed.

## 3.2    Radiative Emission Spectroscopy

Although a complete description of simulating radiative emission is outside the scope of this work, the basic physical phenomena are described in this section, along with modeling approaches.

### 3.2.1    Modeling Physical Processes

Radiative emission and absorption are inherently linked to transitions between electronic and vibrational energy levels. *Spontaneous* excitation and quenching (de-excitation) processes between energy levels leads to absorption and emission of photons at specific wavelengths, usually characteristic of the respective atomic or molecular specie. This is illustrated in Fig. 3.3. Energy transfer via collisions with particles or even electrons can also cause transition to a higher/lower state. When these processes are aggregated over all species and energy levels, they lead to the emission spectra observed in the experiments and measured by spectrometers.

Generally, transitions between electronic energy levels (e.g. A-X or B-X) determine the radiating/absorbing wavelength bands for each specie. For atoms, only transitions between the electronic energy levels need to be considered. Consequently, these typically correspond to very distinct or sharp emission/absorption lines in wavelength
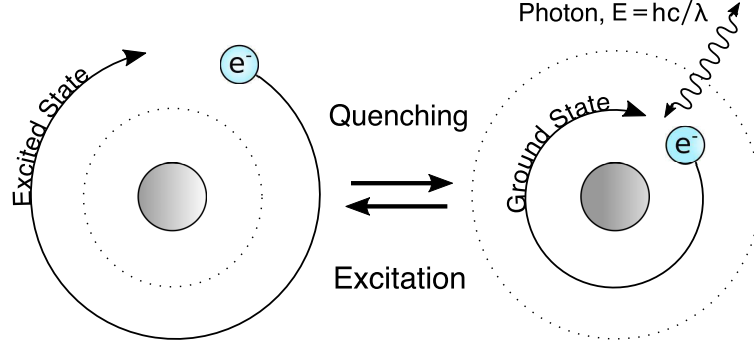
Figure 3.3: Spontaneous excitation and quenching processes.

space. For diatomic molecules, there are significantly more transitions to consider due to the interaction of electronic and vibrational energy levels [12]. The characteristic diatomic potential energy well is illustrated in Fig. 3.4, where $r$ refers to the intermolecular distance. The vibrational levels are populated within *each* electronic level, so every vibrational-specific transition pair (v'-v") contributes to the overall radiation from the electronic transition. Spectrally, this leads to band *shapes* rather than distinct lines.

There are two parts to modeling radiative emission: (1) determining excited level populations, and (2) computing transition probabilities. The first part involves estimation of the excited state populations, whether in equilibrium or nonequilibrium.

For a gas or plasma in LTE, the populations of excited state levels are related by simple thermodynamic relations, according to the Boltzmann distribution in Eq. (3.1). To relate the energy levels to the states, the Boltzmann ratio is weighted by the degeneracies $g_i$ and $g_j$ of levels $i$ and $j$ (number of states that occupy the same level). For molecules, the vibrational-electronic partition function $Q_{ve}$ needs to be included with the electronic degeneracy to normalize the populations, e.g. $g_i Q_{ve,i}$. The overall electronic populations are Boltzmann distributed, as well as the individual vibrational
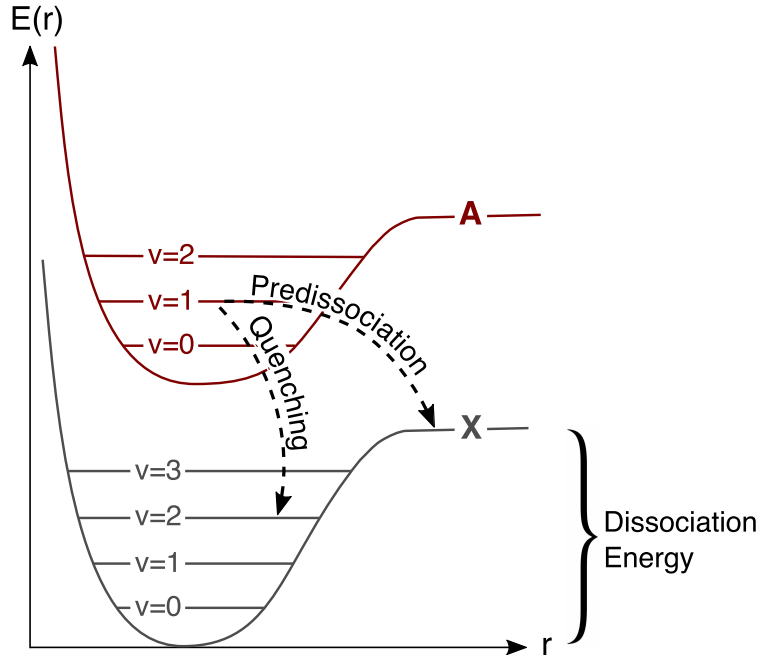
Figure 3.4: Potential energy well for molecules showing electronic and vibrational energy levels.

levels within each electronic level.

$$\frac{n_i}{n_j} = \frac{g_i}{g_j} \exp\left(\frac{\Delta E_{ij}}{k_B T}\right) \tag{3.1}$$

$$\Delta E_{ij} = E_j - E_i = -(E_i - E_j) \tag{3.2}$$

From the Boltzmann relation, a thermodynamic temperature can be defined that relates the populations of two different energy levels $i$ and $j$ in Eq. (3.3). This is defined as the *Boltzmann* temperature.

$$T_B(i,j) = \left[\frac{k_B}{\Delta E_{ij}} \ln\left(\frac{n_i/g_i}{n_j/g_j}\right)\right]^{-1} \tag{3.3}$$

Figure 3.5 shows a sample Boltzmann population distribution for the first three elec-

tronic levels of CN ($X^2\Sigma^+$, $A^2\Pi$, $B^2\Sigma^+$). Equation (3.1) is represented as a straight line on a semi-log plot of the population distribution, and the slope of the distribution is proportional to the inverse of the Boltzmann temperature. Thus, a gas in LTE can be adequately described by a *single* temperature.
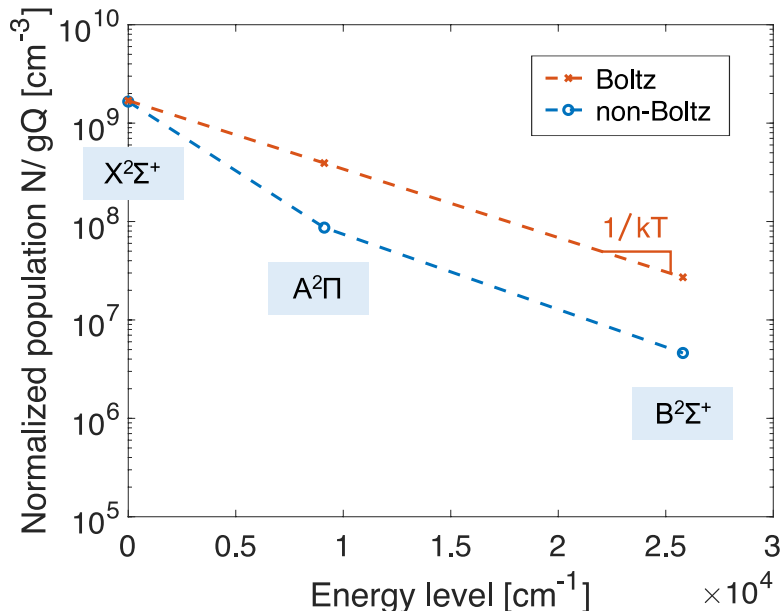


Figure 3.5: Example Boltzmann and non-Boltzmann population distributions for CN.

In contrast, a non-Boltzmann distribution cannot be described by a single temperature. To model non-Boltzmann populations, multi-temperature models approximate deviations from Boltzmann behavior. In addition to defining separate temperatures to describe the distribution of internal energy, separate temperatures can be defined for each electronic transition, such as in Fig. 3.5.

On a more detailed level, the Quasi-Steady State (QSS) assumption models the non-Boltzmann population distribution from individual mechanisms. Excitation and quenching processes are assumed to be related by detailed balance, which relaxes to

the Boltzmann distribution in Eq. (3.1). This is analogous to a state-to-state (STS) or collisional-radiative (CR) finite-rate chemistry approach employed in nonequilibrium CFD. Broadly, these mechanisms can be characterized as heavy-particle (H-P) or electron-impact (E-I). For atoms, only H-P and E-I excitation/quenching mechanisms are involved. For molecules, H-P and E-I excitation processes can lead to dissociation, which preferentially reduces the population of higher energy levels. *Predissociation* can also occur, where a molecule in a high energy state is transferred directly to a dissociative state (right side of the potential energy well in Fig. 3.4), and is independent of quenching. Rates for each of these mechanisms can be found in the literature, particulary the works of Park [49, 50] and Laux [51] for air species.

Recall that both collisional and "spontaneous" (emission/absorption) processes lead to energy level transitions. For both Boltzmann and non-Boltzmann populations, the second component in modeling radiative emission is determining the probability that vibrational-electronic transitions occur through *spontaneous* emission/absorption, rather than through collisional processes. Since only electronic transitions are possible for atoms, this probability is expressed in terms of *Einstein coefficients*. The Einstein $A$ coefficient relates to the radiative emission probability, and the $B$ coefficient relates to the absorption probability, and both are species and transition-specific.

For molecules, the Einstein coefficient $A_{v'v''}$ describes the spontaneous vibrational-specific transition probability between $v'$ and $v''$, and can be expressed in the form of

Eq. (3.4):

$$A_{v'v''} = \text{constant} \times \left[ \int \psi_{v'}^* R_e(r)\psi_{v''} dr \right]^2 \tag{3.4}$$

$\psi_{v'}$ is the vibrational wavefunction for level $v'$, and $R_e(r)$ is the *transition moment.* In practice however, the *r-centroid* approximation in Eq. (3.5) is used to evaluate the integral in Eq. (3.4) [52]:

$$\int \psi_{v'}^* R_e(r)\psi_{v''} dr \approx \left( q_{v'v''} \right)^{1/2} R_e(\bar{r}_{v'v''}) \tag{3.5}$$

$$q_{v'v''} = \left[ \int \psi_{v'}^* \psi_{v''} dr \right]^2 \tag{3.6}$$

$R_e(\bar{r}_{v'v''})$ is the transition moment evaluated at the r-centroid, $\bar{r}_{v'v''}$. The integral $q_{v'v''}$ is the *Franck-Condon* factor, defined in Eq. (3.6). These parameters can be found in the literature for various species and transitions [52]. For reference, Appendix B describes the development of Boltzmann and non-Boltzmann (QSS) radiative models for NH.

To compare with physical spectrometer measurements, convolution of the emission spectra with the spectrometer slit function (typically modeled as a Gaussian, Lorentzian, or Voigt profile) is needed. Note that this effect is due to the spectrometer itself, and not inherently a feature of the radiative emission, such as Stark broadening. Overall, the effect of broadening is to turn sharp spectral features into Gaussian-like profiles. From spectrometer measurements, the Boltzmann temperature of the emitting medium can be estimated by relating the intensity of spectral

lines to the population ratios under the LTE assumption, since each line corresponds to a specific electronic transition (LTE analysis). This is most effective for atomic species which exhibit distinct spectral lines, such as argon or hydrogen.

### 3.2.2 NEQAIR Program

The Nonequilibrium and Equilibrium Radiative Transport Spectra (NEQAIR) code was developed at NASA Ames Research Center to simulate the radiative emission along a line-of-sight (LOS) [53]. NEQAIR v14.0 [40] is used to model the radiative spectrum of a line-of-sight extracted from the CFD solution, corresponding to the spatially-resolved spectrometer measurements in Fig. 3.2(b). NEQAIR performs high spectral resolution radiative calculations for the emission and absorption of species integrated along the LOS, followed by convolution with the instrument slit function [54]. A Gaussian line profile is used with a width equal to the FWHM of the spectrometer. This overall process is illustrated in Fig. 3.6 for CN A-X and B-X emission calculations. The lines-of-sight are extracted radially outward from the axisymmetric line in Fig. 3.7, and mirrored to account for the wall-to-wall line-of-sight. Gas outside the computational domain is assumed to be optically thin.

For the two-temperature model employed in CFD, ground-state chemical kinetic mechanisms assume that the populations of all ground and excited states $i, j$ are described by the equilibrium vibrational-electron-electronic temperature $T_{ve}$, according to the Boltzmann temperature (Eq. 3.3). This is a significant limitation of this approach when performing radiative emission calculations.
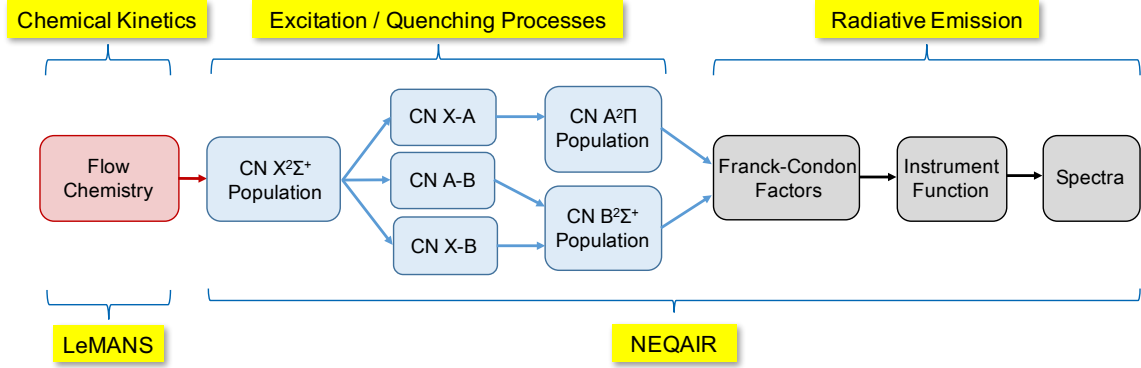
Figure 3.6: Coupling of LeMANS and NEQAIR for CN A-X and B-X non-Boltzmann calculations.

Comparison of the radiative spectra provides data for assessment of the accuracy of CFD predictions of the species number densities and temperatures, obtained using the chemical kinetics mechanism. Non-Boltzmann modeling is used for species if available. NEQAIR supports non-Boltzmann modeling for excited states of CN from Hyun and Park [55], but not OH, argon or atomic hydrogen, which are important for this work. However, there remain some uncertainties in the CN bands (violet and red) [40]. NH, which is a primary radiator for flows with $H_2$ injection and air, was not modeled by NEQAIR at the time of this work. Boltzmann and non-Boltzmann models were later developed for NH emission, described in Appendix B. The total radiative heating to a body can be computed by integrating over solid angles and wavelength space.

## 3.3 Experimental Conditions

Experimental freestream conditions studied are summarized in Tables 3.1. For all conditions reported, the chamber pressure is 21.3 kPa. The freestream plasma

compositions listed in Table 3.1 consist of a predominantly argon plasma. Molecular diluents are added to examine the effects of nitrogen and oxygen individually. Argon is used to dilute the plasma and slow the reaction kinetics because it is chemically inert with respect to other species, although it can ionize and serve as a third body in other reactions inefficiently. Perhaps due to base pressure leakage or impurities in the argon gas, additional air species are present even in the "pure" argon case. Levels of $N_2$ and $O_2$ in Table 3.1 are estimated by fitting $N_2$ and $O_2$ mass fractions to measured spectra [44], and these are accounted for in the simulations performed.

Table 3.1: Experimental ICP Exit Conditions (Freestream)

| Plasma | Gas [SLPM] | $T_{exit}$ [K] | $T_{90mm}$ [K] | $h_{exit}$ [MJ/kg] | $Y_{Ar}$ | $Y_{N_2}$ | $Y_{O_2}$ |
|---|---|---|---|---|---|---|---|
| Pure Ar | 40 Ar | 7750 | 7675 | 4.36 | 98.9% | 0.7% | 0.4% |
| Dilute $N_2$ | 40 Ar + 2 $N_2$ | 6625 | 6584 | 4.96 | 95.3% | 4.3% | 0.4% |
| Dilute $O_2$ | 40 Ar + 2 $O_2$ | 7600 | 7456 | 5.05 | 95.2% | 0.7% | 4.1% |

The plasma temperature is estimated 90 mm downstream from the torch exit using LTE analysis of measured argon lines [56], and values for each transition examined are summarized in Table 3.2. These plasma measurements were performed without the probe present (no blowing effects) for more accurate freestream measurements. The temperature values from LTE analysis vary by 3 - 5% depending on the individual transition examined, and the values reported in Table 3.1 are simply the unweighted average. Note that these values are based on the assumption that the chamber gas is optically thin, which is verified later with numerical emission and absorption simulations along the LOS.

A calibrated MKS M100B mass flow controller is used to measure the blowing

Table 3.2: LTE Temperature Analysis - Experimental Argon Lines

| Measurement | Pure Ar | Dilute $N_2$ | Dilute $O_2$ |
|---|---|---|---|
| *Utilized in simulations* | | | |
| $T_{mean}$ [K][a] | 7675 | 6584 | 7456 |
| Uncertainty[b] | 3.6% | 5.4% | 3.7% |
| *Individual Ar transitions[c]* | | | |
| $T_{734.8nm}$ | 7615 | 6574 | 7447 |
| $T_{763.5nm}$ | 7569 | 6553 | 7417 |
| $T_{772.4nm}$ | 7848 | 6784 | 7636 |
| $T_{794.8nm}$ | 7614 | 6582 | 7420 |
| $T_{912.3nm}$ | 7729 | 6428 | 7358 |

[a] Unweighted mean over individual temperatures
[b] Evaluated as $|T_{max} - T_{min}|/T_{mean}$
[c] All temperatures in K

gas injection rates [44]. For the blowing conditions in Table 3.3, the $CO_2$ injection rates vary from 148 to 493 sccm, but only one flowrate for $H_2$ is tested. Transpiration cooling through the porous plug maintains a relatively cool probe surface, buffers the graphite plug, and protects it from surface oxidation and nitridation. The wall temperature measured at the probe varies with injection rate, and is obtained by averaging over many runs.

Table 3.3: Gas Injection Conditions

| Blowing Gas | Blowing Rate [sccm] | Wall Temperature [K] |
|---|---|---|
| $CO_2$ | 148 | 617 |
| $CO_2$ | 282 | 578 |
| $CO_2$ | 493 | 531 |
| $H_2$ | 282 | 578 |

## 3.4  Simulation Methodology

A CFD-radiation framework is developed utilizing LeMANS and NEQAIR to simulate the plasma experiments and spectrometer measurements described in the preceding sections. The implementation-specific aspects are described here.

### 3.4.1  Chemical Kinetics Mechanism

For plasmas, a distinction must be made between bound and free electrons. In the two-temperature model, the vibrational-electron-electronic temperature $T_{ve}$ describes both bound and free electrons. Free electrons are treated as a distinct species that can be in chemical nonequilibrium with neutral and ionized species, but are assumed to be in thermal equilibrium with the bound electrons and the vibrational mode [23]. The chemistry mechanisms used in this work involve reactions that are assumed to occur between and result in atoms and molecules in thermal equilibrium with the ground-electronic state. Excited states are assumed to follow a Boltzmann distribution. Note that any non-Boltzmann effects are modeled separately in NEQAIR [40].

**Johnston-Brandis Rate Mechanism**

The Johnston-Brandis chemical rate mechanism for $CO_2$-Air chemistry [57] is detailed in Appendix A.1. The mechanism contains 18 species and 34 reactions. However, it lacks Ar and $Ar^+$, which are important for this work. Including these two species with an Ar electron impact ionization reaction from Park and Lee [58] results in a mechanism with *20 species* and *35 reactions*. This mechanism is suitable for sim-

ulating flows with Ar, N, O, and C-bearing species, and is thus used for simulating the test cases with $CO_2$ injection. Validation of the Johnston mechanism was performed with comparisons to shock-tube emission measurements of CN and CO [57], but it is important to note that a non-Boltzmann heavy particle and electron impact excitation model for CN and CO was used in conjunction with the mechanism, unlike in this study.

**Martin Rate Mechanism**

The Martin chemical rate mechanism is described in detail by Martin *et al.* [59] Like the Johnston mechanism, the baseline mechanism neglects Ar and $Ar^+$ and contains 38 species and 158 reactions. Including the argon species and the same electron impact ionization reaction results in a mechanism with *40 species* and *159 reactions*. The resulting mechanism is suitable for simulating flows with Ar, N, O, C, and H-bearing species, and is used for simulating conditions with both $H_2$ and $CO_2$ injection. The Martin mechanism can be simplified significantly if either C or H elements are not present, as species and reactions involving the respective element can be neglected. This mechanism was validated with shock tube measurements of C, CN, and CH concentrations [59], and demonstrated improved accuracy over the models of Park [9], Suzuki [60], and Olynick [61]. However, detailed reactions involving of $H_2$ and OH were not examined by Martin *et al.*, and their accuracy has not been validated prior to this study.

## 3.4.2 Computational Domain

All computational work presented here is two-dimensional axisymmetric. The computational grid is shown in Fig. 3.7 consisting of 22,130 quad elements. Grid convergence is verified when refining the mesh by a factor of 2 in both radial and axial directions results in less than 2% change in the peak centerline species densities. The injection probe has a diameter of 25 mm, and is located 90 mm from the ICP exit. The Reynolds number over the length of interest (the injection probe) is less than 1000 for all cases, so flow is assumed to be laminar throughout the domain.
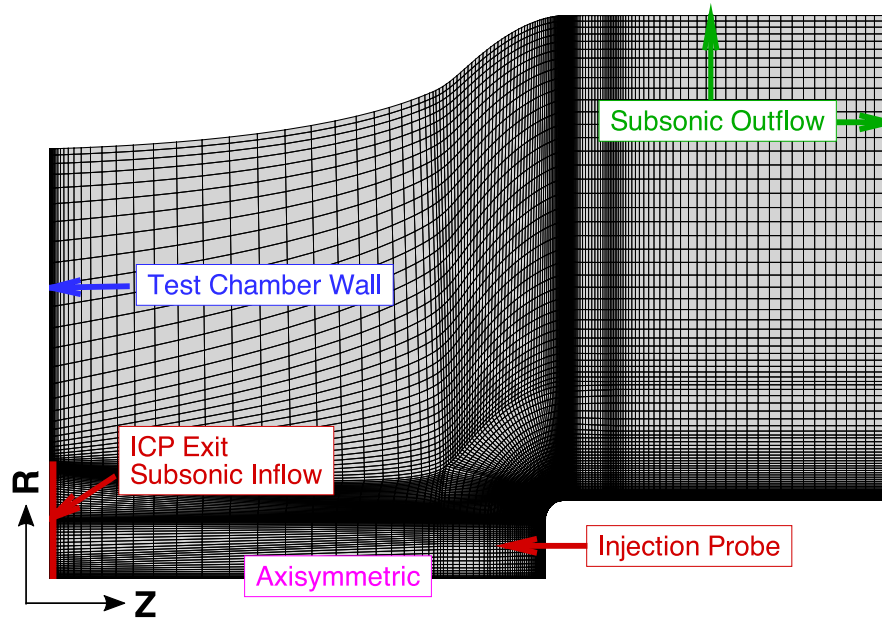


Figure 3.7: Two-dimensional axisymmetric computational mesh and boundary conditions for blowing cases.

**Boundary Conditions**

For the "baseline" simulation, chemical equilibrium analysis (CEA) [62] is performed to obtain the mass fractions of all relevant species at the inlet, using the

freestream plasma conditions in Table 3.1 and chamber pressure of 21.3 kPa. The effects of experimental uncertainty in the LTE temperature measurements are subsequently evaluated by performing corresponding simulations at $\pm5\%$ from these baseline temperatures. Thermal equilibrium $(T_{tr} = T_{ve})$ is assumed at the torch exit due to insufficient characterization of the ICP nonequilibrium, and is consistent with experimental LTE analysis assumptions.

Figure 3.7 shows the boundary conditions imposed on the domain. The chamber pressure is imposed on the subsonic inflow and exit boundaries, and the uniform inflow condition obtained from CEA [62] at the extrapolated state is imposed directly on the cells that are located at the ICP exit. An isothermal temperature of 300K is imposed at the test chamber wall. For cases with blowing, an isothermal wall temperature is imposed at the injection probe using values from Table 3.3. Effects of wall catalysis are included, assuming fully-catalytic recombination for species other than nitrogen. Graphite has been shown to be partially catalytic for atomic nitrogen, for which a recombination efficiency of 0.07 is used [30].

**Blowing Wall Implementation**

A blowing wall boundary condition models the gas injection process, with *uniform* mass fluxes computed from the blowing rates in Table 3.3. The implementation follows Martin and Boyd [31], and Thompson and Gnoffo [63]. Considering the surface momentum balance in Eq. 3.7 with the ideal gas law, one can derive expressions for

the state of the gas in the ghost cells (Eqs. 3.8 to 3.10).

$$p_\eta = p_w(\rho, T_w) + \rho_w u_w^2 \tag{3.7}$$

$$\rho_w = \frac{p_\eta + \sqrt{p_\eta^2 - 4RT_w\dot{m}^2}}{2RT_w} \tag{3.8}$$

$$u_w = \frac{2RT_w\dot{m}}{p_\eta + \sqrt{p_\eta^2 - 4RT_w\dot{m}^2}} \tag{3.9}$$

$$p_w = \frac{p_\eta + \sqrt{p_\eta^2 - 4RT_w\dot{m}^2}}{2} \tag{3.10}$$

A uniform distribution of mass flux is assumed over the plug surface, since the blowing velocities are concentrated at the probe stagnation point, and are typically two orders of magnitude smaller than the freestream velocity of the plasma. The mass fractions at the wall $Y_w$ are obtained by solving the surface mass balance in Eq. 3.11, following Martin and Boyd [8].

$$\rho_w D_s \frac{\partial Y_w}{\partial \eta} + \dot{m}Y_w = \dot{m}Y_g \tag{3.11}$$

## 3.5   Results

Typical CFD results are shown in Fig. 3.8. The propagation of the plasma jet downstream from the ICP exit and onto the injection probe is modeled, allowing for thermal and chemical nonequilibrium in the expanding jet. Convective losses to the chamber environment are accounted for in the simulation, but radiative losses from the hot plasma to the cooler chamber are not. The interaction of the blowing gas and plasma is demonstrated in Fig. 3.8(b), where the formation mechanism of CN
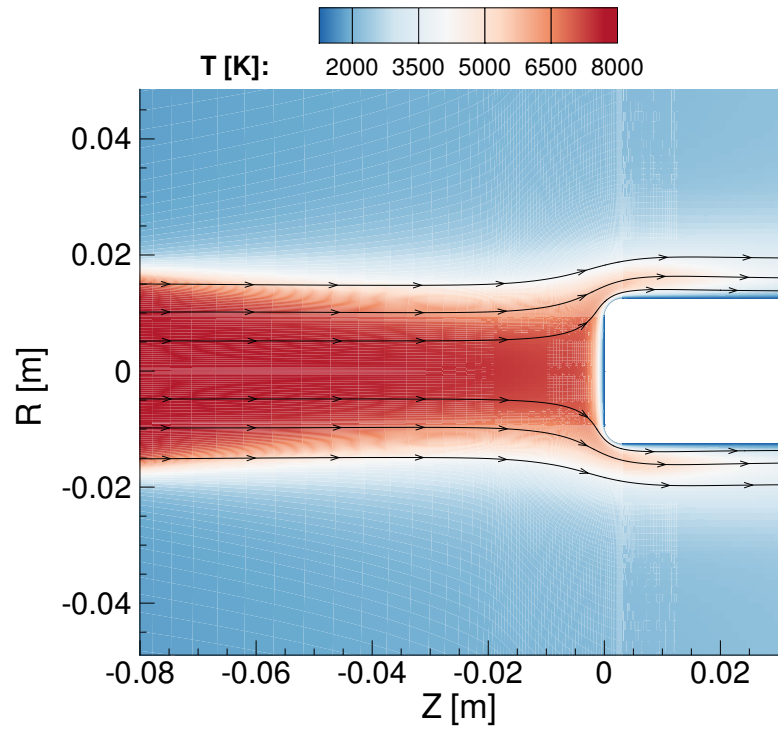
(a) Translational-rotational temperature
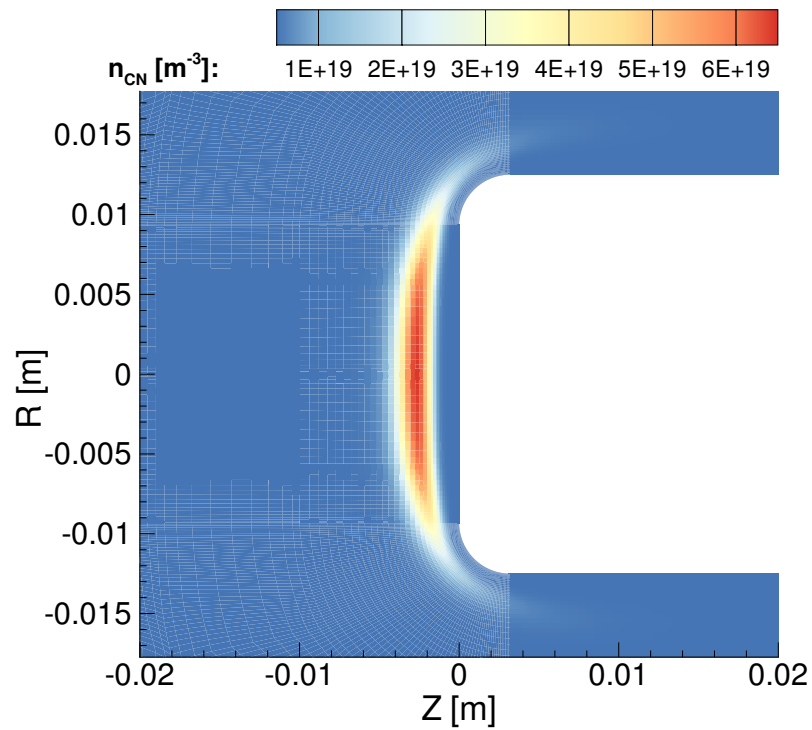


(b) CN number density

Figure 3.8: CFD results for Dilute $N_2$/282 sccm $CO_2$.

involves the dissociation of injected $CO_2$ gas and exchange reactions with plasma species. A peak of CN develops at some offset from the wall. Similar behavior is observed with NH and OH when $H_2$ is injected from the probe. Note that "0" is set to 90 mm downstream from the torch exit, corresponding to the location of the probe face when inserted into the chamber.

### 3.5.1   Argon Calibration Case

The argon calibration case involves the Pure Argon plasma in Table 3.1, and no gas injection. No differences are observed between Johnston and Martin mechanisms for this case, since the argon impact ionization reaction is the same in both mechanisms. Hence, this configuration evaluates and validates the radiative modeling framework.
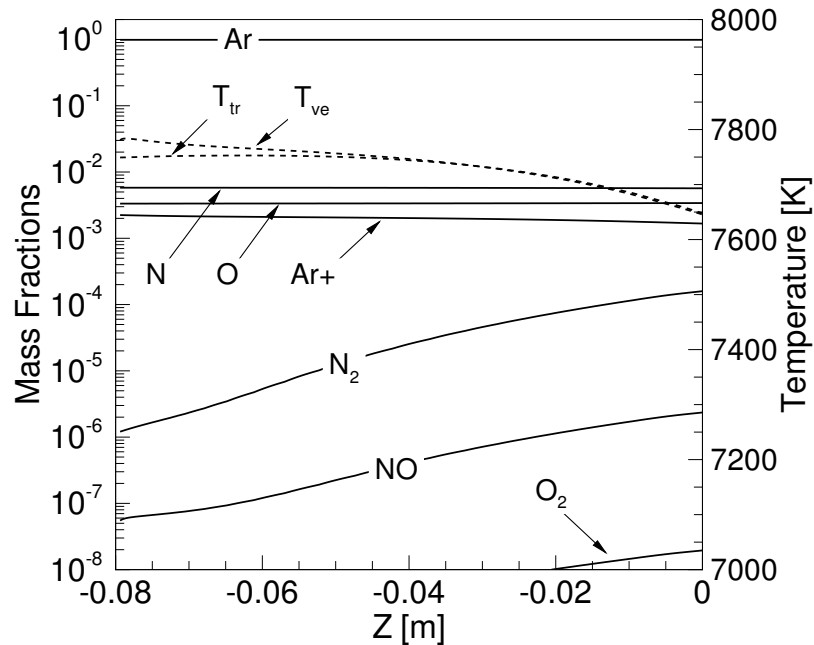


Figure 3.9: Centerline species mass fractions and temperatures for Pure argon plasma, no gas injection.

Predicted species mass fractions on the centerline are shown in Fig. 3.9. Argon is the dominant species, with less than 1% air species, and both oxygen and nitrogen are fully dissociated. No wall effects are present, as the probe is not inserted into the test chamber for this case, although some gas-phase recombination is observed along the stagnation line. With the two-temperature model, the plasma reaches thermal equilibrium well upstream of the probe location.



(a) Spectrally-resolved emission

(b) Spectrally-integrated emission
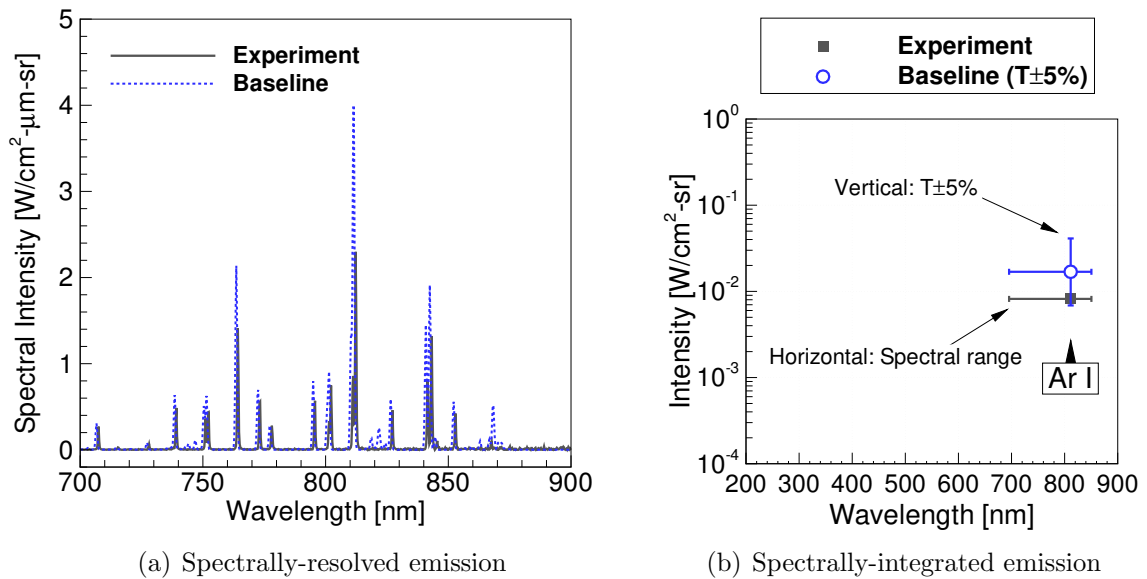
Figure 3.10: (a) Spectrally-resolved emission for Pure argon plasma, no gas injection, 2.0 mm probe offset. (b) Spectrally-integrated emission. Horizontal bars: integration range. Vertical bars: ±5% temperature.

Figure 3.10 compares the experimental and NEQAIR-computed spectra, and argon is the only radiative species observed. Argon is directly affected only by the impact ionization reaction in both chemistry mechanisms, which are identical. The baseline case indicates thermal equilibrium, assuming a Boltzmann distribution at the average LTE temperatures, and matches the experimentally measured peaks within a factor of two in Fig. 3.10(a). Likewise, the spectrally-integrated emissions differ by a

factor of two, and a $\pm 5\%$ uncertainty margin in the experimental LTE temperatures accounts for this difference, as shown in Fig. 3.10(b).

## 3.5.2 $CO_2$ Injection

In $CO_2$ injection cases, CN is the primary radiator. Its formation involves the dissociation of $CO_2$ and exchange reactions with CO and NO described in Eqs. (3.12)–(3.14). The rates of these reactions are described by the Martin and Johnston mechanisms, and dissociation of $CO_2$ is the rate-limiting step [57,64].

$$CO_2 + M \leftrightarrow CO + O + M \tag{3.12}$$

$$CO + N \leftrightarrow CN + O \tag{3.13}$$

$$C + NO \leftrightarrow CN + O \tag{3.14}$$

Both mechanisms have been validated against experimental data [57,59], but the $CO_2$ injection cases allow direct comparison of these mechanisms. Since the formation of CN is directly affected by the activity of atomic N in the flow, the Dilute $N_2$ plasma composition is examined.

Figure 3.11 shows the number densities along the centerline computed with each mechanism for the Dilute $N_2$ plasma at nominal conditions and 282 sccm $CO_2$ injection. The peak levels of each species agree well with both mechanisms, although there are some differences. Importantly, the $CO_2$ number density profiles are nearly identical, although both mechanisms utilize different $CO_2$ dissociation rates [57,59]. As a result of the differences in the chemical kinetics between the two mechanisms,
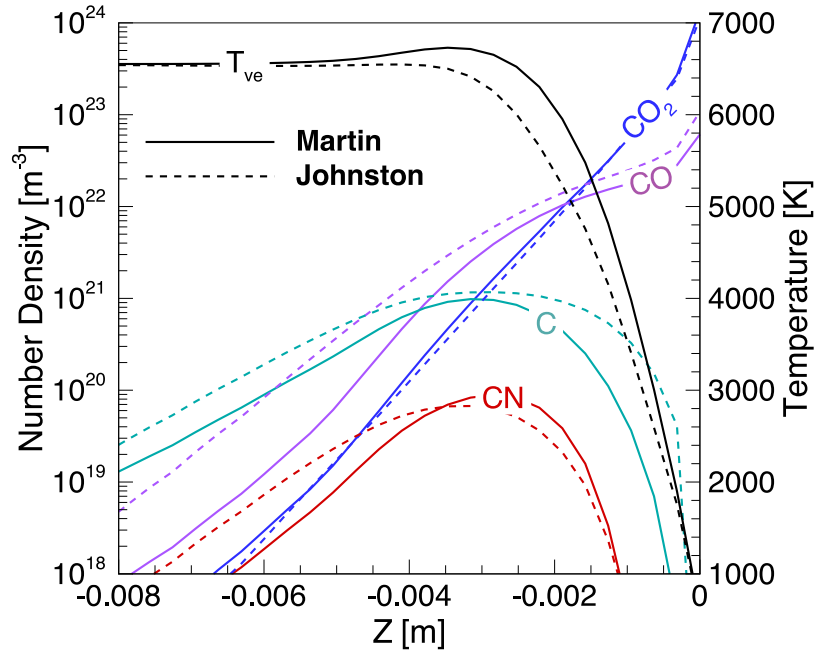
Figure 3.11: Comparison of species number densities with Martin vs. Johnston mechanisms for $N_2$ plasma with 282 sccm $CO_2$ injection.

the predicted vibrational-electronic temperature differs by up to 200 K in the probe boundary layer, with the Martin mechanism predicting overall higher temperatures.

Figure 3.12 shows the overall species mass fractions along the centerline for the Dilute $N_2$ plasma at nominal conditions and 282 sccm $CO_2$ injection. The composition of the flow is predominantly $CO_2$ near the probe where the gas is injected. Only when $CO_2$ dissociates into CO can CN begin to form farther upstream, which demonstrates the rate-limiting behavior. The role of CO dissociation in CN formation is less clear. Cruden showed that CO dissociation rates are likely underpredicted with the Johnston mechanism [65], and found instead that the dissociation rate of Hanson [66] agreed well with shock tube CO emission measurements. Thus, the CO dissociation rate of Hanson is also evaluated in both the Johnston and Martin mechanisms. However,
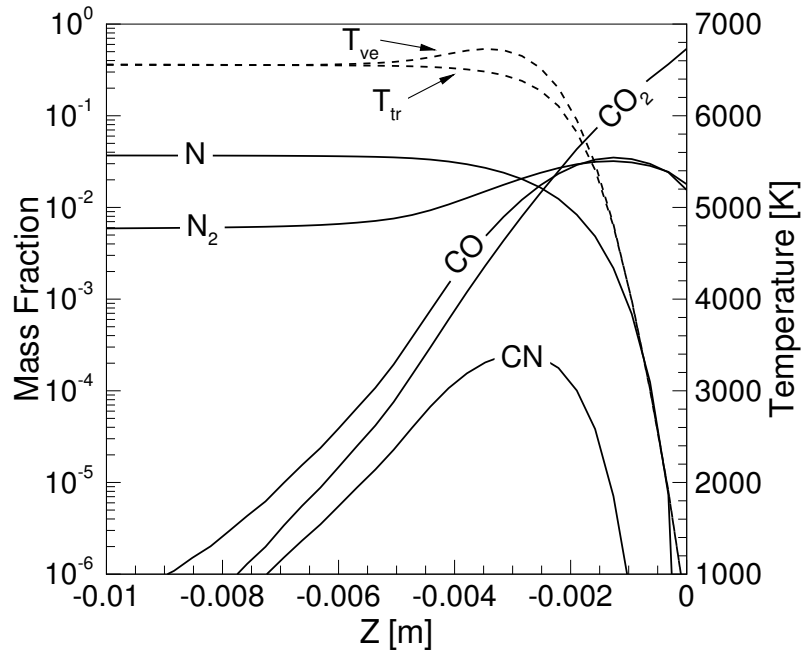
Figure 3.12: Centerline species mass fractions and temperatures for $N_2$ plasma with 282 sccm $CO_2$ injection (Martin mechanism).

negligible differences are observed in the CN concentrations and subsequent emission levels with both mechanisms, suggesting that CO dissociation is not a controlling rate.

The temperature profiles in Fig. 3.12 show slight thermal nonequilibrium with the two-temperature model around 3 mm (offset) due to neutral and ionic recombination reactions near the cooler probe face. The thermal gradient within 2 mm is very steep, and suggests that a slight shift in the spectral measurement location can result in temperature discrepancies of several hundred Kelvin, which may be a significant source of uncertainty.

Comparison of spectrally-resolved emission is shown in Fig. 3.13(a), and argon emission levels are matched relatively well with both mechanisms. Although CN

accounts for less than 0.03% of the flow, it contributes the majority of the radiative emission. There are two distinct emission bands: CN-Violet and CN-Red. The CN-Violet system involves transitions between the 2nd excited and ground state (B-X), and the CN-Red system involves transitions between the 1st excited and ground (A-X), while the argon lines involve transitions between excited states. However, both mechanisms significantly overpredict the CN emission levels in both the violet and red bands.



(a) Spectrally-resolved emission

(b) Spectrally-integrated emission
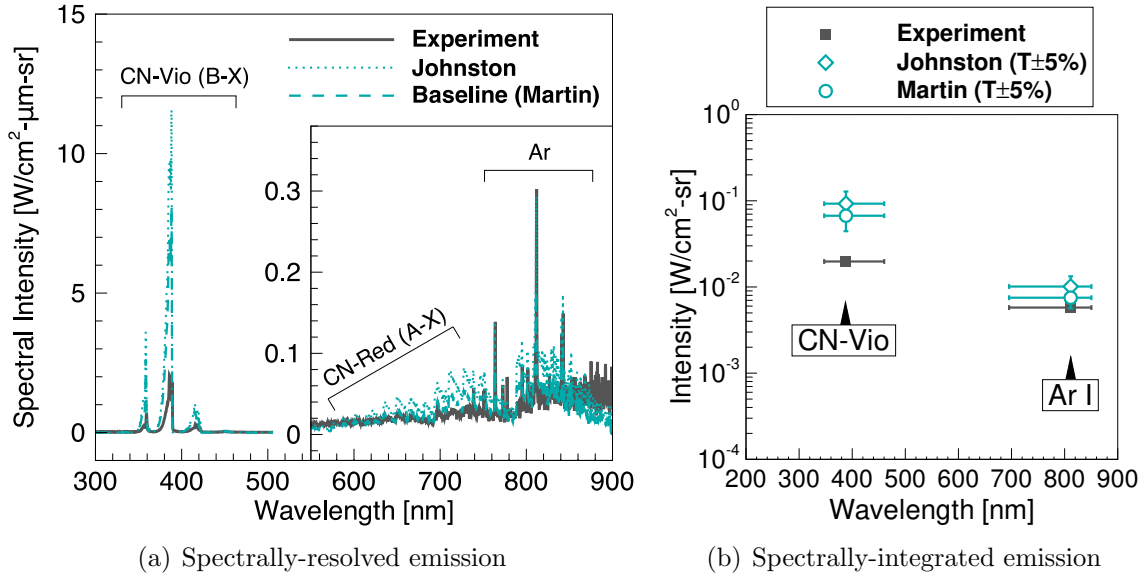
Figure 3.13: (a) Spectrally-resolved emission for $N_2$ plasma with 282 sccm $CO_2$ injection, 2.0 mm probe offset. (b) Spectrally-integrated emission. Horizontal bars: integration range. Vertical bars: $\pm 5\%$ temperature.

The spectrally-integrated emission is shown in Fig. 3.13(b), and the $\pm 5\%$ uncertainty margin in the experimental LTE temperatures does not account for the overprediction of the CN bands. The integrated CN-Red band is not shown, since it is not possible to distinguish the argon from the CN-Red system between 650 and 750 nm. Given that argon bands are matched, the overprediction is due to either

the chemical kinetic mechanisms themselves, or uncertainty in the NEQAIR radia-

tive models, with violet bands exhibiting more uncertainty than the red bands [40].

The overprediction of *both* CN bands suggests that the CN formation is indeed too

high with both chemical kinetic mechanisms, but the degree of overprediction is much

higher for the violet band than the red, which suggests that the QSS radiative models

for CN in NEQAIR may be contributing additional error.
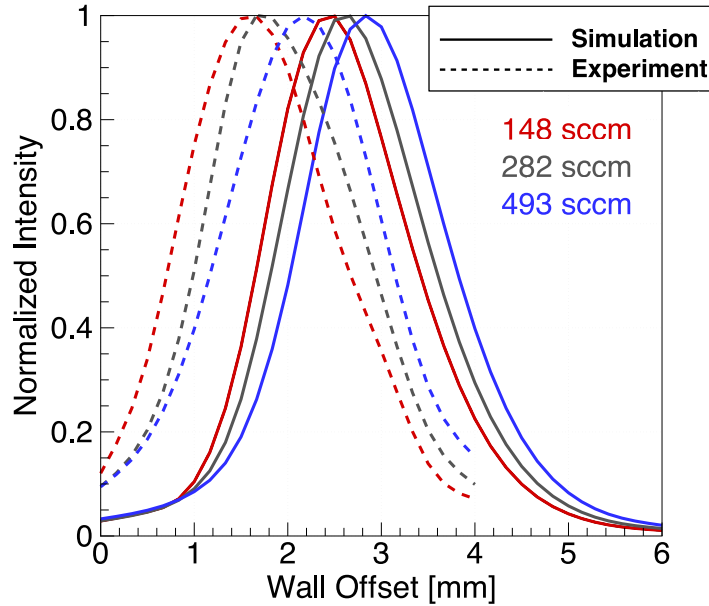


Figure 3.14: Normalized CN-Violet (B-X) integrated intensity for different blowing rates (Martin mechanism). The Johnston mechanism is not shown, but has nearly identical behavior.

Normalized emission of CN-Violet, integrated over the relevant wavelengths, are

shown as a function of blowing rate and distance from the probe face in Fig. 3.14.

Higher gas injection/blowing rates shift the location of peak CN emission upstream.

There is approximately a 1.0 mm discrepancy in the peak emission location between

the experiments and simulations, but overall trends agree well. $CO_2$ dissociation

has been studied extensively, and the range of available rates in the literature do not account for this level of discrepancy, but kinetics of CN exchange reactions may account for the difference in absolute CN emission levels as well as the peak emission location [59]. There is evidence to suggest that vibrational relaxation times of $CO_2$ are an order of magnitude greater than those assumed by Park (and used in the two-temperature model). This leads to longer dissociation induction/incubation times in shock-driven flows that implies vibration-dissociation coupling [67]. This may also explain the discrepancy in the CN levels and the profiles, as $CO_2$ dissociation is the rate-limiting process.

### 3.5.3   $H_2$ Injection

OH and NH are both significant radiators in flows with $H_2$ and air, and the A-X transition for both species emits in the 250-350 nm band. To isolate the effect of OH, the Dilute $O_2$ composition is examined, since it maximizes the activity of oxygen, and minimizes the concentration of nitrogen. Additional results for NH may be found in Appendix B. For all cases with $H_2$ injection, the Martin chemistry mechanism is utilized. Since carbon is not present, the mechanism is significantly simplified. The formation mechanism of OH is not limited by the dissociation of $H_2$, since OH can form directly from reactions with $H_2$ and $H_2O$ [59]:

$$H_2 + O \leftrightarrow OH + H \tag{3.15}$$

$$H_2O + O \leftrightarrow 2OH \tag{3.16}$$

Figure 3.15 shows the computed mass fractions along the centerline for 282 sccm $H_2$ injection. Near the wall, $H_2$ and $H_2O$ are the dominant species, with 6.0% by mass. Upstream, OH forms from $H_2O$ dissociation and $H_2$ exchange reactions. The two-temperature profile indicates thermal equilibrium throughout the boundary layer, although slight deviations are observed. Due to the presence of the cooler probe face, temperature gradients in the boundary layer are again steep, at $\sim 1500$ K/mm.
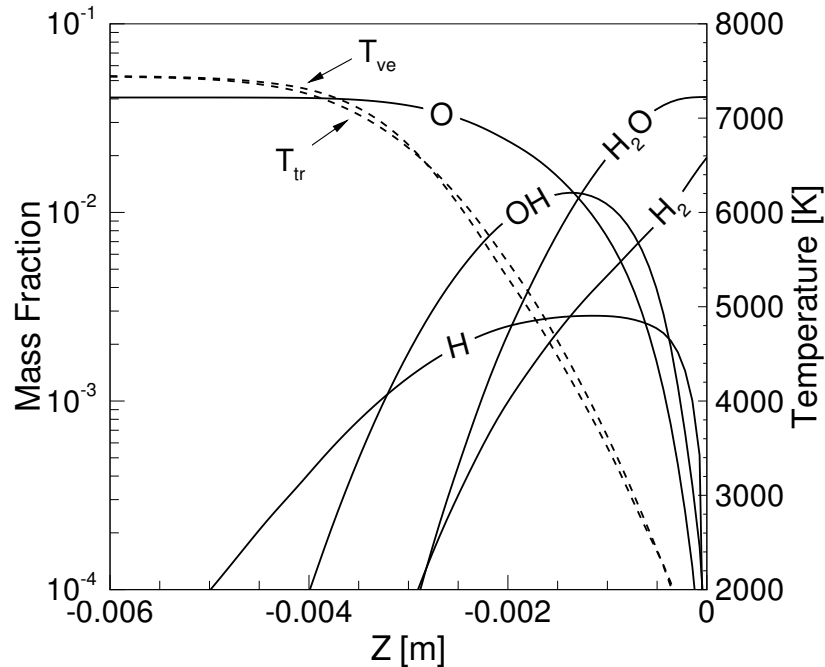


Figure 3.15: Centerline species mass fractions and temperatures for Dilute $O_2$ plasma with 282 sccm $H_2$ injection.

Figure 3.15 shows the computed mass fractions along the centerline for 282 sccm $H_2$ injection. Near the wall, $H_2$ and $H_2O$ are the dominant species, with 6.0% by mass. Upstream, OH forms from $H_2O$ dissociation and $H_2$ exchange reactions. The two-temperature profile indicates thermal equilibrium throughout the boundary layer, although slight deviations are observed. Due to the presence of the cooler probe face,

temperature gradients in the boundary layer are similarly steep, at $\sim 1500$ K/mm.



(a) Spectrally-resolved emission      (b) Spectrally-integrated emission
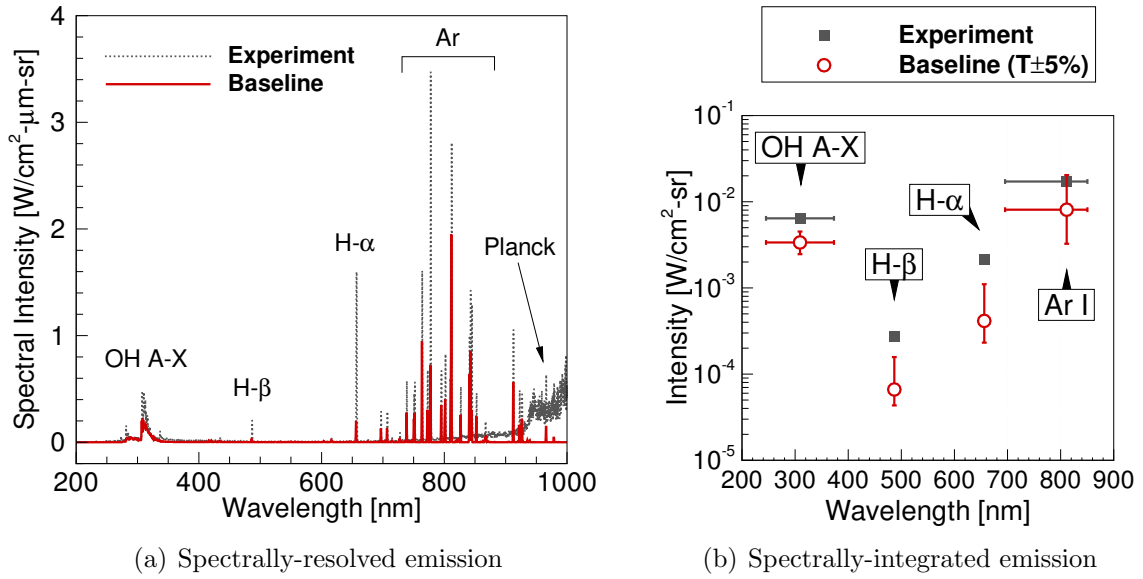
Figure 3.16: (a) Spectrally-resolved emission for $O_2$ plasma with 282 sccm $H_2$ injection, 2.0 mm probe offset. (b) Spectrally-integrated emission. Horizontal bars: integration range. Vertical bars: $\pm 5\%$ temperature.

Spectrally-resolved emission are compared in Fig. 3.16(a). Primary radiators observed in the spectra are OH (A-X), H-$\alpha$, H-$\beta$, and Ar. Both H-$\alpha$ and H-$\beta$ belong to the Balmer series of neutral atomic hydrogen. There is a peak of NH (A-X) noticeable in the experimental spectrum around 336 nm, but is small relative to OH (A-X). At wavelengths above 700 nm, there are differences in the background level of emission, likely due to Planck radiation from the probe surface, not accounted for in the spectral modeling. Overall, the levels of OH, atomic H, and Ar are underpredicted with the baseline LTE temperatures.

To better understand the sensitivity of emission levels to temperature, the band-integrated emission of each species is compared in Fig. 3.16(b). A $\pm 5\%$ uncertainty in the assumed LTE temperature accounts for the difference observed in the argon

71

bands, but not for OH A-X, H-$\alpha$, or H-$\beta$, which are still underpredicted. However, the agreement is still well within an order of magnitude, and the baseline temperature values *consistently* underpredict the emission data for all species. The remaining discrepancy may be due to the underprediction of OH formation and $H_2$ dissociation via the chemical kinetic rates, or errors in the temperature gradient exceeding the 5% margin.
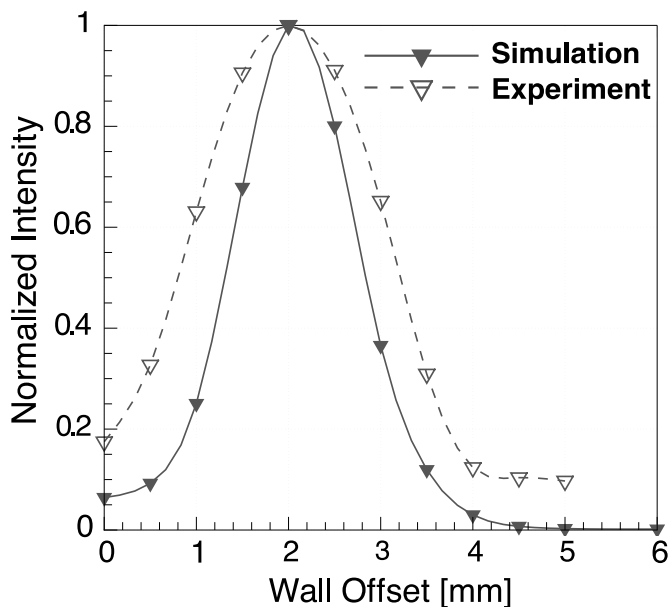


Figure 3.17: Normalized OH A-X integrated intensity, 282 sccm $H_2$.

Spatial distribution of OH A-X integrated emission is compared in Fig. 3.17 as a function of distance from the probe, normalized by the peak emission. The location of peak OH emission occurs 2.0 mm upstream from the probe in both experiment and simulation, although the simulation profile is narrower than the experimental profile, with lower emission levels at the tails. Altogether, the Martin mechanism appears to capture the formation kinetics of OH accurately, although the radiative emissions of OH and H are likely underpredicted by a factor of two or more. The simulations

72

underpredict the H-$\alpha$ and H-$\beta$ bands by a larger degree than the OH A-X band, but these atomic lines also exhibit greater sensitivity to temperature. Compared to $CO_2$, the dissociation of $H_2$ and formation of OH has not been as extensively studied in literature [59], and the results presented here suggest that additional investigations of these processes and rates are needed.

## 3.6   Chapter Summary

Experiments involving the interaction between a high-enthalpy plasma jet and injected pyrolysis gases were simulated using finite-rate chemistry mechanisms and radiative emission calculations [35, 36]. Accounting for $\pm 5\%$ uncertainty in experimental LTE temperature estimates, argon emission levels agreed with experimental measurements in all cases examined, providing a baseline to evaluate CN, OH, and H emission levels predicted with the rate mechanisms. The Johnston rate mechanism was consistent with the Martin mechanism for $CO_2$-air chemistry, and simulations involving Martin and Johnston rate mechanisms overpredicted levels of CN-Violet and CN-Red emission by a factor of 3 to 4. $H_2$-air chemistry evaluated with the Martin rate mechanism underpredicted OH A-X, H-$\alpha$, and H-$\beta$ emission by a factor of 2 to 4.

The effect of experimental uncertainty in the assumed temperature was quantified through simulations, showing that emission levels are sensitive to the temperature, but did not fully account for the discrepancies with experiments in the emission levels observed. This suggests that either the CN and OH formation rates (particularly

the exchange reactions), or radiative emission models in NEQAIR for these species should be better characterized, although it is difficult to distinguish between these factors. Uncertainties in the experimental conditions also need to be evaluated for more accurate comparisons between measured and simulated spectra. The results suggest that the plasma was mostly in thermal equilibrium, but it is critical to verify that LTE assumptions are valid with additional diagnostics [35, 36].

# CHAPTER 4

# Silicon Carbide Oxidation and Nitridation

Within the coupled material-environment framework, material-specific models for the surface chemistry are needed. These models describe the temperature-dependent chemical interactions at the interface of the flowfield and the material. Silicon carbide (SiC) is an UHTC material that has been studied for use in hypersonic leading edges. At temperatures less than 2000 K, SiC forms a stable silica ($SiO_2$) oxide that "passivates" the oxidizing surface in Fig. 4.1(b), limiting further oxidation. Temperatures above 2000 K will volatilize the silica layer into SiO [68], and SiC instead oxidizes "actively," leading to rapid loss of material akin to ablation, shown in Fig. 4.1(c) [69]. Typically, active oxidation is the failure mode of UHTC materials. Composites of $ZrB_2$ and $HfB_2$ diborides with up to 20% SiC by volume have been shown to offer better refractory and oxidation-resistant performance over pure SiC or diborides alone [70] . Thus, it is important to first understand the properties and characteristics of SiC oxidation to model these UHTC composites.

Thermodynamic stability of the passive oxide layer has an important role in determining active-to-passive (A-P) and passive-to-active (P-A) transitions. However, existing theories and calculations for P-A and A-P transitions based on chemical
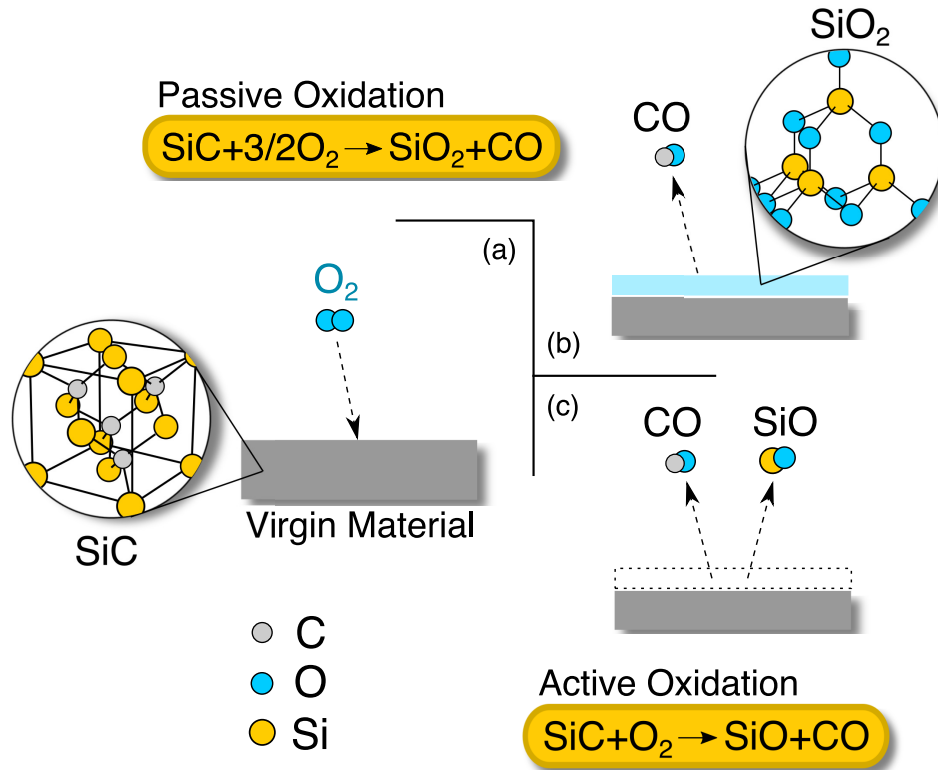
Figure 4.1: Passive and active SiC oxidation.

equilibrium do not adequately describe the mechanisms leading to transitions in an

open-system [71, 72]. In addition, a more detailed thermodynamic description of the

gas-surface interface during passive and active oxidation is needed in order to model

the oxidation processes. For example, a surface "temperature jump" phenomenon is

observed in SiC thermal oxidation experiments [73], where the surface temperature

rises abruptly by 300-400 K during passive-to-active transition. Researchers have

proposed an increase in the chemical heating to the surface as the cause [74], but this

effect cannot be explained with existing thermodynamic calculations.

This chapter addresses several shortcomings in previous thermodynamic calcula-

tions, namely mass transport in the boundary layer, multi-component equilibrium,

and the effects of nitridation. Existing theories describing A-P and P-A transitions

are first briefly reviewed. A multi-reaction thermodynamic chemical equilibrium approach is then described to model the oxidation and nitridation of SiC [75,76]. Results for oxygen, air, and nitrogen are then compared to experimental data in the literature. Passive-to-active transition is modeled, and the temperature jump phenomenon is demonstrated.

## 4.1 Wagner's Theory

Active-to-Passive (A-P) and Passive-to-Active (P-A) oxidation transitions for SiC are typically explained using Wagner's theory, described in this section. Initially proposed by Wagner [77] for pure silicon and developed by Hinze and Graham for SiC [69], the model accounts for mass transport in the boundary layer with thermodynamic equilibrium at the surface based on one or more reactions. However, transitions predicted with this approach are sensitive to the choice of reaction(s) [68], and it is still unclear what the "dominant" reaction is that properly describes A-P or P-A transitions.

### 4.1.1 Equilibrium Vapor Pressure

Recall in Chapter 2.2, equilibrium constants $K_c$ or $K_p$ can be computed from a specific reaction using thermodynamic species data. Assuming that reactions proceed *stoichiometrically*, equilibrium vapor pressure of gaseous products or reactants can be evaluated using the equilibrium constant for heterogeneous reactions (e.g. solid phase-only reactants with gaseous-only products). For example, consider the following

reaction, where the goal is to compute the equilibrium vapor pressure of SiO, $P_{\text{SiO}}^{\text{eq}}$:

$$SiC(s) + 2SiO_2(s) \leftrightarrow 3SiO(g) + CO(g) \tag{4.1}$$

Assuming unit activity for the solid species (i.e. solid activity is *independent* of partial pressure), the equilibrium constant based on partial pressures, $K_p$, is defined as:

$$K_p = [P_{\text{SiO}}]^3 P_{\text{CO}} \tag{4.2}$$

Note that there are no gaseous reactants, so this is a heterogeneous reaction. To close this analysis, $P_{\text{CO}}$ must be known in order to compute $P_{\text{SiO}}$ from $K_p$. Thus, making the assumption that the reaction proceeds stoichiometrically, $P_{\text{SiO}}$ can be expressed in terms of $P_{\text{CO}}$ in Eq. (4.3):

$$P_{\text{SiO}} = 3P_{\text{CO}} \tag{4.3}$$

$$K_p = \frac{1}{3}[P_{\text{SiO}}]^4 \tag{4.4}$$

$$P_{\text{SiO}}^{\text{eq}} = [3K_p]^{1/4} \tag{4.5}$$

Recall from Chapter 2.2 that $P_{\text{SiO}}^{\text{eq}}$ has units equivalent to the *standard* state used to compute $K_p$ from thermodynamic data, typically 1.0 bar.

This approach can be extended to multi-reaction equilibria. For example, consider

the following two-reaction heterogeneous system:

$$SiC(s) + \frac{3}{2}O_2(g) \leftrightarrow SiO_2(s) + CO(g) \tag{4.6}$$

$$SiC(s) + O_2(g) \leftrightarrow SiO(g) + CO(g) \tag{4.7}$$
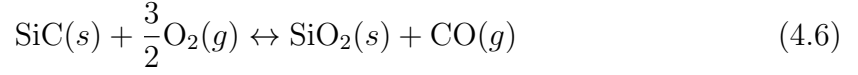
The first reaction corresponds to passive oxidation of SiC in Fig. 4.1(b), while the second corresponds to active oxidation in Fig. 4.1(c). The equilibrium constants are then expressed as:

$$\text{From Eq. (4.6):} \quad K_1 = \frac{P_{CO}}{[P_{O_2}]^{3/2}} \tag{4.8}$$

$$\text{From Eq. (4.7):} \quad K_2 = \frac{P_{SiO} P_{CO}}{P_{O_2}} \tag{4.9}$$

For this two-reaction system to be in equilibrium, the partial pressure of oxygen *must be the same* for both reactions. Solving for $P_{O_2}$ and equating the resulting expressions:

$$\text{From Eq. (4.8):} \quad P_{O_2} = \left(\frac{P_{CO}}{K_1}\right)^{2/3} \tag{4.10}$$

$$\text{From Eq. (4.9):} \quad P_{O_2} = \frac{P_{SiO} P_{CO}}{K_2} \tag{4.11}$$

$$\left(\frac{P_{CO}}{K_1}\right)^{2/3} = \frac{P_{SiO} P_{CO}}{K_2} \tag{4.12}$$

$$P_{SiO} = \frac{K_2}{(K_1)^{2/3}} \frac{1}{(P_{CO})^{1/3}} \tag{4.13}$$

$$(P_{SiO})^{3/4} = \frac{(K_2)^{3/4}}{(K_1)^{1/2}} \frac{1}{(P_{CO})^{1/4}} \tag{4.14}$$

$$(P_{SiO}^{eq})^{3/4}(P_{CO}^{eq})^{1/4} = \frac{(K_2)^{3/4}}{(K_1)^{1/2}} \tag{4.15}$$

The relationship in Eq. (4.15) *must* be satisfied when the system is in equilibrium.

## 4.1.2  Diffusion-Limited Equilibrium

Thus far, no assumptions have been made about the system in equilibrium. The systems discussed in the previous section apply only to the gas-surface interface. In a boundary layer (an "open" system), the ambient/edge conditions differ from the gas-surface interface due to mass and energy transport *within* the boundary layer. These transport effects (e.g. diffusion) may prevent an open-system from ever reaching the "true equilibrium" state illustrated in Fig. 4.2, and the diffusion-limited regime must be considered instead.

$$\boxed{\text{True Equilibrium}} \xrightleftharpoons[\text{Closed System}]{\text{Open System}} \boxed{\text{Diffusion-limited}} \xrightleftharpoons[\text{Chem. Eq.}]{\text{Chem. Non-Eq.}} \boxed{\text{Reaction-limited}}$$
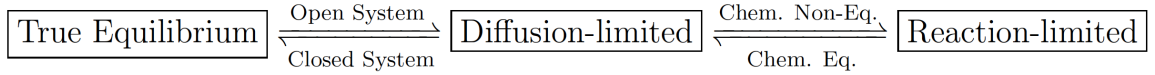
Figure 4.2: Relevant processes for different chemical systems.

To determine the partial pressure of oxygen in the ambient gas at equilibrium, species diffusion relates conditions at the gas-surface interface ($P_i^w$) and the boundary layer edge ($P_i^e$). In the limit of active oxidation, Eq. (4.7) describes the stoichiometric balance at the gas-surface interface. Using Fick's law in terms of number density in Eq. (4.16), and $P_{O_2}^w = 0$, $P_{SiO}^e = 0$, $P_{CO}^e = 0$ as boundary conditions following Hinze and Graham [69], the surface species balance is expressed in Eq. (4.17):

$$J_i = -D_i \frac{P_i^e - P_i^w}{\delta_i} \frac{1}{RT} \tag{4.16}$$

$$J_{O_2} = -J_{SiO} = -J_{CO} \tag{4.17}$$

$$\frac{D_{O_2} P_{O_2}^e}{\delta_{O_2}} = \frac{D_{SiO} P_{SiO}^w}{\delta_{SiO}} = \frac{D_{CO} P_{CO}^w}{\delta_{CO}} \tag{4.18}$$

$$P_{O_2}^e = \frac{D_{SiO}}{D_{O_2}} \frac{\delta_{O_2}}{\delta_{SiO}} P_{SiO}^w = \frac{D_{CO}}{D_{O_2}} \frac{\delta_{O_2}}{\delta_{CO}} P_{CO}^w \tag{4.19}$$

For Re < 1, boundary layer approximations relate the relative diffusion lengths $\delta_i$ to the diffusion coefficients $D_i$ [69, 78]:

$$\frac{\delta_{O_2}}{\delta_{SiO}} = \left( \frac{D_{SiO}}{D_{O_2}} \right)^{-1/2} \tag{4.20}$$

$$\frac{\delta_{O_2}}{\delta_{CO}} = \left( \frac{D_{CO}}{D_{O_2}} \right)^{-1/2} \tag{4.21}$$

Substituting Eqs. (4.20) – (4.21) into Eq. (4.19), the expression derived by Hinze and Graham [69] is obtained in Eq. (4.22):

$$P_{O_2}^e = \left( \frac{D_{SiO}}{D_{O_2}} \right)^{1/2} P_{SiO}^w = \left( \frac{D_{CO}}{D_{O_2}} \right)^{1/2} P_{CO}^w \tag{4.22}$$

Using this relationship, Eqs. (4.23) – (4.25) are mathematically equivalent to Eq. (4.22):

$$(P_{O_2}^e)^{3/4} = \left( \frac{D_{SiO}}{D_{O_2}} \right)^{3/8} (P_{SiO}^w)^{3/4} \tag{4.23}$$

$$(P_{O_2}^e)^{1/4} = \left( \frac{D_{CO}}{D_{O_2}} \right)^{1/8} (P_{CO}^w)^{1/4} \tag{4.24}$$

$$P_{O_2}^e = (P_{O_2}^e)^{3/4}(P_{O_2}^e)^{1/4} = \left( \frac{D_{SiO}}{D_{O_2}} \right)^{3/8} \left( \frac{D_{CO}}{D_{O_2}} \right)^{1/8} (P_{SiO}^w)^{3/4}(P_{CO}^w)^{1/4} \tag{4.25}$$

Assuming the system is in equilibrium at the gas-surface interface, Eq. (4.15) may

be substituted into Eq. (4.25), yielding Eq. (4.26):

$$P_{O_2}^e = \left(\frac{D_{\text{SiO}}}{D_{O_2}}\right)^{3/8} \left(\frac{D_{\text{CO}}}{D_{O_2}}\right)^{1/8} \frac{(K_2)^{3/4}}{(K_1)^{1/2}} \tag{4.26}$$

This final expression is the partial pressure of oxygen in the ambient gas at equilibrium for the two-reaction system, as derived by Balat [79].

Four important assumptions have been made to arrive at this expression. First, the system is assumed to be in the active oxidation regime. For SiC, both the passive and active reactions in Eqs. (4.6) and (4.7) must be occurring simultaneously to some extent at any given state. However, in the active regime, Eq. (4.7) is the "dominant" reaction, meaning there is no barrier for it to proceed, regardless of Eq. (4.6). Second, "clean" boundary conditions along the boundary layer edge and surface are assumed for species diffusion calculations. This implies that all $O_2$ is consumed at the surface, and the ambient is a perfect sink for SiO and CO. Third, reactions are assumed to occur stoichiometrically according to Eq. (4.17). Lastly, by considering the system in equilibrium, $P_{O_2}^e$ from Eq. (4.26) corresponds to the A-P condition, since it is the *maximum* ambient pressure of oxygen that can be consumed at the surface.

### 4.1.3 Active-to-Passive Transition

Reaction (4.27) describes the primary active oxidation reaction. SiO and CO are the primary oxidation products, and Fig. 4.3(a) illustrates that there will be a flux of $O_2$ towards the surface, which is balanced by the flux of oxidation products (SiO, CO) away from the surface during active oxidation. For a bare SiC surface, the equilibrium

vapor pressure of $O_2$ determines the maximum flux of $O_2$ that can be consumed at the surface for a given temperature [78], according to Eq. (4.28).

$$\text{SiC}(s) + O_2(g) \leftrightarrow \text{SiO}(g) + \text{CO}(g) \tag{4.27}$$

$$K_{p,\text{SiC}} = \frac{P_{\text{SiO}}^{\text{eq}} P_{\text{CO}}^{\text{eq}}}{P_{O_2}^{\text{eq}}} \tag{4.28}$$

At equilibrium, the oxygen pressure in the ambient is related to the partial pressures at the surface with Fick's law, and corresponds to the A-P transition point in Eqs. (4.29) – (4.30), derived earlier [69, 78]. Physically, condensation of $SiO_2$ onto the SiC surface at sufficiently high oxygen pressures causes transition from an active to a passive state.

$$P_{O_2}^{\text{A-P}} = \left( \frac{D_{\text{SiO}}}{D_{O_2}} \right)^{1/2} P_{\text{SiO}}^{\text{eq}} \tag{4.29}$$

$$P_{O_2}^{\text{A-P}} = \left( \frac{D_{\text{CO}}}{D_{O_2}} \right)^{1/2} P_{\text{CO}}^{\text{eq}} \tag{4.30}$$

Reactions (4.31) - (4.33) have been proposed by Gulbransen et al. [80] to describe the vapor pressures of SiO and CO at the SiC surface, which are related to the ambient oxygen pressure via Eqs. (4.29) – (4.30).

$$\text{SiC}(s) + 2\text{SiO}_2(s) \leftrightarrow 3\text{SiO}(g) + \text{CO}(g), \quad P_{\text{SiO}}^{\text{eq}} = (3K_p)^{1/4} \tag{4.31}$$

$$\text{SiC}(s) + \text{SiO}_2(s) \leftrightarrow 2\text{SiO}(g) + \text{C}(s), \quad P_{\text{SiO}}^{\text{eq}} = (K_p)^{1/2} \tag{4.32}$$

$$2\text{SiC}(s) + \text{SiO}_2(s) \leftrightarrow 3\text{Si}(l) + 2\text{CO}(g), \quad P_{\text{CO}}^{\text{eq}} = (K_p)^{1/2} \tag{4.33}$$

(a) Active SiC oxidation                    (b) Passive SiC oxidation
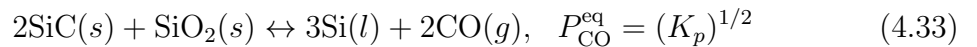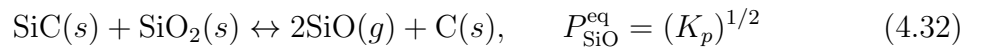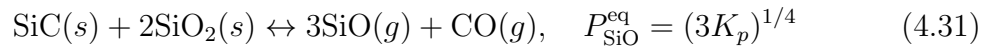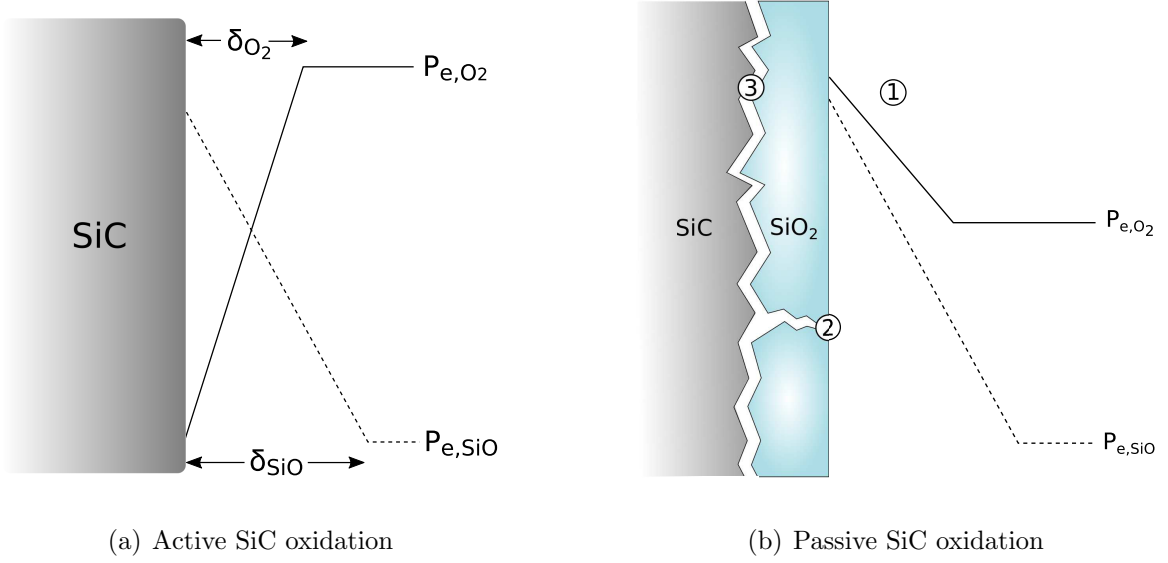
Figure 4.3: Wagner model for active and passive SiC oxidation. In (b), mechanisms include ① $SiO_2$ vaporization according to Wagner's model, ② Rupture/bubbling of $SiO_2$ layer, and ③ $SiO_2$ consumption at SiC interface.

## 4.1.4  Passive-to-Active Transition

Figure 4.3(b) illustrates several proposed mechanisms for P-A transition, which is characterized by loss of the silica layer. One mechanism is dissociative vaporization at the $SiO_2$-gas interface via Eq. (4.34):

$$SiO_2(s) \leftrightarrow SiO(g) + \frac{1}{2}O_2(g) \tag{4.34}$$
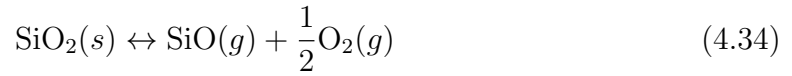
To evaluate Eq. (4.34) using Wagner's theory, equilibrium at the gas-surface interface can be expressed as:

$$K_{p,SiO_2} = (P_{O_2}^{eq})^{1/2} P_{SiO}^{eq} \tag{4.35}$$

$$P_{O_2}^{eq} = \left( \frac{1}{P_{SiO}^{eq}} K_{p,SiO_2} \right)^2 \tag{4.36}$$

84

Assuming the reaction proceeds stoichiometrically, the ambient gas is a perfect sink for SiO but not $O_2$, and using the boundary layer approximation in Eq. (4.20) yields:

$$J_{O_2} = \frac{1}{2} J_{SiO} \tag{4.37}$$

$$D_{O_2} \frac{P_{O_2}^e - P_{O_2}^w}{\delta_{O_2}} = \frac{1}{2} D_{SiO} \frac{-P_{SiO}^w}{\delta_{SiO}} \tag{4.38}$$

$$P_{O_2}^{\text{P-A}} = P_{O_2}^{\text{eq}} - \frac{1}{2} \left( \frac{D_{SiO}}{D_{O_2}} \right)^{1/2} P_{SiO}^{\text{eq}} = \boxed{\left( \frac{1}{P_{SiO}^{\text{eq}}} K_{p,SiO_2} \right)^2 - \frac{1}{2} \left( \frac{D_{SiO}}{D_{O_2}} \right)^{1/2} P_{SiO}^{\text{eq}}} \tag{4.39}$$

The equilibrium vapor pressure SiO, $P_{SiO}^{\text{eq}}$, may be evaluated directly from the equilibrium constants for Reactions (4.31) - (4.32).

Harder et al. [81] showed that this is not the primary mechanism for P-A transition, as experimentally observed P-A transition pressures are 3–4 orders of magnitude higher than that predicted by $SiO_2$ vaporization equilibrium. A more likely mechanism is $SiO_2$ consumption at the SiC-$SiO_2$ interface via Reactions (4.31) - (4.33). Gaseous SiO and CO are formed *below* the $SiO_2$ layer, and can lead to bubbling and subsequent rupture of the thinning silica layer [81, 82]. Wagner's model fails to describe the mechanisms of SiC consumption and bubbling, since these are primarily due to substrate reactions.

## 4.2   SiC Material Model

While useful to determine A-P and P-A transition limits, models based on Wagner's theory are insufficient to describe surface-mass-balance (SMB) and surface-energy-balance (SEB) processes needed to model the detailed material-environment

interactions. Thus, a more general approach is developed in this chapter. Figure 4.4 illustrates an open-system zero-dimensional model for SiC implemented in the ACE code [17], and can be generalized to include $N_2$ in the boundary layer and any condensed nitrides/oxynitrides at the surface. Three regions are present: the boundary layer edge, the gas-surface interface, and the substrate/bulk material. The surface coverage exists *between* the gas-surface interface and the substrate, and gas-phase mass transport effects are modeled between the ambient boundary layer and the surface.
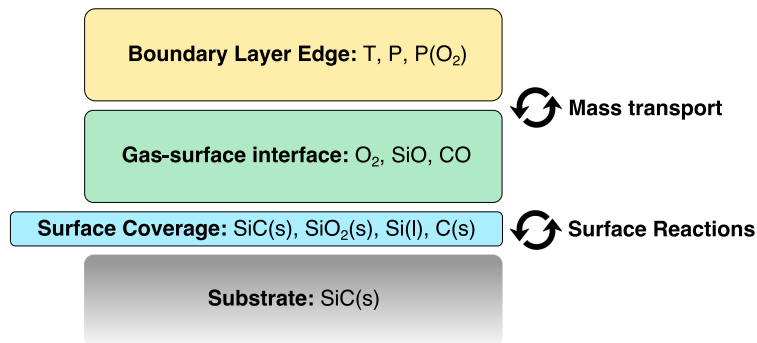


Figure 4.4: Open-system, zero-dimensional SiC-$O_2$ reactor model.

## 4.2.1 Mass and Energy Transport

Assuming constant Prandtl and Lewis numbers, similarity between thermal and mass transport allows the steady-state boundary layer conservation equations to be written in terms of mass and heat transfer coefficients, $C_M$ and $C_H$:

$$Q_w = \rho_e u_e C_H (h_e - h_w) \tag{4.40}$$

$$J_i = \rho_e u_e C_M (Y_e - Y_w) \tag{4.41}$$

$$Le = \frac{C_H}{C_M} \tag{4.42}$$

Here $Q_w$ is the surface heat flux, $J_i$ is the mass flux of a species $i$ to/from the surface (analogous to Fick's law), $Y_e$ is the mass fraction of a species at the boundary layer edge, and $\rho_e u_e C_M$ is the bulk flux from the boundary layer edge to the gas-surface interface. In the steady-state limit, the total blowing mass flux *into* the gas-surface interface, $\dot{m}_g$ from the surface, equals the net mass flux *away* to the boundary layer, $\dot{m}_w$, and is non-dimensionalized into the B' parameter from Eq. (4.43), which is the same parameter defined previously in Eq. (2.62).

$$B' = \frac{\dot{m}_g}{\rho_e u_e C_M} = \frac{\dot{m}_w}{\rho_e u_e C_M} \tag{4.43}$$

Assuming *equal* diffusion coefficients, Eq. (4.44) describes the species mass balance at the gas-surface interface:

$$\overbrace{\dot{m}_w Y_w}^{\text{Net flux}} = \overbrace{\dot{m}_g Y_g}^{\text{Oxid. flux}} - \overbrace{\rho_e u_e C_M (Y_w - Y_e)}^{\text{Diffusion flux}} \tag{4.44}$$

Combining Eq.(4.43) with Eq. (4.44) yields the overall mass fraction of a species in Eq. (4.45):

$$Y_w = \frac{B'Y_g + Y_e}{1 + B'} \tag{4.45}$$

An analogous expression may be derived for *unequal* diffusion coefficients with the bifurcation approximation for binary diffusion coefficients [29] described earlier in Chapter 2.3.3, which is also used here.

## 4.2.2 Multi-Component Chemical Equilibrium

To describe the surface reactions between the ambient and the substrate, an equilibrium condition based on a limited set of reactions may be insufficient, as in Wagner's model [69, 77, 79]. Here, an equilibrium constant approach is utilized over a *much broader* set of reactions. The individual reactions considered are the formation of each gaseous and condensed species from gaseous constituent species. Notably, this includes reactions *between* condensed species and the substrate via the surface coverage in Fig. 4.4, which are neglected in Wagner's model.

From Eq. (4.45), the B' parameter effectively describes the elemental mass fractions at the gas-surface interface with species diffusion. Using the ACE multiphase equilibrium solver described in Section 2.2, the system of equations is then solved over a range of B' values to determine the equilibrium temperature and species composition *at each B' value*, and mixture properties at the gas-surface interface are calculated from the species thermochemical data at the equilibrium temperature and

composition.
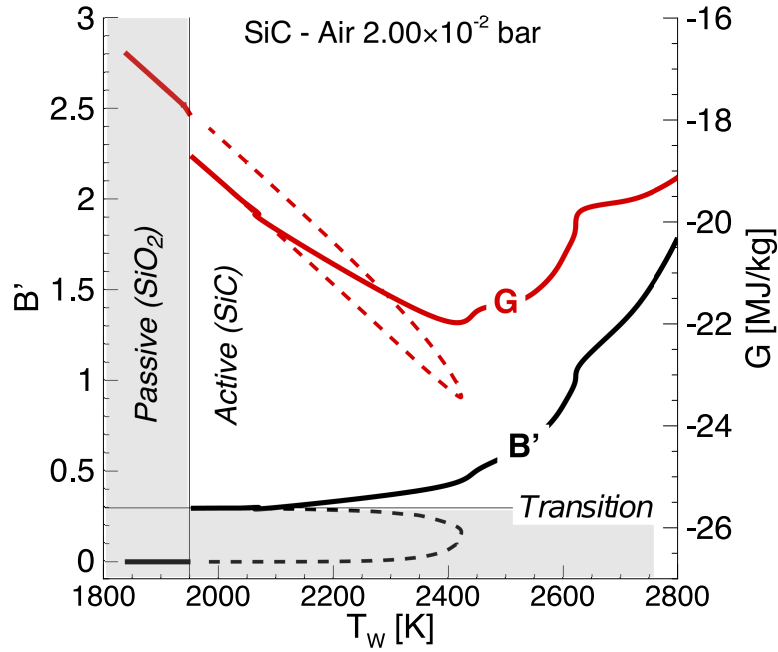


Figure 4.5: B' plot for SiC-air. P-A transition occurs at ~1950 K and B' = 0.30. Shaded region corresponds to passive oxidation (SiO$_2$). Dashed lines denote non-physical solutions.

Importantly, the temperature at equilibrium may not be unique with this approach. Each B' value can be mapped to a unique temperature, but not vice-versa. Following the principle of free energy minimization, the thermodynamically-favored state can still be determined. Figure 4.5 shows a set of solutions, where B' and mixture Gibbs free energy, $G$, are plotted against temperature. Between 2000 K and 2400 K, there are multiple equilibrium solutions at *different* B' and $G$. The thermodynamically-favored solution corresponds to the lowest $G$, and other solutions at the same temperature are thermodynamically *unstable*, shown in the dashed lines.

The oxidation transition criteria is when SiO$_2$ begins/ceases to be a stable condensed phase. At constant oxygen pressure, A-P oxidation transition is predicted

to occur at the *highest temperature* that $SiO_2$ begins to be stable. Conversely, at constant oxygen pressure, P-A transition occurs at the *lowest temperature* that $SiO_2$ ceases to be stable. Likewise, nitridation transitions depend on ambient nitrogen pressure and silicon nitride ($Si_3N_4$). Hysteresis exists if the A-P and P-A transition temperatures are different under constant pressure, and Fig. 4.5 suggests a $\sim$400 K thermodynamic hysteresis.

It is important to note that thermodynamics and mass transport alone do not drive A-P and P-A transitions, as the physical mechanism of each transition differs. Researchers have shown that there exists an intermediate "passive-to-bubble" transition that ultimately leads to P-A transition during oxidation of SiC [82, 83]. Since bubbling is the result of mechanical oxide rupture, such mechanisms are not accounted for in the current approach. However, the thermodynamic conditions for $SiO_2$ and $Si_3N_4$ stability must still be satisfied during transition between passive and active states, regardless of the mechanism.

## 4.3 Model Evaluation

### 4.3.1 Oxidation

Results for oxidation transitions and equilibrium compositions for ambient oxygen and air environments are presented here, and comparisons are made to experimental data and Wagner's theory. The bulk material is SiC, consisting of Si and C in a stoichiometric ratio, and the boundary layer edge composition is adjusted according

to ambient oxygen or air environments.

**Oxidation in Oxygen**

Four elements are considered: Si, C, O, and Ar. Argon is an inert gas commonly used in oxidation experiments, and mass fractions of O and Ar at the boundary layer edge are adjusted to achieve the desired oxygen pressure for a given total pressure. SiC(s), $SiO_2$(s,l), Si(l), and C(s) are the condensed surface species included in the analysis.

Experiments and theories in the literature have demonstrated that oxidation transition conditions are relatively independent of total pressure, and by extension, the presence of inert diluents. Experimentally-measured temperatures for A-P and P-A transitions in oxygen environments are summarized in Fig. 4.6 over oxygen pressures from 0.1 to 1000 Pa. [69, 78, 80–82, 84–89] Blue symbols denote P-A transitions, and red symbols denote A-P. Results for Wagner's theory based on Eqs. (4.31) - (4.34) are also shown in dashed lines. The blue solid line represents the P-A transition predicted with the new model for oxygen environments, demonstrating a clear Arrhenius relationship.

The scatter in the experimental data points can be accounted for by facility effects, SiC polytype and microstructure, composition (including impurities), and transition criterion. Notably, the data of Narushima [87] accounts for the effect of flowrate, which decreases the effective boundary layer length, and is consistent with Wagner's model [77]. Similarly, Jacobson attributed the large spread in P-A transitions to "local variations at the gas/solid interface," involving differences in the boundary layer

gradients [78]. Most transition data for the SiC–O$_2$ system appear to be clustered in Figure 4.6 and represent oxidation experiments performed in a diffusion-limited regime. However, the results of Dawi [86], Ogura [82], and Rosner [89] were obtained from experiments performed at very low oxygen pressures and represent a reaction-limited regime.
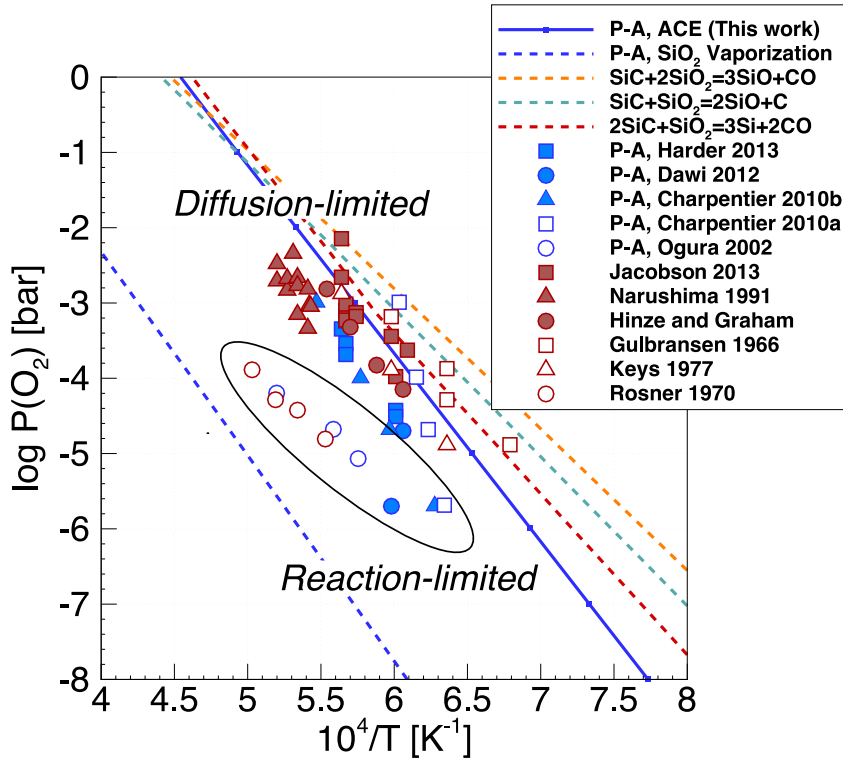


Figure 4.6: Experimental (symbols) and theoretical (lines) transitions for SiC-O$_2$. Left side corresponds to active oxidation, right corresponds to passive. A-P (red) and P-A (blue) transitions correspond to A-P unless noted.

This new P-A transition prediction is comparable to the results of Eqs. (4.31) - (4.33) evaluated with Wagner's model, due to similar treatment of mass transport and thermodynamic equilibrium. Moreover, the new prediction improves overall agreement with experimental measurements compared to Wagner's theory. Despite the large scatter in the experimental A-P and P-A measurements, there is no clear evi-

dence of hysteresis in SiC oxidation, suggesting that A-P and P-A transitions are similar, as Jacobson and Myers [68,90] observed. Notably, there is an order-of-magnitude larger difference between the diffusion-limited measurements where Wagner's model is valid, and the reaction-limited regime at very low oxygen pressures. Since the model assumes chemical equilibrium, P-A transition results are more consistent with the diffusion-limited measurements.

Figure 4.7(a) shows the gas-phase equilibrium composition during SiC oxidation in an argon-diluted oxygen environment from 1300 K to 2800 K at 21.2 Pa oxygen pressure. Left and right sides of the plots correspond to passive and active oxidation, with $SiO_2$ and SiC surfaces, respectively. There is a distinct bifurcation behavior between passive and active oxidation at ~1700 K, corresponding to P-A transition. Concentrations of atomic and molecular oxygen in the passive region indicate that oxygen is not being consumed at the surface. In the active region, oxygen concentrations are more than five orders of magnitude *lower* than in the passive region, indicating consumption at the SiC surface. Mole fractions of $O_2$ are less than $10^{-12}$ in the active oxidation region. As a result, there is significant outgassing of oxidation products from the surface. Initially, SiO and CO are present in equal amounts and are the dominant oxidation products, suggesting that Eq. (4.27) is valid. Above 2300 K, SiC sublimates Si preferentially, leaving a graphitic surface [89], and is marked by a decrease in SiO and increase in gaseous Si. $SiC_2$ is also preferred at these higher temperatures, and CO concentrations remain relatively constant throughout the active region.
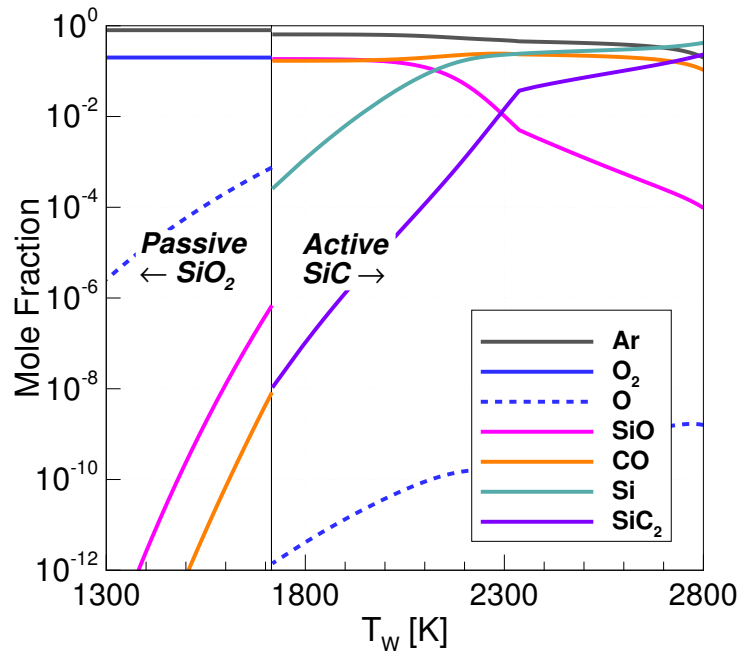
(a) SiC-Ar/$O_2$
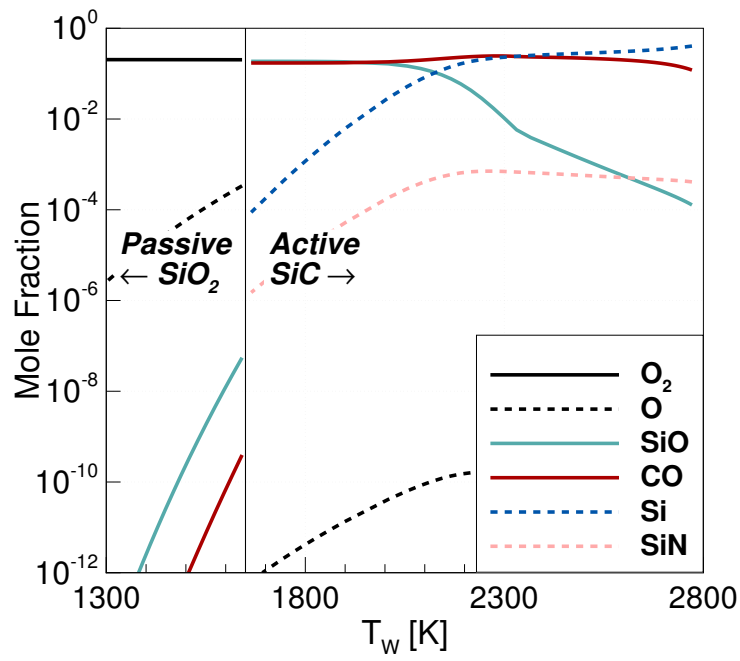


(b) SiC-air

Figure 4.7: Gaseous species for SiC oxidation in oxygen and air, $P_{total} = 100$ Pa, $P_{O_2} = 21.2$ Pa for both cases.

## Oxidation in Air

The effect that nitrogen has on oxidation behavior in air environments is not well understood. In the literature, nitridation effects are typically neglected in experiments and oxidation theory, assuming nitrogen is chemically inert [79,91]. Thus, thermodynamic calculations are required to quantify the significance of nitridation in combined oxygen and nitrogen environments. For oxidation in air, four elements are considered: Si, C, N, and O. The N and O mass fractions in air are imposed at the boundary layer edge (76.5% N, 23.5% O) for all total pressures examined. Gaseous $SiN(g)$, $Si_2N(g)$, condensed $Si_3N_4(s)$, and $Si_2N_2O(s)$ are added to the previously considered species set (except for Ar).
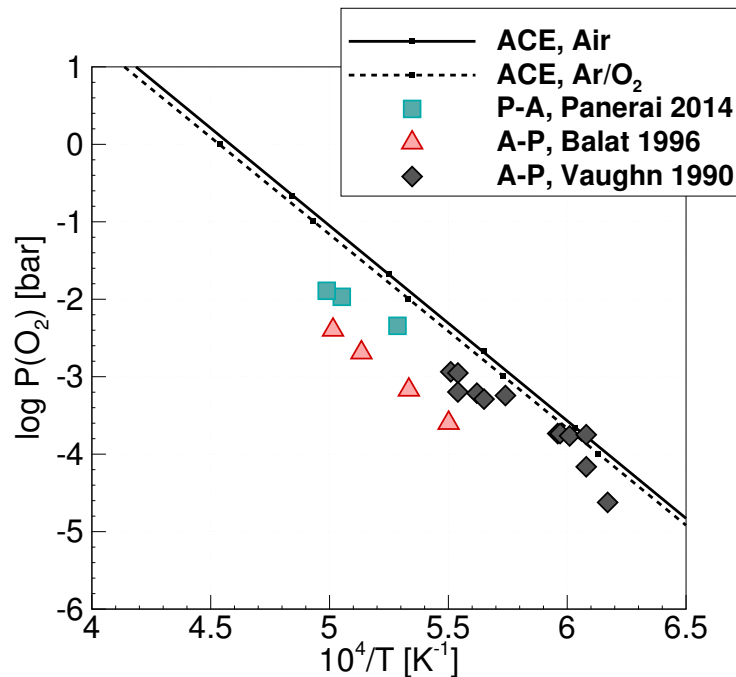


Figure 4.8: Predicted transitions for the SiC-air system. The SiC-Ar/$O_2$ transition from Fig. 4.6 is also shown for comparison.

SiC oxidation transitions in air have been measured in experiments performed by

Panerai, Balat, and Vaughn [73, 79, 91], summarized in Fig. 4.8. The predicted P-A transition temperature for air environments is also plotted, and compared to the pure oxidation case at equivalent oxygen pressures. At the same oxygen partial pressure and total pressure, the predicted P-A transition temperature in air is 3% lower, and *both* lines agree with the experimental data of Vaughn [91]. The measurements of Balat and Panerai suggest that A-P and P-A transition should occur at lower oxygen pressures and higher temperatures than predicted with the new model, but fall within the range of diffusion-limited measurements for *pure* oxygen environments in Fig. 4.6.

From these comparisons, it is evident then that the presence of nitrogen has minimal effect on oxidation transitions, and likewise suggests little to no hysteresis. The equilibrium composition during oxidation in air is shown in Fig. 4.7(b), and is similar to the pure oxidation case in Fig. 4.7(a) except for the presence of SiN and $Si_2N$ in mole fractions on the order of $10^{-4}$. P-A transition occurs at ~1650 K for the same oxygen partial pressure of 21.2 Pa. Importantly, thermodynamic stability of $SiO_2$ still determines the transition between passive and active oxidation.

## 4.3.2  Nitridation

Experiments and theory describing nitridation of SiC are sparse in comparison to oxidation. In nitrogen environments, SiC forms silicon nitride ($Si_3N_4$) as a condensed phase, which acts to limit further nitridation similar to a passive state. Nickel et al. performed calculations for the thermodynamic stability of $Si_3N_4$ and SiC in pure nitrogen environments [92]. They suggested that equilibrium between SiC and $Si_3N_4$

is governed by Eq. (4.46):

$$3\mathrm{SiC}(s) + 2\mathrm{N}_2(g) \leftrightarrow \mathrm{Si}_3\mathrm{N}_4(s) + 3\mathrm{C}(s) \hspace{2cm} (4.46)$$
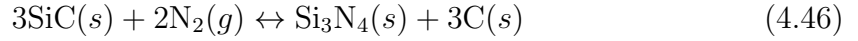
This corresponds to the criterion for P-A transition used in this work. Panerai et al. showed that $\mathrm{Si}_3\mathrm{N}_4$ is volatilized at higher temperatures, akin to active oxidation [93]. $\mathrm{Si}_3\mathrm{N}_4$ decomposes according to Eq. (4.47):

$$\mathrm{Si}_3\mathrm{N}_4(s) \leftrightarrow 3\mathrm{Si}(l) + 2\mathrm{N}_2(g) \hspace{2cm} (4.47)$$

Arrhenius lines for both reactions are plotted in Fig. 4.9(a), and are compared to the P-A nitridation model prediction. The P-A prediction agrees well with Eq. (4.46), and is bounded at higher temperatures by Eq. (4.47). Nickel did not account for mass transport effects at the surface, which explains the shift towards slightly higher temperatures/lower pressures in the $\mathrm{N}_2$ predicted transition line. At equivalent partial pressures, P-A transitions in $\mathrm{N}_2$ environments occur at lower temperatures than in $\mathrm{O}_2$, and $\mathrm{Si}_3\mathrm{N}_4$ thermally decomposes before P-A oxidation occurs. This suggests that oxidation processes are relatively unaffected by nitridation processes in air mixtures, and no condensed nitrides are present during active oxidation.

The equilibrium gas-phase composition during thermal nitridation at 100,000 Pa nitrogen pressure is shown in Fig. 4.9(b). P-A nitridation is predicted to occur at ~1790 K, when the surface transitions from predominantly $\mathrm{Si}_3\mathrm{N}_4$ to SiC. However, important differences are observed in the nitridation behavior relative to oxidation.
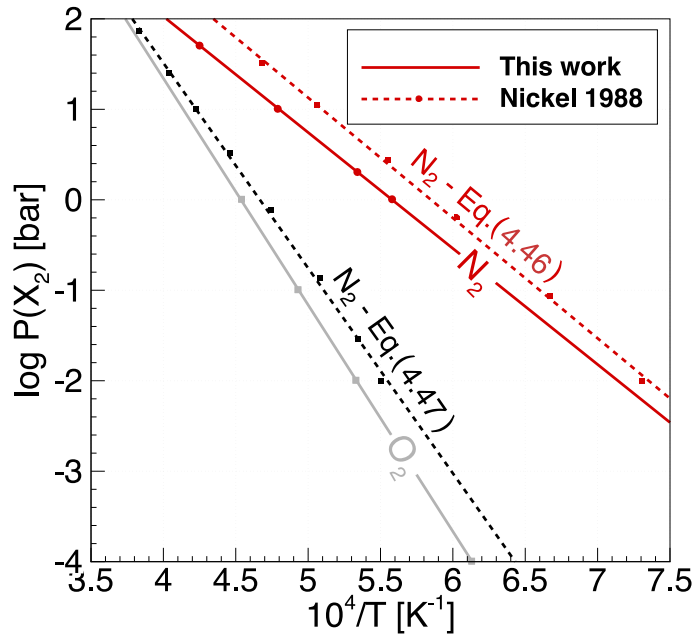
(a) Nitridation passive-to-active transitions
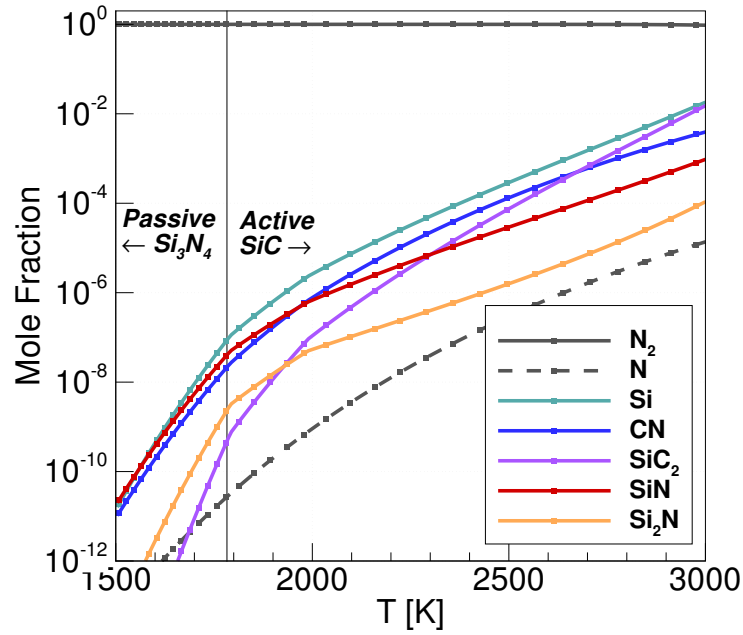


(b) SiC-N$_2$

Figure 4.9: (a) Predicted P-A nitridation transitions (solid), compared to thermodynamic calculations of Nickel [92] (dashed). Oxidation in O$_2$ is shown for comparison. (b) Gaseous species for SiC nitridation in P$_{N_2}$ = 1.00 bar.

The transition process appears more gradual and not marked by a sudden change in the surface composition, and outgassing is six orders of magnitude less than observed in oxidation at transition. This behavior is consistent with that observed by Panerai et al. [93]. Concentrations of molecular and atomic nitrogen remain at ambient levels throughout passive and active states, and suggests that SiC nitridation is reaction-limited, unlike oxidation which is primarily diffusion-limited at higher partial pressures.

### 4.3.3 Predominant Condensed Phases

Predominance diagrams are typically isothermal plots describing equilibrium condensed species, given the partial pressures of gaseous species. Figure 4.10 instead shows the *predominant* condensed species via Eq. (2.32) as a function of oxygen/nitrogen pressure and surface temperature. The total pressure in each case is equal to the oxygen/nitrogen pressure (no diluents). P-A transition conditions are easily inferred from these plots at the boundaries where $SiO_2$ or $Si_3N_4$ is no longer the predominant condensed phase, or when $SiO_2$ or $Si_3N_4$ is not thermodynamically stable.

For $SiC$-$O_2$ in Fig. 4.10(a), condensed silicon is stable in the active oxidation region at oxygen pressures above 1500 Pa. The mechanism for silicon condensation is unclear, but Fig. 4.10(a) suggests that Si is thermodynamically preferred over SiC at higher oxygen and total pressures. At temperatures more than 500 K above the P-A transition point, SiC sublimates silicon preferentially, leading to a carbon-rich

surface layer [94]. The passive $SiO_2$ region overlaps the active SiC and Si regions, corresponding to the non-physical solutions in Fig. 4.5 (dashed lines), and suggests a "thermodynamic hysteresis" between A-P and P-A transitions.



(a) $SiC$-$O_2$ (oxidation)　　　(b) $SiC$-$N_2$ (nitridation)
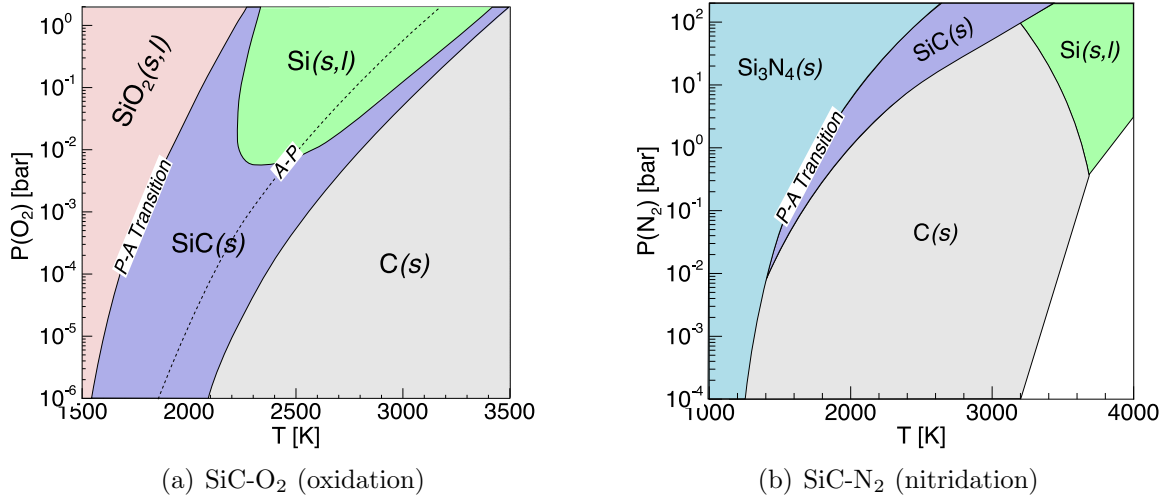
Figure 4.10: Predominant condensed surface phases for SiC oxidation and nitridation at reduced total pressure. (a) exhibits an "overlap" region that is indicative of thermodynamic hysteresis between P-A and A-P transitions.

$SiC$-$N_2$ nitridation is described in Fig. 4.10(b), and differs notably from the oxidation case. The phases observed are generally consistent with the reactions proposed by Nickel [92]. The graphitic C(s) surface is observed at much lower temperatures, so Si sublimation from SiC is not the mechanism. Instead, a two-step process with Eq. (4.46) and Eq. (4.47) explains the formation of a carbon-rich surface. $Si_3N_4$ is not thermodynamically stable in the active region, and silicon evaporates at reduced total pressures, leaving behind only C(s). For both cases, P-A transition conditions are relatively independent of the total pressure, since thermodynamic stability of the silica oxide/silicon nitride controls P-A transition. However, total pressure affects evaporation-condensation equilibria, and thus may affect condensed species such as

silicon.

## 4.3.4  Mass Loss Rates

In the open-system analysis, the B' parameter describes the steady-state mass flux from the surface, which is equal to the rate of mass loss due to oxidation or nitridation. The mass loss rates due to oxidation and nitridation of SiC at constant temperature and pressure have been measured in experiments performed by Rosner and Allendorf [89, 95]. These experiments were performed at very low pressures in the reaction-limited regime.

A SiC "removal probability" $\varepsilon$ is defined by Rosner in Eq. (4.48):

$$\varepsilon = \frac{J_{\text{Si,C}}}{J_{\text{x}_2}} \tag{4.48}$$

Rosner evaluated the reactant $O_2$ or $N_2$ flux to the surface using the Hertz-Knudsen equation [89]. The removal probability is related to the B' parameter via Eq. (4.49):

$$\varepsilon = B' \frac{M_e}{M_w} \frac{X_{w,\text{C}}}{X_{e,\text{x}_2}} \tag{4.49}$$

Here, $X_{\text{w,C}}$ is the elemental mole fraction of carbon at the surface in any molecular configuration, and $X_{e,\text{x}_2}$ is the reactant mole fraction in the ambient environment.
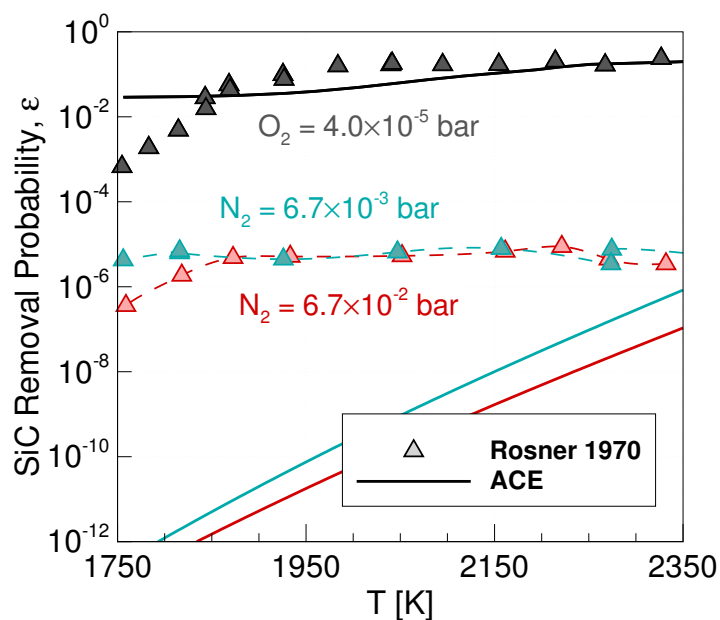
Figure 4.11: Comparison of predicted SiC oxidation and nitridation mass loss rates to experimental data from Rosner and Allendorf [89].

Figure 4.11 compares the measurements of Rosner and Allendorf to model results evaluated with Eq. (4.49) at equivalent total pressures and oxygen/nitrogen partial pressures. Measured oxidation rates in the active regime (above 1850 K) agree well with the model results, but below 1850 K there is a growing discrepancy between measured mass loss rates and those derived from the model. This suggests that the oxidizing surface tends towards equilibrium at higher temperatures during active oxidation, but perhaps not at temperatures close to passive/active transition.

For nitridation, the overall agreement is much poorer, but follows the same trend, tending towards equilibrium at higher temperatures. Although the discrepancy between the predictions and experimental measurements is six orders of magnitude, the *absolute* error is actually quite small, on the order of $10^{-6}$. Of greater significance is

the qualitative difference between oxidation and nitridation mass loss rates. Experimental measurements and model predictions both indicate that material loss due to oxidation should be at least four orders of magnitude greater than that of nitridation. Interestingly, Rosner and Allendorf also observed differences in the behavior of molecular vs. atomic oxygen/nitrogen [89], observing enhanced oxidation/nitridation with *atomic* oxygen/nitrogen. This is difficult to examine with the equilibrium approach, since both oxygen and nitrogen in equilibrium are negligibly dissociated below temperatures of ∼2000 K.

### 4.3.5 Passive-to-Active Transition Mechanisms

Although multiple equilibrium states may exist at the *same* temperature and oxygen pressure, each state exhibits different thermodynamic properties and mass loss rates. The path that the system will follow during P-A transition minimizes the free energy at the surface for each temperature, and other equilibrium solutions at that temperature are thermodynamically unstable. Once the system transitions from passive to active oxidation, A-P mechanisms such as attainment of sufficient $SiO(g)$ pressure at the surface prevent transition back to a passive state.

Experiments in the literature show two mechanisms for P-A transitions: constant pressure and constant temperature. *Thermal* oxidation/nitridation involves heating silicon carbide in constant pressure oxidizing or nitridizing environments (moving from right to left on the Arrhenius plot). Aerothermal heating facilities, used in the experiments of Panerai et al. [73, 93], demonstrate constant pressure transitions.

P-A transition can also be achieved at constant temperature by reducing the ambient oxygen/nitrogen pressure (moving downwards on the Arrhenius plot). Thermogravimetric Analysis (TGA) facilities utilize this mechanism [78, 81].
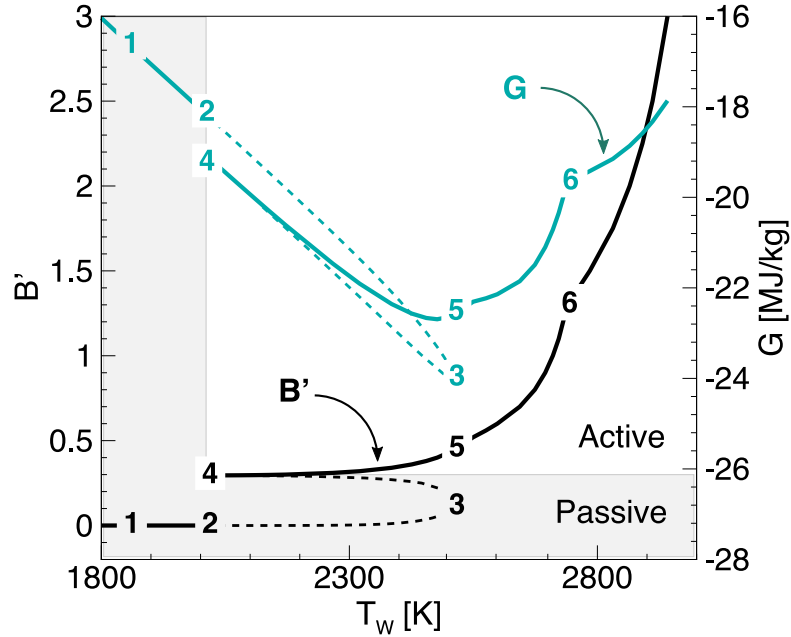


Figure 4.12: Modified B' plot for passive-to-active transition via thermal oxidation at constant pressure at $5.0 \times 10^{-2}$ bar air. Dashed lines denote solutions that are thermodynamically unstable, and passive states are in the shaded region.

The mechanism for thermal oxidation of SiC at constant pressure is described in Fig. 4.12. Gibbs free energy of the mixture determines thermodynamic stability and behavior, and the B' parameter describes the relative flux of oxidation products from the surface. The proposed thermal oxidation mechanism for SiC is presented in Fig. 4.12 with the solid line. At $5.0 \times 10^{-2}$ bar air, passive oxidation occurs below 1800K. As surface temperature increases further, the mechanism is described in detail as follows:

1. In the passive oxidation state between $\boxed{1} \to \boxed{2}$, only one equilibrium solution

exists, and the B' values indicate that the $SiO_2$(s) surface is relatively inert.

2. Around 2000 K, multiple equilibrium solutions exist at states $\boxed{2}$ and $\boxed{4}$. State $\boxed{2}$ is in the passive oxidation regime, but $\boxed{4}$ is the transition to active oxidation. However, the free energy at state $\boxed{4}$ is actually lower than state $\boxed{2}$, and suggests that $\boxed{4}$ is thermodynamically favored. Thus, it follows that P-A transition occurs directly from $\boxed{2} \rightarrow \boxed{4}$, and is discontinuous with respect to mixture thermodynamic properties and mass loss rates.

3. Above 2000 K, the predicted path is $\boxed{4} \rightarrow \boxed{5}$, and the surface is actively oxidizing. Other states are thermodynamically unstable, shown in Fig. 4.12 with dashed lines. Although path $\boxed{4} \rightarrow \boxed{3}$ has a lower free energy overall, this would imply transition back to the passive state, which is physically unattainable due to A-P mechanisms.

4. Above 2500 K for states $\boxed{5} \rightarrow \boxed{6}$, the surface is still oxidizing actively, and there is again only one equilibrium solution. The B' plot indicates that the surface mass loss rate increases rapidly beyond 2500 K.

During thermal oxidation of SiC, transition from a passive to active state is marked by a sudden change in the equilibrium species composition, illustrated in Fig. 4.7. Comparatively, the transition from passive to active nitridation in Fig. 4.9(b) is much more gradual, and no clear change in the species composition is observed. This suggests fundamental differences in the thermodynamics of SiC oxidation versus nitridation.

(a) Air, constant pressure oxidation

(b) $O_2$, constant temperature oxidation

(c) $N_2$, constant pressure nitridation
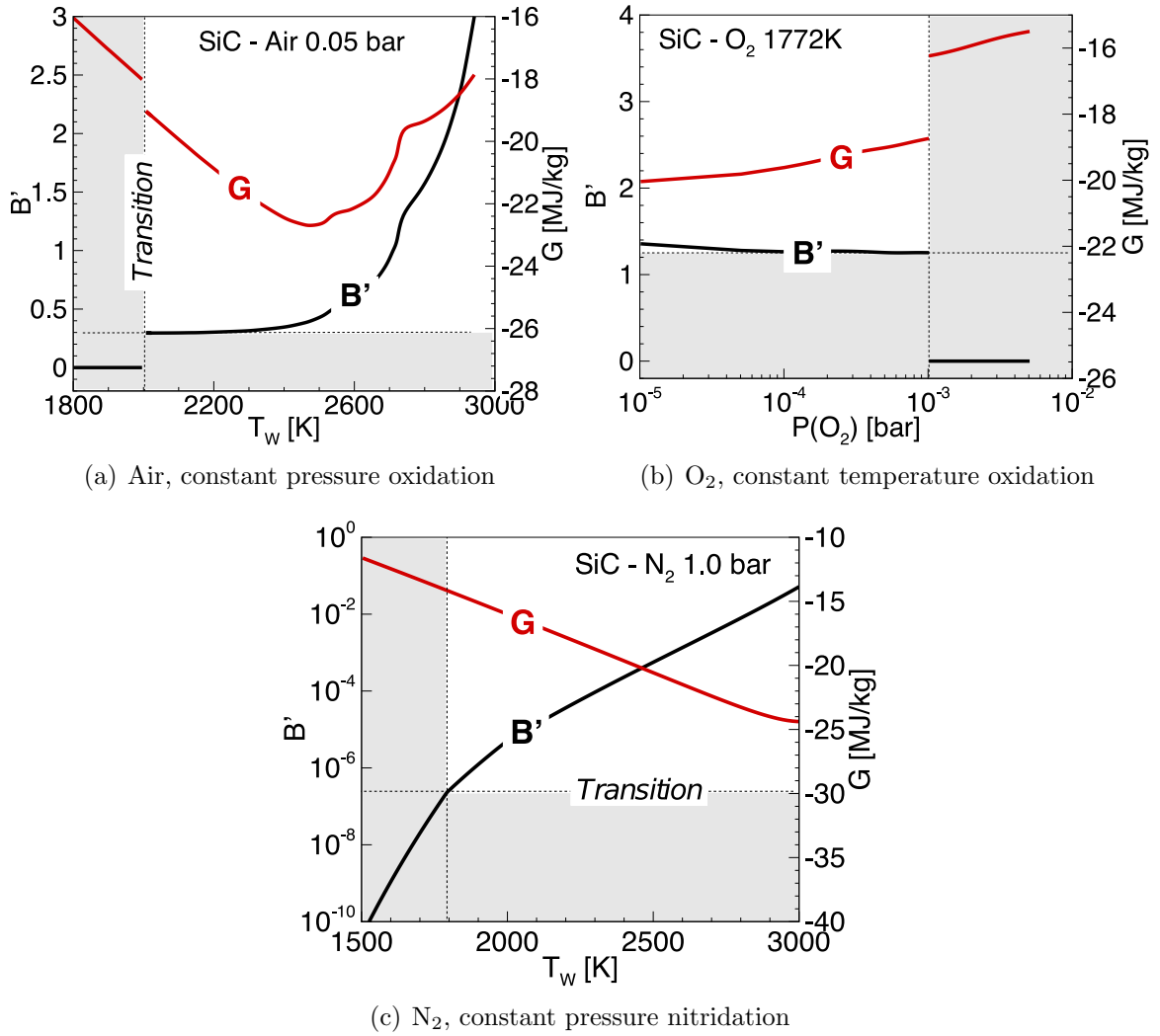
Figure 4.13: Thermodynamics of different mechanisms for SiC P-A transition. Shaded regions represent a passive state with stable condensed oxide/nitride. Oxidation P-A transitions exhibit a "jump" in both B' and free energy.

Figure 4.13 illustrates the different mechanisms for P-A transitions, following the same procedure shown in Fig. 4.12 to determine the equilibrium state. For oxidation, Figs. 4.13(a) and 4.13(b) show that P-A transitions for both mechanisms are discontinuous with respect to the mixture thermodynamic properties, and B' values are $\mathcal{O}(1)$. Thermal nitridation (constant pressure) in Fig. 4.13(c) is smooth in comparison, with B' values around $\mathcal{O}(10^{-6})$, indicating minimal contribution from nitridation

products. These plots readily explain the difference between oxidation and nitridation behavior.

## 4.3.6  Temperature Jump

In an aerothermal heating environment, Eqs. (2.63) represents the surface energy balance at the oxidizing surface. One-dimensional material response calculations are performed to model the P-A thermal oxidation and nitridation of SiC, analyzing the surface temperature and in-depth heat conduction over a 0.025 m SiC domain. Equation (2.63) is imposed as a boundary condition for the one-dimensional transient heat equation. Table 4.1 shows the representative properties of SiC used in the material response. Note that thermal conductivity and heat capacity are functions of temperature, and not constant.

Table 4.1: Properties of SiC at 1750 K

| Property | | Value | |
|---|---|---|---|
| Thermal Conductivity | $\kappa$ | 25.0 | W/m-K |
| Heat Capacity | $C_p$ | 1.317 | kJ/kg-K |
| Heat of Formation | $\Delta H_f$ | -1.784 | MJ/kg |
| Emissivity | $\epsilon$ | 0.7 | |

Three test cases are examined based on the ICP experiments of Panerai et al. in air [73] and nitrogen [93], summarized in Table 4.2. For each case, the SiC model is evaluated at the ambient gas composition and total pressure to obtain B' and wall enthalpy, $h_w$, as a function of temperature, and tabulated. Edge enthalpies at the stagnation point are estimated from the measured flowrate and electrical input power, accounting for flow non-uniformity. The aerothermal heating coefficient is

then calculated from the edge enthalpy and reported cold-wall heat flux [73, 93] with Eq. (2.73), and assumed to be *constant.* This assumption is re-examined and verified later in Chapter 5. Unity Lewis number is assumed for both air and nitrogen mixtures in Eq. (4.50):

$$Le_{\mathrm{air}} \approx Le_{\mathrm{N_2}} \approx 1.0 = \frac{C_H}{C_M} \qquad (4.50)$$

Table 4.2: Aerothermal Parameters for Surface Energy Balance

| No. | Gas | $P_{\mathrm{total}}$ [Pa] | $h_e$ [MJ/kg] | $\rho_e u_e C_H$ [kg/m$^2$-s] |
|---|---|---|---|---|
| HER-17 | Air | 2189 | 19.3* | 0.0675 |
| MTA-12 | Air | 5085 | 17.0* | 0.0826 |
| MTA M23 | N$_2$ | 2165 | 20.1† | 0.0597 |

* Enthalpy estimated with inductive coupling efficiency $\eta = 0.3$, average $h_e = \eta P_{el}/\dot{m}$, and Gaussian enthalpy profile with $\sigma = 0.76$
† Reported by Panerai et al. [93]

Surface temperature measurements from Panerai are compared to the material response results in Table 4.3. At the P-A transition point, both air cases exhibit the same temperature jump effect observed in experiments, shown in Fig. 4.14, although pre- and post-jump temperatures differ by up to 8%. The temperature jump corresponds to a nearly-stepwise change in B' between passive and active states, along with significant surface outgassing consistent with Fig. 4.13(a). By extension, the nitridation mechansim in Fig. 4.13(c) suggests *no temperature jump* during P-A transition for SiC-N$_2$. Indeed, no temperature jump is observed in the N$_2$ case, agreeing with the experiments of Panerai [93], and steady-state temperatures differ by only 3%.

Table 4.3: Surface Temperature Comparison

| Measurement | Experiment | Simulation | % Error |
|---|---|---|---|
| HER-17 | | | |
| Pre-jump | 2115K* | 1952K | 7.71% |
| Post-jump | 2512K* | 2327K | 7.36% |
| MTA-12 | | | |
| Pre-jump | 2064K* | 2012K | 2.52% |
| Post-jump | 2542K* | 2388K | 6.06% |
| MTA M23 | | | |
| Steady-state | 2350K† | 2273K | 3.28% |

* Reported by Panerai et al. [73]
† Reported by Panerai et al. [93]
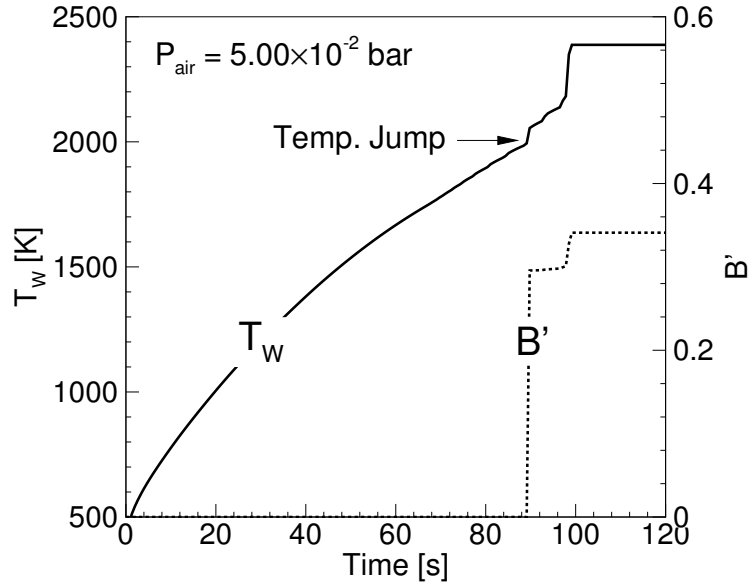


Figure 4.14: Predicted surface temperature jump during P-A thermal oxidation for MTA-12 test case occurs at ∼90s, corresponding to a jump in B'.

There is a clear relationship between the thermodynamic mechanisms in Fig. 4.13 and the observed temperature jump during thermal oxidation of SiC. With the thermodynamic approach, the temperature at which P-A transition and hence the jump occurs depends only on the oxygen/nitrogen partial pressure. Furthermore, the tem-

perature jump phenomenon is accurately predicted in terms of thermodynamic properties and surface mass fluxes, concurrent with the onset of P-A transition in *oxidizing* environments. These results validate the thermodynamic model for oxidation and nitridation in both passive and active states, including P-A transition.

## 4.4  Chapter Summary

Chemical equilibrium calculations were performed to analyze the thermodynamics of silicon carbide oxidation and nitridation, accounting for boundary layer mass transport and multi-component equilibrium [75,76]. Passive-to-active oxidation transitions showed good agreement with Wagner's theory and were validated with experimental measurements, and nitridation transitions were verified with thermodynamic calculations. Oxidation transitions in oxygen and air were primarily dependent on oxygen partial pressure and temperature, and the addition of nitrogen to oxygen mixtures showed only a 3% difference in transition temperature. SiC oxidation exhibited a bifurcation in the thermodynamics, species composition and surface mass fluxes between passive and active states, but nitridation did not.

Material response calculations utilizing mixture thermodynamic properties and mass fluxes from the equilibrium model validated the thermodynamics of oxidation and nitridation. The surface temperature jump phenomenon was demonstrated during thermal oxidation, and elucidated the relationship between passive-to-active transition mechanisms and the temperature jump. Predicted surface temperatures agreed with experimental measurements within 8%, and the lack of temperature jump for

nitridation was confirmed.

Although the thermodynamic equilibrium approach was validated with several important metrics [75, 76], limitations in the model were also identified. Differences in passive-to-active oxidation states between the equilibrium model and experiments were observed at very low reactant pressures, suggesting a nonequilibrium, reaction-limited regime. In addition, the effect of atomic oxygen in highly dissociated flows was not able to be studied with the equilibrium approach.

# CHAPTER 5

# Coupled Oxidation Simulations

In this chapter, analyses of SiC oxidation are presented, demonstrating the coupling between the surface chemistry model developed in Chapter 4, CFD techniques described in Chapter 3, and material response. In hypersonic flight applications, ambient conditions are dynamic and change with the trajectory. Although the SiC material behavior is well understood during oxidation, the effect of oxidation products (e.g. SiO, CO) in the boundary layer has not been investigated. In fact, these are coupled processes, since the state and composition of the boundary layer directly affect the oxidation behavior. Interactions between the reacting boundary layer and the oxidizing surface may be responsible for gas-surface phenomena, such as the temperature-jump observed [73, 96]. Therefore, a more detailed understanding of the coupled boundary layer is needed.

The goal of this chapter is to investigate the effect that gaseous oxidation products (Si, SiO, CO) have on the composition of the boundary layer in nonequilibrium, as well as surface properties. The SiC gas-surface model developed in Chapter 4 is coupled to nonequilibrium CFD flowfield analyses, and simulations are performed to investigate the coupled boundary layer under thermal and chemical nonequilib-

rium [97]. The CFD methodology is discussed first, extending the CFD-radiation framework developed in Chapter 3 but requiring some modifications to the blowing boundary condition to account for surface chemistry. Results are then presented for the boundary layer under both passive and active oxidation for subsonic and hypersonic flows.

## 5.1 Modifications

Modifications to the previously developed CFD-radiation framework (Chapter 3) are described in this section. These modifications are necessary to account for the effects of surface chemistry on the flowfield, as well as parameters specific to SiC-air chemistry.. The LeMANS CFD code is coupled with the equilibrium SiC oxidation model, including the use of NEQAIR [40] to simulate the radiative emission from the boundary layer. Note that only steady-state solutions are sought.

### 5.1.1 Equilibrium Oxidation Surface Chemistry

An equilibrium oxidation wall boundary condition is implemented in the LeMANS CFD code. The coupling between CFD, radiation, and surface chemistry is illustrated in Fig. 5.1. Radiation coupling is one-way, and is identical to the approach described in Chapter 3. Species mass fractions $Y_w$, wall enthalpy $h_w$, and B' from the SiC gas-surface oxidation model are tabulated over a range of pressures (500 to 500,000 Pa) and temperatures (300 K to 3000 K) for air, and bilinear interpolation is used at the local wall temperature and pressure to determine the properties at each surface

face.

Surface mass balance calculations are already accounted for in Eqs. (4.44) and
(4.45) between boundary layer and blowing gases, so mass fractions from the oxidation
model, $Y_w$, are directly imposed at the wall based on the local wall temperature
and pressure. The species mass fractions imposed at the surface account for both
consumption of reactants and blowing of gaseous oxidation products. The surface
coverage is implicitly modeled with $Y_w$, since $Y_w$ is inherently related to the surface
coverage (see Figs. 4.7 and 4.10). The composition of the blowing flux is defined
by $Y_w$, and the total blowing flux is computed from Eq. (5.1), which is simply a
rearrangement of Eq. (2.62).

$$\dot{m}_w = B' \rho_e u_e C_M \tag{5.1}$$

The mass transfer coefficient, $C_M$, for surface chemistry calculations is determined
indirectly from the heat transfer coefficient $C_H$ and the Lewis number in Eq. 4.42.
A Lewis number of $Le = 1.4$ is assumed for air. The heat transfer coefficient is
then computed from CFD analysis of the flowfield in Eq. (2.73), described earlier in
Chapter 2.4.2. Note that Eq. (2.73) is a rearrangement of Eq. (4.40), and the quantity
$\rho_e u_e C_H$ is evaluated directly from Eq. (2.73) using the CFD-computed heat flux, $Q_w$,
and normalizing by the interpolated wall enthalpy from the SiC oxidation model,
$h_w$, *without* evaluating exact edge properties. This approach explicitly computes the
mitigating effects of blowing on the surface heating, without relying on empirical
correlations [34].
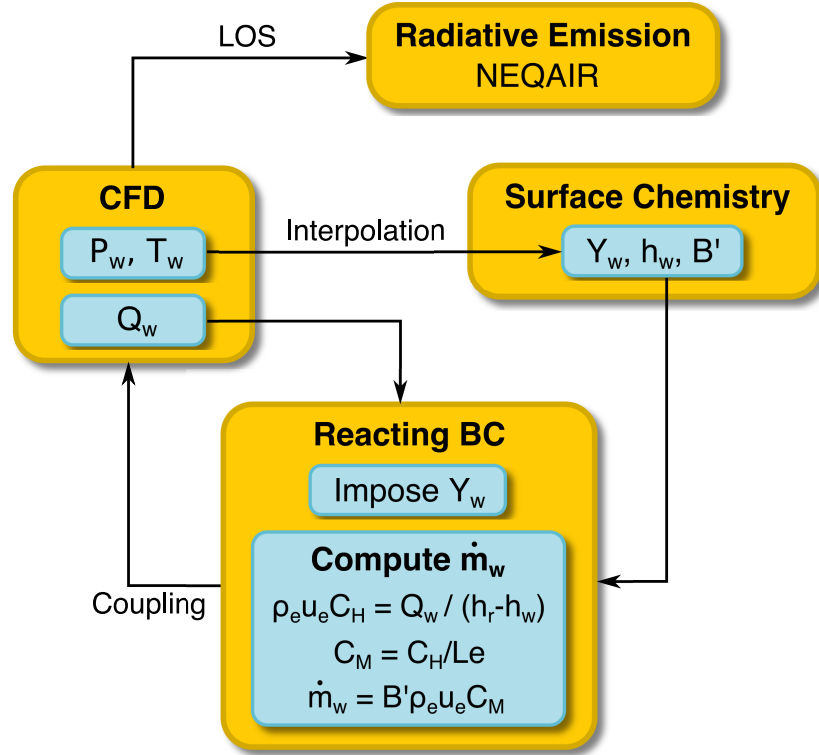
Figure 5.1: CFD-radiation-surface chemistry coupling.

Following the previous approach developed by Martin and Boyd [31] in Eqs. (3.7) - (3.10), momentum balance at the wall along with the ideal gas relation determines the blowing parameters of density, velocity, and pressure.

## 5.1.2 Radiative Equilibrium

The equilibrium surface temperature can also be computed by extending this approach. From the full SEB in Eq. (2.63), in the steady-state limit the local in-depth conduction is approximated as zero, resulting in Eq. (5.2):

$$\overbrace{\rho_e u_e C_H (h_r - h_w)}^{\text{convection}} - \overbrace{\epsilon \sigma T_w^4}^{\text{radiation}} - \overbrace{\dot{m}_w h_w}^{\text{oxidation}} \approx 0 \qquad (5.2)$$

Note that $B'$, $\dot{m}_w$, and $h_w$ are all functions of wall temperature $T_w$. The steady-state *non-uniform* wall temperature can thus be computed using an iterative zero-finding technique (e.g. Newton-Raphson, Bi-section). The function to zero is $f(T_w)$:

$$f(T_w) = Q_{\text{conv}} + Q_{\text{rad}} + Q_{\text{oxid}} \tag{5.3}$$

Using the Newton-Raphson method, the iterative calculation is expressed simply as:

$$T_w^{n+1} = T_w^n - \frac{f(T_w^n)}{f'(T_w^n)} \tag{5.4}$$

However, the derivative $f'(T_w)$ cannot be explicitly evaluated due to the tabulated values of $h_w$ and B' needed to evaluate $\dot{m}_w$. A finite-difference approximation is needed for the derivative, which simplifies to the secant method:

$$f'(T_w^n) = \frac{f(T_w^n) - f(T_w^{n-1})}{T_w^n - T_w^{n-1}} + \mathcal{O}^2(\Delta T_w) \tag{5.5}$$

$$\boxed{T_w^{n+1} = T_w^n - f(T_w^n)\frac{T_w^n - T_w^{n-1}}{f(T_w^n) - f(T_w^{n-1})}} \tag{5.6}$$

Convergence is obtained when $T_w^{n+1} - T_w^n < \varepsilon$, where $\varepsilon = 1.0 \times 10^{-3}$ K is found to work well, resulting in stable surface temperature predictions. Note that the above iteration requires two initial values, but the method is not sensitive to the choice of these initial conditions. This calculation is performed for *each* wall face in the CFD domain to evaluate the radiative equilibrium temperature at that face.

### 5.1.3 Chemical Kinetics

Characteristic vibrational temperatures are defined for each molecular species according to Eq. (5.7), where $\omega_e$ is the wavenumber in cm$^{-1}$ and $h$ is Planck's constant. Ground state molecular constants from NIST spectroscopic data [98] are used to determine the characteristic vibrational temperatures for SiO as 1782 K, and for SiN as 1655 K with the NRR/AHO model [12].

$$\Theta_{vib} = \frac{100\omega_e hc}{k_B} \tag{5.7}$$

Relaxation times for air species are from Hash et al. [99], and for CO and CO$_2$ from Park et al. [64]. Relaxation times for CN, SiO and SiN are modeled from the functional relationship of Millikan and White [26] in Eq. (2.42), and the model parameters for SiO and SiN are tabulated in Table 5.1 for various collision partners.

The chemical kinetics mechanism used in this chapter is based on the Johnston-Brandis model for air and CO$_2$ [57] in Appendix A.1. The mechanism involves 18 species and 34 reactions. From equilibrium surface chemistry, gaseous species from the oxidation of SiC include Si, Si$^+$, SiO, and SiN. Reactions involving these species are shown in Table A.2 in Appendix A.2. Only the neutral species for SiO, and SiN are considered since all ions are assumed to recombine at the surface. Additionally, the surface is typically at much lower temperatures than the gas outside the boundary layer, so ionization effects should be minimal near the surface. Overall, the mechanism used in this chapter involves 24 species and 42 reactions. Although SiO(g) and CO(g) are by far the most dominant products of surface chemistry, equilibrium analyses

Table 5.1: SiO and SiN Vibrational Relaxation Constants

| | $M$ | $a$ | $b$ |
|---|---|---|---|
| SiO | | $\Theta_{vib} = 1782$ K | |
| | SiO | 117.662 | 0.0325 |
| | $CO_2$ | 117.605 | 0.0325 |
| | CO | 103.718 | 0.0305 |
| | Ar | 114.768 | 0.0321 |
| | $N_2$ | 103.706 | 0.0305 |
| | $O_2$ | 107.913 | 0.0311 |
| | N | 81.692 | 0.0271 |
| | O | 85.867 | 0.0278 |
| SiN | | $\Theta_{vib} = 1655$ K | |
| | SiN | 104.170 | 0.0321 |
| | $CO_2$ | 105.322 | 0.0323 |
| | CO | 93.125 | 0.0304 |
| | Ar | 102.838 | 0.0319 |
| | $N_2$ | 93.115 | 0.0304 |
| | $O_2$ | 96.820 | 0.0310 |
| | N | 73.603 | 0.0270 |
| | O | 77.318 | 0.0277 |

suggest that $Si_2C(g)$, $SiC_2(g)$, and $Si_2N(g)$ may be present in significant amounts. However, reliable chemical rate data are not available for these species to the author's knowledge, so these species are assumed inert within the gas phase.

## 5.2    Coupled Results

### 5.2.1    Test Cases

Table 5.2 summarizes the simulations performed. In Cases #1 through #4, the Iso-Q test geometry in Fig. 5.2(a) is exposed to high-enthalpy, subsonic flow. The Iso-Q geometry has a diameter equal to the nose radius, and maintains a relatively uniform heat flux over the surface. An axisymmetric structured mesh for the Iso-Q geometry is utilized for the flowfield, and three different wall boundary conditions

are imposed: non-catalytic, fully-catalytic, and equilibrium surface chemistry. The
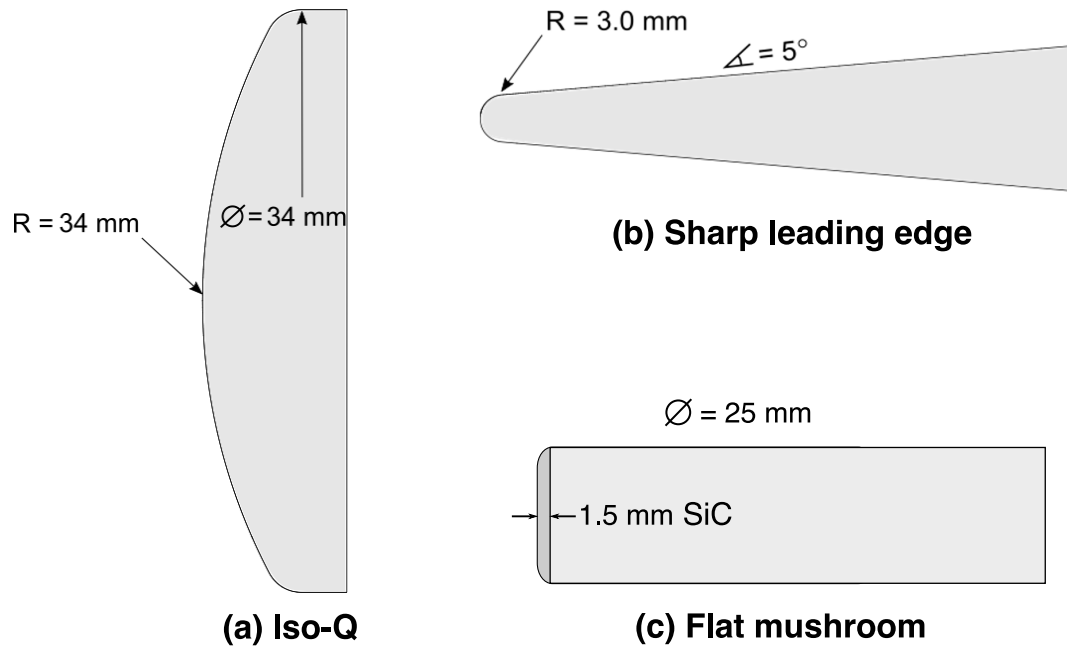


Figure 5.2: Test sample geometries.

non-catalytic wall is effectively *inert*, while the fully-catalytic wall condition has only ion and atom recombination. The "passive" and "active" wall conditions utilize the same equilibrium surface chemistry boundary condition, but impose different wall temperatures. The "passive" temperature is chosen from the equilibrium SiC model to be slightly below the predicted passive-to-active transition temperature, while the "active" temperature is slightly above.

Case #5 utilizes the same Iso-Q geometry, but at *hypersonic* flow conditions of 7.1 km/s. The stagnation enthalpy closely matches the subsonic case, and post-shock stagnation pressures are also comparable at the 70 km ambient state. This provides a useful comparison of subsonic versus hypersonic flow considerations, including any nonequilibrium effects.

Table 5.2: Geometry, Freestream, and Wall Conditions

| No. | Dim. | Geom. | Gas | $P_\infty$[Pa] | $T_\infty$[K] | $u_\infty$[m/s] | $h_0[\frac{MJ}{kg}]$ | $T_w$[K] | Wall Cond. |
|---|---|---|---|---|---|---|---|---|---|
| 1 | Axi | Iso-Q | Air | 5000 | 6000 | 184.6 | 25.14 | 2005 | Non-catalytic |
| 2 | Axi | Iso-Q | Air | 5000 | 6000 | 184.6 | 25.14 | 2005 | Fully-catalytic |
| 3 | Axi | Iso-Q | Air | 5000 | 6000 | 184.6 | 25.14 | 2005[P] | Eq. Surf. Chem. |
| 4 | Axi | Iso-Q | Air | 5000 | 6000 | 184.6 | 25.14 | 2025[A] | Eq. Surf. Chem. |
| 5 | Axi | Iso-Q | Air | 5.4 | 219.6 | 7090.8[a] | 25.36 | 2025[A] | Eq. Surf. Chem. |
| 6 | 2D | Edge | Air | 1937 | 210 | 3000.0[b] | 4.71 | 1950 | Non-catalytic |
| 7 | 2D | Edge | Air | 1937 | 210 | 3000.0[b] | 4.71 | 1950 | Fully-catalytic |
| 8 | 2D | Edge | Air | 1937 | 210 | 3000.0[b] | 4.71 | 1950[P] | Eq. Surf. Chem. |
| 9 | 2D | Edge | Air | 1937 | 210 | 3000.0[b] | 4.71 | 2250[A] | Eq. Surf. Chem. |
| 10 | 2D | Edge | Air | 1937 | 210 | 4000.0[c] | 8.21 | 2250[A] | Eq. Surf. Chem. |
| 11 | Axi | Flat | Air | 2000 | 5211 | 813.3 | 15.56 | 2470[A] 2405[R] | Eq. Surf. Chem. |

[a] Mach 23.8 at 70 km          [P] Passive oxidation, Isothermal
[b] Mach 10.3 at 30 km          [A] Active oxidation, Isothermal
[c] Mach 13.7 at 30 km          [R] Computed from radiative equilibrium

Cases #6 through #10 involve a hypersonic flowfield over the leading edge geometry in Fig. 5.2(b). The same isothermal wall boundary conditions are imposed as before. Freestream conditions are based on Mach 10.3 and Mach 13.7 flight at 30 km altitude, which are representative flight conditions. In the previous subsonic case, static pressure is expected to be reasonably constant over the surface. However, the hypersonic case is a shock-driven flow, and properties (including pressure) are generally not constant over the surface in the post-shock region.

Case #11 utilizes the flat mushroom model in Fig. 5.2(c), and both geometry and freestream conditions are based on the "HER M32" case from subsonic experiments performed by Panerai et al. in the Von Karman Institute's (VKI) Plasmatron facility [73, 93]. CFD results from this case are used as inputs to NEQAIR to compare boundary layer emission spectra (following the approach described in Chapter 3). In all cases, chemical equilibrium analysis (CEA) [62] is performed at the conditions listed to obtain detailed species mass fractions in the freestream, and laminar flow
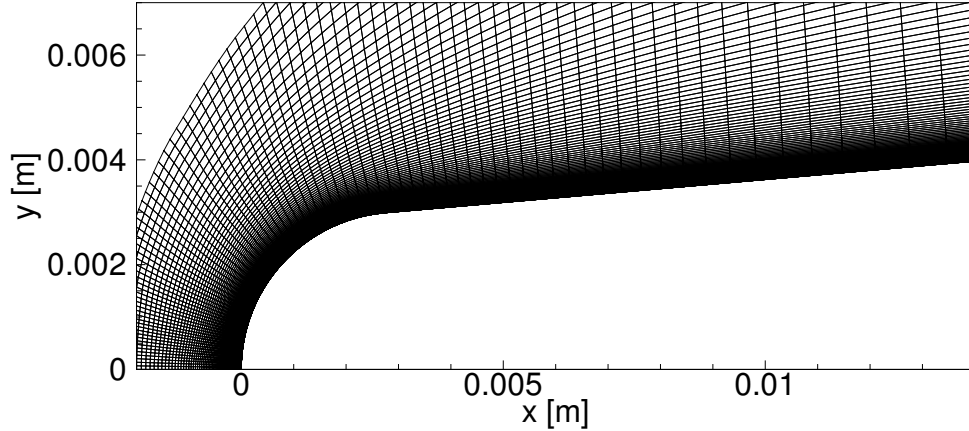
Figure 5.3: Structured quad mesh for leading edge geometry.

is assumed. Structured quadrilateral meshes are constructed for each geometry in Fig. 5.2. Grid convergence is verified when refining the mesh by a factor of 2 in both directions (i.e. "x" and "y", or "r" and "z") results in less than 2% change in the computed surface heat fluxes, pressures, and stagnation line properties, including for the subsonic cases where these metrics are more sensitive to the freestream boundary location. Shock tailoring is performed where relevant. At the wall, $y^+ < 0.1$ to ensure that gradients are resolved, shown in Fig. 5.3 for the leading edge mesh.

## 5.2.2  Iso-Q: High Enthalpy, Subsonic Flow

Figure 5.4 shows the flowfield temperature, velocity, and density contours for the subsonic Iso-Q active oxidation Case #4. The effect of active oxidation on the boundary layer is illustrated in Fig. 5.4(c), with SiO blowing near the surface causing a ~0.5 mm region of flow *away* from the wall.

Centerline properties near the wall are shown in Fig. 5.5. Note that the wall is located at z = 0. The boundary layer extends to ~3.0 mm for all Iso-Q cases,

(a) Temperature ($T_{tr}$)      (b) Velocity      (c) SiO density
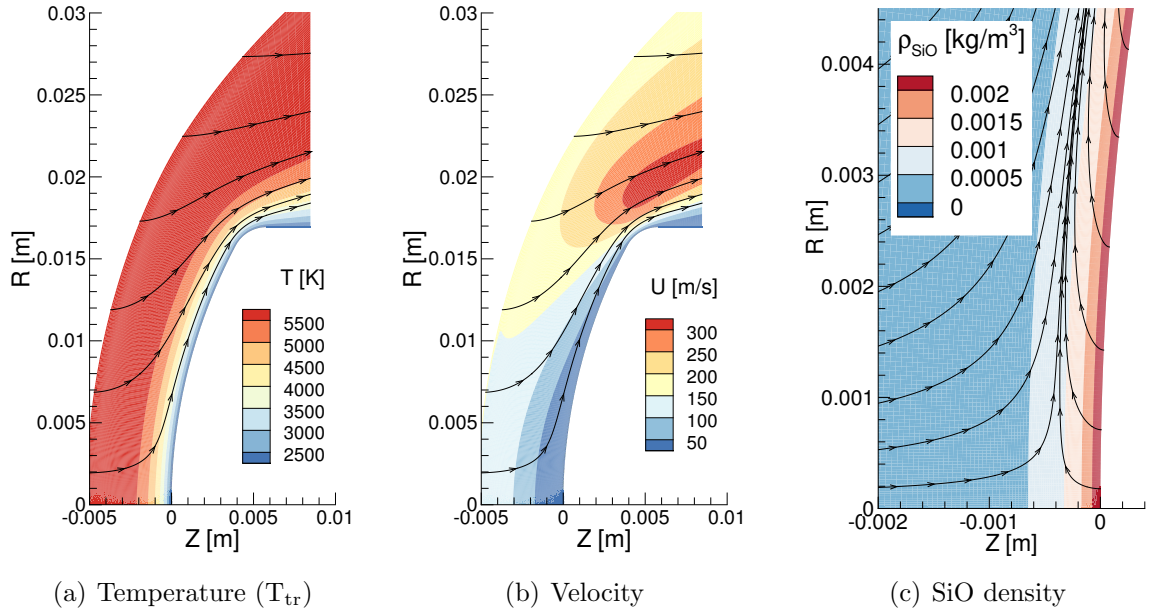
Figure 5.4: Contour plots for Iso-Q Case #4, active oxidation ($T_w = 2025$ K).

as measured by the temperature and mole fraction gradients. Vibrational nonequilibrium is negligible for these subsonic cases due to the lack of shocks, and flow is well described by a single temperature. The temperature profiles in Fig. 5.5(a) show subtle but important differences between each wall condition. The fully-catalytic and passive oxidation cases show nearly *identical* temperature profiles, and steeper gradients than the non-catalytic wall. The active oxidation case shows a much smaller thermal gradient due to blowing effects, implying lower surface heating rates.

This blowing effect is apparent from the momentum profile in Fig. 5.5(b), showing a deficit region near the wall for the active case, corresponding to a 0.03 kg/m²-s flux of oxidation products. The deficit region extends to 0.4 mm, but the momentum profile does not recover to freestream values until 1.5 mm upstream. This plot also demonstrates that blowing is negligible or nonexistent for the other cases, which have

(a) Temperature (translational)

(b) Momentum

(c) O$_2$

(d) O-atom

(e) SiO

(f) CO
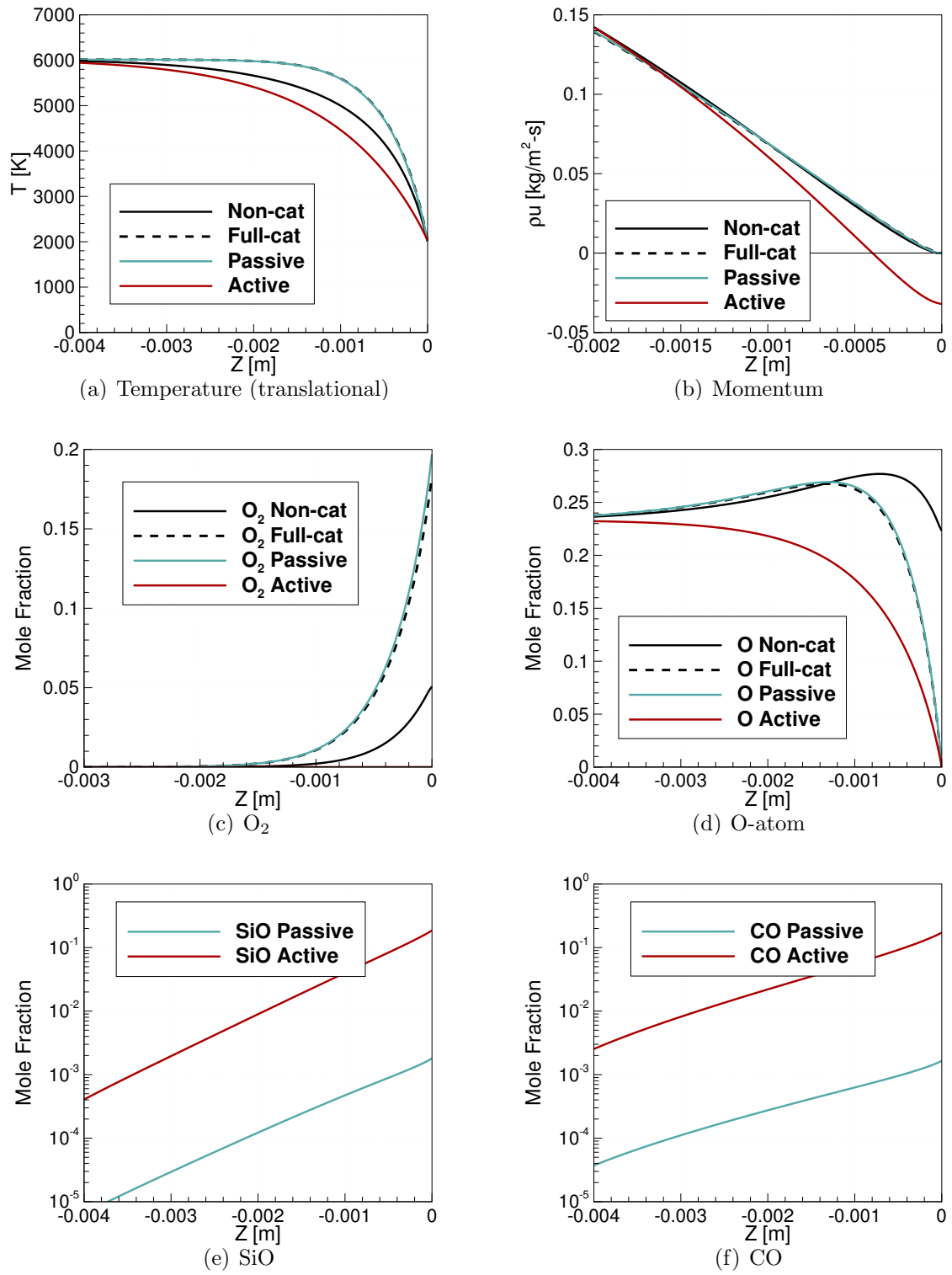
Figure 5.5: Centerline properties for *subsonic* Iso-Q case, surface is located at z = 0.

identical momentum profiles.

Figure 5.5(c) shows the $O_2$ concentration, increasing near the surface in the fully-catalytic and passive cases due to O-atom recombination. Complete recombination is predicted with the equilibrium surface chemistry wall, independent of catalycity. This is because chemical equilibrium is enforced at the passive wall, and $O_2$ is negligibly dissociated at 2000 K. The non-catalytic case shows a smaller increase in $O_2$ concentration near the surface due to flow thermalizing at the relatively cooler wall. In contrast, the active oxidation case exhibits effectively *zero* $O_2$ concentration throughout. $O_2$ is completely dissociated in the freestream at 6000 K, and any $O_2$ that would form from recombination near the cooler wall is consumed at the active SiC surface instead.

Panerai et al. estimated the catalycity of silica ($SiO_2$) to be between 0.002 - 0.03 [100]. The observed agreement between passive oxidation and fully-catalytic wall conditions is due to the equilibrium chemistry assumption, not catalycity. Thus, one should expect surface properties from the passive oxidation case to deviate from the fully-catalytic case at higher surface temperatures where $O_2$ is more dissociated.

The O-atom concentrations in Fig. 5.5(d) demonstrate a consistent trend as well. The O-atom concentration goes to zero at the wall for the fully-catalytic and passive oxidation cases due to complete recombination into $O_2$, and show identical profiles. Likewise, the non-catalytic case shows only partial recombination due to the cooler wall. For the active oxidation case, the decrease in O-atom concentration at the wall is due to O-atom *consumption* at the surface. SiO and CO are the dominant oxidation products released into the boundary layer during active oxidation, but are

124

effectively zero for the passive case in Figs. 5.5(e)–(f). The primary reaction during active oxidation is shown in the literature [69] to be Eq. (4.27):

$$SiC(s) + O_2(g) \leftrightarrow SiO(g) + CO(g)$$

In Fig. 5.5(d), the O-atom mole fractions are higher than the freestream values, which is non-intuitive. The mole fraction metric is somewhat misleading, and it is perhaps more instructive to consider the absolute number density or concentration. Nitrogen recombination occurs further upstream at higher temperatures than oxygen recombination, reducing the *total* number density downstream. As a result, the mole fraction of atomic oxygen increases, reaching a maximum around $z = $ -0.001 m. This leads to an increase in the oxygen mole fraction, even if the oxygen concentration is constant.

**Relation to Temperature Jump**

Profiles of convective heat fluxes over the Iso-Q sample are shown in Fig. 5.6(a). The aerothermal heating coefficient can be computed from Eq. (2.73) by normalizing the convective heat flux, and is plotted in Fig. 5.6(b). The heat flux is largely constant over the surface (due to the aptly-named Iso-Q geometry), but increases at the edges due to higher flow velocities around the shoulder, as seen in Fig. 5.4(b). Not surprisingly, the heat flux profile is identical for the fully-catalytic and passive oxidation cases, and is approximately three times lower for the non-catalytic case. Interestingly, the active oxidation case shows roughly the same heat flux as the passive

case.



(a) Total convective surface heat flux      (b) Heat transfer coefficient
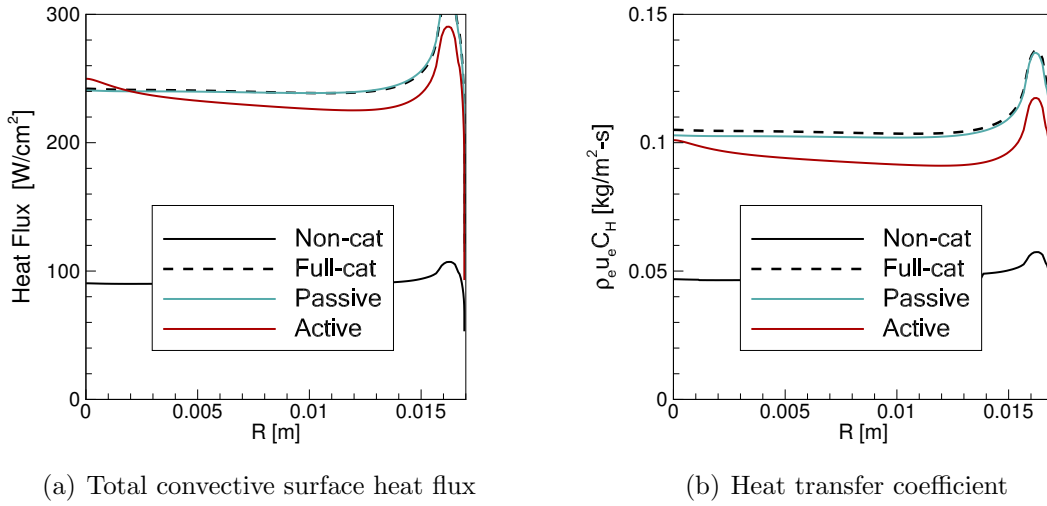
Figure 5.6: Surface heating for subsonic Iso-Q case.

This effect is readily understood by examining the contribution of various heat flux components at the stagnation point in Fig. 5.7. $Q_{\mathrm{tr}}$ and $Q_{\mathrm{ve}}$ are consistent across the non-catalytic, fully-catalytic, and passive cases. The fully-catalytic and passive wall conditions introduce a diffusive flux component that accounts for 60% of the total convective heat transfer. $Q_{\mathrm{tr}}$ is noticeably lower for the active oxidation case due to smaller thermal gradients in Fig. 5.5(a). However, this reduction is offset by an increase in the diffusive component $Q_{\mathrm{diff}}$, which now accounts for 84% of the total convective heating. Overall, the aerothermal heat transfer coefficient in Fig. 5.6(b) does not deviate throughout passive-to-active transition by more than $\pm 10\%$. A range of emissivity values from 0.70 to 0.88 have been proposed by various researchers for SiC [94, 101], and a value of $\epsilon = 0.83$ is used here.

The increase in the diffusive component is consistent with the analysis of Marschall et al. [96]. During transient heating with non-isothermal wall temperatures, Marschall
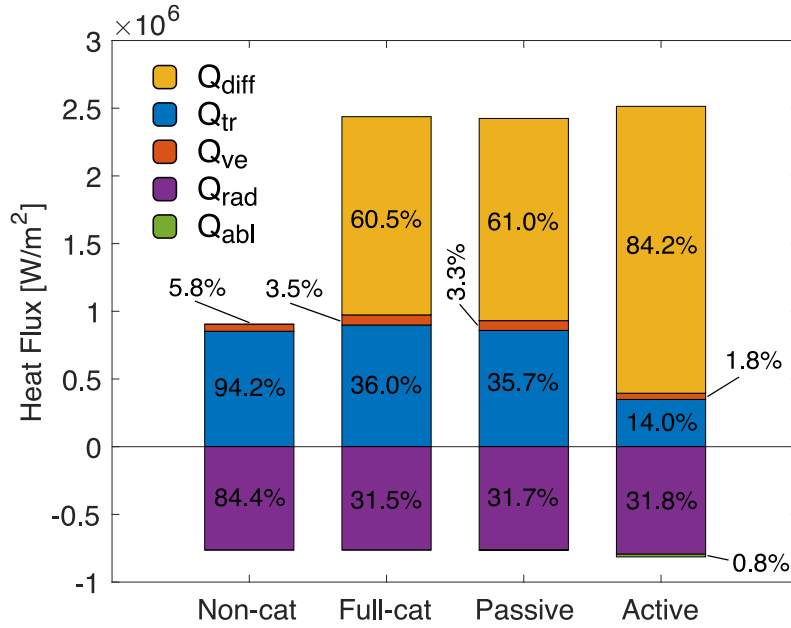
Figure 5.7: Stagnation point surface energy balance for Iso-Q case, positive denotes heating.

suggested that temperature jump in SiC composites occurs due to an increase in surface chemistry during passive-to-active transition. The increased reactivity of SiC over $SiO_2$ is apparent in the $O_2$ concentrations at the surface in Fig. 5.5(c), which accounts for the increase in diffusive heating. Chapter 4.3.6 demonstrated that the temperature jump can occur under *constant* aerothermal heating conditions when wall temperature is not fixed. Figure 5.6(b) suggests that the aerothermal heating coefficient is indeed relatively constant throughout the passive-to-active transition, which is sufficient to trigger the temperature jump phenomenon.

**Radiative Equilibrium Results**

Figure 5.7 indicates an imbalance in the surface heating versus cooling components at the imposed wall temperature of 2025 K. To evaluate the accuracy of the surface

energy balance calculations, the predicted steady-state temperature is compared to the experimentally-measured temperature for Case #11, based on the "HER M32" experiment from Panerai et al. [73, 93]. The isothermal wall temperature in Table 5.2 is the steady-state *post-jump* temperature measured in the subsonic plasma flow experiment [73]. To compute the local steady-state temperature at each wall face, a Newton iteration balances radiative and ablative cooling with convective heat transfer. The predicted equilibrium temperature reaches a maximum of 2405 K at the given flow conditions, and agrees with the experimentally-measured surface temperature of 2470 K within 2.6%.



(a) Case #11, Radiative Equilibrium            (b) Cases #8 and #9, Isothermal
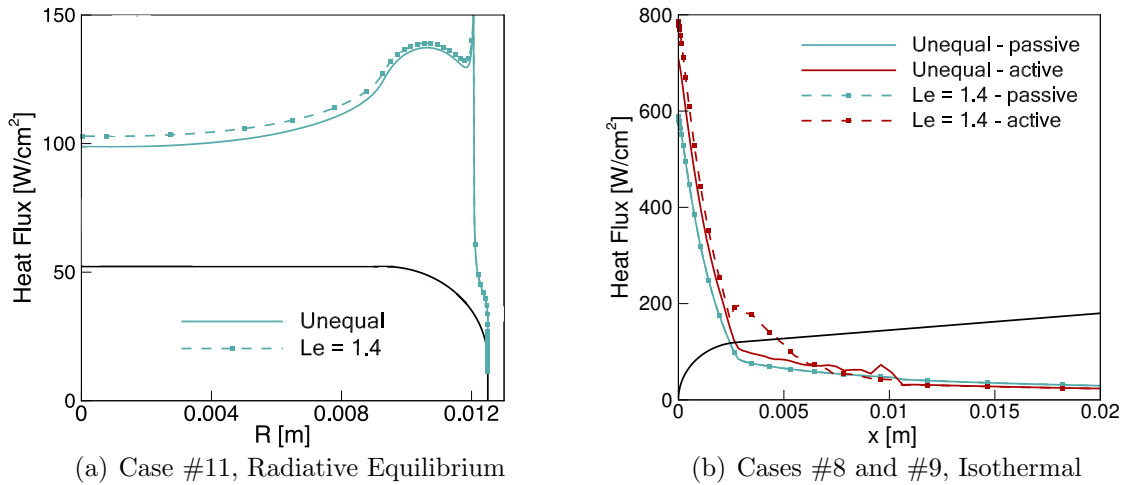
Figure 5.8: Effect of species diffusion models on total convective heating (geometries in black).

Since the chemical diffusive component dominates the convective heating, the choice of diffusion models is also evaluated. Figure 5.8 compares the total convective heating predicted using $Le = 1.4$ (baseline) with the unequal bifurcation model [29], and the bifurcation model predicts overall *lower* heating. The unequal bifurcation

model [29] results in 4% lower total heating for Case #11 in Fig. 5.8(a). Given that radiation is the primary cooling mechanism and scales with $T_w^4$, there is negligible difference ($< 1\%$) in maximum steady-state temperature over the previously computed value. The hypersonic flow in Fig. 5.8(b) exhibits a 10% reduction at the stagnation point during active oxidation (Case #9), but both diffusion models are identical for passive oxidation (Case #8).

### 5.2.3   Leading Edge: Hypersonic flow

Simulations of hypersonic flow over the leading edge geometry represent a flight-realistic application of SiC materials. Ambient conditions are largely altitude-dependent, and post-shock properties depend on both the ambient state and relative flow velocity. Figure 5.9 shows the temperature and pressure contours for active oxidation at Mach 10 (Case #9). The thermodynamic SiC model from Chapter 4.4 showed that local surface pressure has a direct effect on the equilibrium surface chemistry properties. Unlike the previous subsonic case, the pressure varies significantly in the post-shock region, reaching as high as 266 kPa for the Mach 10 case, and 480 kPa for the Mach 14 case.

Significant vibrational nonequilibrium is present in the post-shock region, characteristic of hypersonic flows. Figure 5.10(a) compares the translational-rotational temperature and the vibrational-electronic temperature along the centerline for Mach 10 cases. Shock stand-off distance is 1.2 mm for the Mach 10 case, resulting in *extremely thin* boundary layers over the sharp leading edge. Despite the small length scales

(a) Temperature (translational)

(c) Pressure

(b) SiO density
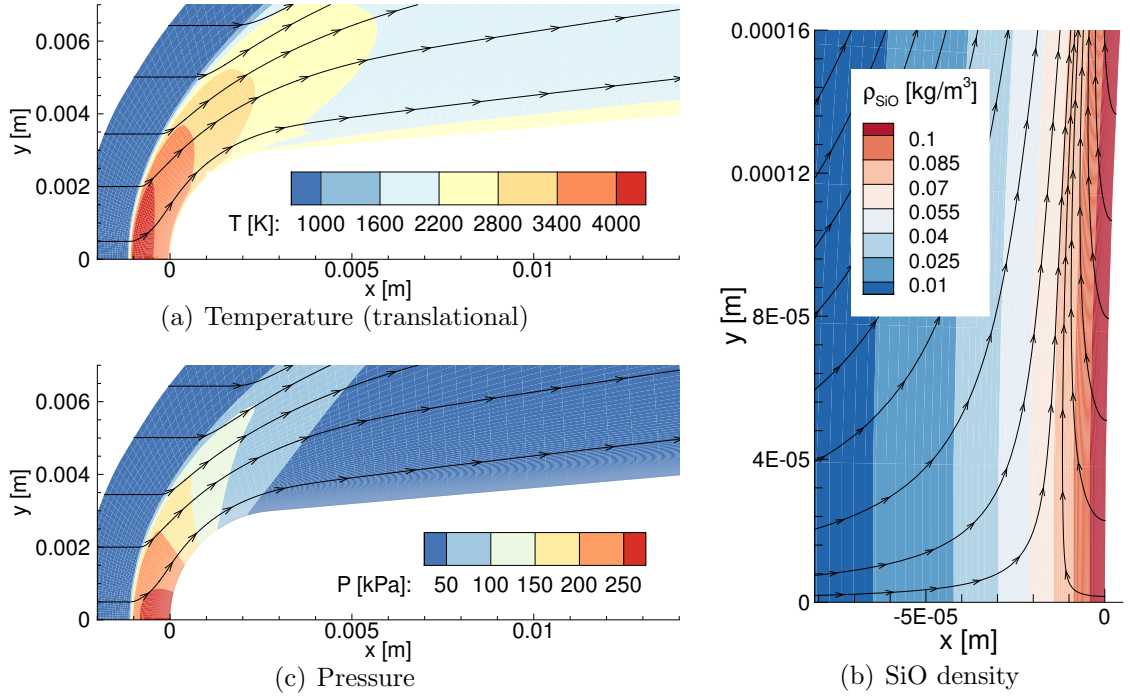
Figure 5.9: Contour plots for leading edge Case #9, active oxidation ($T_w = 2250$ K).

of the post-shock region, thermal equilibrium is achieved at the boundary layer edge due to post-shock pressures exceeding two atmospheres. There are no noticeable differences in temperature and momentum profiles between the passive, non-catalytic, and fully-catalytic wall cases at the same freestream conditions.

The momentum profile for the blowing active oxidation case never recovers to the non-blowing edge value in Fig. 5.10(b), indicating a *thickening* of the boundary layer due to blowing. The size of the momentum deficit region is also much smaller compared to the previous subsonic case, at 0.01 mm versus 0.4 mm. The 0.6 kg/m²-s momentum offset at the wall slightly increases the overall shock stand-off distance (by ∼0.01 mm).

Chemical equilibrium calculations indicate that $O_2$ should be 62% dissociated at

(a) Temperatures

(b) Momentum

(c) $O_2$

(d) O-atom

(e) SiO

(f) Si-atom
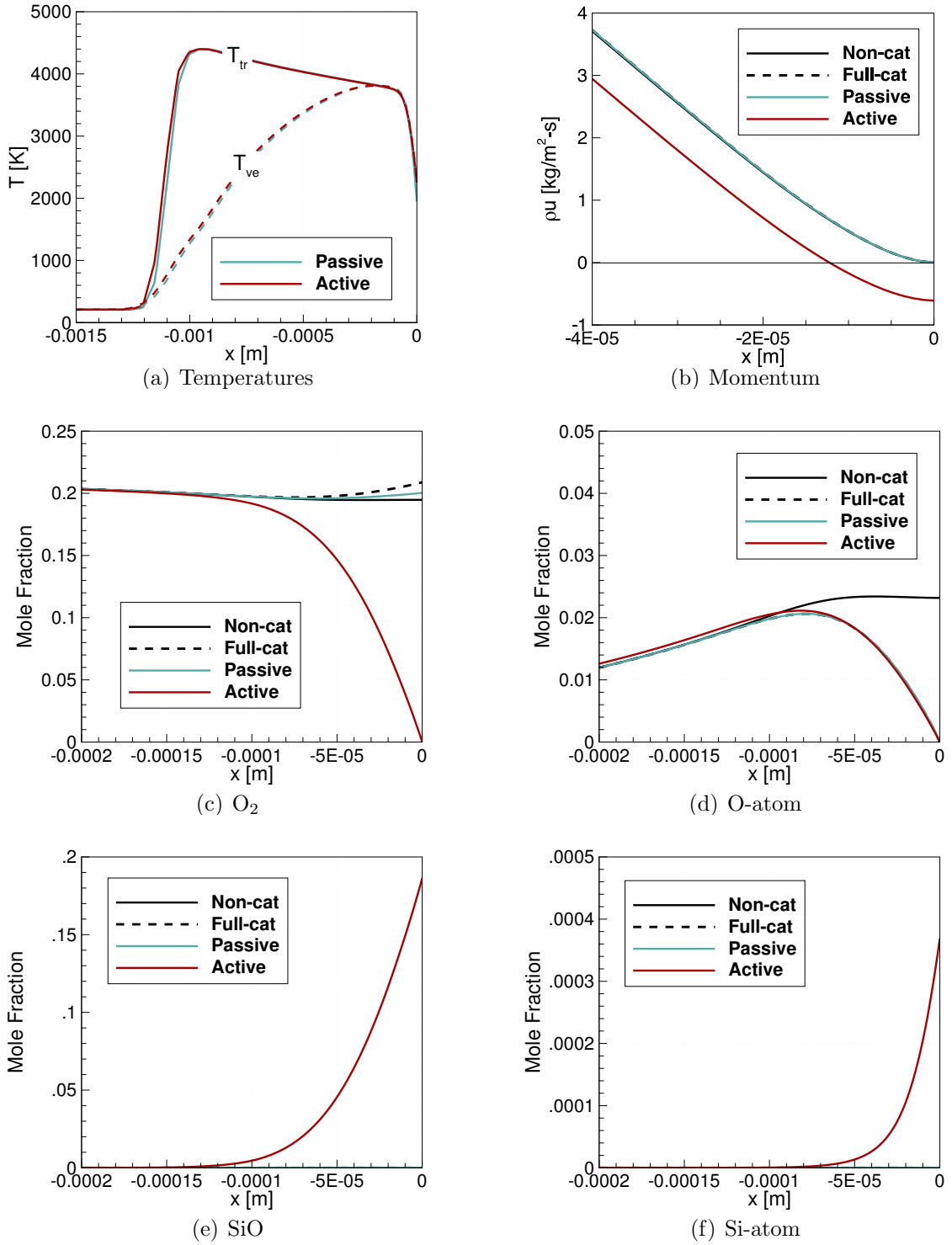
Figure 5.10: Centerline properties for leading edge case, surface is located at x = 0.

the edge conditions of 3900 K and 260 kPa. $O_2$ dissociation occurs at a finite-rate influenced by the thermal nonequilibrium throughout most of the post-shock region. Figures 5.10(c)–(d) show that the O-atom mole fraction increases downstream from the shock, but only up to $\sim$5% dissociation, far *below* the equilibrium degree of dissociation. This suggests that the boundary layer is in a state of chemical nonequilibrium.

However, SiC oxidation is not very sensitive to the degree of dissociation of oxygen, and measured reactivities of SiC to both molecular and atomic oxygen are likewise high, although atomic oxygen has been shown to have greater reactivity with SiC than molecular oxygen [89]. For the passive oxidation case, equilibrium surface chemistry enforces that nearly all atomic oxygen recombines at the SiC surface the wall temperature of 2250 K. Nonetheless, the $O_2$ and O-atom profiles from the active oxidation case demonstrate that both molecular and atomic oxygen are consumed at the actively oxidizing SiC surface, similar to what is observed in the Iso-Q case.

Figure 5.11 compares stagnation point heating values for the different wall conditions. The diffusive component in the fully-catalytic and passive oxidation cases is comparatively low at Mach 10, because $N_2$ and $O_2$ are not dissociated at the boundary layer edge, so *very little* recombination occurs near the surface. This result suggests that the choice of SiC catalycity is relatively unimportant for this case. The vibrational temperature gradient has a larger contribution to heating, due to the thermal nonequilibrium in the boundary layer. Similar to the Iso-Q case, passive-to-active transition reduces the translational-rotational heating due to surface blowing, but increases the diffusive heating as a result of surface reactions with SiC. Not surpris-
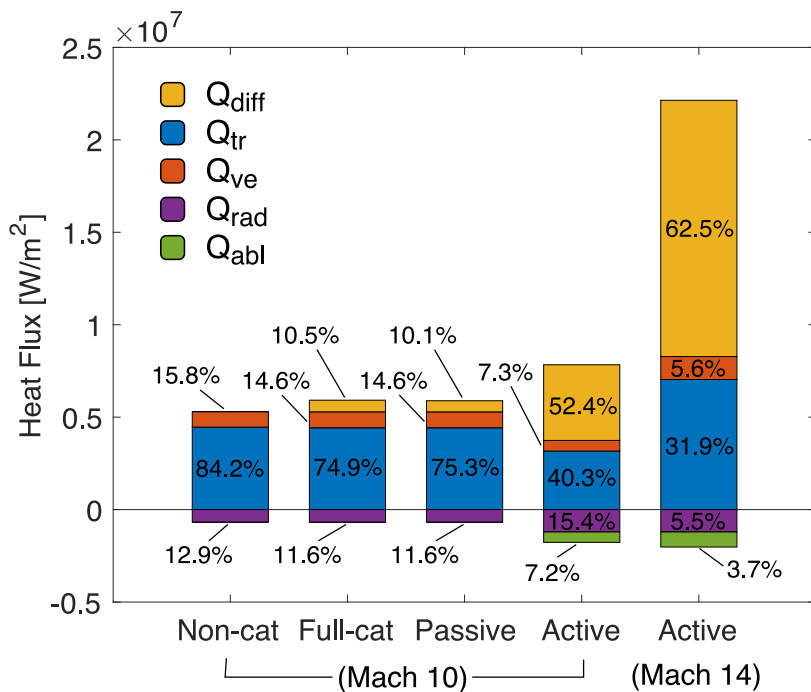
Figure 5.11: Stagnation point surface energy balance for leading edge case.

ingly, the stagnation point heat transfer is significantly higher for the Mach 14 case. Post-shock temperatures and pressures are 20% and 80% higher respectively, which increases peak heating rates by a factor of three. Overall, the relative contributions of each heating component do not change significantly at higher Mach numbers though.

## 5.2.4   Chemical Nonequilibrium

A subsonic, high-enthalpy flow can simulate the local heat transfer experienced within the hypersonic post-shock region if stagnation enthalpy, pressure, and velocity gradient are matched at the boundary layer edge [42]. Cases #4 and #5 match the stagnation enthalpy and pressure at the surface, although velocity gradients differ. Species mole fractions during active oxidation are plotted in Fig. 5.12 for these two cases. Both boundary layers have comparable length scales, approximately ∼3.0 mm,

although the concentrations of air species differ due to the thermal and chemical nonequilibrium. $O_2$ should be completely dissociated above 6000 K, but a significant $O_2$ fraction remains in Fig. 5.12(b). Si and CO are produced in nearly equimolar concentrations at the SiC surface in both cases, and the production of SiO and CO from SiC via Eq. (4.27) is assumed to be in equilibrium at the surface, though not with gas-phase reactions.
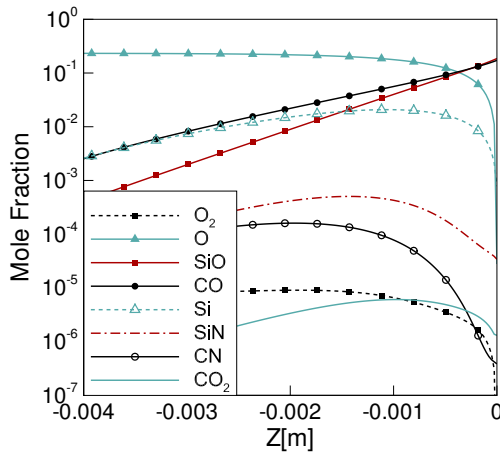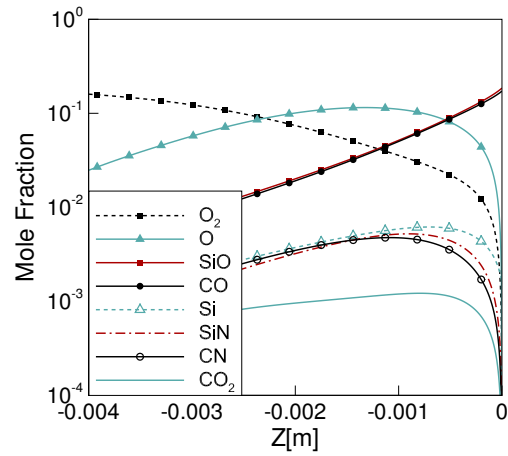


(a) Mach < 1: $h_0$=25.14 MJ/kg, $P_0$=5370 Pa K    (b) Mach 24: $h_0$=25.36 MJ/kg, $P_0$=4306 Pa K
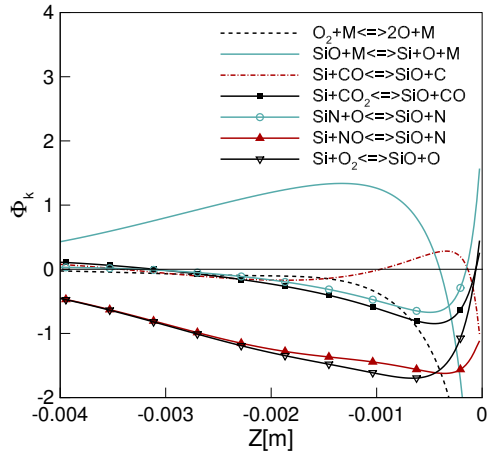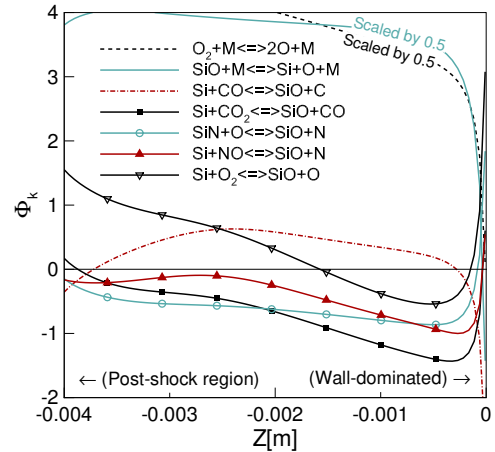
(c) Mach < 1: $h_0$=25.14 MJ/kg, $P_0$=5370 Pa K    (d) Mach 24: $h_0$=25.36 MJ/kg, $P_0$=4306 Pa K

Figure 5.12: Comparison of "equivalent" subsonic and hypersonic Iso-Q active oxidation conditions along centerline ($T_w$=2025 K for all cases).

SiO begins to dissociate and form SiN and Si-atoms from exchange reactions (Table A.2). CN forms from exchange reactions between CO and N [57]. Although SiO is the primary silicon-bearing specie initially, this distribution changes in the boundary layer. The detailed chemical nonequilibrium from each reaction in Table A.2 is evaluated from the thermodynamic equilibrium constant in Eq. (2.27), corresponding to Eq. (5.8). For a generic reaction $A + B \leftrightarrow C + D$, the *nonequilibrium factor* $\Phi$ is computed with Eq. (5.9). A value of $\Phi_k = 0$ implies that reaction $k$ is in equilibrium, $\Phi_k > 0$ implies that the reaction is proceeding in the forward direction, and vice-versa.

$$K_{\text{eq},k} = \frac{N_C^{\text{eq}} N_D^{\text{eq}}}{N_A^{\text{eq}} N_B^{\text{eq}}} \tag{5.8}$$

$$\Phi_k = \log_{10}\left(K_{\text{eq},k} \frac{N_A N_B}{N_C N_D}\right) \tag{5.9}$$

The nonequilibrium factors for each silicon reaction are plotted in Figs. 5.12(c) and 5.12(d) for subsonic and hypersonic boundary layers, respectively. The subsonic flow shows significant chemical nonequilibrium near the actively oxidizing SiC surface, but all reactions tend towards equilibrium upstream. However, Fig. 5.12(d) suggests that no equilibrium is reached in the hypersonic boundary layer, with SiC oxidation reactions near the wall and post-shock processes upstream. In particular, the $O_2$ and SiO dissociation are very far out of equilibrium with respect to the other reactions.

Case #9 represents a more flight-realistic condition, and nonequilibrium factors are plotted in Fig. 5.13. Recall that the shock is much closer to the surface for a sharp leading edge, with wall-dominated nonequilibrium downstream and shock-
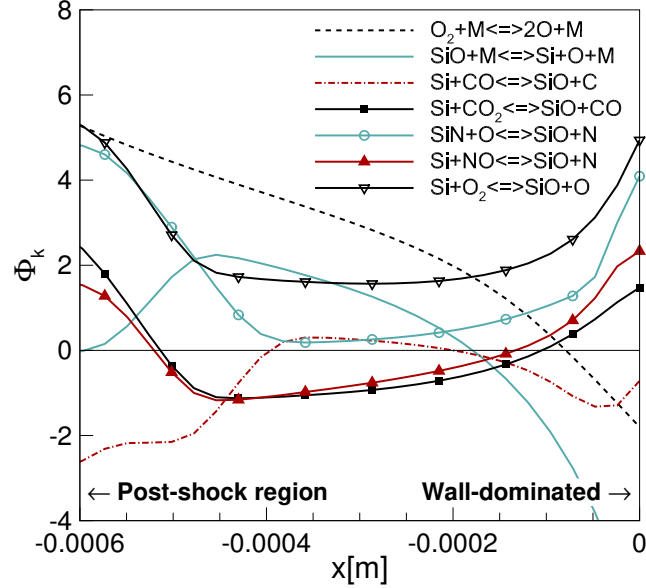
Figure 5.13: Chemical nonequilibrium along centerline for Case #9.

driven nonequilibrium upstream. Two factors contribute to the thermal and chemical nonequilibrium. First, flow timescales are much shorter in the hypersonic case, so oxidation products are convected away before they diffuse upstream. Second, chemical kinetics need sufficiently long time and length scales to equilibrate, which are limited in the hypersonic post-shock boundary layer.

### Effect of Oxidation Products in the Boundary Layer

The effect of silicon-bearing species (Si, SiO, SiN) in the boundary layer has been investigated throughout this chapter, although somewhat indirectly. Both the mitigating effects of blowing and the chemical interactions of gaseous oxidation products in the reacting boundary layer have been modeled. SiO and CO are the primary gaseous species produced during oxidation, which then form "secondary" products (Si, $Si^+$, SiN, C, $CO_2$) through dissociation, ionization, and exchange reactions in Table A.2.

"Tertiary" products ($C^+$, $C_2$, CN) are produced through additional reaction mechanisms in Table A.1. Silicon-bearing species are only present in significant amounts during *active* oxidation. These species contribute to the near-wall chemical nonequilibrium, and the above analyses indicate that dissociation reactions, particularly SiO dissociation, may be very far out of equilibrium near the surface at hypersonic conditions. In general, these dissociation reactions are *endothermic*, taking energy *out* of the boundary layer, so nonequilibrium gas-phase thermochemistry is important for accurate prediction of surface properties, particularly heating.

### 5.2.5   Emission Spectra

Limited experimental data is available in the literature to validate the boundary layer thermochemical state during SiC oxidation. Panerai et al. measured emission spectra during oxidation of SiC composites in VKI's Plasmatron inductively coupled plasma (ICP) facility [73]. These are subsonic high-enthalpy flow conditions similar to the Iso-Q case presented earlier, so thermal equilibrium is expected. Reconstructed test conditions for the "HER M32" case were estimated from numerical boundary layer analysis [93], matching measured surface heat fluxes from copper calorimeters, and are summarized again in Table 3.1 as Case #11. CFD simulations at the reported conditions are performed using the same geometry, and lines of sight are extracted radially upstream from the SiC surface.

To support emission analysis of SiC oxidation, Si and $Si^+$ electronic energy levels and transitions from the NIST database [98] are added to NEQAIR [40]. Stark

broadening parameters for Si transition lines are taken from Purić et al [102]. Profiles of species number densities and temperatures along the line of sight are used as inputs to NEQAIR, along with the spectrometer slit function. The reported spectrometer resolution is 0.65 nm full-width half maximum (FWHM), modeled as a Gaussian. The experimental spectrum in Fig. 5.14 shows that several atomic Si lines and the CN violet (B-X) band are the primary radiative transitions between 200 and 500 nm. A Boltzmann distribution of electronic energy level populations is assumed for Si and Si$^+$ transitions, while non-Boltzmann QSS excitation rates are used to compute the transitions between CN energy levels (see Chapter 3).
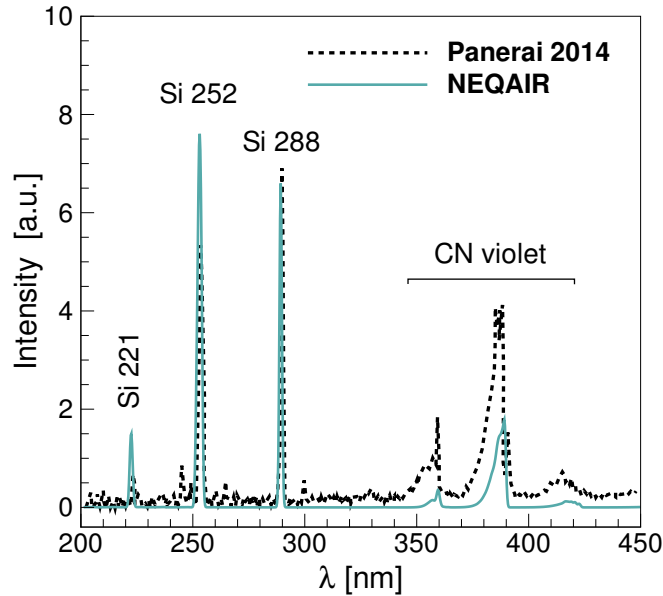


Figure 5.14: Emission spectra comparison for Case #11, experimental spectra from Ref. [73].

Importantly, the emission measurements are reported in calibrated, *arbitrary* intensity units, since absolute spectra are not available. Comparison between the LeMANS-NEQAIR [40] simulation and experimental spectrum is shown in Fig. 5.14,

and there is reasonable agreement between the relative Si and CN lines at the 2.0 mm measurement location, although CN emission levels appear to be under-predicted by a factor of two or more. Conversely, Si lines may be overpredicted instead. Since the intensity levels are arbitrarily scaled here, it is unclear if this is due to errors in number density and/or temperature. The Si-atom is a "secondary" oxidation product, and CN is a "tertiary" product based on the chemical rate mechanisms used in this chapter, so both are very sensitive to the thermochemistry model. Although more detailed experimental measurements are required for further validation, the comparisons presented here are promising, and suggest that the relative concentrations of Si-atoms and CN are largely in agreement with experimental values.

## 5.3    Chapter Summary

The new equilibrium surface chemistry model for SiC oxidation in air was implemented within a nonequilibrium CFD-radiation framework. The coupled, chemically-reacting boundary layer under passive and active oxidation was investigated to better understand the change in surface properties during passive-to-active transition. Whereas the $SiO_2$ surface during passive oxidation can be effectively treated as an inert catalytic wall, equilibrium surface chemistry showed that the actively oxidizing SiC surface significantly differed from both non-catalytic and fully-catalytic wall conditions [97]. Surface heating due to species diffusion *increased* due to the elevated reactivity of bare SiC during passive-to-active transition. The normalized aerothermal heating coefficient during active oxidation remained within 10% of passive heating val-

ues, and verified that surface heating behavior is sufficient to trigger the temperature jump phenomenon.

Predicted steady-state temperature from surface energy balance calculations agreed with experimental measurements within 3%. Simulated radiative emission spectra showed good qualitative agreement to experimental measurements in subsonic high-enthalpy flows, although *absolute* intensity measurements need to be validated [97]. Significant vibrational and chemical nonequilibrium were observed in the hypersonic post-shock region, indicating the importance of a nonequilibrium modeling approach in the boundary layer.

Although the model agreed well with available experimental data in the high-enthalpy, subsonic regime, there were two important limitations. First, the zero-dimensional surface oxidation model did not account for the effect of pressure gradients and shear (which are two or three-dimensional effects). The analysis presented in this chapter demonstrated that the thermodynamic behavior itself is largely independent of these factors, though these additional effects may influence the passive-to-active limit in thin hypersonic boundary layers and for sharp leading edge geometries. Second, equilibrium surface chemistry captured the steady-state oxidation, but nonequilibrium effects may be needed to accurately model the *transient* behavior. This includes the increased reactivity of atomic oxygen and nitrogen (compared to the molecular species) observed in experiments.

# CHAPTER 6

# ZrB$_2$-SiC Oxidation Model

In this chapter, a material response model is developed to describe the in-depth, transient oxidation behavior of a UHTC material. Pure SiC and ZrB$_2$ are both insufficient for applications with surface temperatures exceeding 3000 K [70]. Composites of ZrB$_2$-SiC with up to 30% SiC by volume have been studied to improve the oxidation resistance of pure ZrB$_2$ [103]. Experiments show that ZrB$_2$-SiC retains oxidation resistance up to temperatures of 2000 K [104], slightly above the oxidation limit of pure SiC but still below the desired range of 2500 - 3000 K. Despite this, it is useful to first understand the oxidation processes of ZrB$_2$-SiC before evaluation of other UHTC materials, such as alternate binary [10] and ternary composites with SiC [105]. These ceramic matrix composites with SiC also exhibit a temperature jump in aerothermal environments during passive-to-active oxidation, although the mechanisms involved in passive-to-active transition are not as straightforward as that of pure SiC [96].

This work presents a general framework for analysis of ZrB$_2$-SiC ceramic matrix composites, and can be extended to other UHTC materials [106]. The objective of this analysis is to predict in-depth thermal and chemical oxidation behavior across both passive and active oxidation regimes. First, the physical processes of ZrB$_2$-SiC

oxidation are described, along with related work in the literature. Next, details of the modeling framework are presented. Results are then shown for $ZrB_2$ oxidation, the primary constituent of the $ZrB_2$-SiC ceramic matrix composite of interest in this work. Finally, model results are discussed for combined $ZrB_2$-SiC oxidation.

## 6.1  Physical Oxidation Processes

Chapters 4 and 5 demonstrated that pure SiC oxidation is well approximated as a surface process, with no significant effects in-depth [81]. However, $ZrB_2$ and $ZrB_2$-SiC oxidation involve significantly more phases, and occur across a depth of $\sim$1 mm, with temperature differentials up to $\sim$600 K over the thickness of the oxide scale and steep gradients in the microstructure [10]. Thus, a *meso*-scale model is needed to resolve the processes that occur within this oxide layer.

### 6.1.1  Pure $ZrB_2$ Oxidation Processes

Parthasarathy et al. summarize several key processes during $ZrB_2$ oxidation in diffusion-limited environments [107–109]. The model of Parthasarathy [107–109] accounts for morphology of the microstructure, but only in *passive* oxidation conditions where growth of the oxide layer is favored. These are described in steps #1 and #2 below, corresponding to Figure 6.1. Hafnium diboride ($HfB_2$) composites have been shown to be qualitatively similar to $ZrB_2$, so are included in this description [10,107].

1. The primary oxidation reaction of $ZrB_2(s)$ is Eq. (6.1), and the resulting
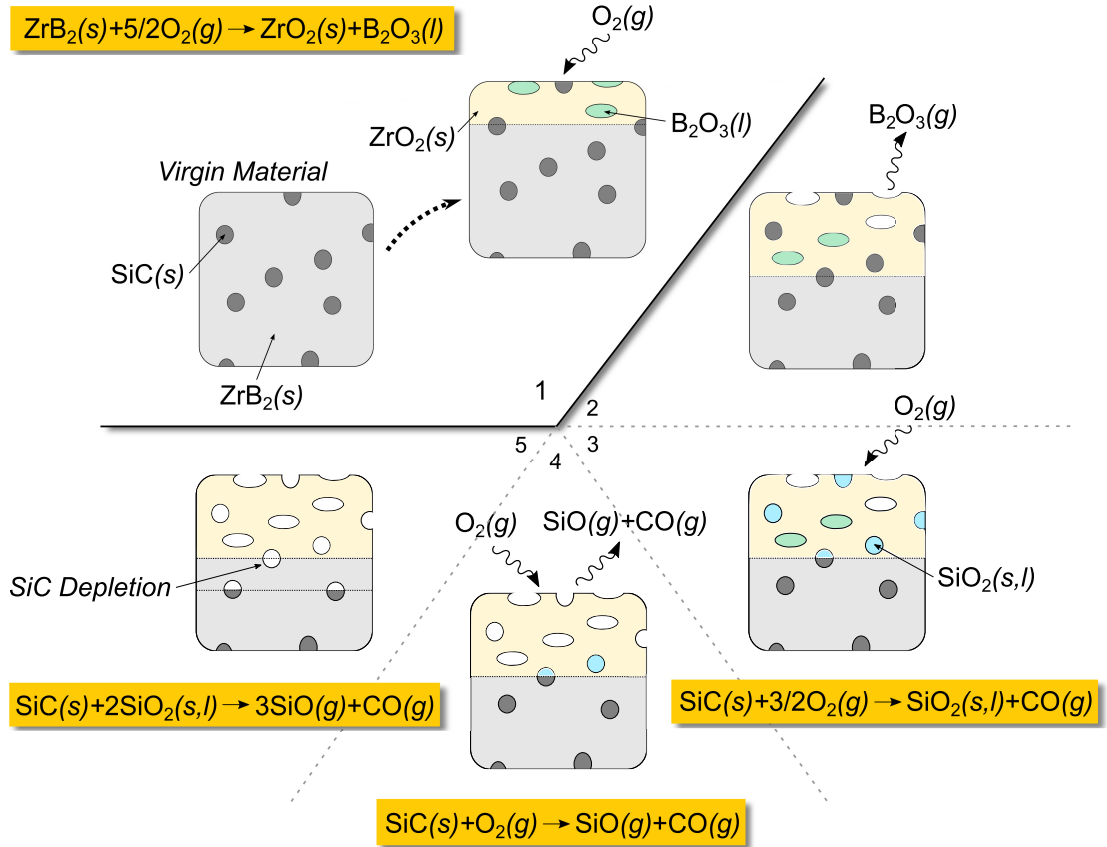
Figure 6.1: Schematic of $ZrB_2$-SiC oxidation cross-section.

$ZrO_2(s)$ matrix is porous. Condensed $B_2O_3(l)$ from Eq. (6.1) fills the $ZrO_2(s)$ porous matrix, limiting oxygen diffusion under moderate conditions ($T < 1600$ K).

$$ZrB_2(s) + 5/2O_2(g) \rightarrow ZrO_2(s) + B_2O_3(l) \tag{6.1}$$
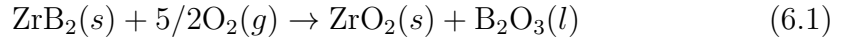
2. $B_2O_3(l)$ evaporates, resulting in mass loss according to Eq. (6.2) at temperatures exceeding 1600 K. $B_2O_3(g)$ egress is facilitated by diffusion through $ZrO_2(s)$ pores into the ambient boundary layer.

$$B_2O_3(l) \rightarrow B_2O_3(g) \tag{6.2}$$

In order for oxidation to proceed, $O_2(g)$ ingress is maintained through diffusion into the $ZrO_2(s)$ pores. Dissolution of $O_2$ through the $B_2O_3(l)$ phase occurs at a small but finite rate, allowing in-depth oxidation to continue. $ZrO_2(s)$ is generally inert below $\sim$2500 K.

## 6.1.2 Combined ZrB$_2$-SiC Oxidation Processes

There are limited models in the literature describing combined ZrB$_2$-SiC oxidation in both passive and active regimes. Fahrenholtz constructed a volatility diagram of the ZrB$_2$-SiC-O$_2$ system [110], providing a useful qualitative description of SiC oxidation processes, particularly the formation of a SiC-depletion zone within the oxide layer observed in several experiments [70, 103, 111]. However, this is insufficient for detailed surface mass and energy calculations. Perhaps the most detailed analysis of ZrB$_2$-SiC in the literature was performed by Parthasarathy et al., but is likewise limited to passive oxidation conditions [109].

Importantly, the volatility diagram suggests that ZrB$_2$ and SiC oxidation are largely *independent*, apart from a eutectic that may form between $B_2O_3(l)$ and $SiO_2(s, l)$ [110]. SiC oxidizes in parallel with ZrB$_2$, and embedded SiC particles contribute to the overall porosity of the resulting ZrO$_2$ matrix when oxidized. For combined ZrB$_2$-SiC oxidation, additional processes that need to be modeled include steps #3 through #5, also illustrated in Fig. 6.1.

3. A condensed $SiO_2(s, l)$ phase forms from passive SiC oxidation, described by Eq. (6.3) [78], filling in the porous matrix and inhibiting the ingress of gaseous

oxygen.

$$SiC(s) + 3/2O_2(g) \rightarrow SiO_2(s,l) + CO(g) \qquad (6.3)$$
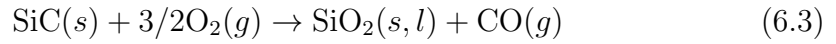
4. At higher temperatures ($T > 2000$ K), active oxidation is described by Eq.
   (6.4) [78], resulting in gaseous oxidation products that do not inhibit oxygen
   ingress. The gaseous oxidation products $SiO(g)$ and $CO(g)$ also egress via
   diffusion and dissolution similar to step #2.

$$SiC(s) + O_2(g) \rightarrow SiO(g) + CO(g) \qquad (6.4)$$
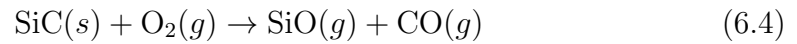
5. Selective oxidation of SiC has been proposed as a mechanism for SiC depletion
   by other researchers [10, 110]. When $SiC(s)$ is embedded in the $ZrB_2(s)$ matrix,
   internal SiC depletion can occur via Eq. (6.5) *without* the presence of oxygen,
   which is the same reaction as Eq. (4.31) discussed in Chapter 4.

$$SiC(s) + 2SiO_2(s,l) \rightarrow 3SiO(g) + CO(g) \qquad (6.5)$$
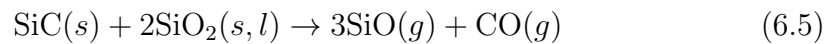
The mechanical, thermodynamic, and chemical stability of the $SiO_2(s,l)$ phase
determines the overall transition between passive and active oxidation behavior for
$ZrB_2$-SiC composites, as it presents a barrier to oxygen ingress and $B_2O_3(g)$, $SiO(g)$,
and $CO(g)$ egress.

## 6.2 Thermodynamic Oxidation Model

Previous thermodynamic calculations of Fahrenholtz [110, 112] and Poerschke et al. [10] considered only closed systems without mass and energy transport effects ("true" equilibrium). While useful for describing a homogeneous zero-dimensional system, transport processes are important where gradients exist in chemical and thermodynamic properties. Parthasarathy's models for both $ZrB_2$ [107, 108] and $ZrB_2$-SiC [109] consider material-specific internal oxidation and diffusion mechanisms. Importantly, internal gradients are assumed to be *linear* in the zero-dimensional formulation. While comparing well to experimental data in the passive oxidation regime, it lacks the generality needed for detailed aerothermal analysis of UHTC materials. Additionally, understanding the active oxidation regime (particularly passive-to-active transition) is vital to better characterize the limitations of these UHTC materials in practical applications.

The model proposed and evaluated in this chapter represents a more general approach to $ZrB_2$ and $ZrB_2$-SiC oxidation – no *a priori* assumptions are made about the dominant reaction mechanisms, and a generalized formulation is developed that is applicable in both passive and active oxidation regimes. A discretized, one-dimensional system is considered to resolve internal gradients.

### 6.2.1 Volume-Averaged Properties

To model a system with gradients in species concentrations and microstructure, a one-dimensional approach is developed in this chapter. Physically, the virgin $ZrB_2$-

SiC microstructure is composed of SiC($s$) phases dispersed throughout a ZrB$_2$($s$) matrix [103], illustrated in Fig. 6.2. When oxidized, B$_2$O$_3$($l$) and SiO$_2$($s, l$) phases exist within the oxidized ZrO$_2$($s$) matrix, and gaseous species occupy the vacant pores.
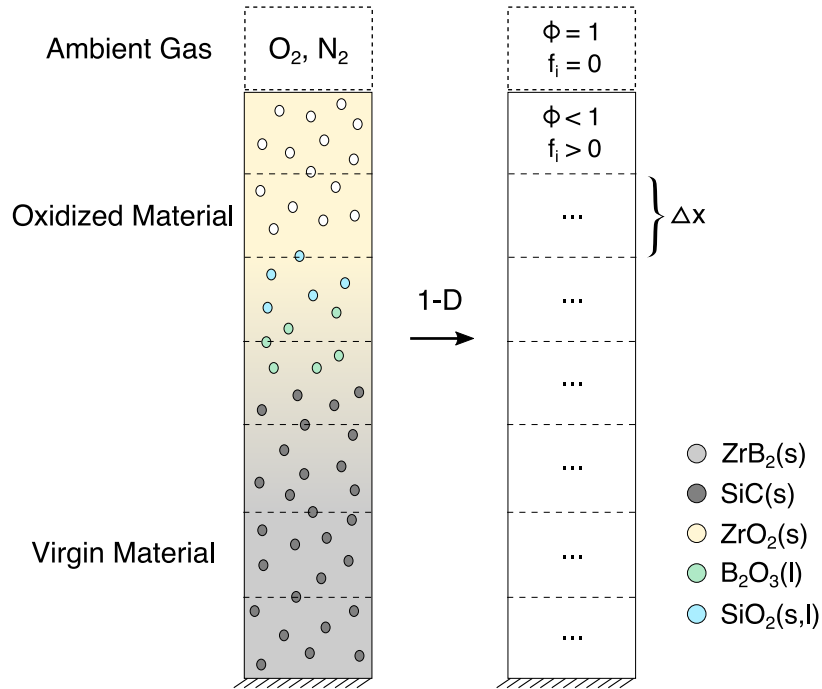


Figure 6.2: 1-D volume averaging approach.

In the one-dimensional framework, individual phases are averaged over each discrete volume element defined by $\Delta x$. Within each discrete volume element, phases and porosity are assumed to be locally homogeneous, occupying volume proportional to the volume fraction $f_i$. This simplification still allows gradients to exist over the domain *between* volume elements. The phase fractions $f_i$ parameterize the local mi-

crostructure and extent of oxidation, enforcing Eqs. (6.6 - 6.8):

$$\sum f = f_{\rm s} + f_\ell + f_{\rm g} = 1 \qquad (6.6)$$

$$f_{\rm s} = \sum_i f_{{\rm s}_i} \text{ for solid species } i \qquad (6.7)$$

$$f_\ell = \sum_j f_{\ell_j} \text{ for liquid species } j \qquad (6.8)$$

The porosity $\phi$ denotes the non-solid or *unoccupied* volume fraction, and can be determined from Eq. (6.9). Gaseous species are assumed to exist within the unoccupied volume $\phi$.

$$\phi = f_{\rm g} = 1 - f_{\rm s} - f_\ell \qquad (6.9)$$

Since gaseous and condensed phases are assumed to occupy the same volume element, an *effective* number density $\tilde{n}_i$ is considered which includes the volumetric contribution of porosity and voids. Within a volume element, the volume fractions $f_i$ and porosity $\phi$ are related to the effective number density $\tilde{n}_i$ through the *molar volume* $\hat{\nu}_i$ in Eq. (6.10). The chemical activity $a_i$ is proportional to the species number density, and is related through Eq. (6.11), where $c^o$ is a reference concentration:

$$\tilde{n}_i = \frac{N_i}{\Delta V} = \frac{f_i}{\hat{\nu}_i} \qquad (6.10)$$

$$a_i = \frac{\tilde{n}_i}{c^o} \qquad (6.11)$$

The *true* number density of gaseous species $n_i$, which is a thermodynamic state

variable, depends on the *effective* number density $\tilde{n}_i$ and the porosity $\phi$:

$$n_{g_i} = \frac{\tilde{n}_{g_i}}{\phi} \text{ for gaseous species } i \tag{6.12}$$

Similarly for solid and liquid species, the individual species volume fraction determines the true number density:

$$n_{s_j} = \frac{\tilde{n}_{s_j}}{f_{s_j}} \text{ for condensed species } j \tag{6.13}$$

Locally, the dispersion of each species is assumed to be homogeneous over the occupied and unoccupied volume fractions (hence volume averaged), but varying with depth $x$ and time $t$. The variables $\tilde{n}_i$ and $f_i$ thus parameterize the local state of the microstructure.

## 6.2.2 Governing Equations

The governing equations for a one-dimensional porous system are described by Martin et al. [33] in Eqs. (6.14)–(6.18). These equations are cast into the same form as the general Navier-Stokes equations in Eq. (2.33), but modified to account for porosity and condensed phase continuity.

$$\frac{\partial \mathbf{Q}}{\partial t} + \nabla \cdot (\mathbf{F}_{\text{adv}} - \mathbf{F}_{\text{diff}}) = \mathbf{S} \tag{6.14}$$

$$\mathbf{Q} = \left\{ \begin{array}{c} \phi\rho_{g_1} \\ \vdots \\ \phi\rho_{g_{ngs}} \\ f_{s_1}\rho_{s_1} \\ \vdots \\ f_{s_{nss}}\rho_{s_{nss}} \\ \phi\rho_g u \\ \phi\rho_g e + (1-\phi)\rho_s e_s \end{array} \right\} \quad (6.15) \qquad \mathbf{F}_{\text{adv}} = \left\{ \begin{array}{c} \phi\rho_{g_1} u \\ \vdots \\ \phi\rho_{g_{ngs}} u \\ 0 \\ \vdots \\ 0 \\ \phi\rho_g u^2 + P \\ \phi\rho_g u h \end{array} \right\} \quad (6.16)$$

$$\mathbf{F}_{\text{diff}} = \left\{ \begin{array}{c} -J_1 - J_{\ell,1} \\ \vdots \\ -J_{ngs} - J_{\ell,ngs} \\ 0 \\ \vdots \\ 0 \\ 0 \\ -\dot{q}'' - \sum_i^{ngs}(J_i h_i) \end{array} \right\} \quad (6.17) \qquad \mathbf{S} = \left\{ \begin{array}{c} \dot{\omega}_{g_1} \\ \vdots \\ \dot{\omega}_{g_{ngs}} \\ \dot{\omega}_{s_1} \\ \vdots \\ \dot{\omega}_{s_{nss}} \\ D_x \\ D_x u + R \end{array} \right\} \quad (6.18)$$

In order from top to bottom, these are the full mass conservation equations for both gaseous species and condensed phases, followed by the gas-phase momentum conservation equation, and finally the mixture energy conservation equation. These general equations are valid for one-dimensional porous multiphase materials, and no special assumptions have been made.

For the results presented in this chapter, only the gas and condensed-phase mass conservation equations are solved, corresponding to an isothermal, isobaric system. Equation (6.19) describes this reduced set of equations:

$$
\frac{\partial}{\partial t}
\left\{
\begin{array}{c}
\phi\rho_{g_1} \\
\vdots \\
\phi\rho_{g_{ngs}} \\
f_{s_1}\rho_{s_1} \\
\vdots \\
f_{s_{nss}}\rho_{s_{nss}}
\end{array}
\right\}
+
\frac{\partial}{\partial x}
\left\{
\begin{array}{c}
\phi\rho_{g_1}u \\
\vdots \\
\phi\rho_{g_{ngs}}u \\
0 \\
\vdots \\
0
\end{array}
\right\}
-
\frac{\partial}{\partial x}
\left\{
\begin{array}{c}
-J_1 - J_{\ell,1} \\
\vdots \\
-J_{ngs} - J_{\ell,ngs} \\
0 \\
\vdots \\
0
\end{array}
\right\}
=
\left\{
\begin{array}{c}
\dot{\omega}_{g_1} \\
\vdots \\
\dot{\omega}_{g_{ngs}} \\
\dot{\omega}_{s_1} \\
\vdots \\
\dot{\omega}_{s_{nss}}
\end{array}
\right\}
\qquad (6.19)
$$

For the $ZrB_2$-SiC-$O_2$ system of interest in this chapter, six volume fractions $f$ are defined for each phase that exists within the material: $f_{gas}$, $f_{ZrB_2}$, $f_{SiC}$, $f_{ZrO_2}$, $f_{B_2O_3(l)}$, $f_{SiO_2}$, with an arbitrary number of gaseous species (ngs). Phases are assumed to be distributed homogeneously (locally) according to $f$.

## 6.2.3 Modeling Transport and Source Terms

**Chemical Source Terms**

The "reduced" conserved variable vector $\mathbf{Q}$ is expressed again in Eq. (6.20), dropping the gas momentum and mixture energy equations. This vector describes the multiphase state at each discrete point $x$.

$$\mathbf{Q}(\mathbf{x}, \mathbf{t}) = \begin{Bmatrix} \phi \rho_{g_1}(x,t) \\ \vdots \\ \phi \rho_{g_{ngs}}(x,t) \\ f_{s_1} \rho_{s_1}(x,t) \\ \vdots \\ f_{s_{nss}} \rho_{s_{nss}}(x,t) \end{Bmatrix} \tag{6.20}$$

The reference *equilibrium* state of mixture $\mathbf{Q}$ is denoted by $\tilde{\mathbf{Q}}$. To approximate equilibrium, an effective *rate* for the chemical source terms in Eq. (6.18) is computed with Eq. (6.21):

$$\dot{\omega}_i = \alpha \frac{\tilde{q}_i - q_i}{\Delta t}, \quad 0 \leq \alpha \leq 1 \tag{6.21}$$

The equilibrium composition is computed at *each timestep*, and the source terms are evaluated with Eq. (6.21) as the average change in the conserved gas/solid density over the timestep, $\Delta t$, *in the absence of any transport effects*. Elemental mass conservation is implicitly enforced with this method. In general, the reference equilibrium state at time $t$ is *not* equal to the conserved state at the following timestep $t + \Delta t$:

$$\mathbf{Q}(x, t + \Delta t) \neq \tilde{\mathbf{Q}}(x, t) \tag{6.22}$$

This is due to the limiting effects of diffusion and mass transport, so $\tilde{\mathbf{Q}}$ is simply a

152

reference state. The parameter $\alpha$ is the *nonequilibrium factor*, and scales the effective equilibrium rate. In the limit of $\alpha \to 1$, the system is diffusion-limited. Conversely, as $\alpha \to 0$, the system is reaction-limited. For the results presented in this chapter, $\alpha = 1$ is used.

The multiphase equilibrium solver of Cantera [20] is used to evaluate $\tilde{\mathbf{Q}}$ and the source terms for the gas-continuity and solid-continuity equations together consistently. The gas phase itself consists of various gaseous species within the pores (air, SiO, CO, etc.), and each specie corresponds to a continuity equation. Thermodynamic data for gaseous and condensed species come from NASA polynomials [16], with the exception of $ZrB_2$ which is obtained from the NIST-JANAF database [15]. For the multiphase equilibrium calculations, Cantera requires specification of the mole fractions and effective number densities of the various phases, so a conversion needs to be made from the volume/mass formulation used in the governing equations to *effective* moles/number densities for Cantera. For both gaseous and solid phases, this is evaluated with Eq. (6.23):

$$\tilde{n}_{s_i} = f_{s_i} \rho_{s_i} \frac{N_A}{\mathcal{M}_i} \tag{6.23}$$

$\mathcal{M}_i$ is the molecular weight of species/phase $i$, and $N_A$ is Avogadro's number. Notably, in the *non-porous* limit (when $\phi \to 0$), this storage term is effectively zero for the gas phase regardless of transport effects, so a minimum porosity of $\phi = 1 \times 10^{-3}$ is used at the surface cell for this calculation.

This approach is also easily extensible to finite-rate modeling, where rates of formation are known for $ZrB_2$-SiC oxidation. In the absence of that data, this method

describes diffusion-limited systems in chemical equilibrium with $\alpha = 1$, and provides a useful approximation for reaction-limited systems in chemical nonequilibrium with $\alpha < 1$.

**Mass Transport**

Internal oxidation of the porous matrix is facilitated by the diffusion of gaseous species *within* the pores. This includes the ingress of ambient gases ($O_2$, $N_2$) as well as the egress of oxidation products ($B_2O_3$, SiO, CO). In the absence of significant boundary layer convection, inward diffusion of oxygen and outward diffusion of oxidation products are the primary mechanisms for continued oxidation of $ZrB_2$-SiC composites. A modified Fick's law [28] is used to compute the species diffusion fluxes within the pores in Eq. (6.24), accounting for the local porosity:

$$J_i = -\phi \rho_g D_i \frac{\partial Y_i}{\partial x} + \phi Y_i \rho_g \sum_{k=1}^{\text{ngs}} D_k \frac{\partial Y_k}{\partial x} \tag{6.24}$$

The pore fraction $\phi$ is assumed to be continuous within the oxidized material. Effective mixture diffusion coefficients for each gaseous specie are approximated using the bifurcation model in Eqs. (2.56 - 2.57) [29].

At more moderate conditions where liquid boria ($B_2O_3(l)$) is stable, diffusion of gases across liquid boria are also included in the diffusion term, although this contribution is typically small compared to diffusion through the empty pores. This mechanism is evaluated with Eq. (6.25). Both diffusion mechanisms enable the continual penetration of oxygen in-depth, and the diffusion of gaseous oxidation products

154

outward.

$$J_{\ell,i} = -f_{\text{B}_2\text{O}_3(\text{l})} \mathcal{M}_i \Pi_{i-\text{B}_2\text{O}_3(\text{l})} \frac{\partial P_i}{\partial x} \tag{6.25}$$

The permeability of $\text{O}_2$ via $\text{B}_2\text{O}_3(\text{l})$ is determined from Eq. (6.26), consistent with the model of Parthasarathy et al. [107]. The permeability of other gaseous species is assumed to be equal to that of $\text{O}_2$. Note that $\text{SiO}_2(s,l)$ is assumed to have zero oxygen permeability in this chapter [78], consistent with the SiC model described in Chapter 4.

$$\Pi_{\text{O}_2-\text{B}_2\text{O}_3(\text{l})} = 0.15 \exp\left\{ \left( \frac{-16,000}{T} \right) \right\} \ \left[ \frac{\text{mol}}{\text{m} \cdot \text{s} \cdot \text{atm}} \right] \tag{6.26}$$

Transport phenomena are not considered for the condensed phases, such as the transport of liquid boria within the porous matrix due to internal pressure gradients.

**Momentum Transport**

The momentum conservation equation is used to solve for the effective gas velocity induced from internal pressure gradients and gas production (outgassing). For the cases examined in this work, outgassing is relatively insignificant, especially in the passive oxidation regime where only condensed oxide phases are produced via Eq. (6.1) and $\text{B}_2\text{O}_3(l)$ is stable. Thus, the momentum equation may be neglected in Eq. (6.19). As part of this 1-D framework however, the effect of pressure gradients and momentum transport can be modeled by including the momentum conservation equation in the system of equations. In these cases, the effective gas velocity $u$ is defined by Eq. (6.27).

$$u = \frac{\phi \rho_{\text{g}} u}{\sum_{i=1}^{\text{ngs}} \phi \rho_{\text{g}_i}} \tag{6.27}$$

155

For porous materials, the *permeability* $\kappa_v$ is related to the porosity as well as the *tortuosity* $\tau$. Tortuosity is the ratio of the volume fraction of all pores (the "actual" porosity $f_{\text{pore}}$) to the volume fraction of *continuous* pores (the "effective" porosity $\phi$) [108]:

$$\tau = \frac{f_{\text{pore}}}{\phi} \qquad (6.28)$$

In the volume-averaged approach described in this chapter, all pores formed are assumed to be continuous ($\tau = 1$), hence the porosity $\phi$ describes the continuous pore fraction. The relationship between permeability and porosity in one-dimension is given by Eq. (6.29).

$$\kappa_v = \phi u \mu \frac{\Delta x}{\Delta P} \qquad (6.29)$$

A representative permeability of $\kappa_v = 6.68 \times 10^{-13}$ m$^2$ is assumed for the oxide layer of ZrB$_2$-SiC based on typical pore sizes [107, 108], although this parameter has no impact on model predictions in the absence of internal pressure gradients or velocity.

The source term for the full momentum equation is computed from Darcy's law in Eq. (6.30), describing the momentum dissipation from flow through porous media [33]:

$$D_x = -\frac{\phi \mu}{\kappa_v} u \qquad (6.30)$$

$\kappa_v$ is the effective permeability and $\mu$ is the fluid mixture viscosity. However, even for cases that involve significant outgassing, it may still be unnecessary to solve the

156

full momentum equation to compute internal gas velocities. In lieu of solving the full momentum equation, one can approximate the internal gas velocity directly using an alternate form of Darcy's law in Eq. (6.31). This method is commonly used in other material response codes [113, 114].

$$u = -\frac{\kappa_v}{\phi\mu}\frac{\partial P}{\partial x} \tag{6.31}$$

**Energy Transport**

The mixture energy conservation is needed to evaluate in-depth temperature gradients within the material. However, the cases examined in the work are assumed to be *isothermal*, with no in-depth temperature gradients, so the mixture energy equation is also neglected. In cases with strong aerothermal or convective heating, strong temperature gradients may be present near the surface, so the mixture energy equation should be included in the system of equations.

The mixture energy equation in Eq. (6.18) includes gas-phase and condensed-phase contributions to the total energy. The diffusive energy flux includes both solid heat conduction and enthalpy transport via gaseous diffusion. The solid conduction term $\dot{q}''$ is modeled using Fourier's law in Eq. (6.32):

$$\dot{q}'' = -\kappa_{\text{avg}}\frac{\partial T}{\partial x} \tag{6.32}$$

The effective thermal conductivity $\kappa_{\text{avg}}$ can be evaluated as the sum of the volume

fraction-weighted thermal conductivities of each phase:

$$\kappa_{\mathrm{avg}} = \sum_{i=1}^{n_{\mathrm{phases}}} f_i \kappa_i \tag{6.33}$$

An energy dissipation term from Darcy's law is included in the energy equation source term. An additional term is added to the energy source to account for the change in enthalpy due to chemical reactions. This is evaluated as the average rate of change in enthalpy of reactants and products in Eq. (6.34). The enthalpy of reactants is determined from the current state, and the enthalpy of products corresponds to the reference equilibrium state.

$$R = \alpha \frac{\left( \sum_{i=1}^{\mathrm{ngs}} \phi \rho_{g_i} h_i + \sum_{i=1}^{\mathrm{nss}} f_{s_i} \rho_{s_i} h_i \right)^{\mathrm{eq}} - \left( \sum_{i=1}^{\mathrm{ngs}} \phi \rho_{g_i} h_i + \sum_{i=1}^{\mathrm{nss}} f_{s_i} \rho_{s_i} h_i \right)}{\Delta t} \tag{6.34}$$

### 6.2.4 Limitations

Although phenomena affecting mass, momentum, and energy transport are discussed, simplifying assumptions are also required in the proposed model. During change in chemical phase (e.g. from $ZrB_2 \rightarrow ZrO_2$), the volume occupied by solid and liquid phases may grow/shrink [108]. Properties of relevant phases are compiled in Table 6.1 at standard conditions (298 K, 100 kPa), and data are from NIST [98].

Thermodynamic data utilized for each phase are highly temperature-dependent [16, 98], but *constant* density is assumed for condensed phases, which is a limitation of the current model. This is largely due to a lack of consistent data for how density

Table 6.1: Properties of Phases at Standard Conditions

| Phase | Molar Mass [g/mol] | Density [g/cm$^3$] | Molar Volume [cm$^3$/mol] |
|---|---|---|---|
| ZrB$_2$(s) | 112.85 | 6.08 | 18.56 |
| ZrO$_2$(s) | 123.22 | 5.68 | 21.69 |
| B$_2$O$_3$(l) | 69.62 | 2.55 | 27.30 |
| SiC(s) | 40.10 | 3.16* | 12.69 |
| SiO$_2$(s,l) | 60.08 | 2.20† | 27.31 |

* Assuming $\beta$-phase, predominant from 300–3100 K [16]
† Assuming amorphous/liquid, predominant from 2000–6000 K [16]

changes with temperature (i.e. thermal expansion). In general, this simplification applies to isothermal systems, but not when strong temperature gradients are present.

Assuming that Eq. (6.1) is the dominant oxidation reaction for ZrB$_2$(s) and proceeds stoichiometrically, one mole of ZrB$_2$(s), occupying 18.56 cm$^3$, oxidizes and forms one mole each of ZrO$_2$(s) and B$_2$O$_3$(l), together occupying 48.99 cm$^3$. This suggests an *expansion ratio* of 2.64 during oxidation if no B$_2$O$_3$(l) evaporates. Likewise, passive SiC oxidation according to Eq. (6.3) suggests an expansion ratio of 2.15. These results imply that volume elements should *grow* as the material oxidizes. Note that the volume fraction of each phase is proportional to its molar volume, so to enforce that the sum of volume fraction equals unity ($\sum f = 1$), the intrinsic volume element $\Delta V$ must have a fixed volume.

Thus, the densities of condensed oxides in Table 6.1 are adjusted such that the expansion ratio is unity for both ZrB$_2$ and SiC oxidation, and the solid volume fraction in the ZrO$_2$(s) oxide layer is $f_s = 0.95$ following Parthasarathy [107]. Additionally, volumetric effects of phase changes *within* condensed species (e.g. SiC-$\alpha \rightarrow$ SiC-$\beta$) are currently neglected. Parthasarathy showed that phase change from monoclinic

$ZrO_2$(III) to tetragonal $ZrO_2$(II) around 1400 K results in a $\sim 3\%$ volume change [108, 115], which is small compared to the values in Table 6.1. Overall, this simplification only affects the volume occupied, not the mass gained/loss due to reactions (which is directly related to the reaction rates), and ensures that a non-porous material remains non-porous during oxidation if no condensed phases are volatilized.

The work in this chapter focuses on $ZrB_2$ ceramic matrix composites. $HfB_2$ composites with SiC have demonstrated higher oxidation resistance than $ZrB_2$-SiC by around 100 K [10], which researchers have attributed to the lower oxygen permeability of $HfB_2$ [108]. Since the oxidation mechanisms of both $ZrB_2$-SiC and $HfB_2$-SiC are qualitatively similar [10,107], the framework described in this chapter can be extended to include $HfB_2$ composites if thermodynamic and transport data are available for the appropriate species. Reliable thermochemistry data for hafnium-containing species are not available from either the NASA polynomials [16] nor the NIST database [98].

Although this model only describes the thermal and chemical material response, thermostructural and mechanical factors are also important in physical TPS applications. Due to the brittle nature of most UHTC materials, strong temperature gradients at the surface induce thermostructural stresses, leading to cracking and mechanical failure of the TPS, but are not addressed in this work. [70, 111] However, thermodynamic and chemical constraints must still be satisfied, independent of mechanical and thermostructural limits.

### 6.2.5 Numerical Implementation

Importantly, the system of equations in Eqs. (6.14)–(6.18) are independent of each other except for the evaluation of the flux terms and the source terms, which are evaluated explicitly. The fully discrete form of the conserved variable vector $\mathbf{Q}(\mathbf{x}, \mathbf{t})$ is denoted by $\hat{\mathbf{Q}}^{\mathbf{k}}$ at timestep $j$, and expressed in Eq. (6.35), where "neq" is the total number of equations in the system.

$$
\hat{\mathbf{Q}}^{\mathbf{k}} = 
\left\{
\begin{array}{ccc}
\phi\rho_{g_1}(x_1, t_k) & \dots & \phi\rho_{g_1}(x_n, t_k) \\
\vdots & & \vdots \\
\phi\rho_{g_{ngs}}(x_1, t_k) & \dots & \phi\rho_{g_{ngs}}(x_n, t_k) \\
f_{s_1}\rho_{s_1}(x_1, t_k) & \dots & f_{s_1}\rho_{s_1}(x_n, t_k) \\
\vdots & & \vdots \\
f_{s_{nss}}\rho_{s_{nss}}(x_1, t_k) & \dots & f_{s_{nss}}\rho_{s_{nss}}(x_n, t_k)
\end{array}
\right\}
=
\left\{
\begin{array}{ccc}
\Big| & & \Big| \\
\hat{\mathbf{Q}}^{\mathbf{k}}_{\mathbf{1}} & \dots & \hat{\mathbf{Q}}^{\mathbf{k}}_{\text{neq}} \\
\Big| & & \Big|
\end{array}
\right\}^{\mathbf{T}}
\tag{6.35}
$$

Each row of $\hat{\mathbf{Q}}^{\mathbf{k}}$ corresponds to an individual continuity equation, so the sub-vector $\hat{\mathbf{Q}}^{\mathbf{k}}_{\mathbf{i}}$ consists of the *same* conserved variable evaluated at each discrete spatial point $x_i$, shown in Eq. (6.36). Discrete forms of the flux and source term vectors ($\hat{\mathbf{F}}^{\mathbf{k}}_{\text{adv}}$, $\hat{\mathbf{F}}^{\mathbf{k}}_{\text{diff}}$, and $\hat{\mathbf{S}}^{\mathbf{k}}$) are expressed similarly.

The resulting system of equations is solved explicitly using a finite-difference scheme. In general, the Reynolds number of internal porous flow is very small (Re < 1), and flow is diffusion dominated. Furthermore, when there is no internal velocity or outgassing (such as in the passive oxidation limit), the advection terms

are zero, and the equations are parabolic in nature. The *explicit* finite-difference method is thus relatively straightforward using Forward Euler for temporal integration and central differencing for spatial integration. This is expressed discretely in Eqs. (6.36)–(6.39) for the $i^{\text{th}}$ equation and timestep $k$ corresponding to $t_k$:

$$\hat{\mathbf{Q}}_{\mathbf{i}}^{\mathbf{k}} = \begin{Bmatrix} q_i(x_1, t_k) \\ \vdots \\ q_i(x_n, t_k) \end{Bmatrix} \tag{6.36}$$

$$\frac{\partial}{\partial x} \hat{\mathbf{F}}_{\text{diff},\mathbf{i}}^{\mathbf{k}} = \mathbf{A} \hat{\mathbf{F}}_{\text{diff},\mathbf{i}}^{\mathbf{k}} \tag{6.37}$$

$$\mathbf{A} = \text{tridiag} \left\{ \frac{1}{2\Delta x} \quad 0 \quad -\frac{1}{2\Delta x} \right\} \tag{6.38}$$

$$\boxed{\hat{\mathbf{Q}}_{\mathbf{i}}^{\mathbf{k+1}} = \hat{\mathbf{Q}}_{\mathbf{i}}^{\mathbf{k}} + \mathbf{\Delta t} \left[ \hat{\mathbf{S}}_{\mathbf{i}}^{\mathbf{k}} + \mathbf{A}\hat{\mathbf{F}}_{\text{adv},\mathbf{i}}^{\mathbf{k}} - \mathbf{A}\hat{\mathbf{F}}_{\text{diff},\mathbf{i}}^{\mathbf{k}} \right]} \tag{6.39}$$

The matrix $\mathbf{A}$ is a tridiagonal matrix of size $n \times n$, where $n$ is the number of spatially-discretized volume elements. This leads to first-order accuracy in time and second-order accuracy in space.

The explicit integration scheme imposes restrictions on the temporal and spatial discretizations according to the CFL condition. An implicit integration method was also investigated, but was not worth the additional computational expense. To resolve the physical oxide layer, spatial discretizations on the order of $\Delta x \simeq 10^{-5}$ m or smaller are needed. This requires time steps on the order of $\Delta t \simeq 10^{-4}$ s to satisfy the CFL condition.

Boundary conditions are implemented using "ghost cells" at the edges of the one-
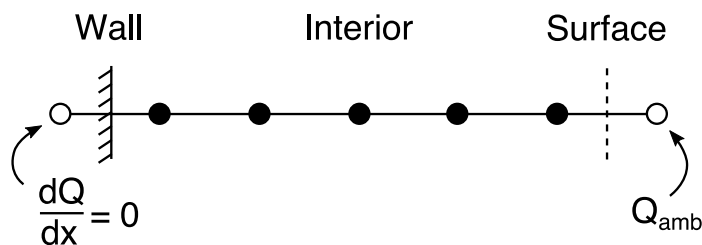
Figure 6.3: Ghost cell boundary conditions.

dimensional domain, illustrated in Fig. 6.3. Internally, an impermeable wall enforces that fluxes and gradients are zero at the wall. The conserved variables, pressure and temperature in the internal ghost cell are evaluated using 2nd-order extrapolation to enforce zero gradients (i.e. symmetry). Internal velocity and diffusive fluxes are set to zero. At the surface, the values in the ghost cell are set to reservoir/ambient values, including velocity, pressure, and temperature. Gradients in the conserved and primitive variables are computed using 2nd-order one-sided differences, and diffusive fluxes from the reservoir cell to the internal cells are evaluated accordingly. With this implementation, no modifications are needed to compute the gradients of fluxes.

The method described in this chapter is implemented in both MATLAB and Python environments, utilizing the Cantera [20] software library. The general implementation is detailed in Fig. 6.4. The one-dimensional domain is initialized to a uniform initial condition, and the multiphase equilibrium solver in Cantera [20] is invoked with the "equilibrate()" function. From the uniform initial condition, the system is time-marched every timestep, $\Delta t$. The fluxes are re-evaluated at each timestep, which account for the advective and diffusive transport within the material.
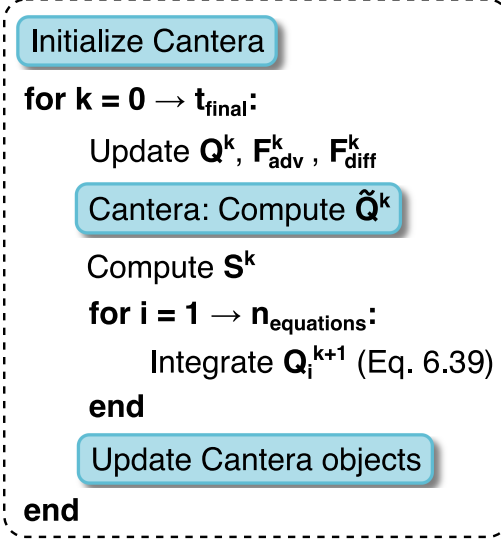
Figure 6.4: Pseudo-code to compute $ZrB_2$-SiC oxidation with Cantera [20].

## 6.2.6 Verification: 1-D Fick's Law

To verify the implementation of the model, a test case is considered for 1-D binary gas diffusion with constant density via Fick's 2$^{nd}$ law in Eq. (6.40).

$$\frac{\partial Y}{\partial t} - D\frac{\partial^2 Y}{\partial x^2} = 0 \tag{6.40}$$

$$Y(x,t): \ Y(x,0) = Y_0, \ \ \frac{\partial}{\partial x}Y(0,t) = 0, \ \ Y(L,t) = Y_\infty \tag{6.41}$$

Non-dimensionalization of Eq. (6.40) yields:

$$\hat{Y} = \frac{Y - Y_\infty}{Y_\infty}, \ \hat{x} = \frac{x}{L}, \ \hat{t} = \frac{t}{L^2/D} \tag{6.42}$$

$$\frac{\partial \hat{Y}}{\partial \hat{t}} - \frac{\partial^2 \hat{Y}}{\partial \hat{x}^2} = 0 \tag{6.43}$$

$$\hat{Y}(\hat{x}, \hat{t}): \ \hat{Y}(\hat{x}, 0) = \frac{Y_0 - Y_\infty}{Y_\infty} = \Phi_0, \ \ \frac{\partial}{\partial \hat{x}}\hat{Y}(0, \hat{t}) = 0, \ \ \hat{Y}(1, \hat{t}) = 0 \tag{6.44}$$

164

Performing separation of variables on Eq. (6.43):

$$\hat{Y}(\hat{x}, \hat{t}) = f(\hat{x})g(\hat{t}) \tag{6.45}$$

$$\frac{g'(\hat{t})}{g(\hat{t})} = \frac{f''(\hat{x})}{f(\hat{x})} = -\lambda \tag{6.46}$$

Solving for $f(\hat{x})$ and $\lambda > 0$:

$$f''(\hat{x}) + \lambda f(\hat{x}) = 0 \tag{6.47}$$

The generic solution to this ODE is in the form of Eq. (6.48):

$$f(\hat{x}) = A\cos\left(\sqrt{\lambda}\hat{x}\right) + B\sin\left(\sqrt{\lambda}\hat{x}\right) \tag{6.48}$$

$$f'(\hat{x}) = -A\sqrt{\lambda}\sin\left(\sqrt{\lambda}\hat{x}\right) + B\sqrt{\lambda}\cos\left(\sqrt{\lambda}\hat{x}\right) \tag{6.49}$$

$$f'(0) = 0 = B\sqrt{\lambda}, \quad B = 0 \tag{6.50}$$

$$f(1) = 0 = A\cos\left(\sqrt{\lambda}\right) \tag{6.51}$$

$$\cos\left(\sqrt{\lambda}\right) = 0, \quad \lambda_n = (\frac{n}{2}\pi)^2, \quad n = 1, 3, 5... \tag{6.52}$$

$$\lambda_n = (\frac{2n-1}{2}\pi)^2, \quad n = 1, 2, 3, ... \tag{6.53}$$

$$f_n(\hat{x}) = a_n\cos\left(\frac{2n-1}{2}\pi\hat{x}\right), \quad n = 1, 2, 3, ... \tag{6.54}$$

Now solving for $g(t)$ and $\lambda = (\frac{2n-1}{2}\pi)^2$:

$$g'(\hat{t}) = -(\frac{2n-1}{2}\pi)^2 g(\hat{t}) \tag{6.55}$$

$$g_n(\hat{t}) = c_n e^{-(\frac{2n-1}{2}\pi)^2 \hat{t}} \tag{6.56}$$

Substituting Eqs. (6.54) and (6.56) into Eq. (6.45), and imposing the initial and boundary conditions from Eq. (6.44):

$$\hat{Y}_n(\hat{x}, \hat{t}) = B_n e^{-(\frac{2n-1}{2}\pi)^2 \hat{t}} \cos\left(\frac{2n-1}{2}\pi\hat{x}\right), \quad B_n = a_n c_n \tag{6.57}$$

$$\hat{Y}(\hat{x}, \hat{t}) = \sum_{n=1}^{\infty} \hat{Y}_n(\hat{x}, \hat{t}) \tag{6.58}$$

$$\Phi_0 = \hat{Y}(\hat{x}, 0) = \sum_{n=1}^{\infty} B_n \cos\left(\frac{2n-1}{2}\pi\hat{x}\right) \tag{6.59}$$

$$\Phi_0 \int_0^1 \cos\left(\frac{2m-1}{2}\pi\hat{x}\right) d\hat{x} = \sum_{n=1}^{\infty} B_n \int_0^1 \cos\left(\frac{2m-1}{2}\pi\hat{x}\right) \cos\left(\frac{2n-1}{2}\pi\hat{x}\right) d\hat{x}$$
$$\tag{6.60}$$

Note that the RHS of Eq. (6.60) is only non-zero for $m = n$:

$$\Phi_0 \int_0^1 \cos\left(\frac{2m-1}{2}\pi\hat{x}\right) d\hat{x} = \sum_{n=1}^{\infty} \frac{1}{2} B_n \delta_{nm} = \frac{1}{2} B_m \tag{6.61}$$

$$B_m = 2\Phi_0 \int_0^1 \cos\left(\frac{2m-1}{2}\pi\hat{x}\right) d\hat{x} = 2\Phi_0 \left[\frac{2}{(2m-1)\pi} \sin\left(\frac{2m-1}{2}\pi\hat{x}\right)\right]_0^1 \tag{6.62}$$

$$B_m = \frac{4\Phi_0}{(2m-1)\pi}(-1)^{n+1} \tag{6.63}$$

166

Finally, the analytical solution to this equation is in the form of an infinite series:

$$\hat{Y}(\hat{x}, \hat{t}) = \frac{4\Phi_0}{\pi} \sum_{n=1}^{\infty} \frac{\cos\left(\frac{2n-1}{2}\pi\hat{x}\right)}{(2n-1)} (-1)^{n+1} e^{-\left(\frac{2n-1}{2}\pi\right)^2 \hat{t}} \qquad (6.64)$$
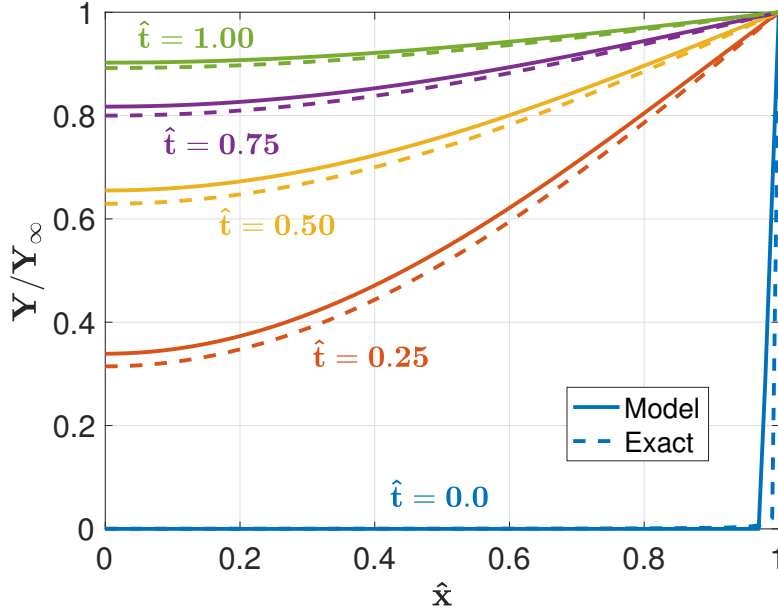


Figure 6.5: Verification of model with 1-D Fick's law.

The exact solution is computed for $Y_0 = 0.0$ and $Y_\infty = 1.0$, and plotted in Fig. 6.5. To implement the equivalent system using the prescribed model, the porosity is set to $\phi = 1.0$ throughout the domain, so only gas-phase transport is being modeled. A binary $O_2$/Ar gas is used, and chemical reactions are turned off (no source terms). Note that the gas diffusion coefficient is assumed constant and equal for both $O_2$ and Ar, but no other changes are made to the implementation. The numerical solution computed from the prescribed model is shown also in Fig. 6.5, and compares well to the exact solution. Slight differences are expected from Fick's 2nd law, since the model utilizes the *modified* Fick's law to compute the species flux in Eq. (6.24), which

167

includes an additional correction term to enforce that the sum of fluxes is zero. This more closely approximates Maxwell-Stefan diffusion, and is more physically accurate than Fick's 2nd law [28].

## 6.3   Model Evaluation

For the simulation results presented in this section, a 1.0 mm domain is initialized to a uniform initial condition with the desired volume fractions of $ZrB_2$ and SiC. The simulation is then iterated until the final time to investigate the transient behavior.

### 6.3.1   $ZrB_2$ Oxidation

Thermogravimetric analysis (TGA) and furnace experiments provide useful validation data for the 1-D model [116–119]. The ambient temperature and pressure conditions in these facilities are well controlled, and typically exhibit diffusion-limited oxidation. Given the long test times of these experiments (on the order of hours), the material is assumed to be isothermal and isobaric internally to simplify the system of equations in Eq. (6.19), where mass diffusion is the dominant transport mechanism. Experimental TGA mass change data from Tripp and Graham is plotted in Fig. 6.6 for several temperatures and fixed 33.3 kPa $O_2$ pressure. The rate of mass change is directly related to the effective oxidation rate in the case of no $B_2O_3(l)$ evaporation. The data show that the oxidation rate *increases* with temperature, and is parabolic with respect to time [116].

Pure $ZrB_2$ oxidation is simulated using $f_{ZrB_2} = 1.0$ and $f_{SiC} = 0.0$. The mass gain
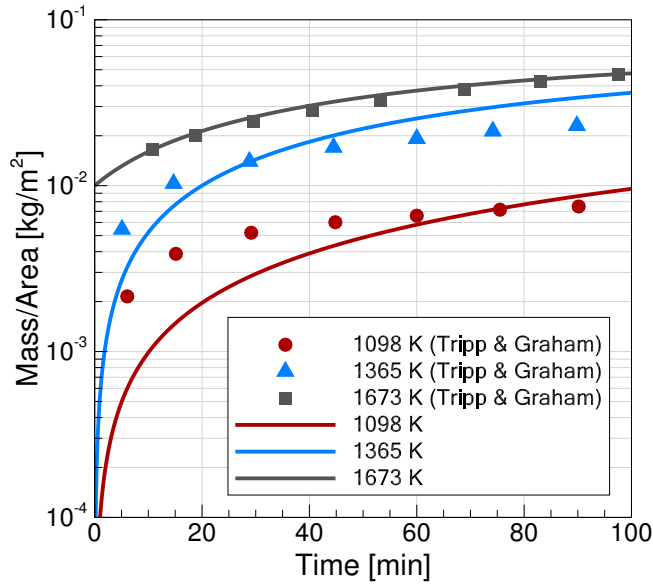
Figure 6.6: Predicted ZrB$_2$ mass change vs. time during passive oxidation compared to experimental data of Tripp and Graham [116] in 33.3 kPa O$_2$.

predictions from the model are compared to the experimental data from Tripp and Graham [116] at the same conditions in Fig. 6.6. The agreement between simulations and experiments in Fig. 6.6 is reasonable, showing the correct temperature trends, although differences are observed in the initial rise below 1600 K. The parabolic oxidation rate is also correctly predicted.

For the coupled material-environment framework, the surface fluxes during oxidation need to be characterized. The fluxes at the gas-surface interface provide additional insight into the interactions between ZrB$_2$ and the ambient environment. Gaseous oxygen is consumed at the surface, producing gaseous B$_2$O$_3(g)$ and B$_2$O$_2(g)$ in nearly equal concentrations from evaporation of liquid B$_2$O$_3(l)$. The overall blowing rate into the boundary layer increases with temperature, evaluated as the sum of all outgoing fluxes. A large imbalance in the surface fluxes is observed, implying
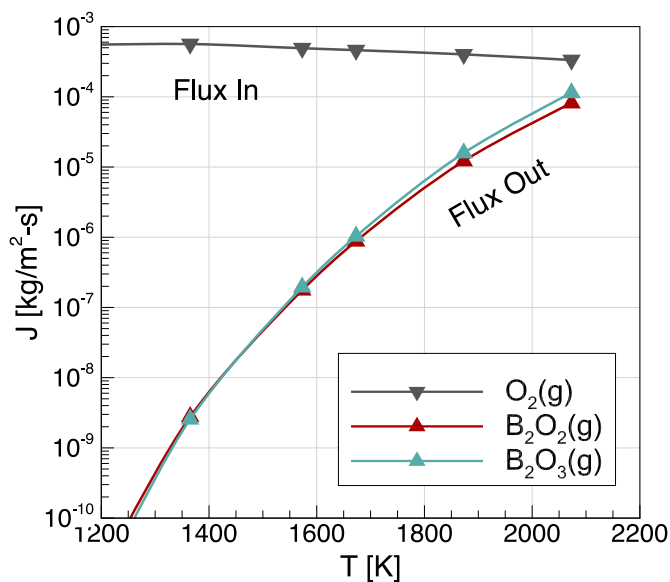
Figure 6.7: Gaseous fluxes at surface for $ZrB_2$ after 2 hrs, 33.3 kPa $O_2$.

formation of condensed rather than gaseous oxides below 2000 K, and leading to the mass *gain* behavior observed in Fig. 6.6. Note that a true "steady-state" condition is not reached, but the parabolic mass gain behavior at lower temperatures suggests that the fluxes are reasonably steady past 1 hr for this experiment [116].

The 1.0 mm domain is large enough that surface oxidation effects are sufficiently isolated, and "grid convergence" is verified with respect to the mass change rates and fluxes using $\Delta x = 2 \times 10^{-5}$ m. There remains a weak dependency on the timestep, since the chemical source terms in Eq. (6.21) depend on $\Delta t$, but these are within $\pm 10\%$ for a diffusion-limited system. The Knudsen numbers (based on $\Delta x$ and the mean free path $\lambda$) evaluated using Eq. (6.65) across the range of conditions are on the order of $Kn \simeq 10^{-2}$, which is at the limit of the continuum regime.

$$Kn = \frac{\lambda}{\Delta x} \tag{6.65}$$

170

## 6.3.2  ZrB$_2$-SiC Oxidation

Experimental data for ZrB$_2$-SiC materials appear to be more inconsistent than pure ZrB$_2$, varying across SiC content, microstructure, manufacturing process, and even experiments [119–121]. Materials manufactured from ZrB$_2$ and SiC powders generally have more homogeneous phase distributions than those involving SiC fibers [70,119], shown in Fig. 6.8, and the powder-manufactured ZrB$_2$-SiC material is most consistent with model assumptions.



(a) 14 vol% SiC from powder    (b) 20 vol% SiC from fibers
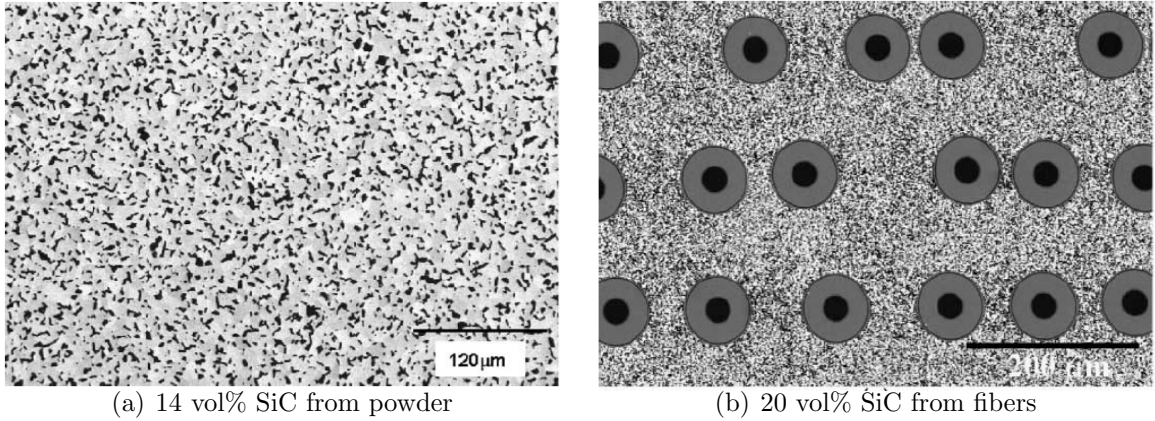
Figure 6.8: Different microstructures for ZrB$_2$-SiC composites. Images are reproduced from Ref. [119].

Simulations are performed for a ZrB$_2$ composite with 20 vol% SiC in an O$_2$/Ar environment ($f_{\text{ZrB}_2} = 0.8$, $f_{\text{SiC}} = 0.2$). The predicted mass change over time is plotted in Fig. 6.9. The predictions are compared to the oxidation data of Levine et al. [119], using the powder-manufactured ZrB$_2$-SiC material. Overall, the model underpredicts the experiments. More importantly however, the temperature dependency is *opposite* that observed in experiments [119,120], predicting a slower rate of mass gain at higher temperatures.
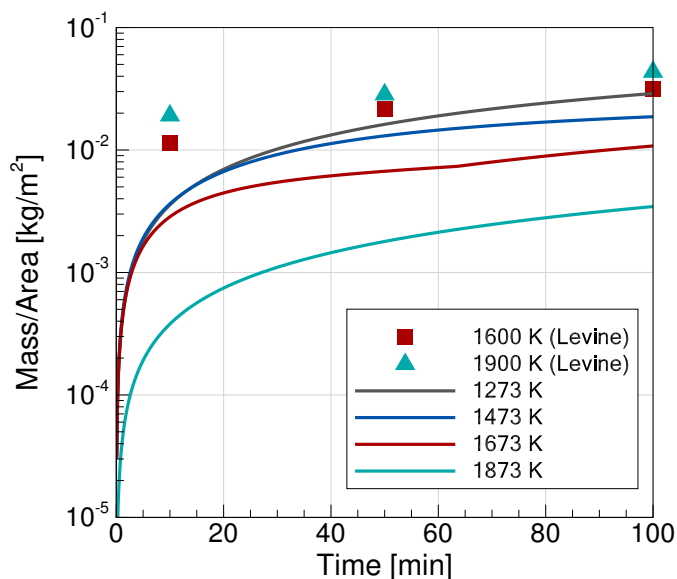
Figure 6.9: Mass change vs. time for $ZrB_2/20$ vol% SiC, 21% $O_2/79$% Ar at 101.3 kPa. Experimental data from Levine et al. [119]

The surface fluxes in Fig. 6.10 provide some insight into this discrepancy in temperature trends. Compared to the surface fluxes in Fig. 6.7, there is significantly more outgassing of $SiO(g)$ and $CO(g)$ from oxidation of the SiC phase than $B_2O_3(g)$, contributing to increased mass loss. This mass *loss* from gas production offsets the mass *gain* from condensed $ZrO_2(s)$ and $B_2O_3(l)$ production, resulting in slower *net* rates compared to pure $ZrB_2$ oxidation.

Between 1200 K and 1700 K, the higher levels of $CO(g)$ over $SiO(g)$ imply passive SiC oxidation and formation of $SiO_2(s, l)$, consistent with the reaction mechanism in Eq. (6.3). Around 1900 K, active oxidation of SiC occurs following Eq. (6.4), where $SiO(g)$ and $CO(g)$ are produced in nearly equal amounts. Hence, the mass loss data in Fig. 6.9 are not an accurate indicator of the overall oxidation rate, since volatilization occurs simultaneously. The relative magnitude of $SiO(g)$ to $B_2O_3(g)$ indicates that

172
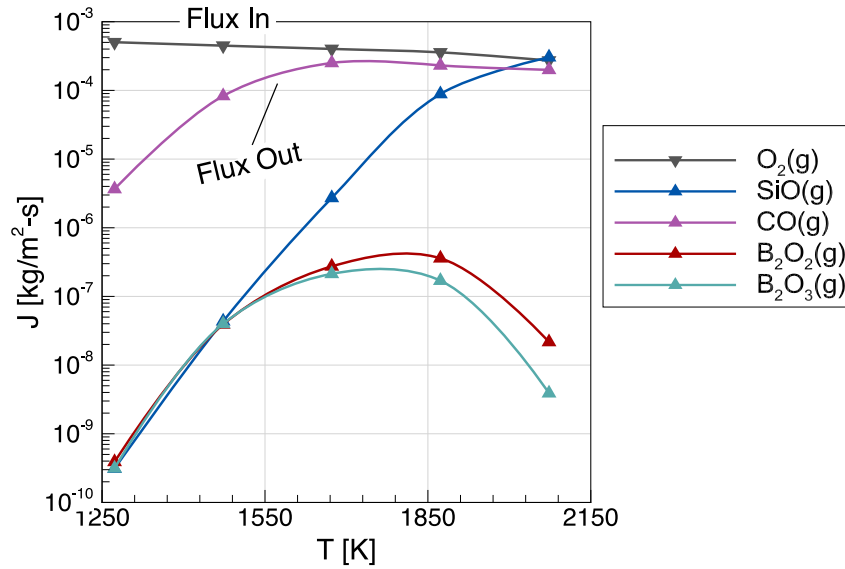
Figure 6.10: Gaseous fluxes at surface for $ZrB_2$/20 vol% SiC after 1 hr, 21% $O_2$/79% Ar at 101.3 kPa.

SiC oxidation is preferred over $ZrB_2$ oxidation in oxygen-limited environments, supporting the selective oxidation mechanism proposed by other researchers that leads to SiC depletion [10, 110].

These results suggest that the observed discrepancy is primarily attributed to SiC oxidation and $SiO_2$ volatilization. Physically, a borosilicate glass mixture ($B_2O_3$– $SiO_2$) forms during oxidation of $ZrB_2$-SiC that is less volatile than $B_2O_3(l)$ and contributes to the increased oxidation resistance of $ZrB_2$-SiC over SiC or $ZrB_2$ alone [10]. Although previous modeling results for the SiC and $ZrB_2$ constituents are largely in agreement with experimental data, the formation of the borosilicate glass is *not* captured with the model, which may account for the increased volatilization of the SiC phase.

Passive-to-active transition for the SiC/$SiO_2$ phase may also lead to the under-

prediction and incorrect temperature trend in Fig. 6.9. Experimental results for SiC in Chapter 4 demonstrated that $SiO_2$ volatilization occurs at *higher* temperatures in reaction-limited environments than in diffusion-limited environments (see Fig. 4.6) [82, 89]. In reality, internal SiC volatilization rates may be reaction-limited due to the low oxygen potentials [110], which would explain the discrepancy with experiments. Importantly, both these factors imply that the equilibrium approach is insufficient to accurately model $ZrB_2$-SiC oxidation.

## 6.4 Chapter Summary

A general model describing oxidation in porous, multiphase composite materials was presented as the first step towards developing a robust simulation capability for $ZrB_2$-SiC and more advanced UHTC materials. A reduced model was evaluated based only on thermodynamics and internal diffusion mechanisms. Simulations were performed for both pure $ZrB_2$ and composite $ZrB_2$-SiC oxidation, and compared to data in the literature. For pure $ZrB_2$ oxidation, the model demonstrated reasonable agreement with measured mass change data, and by extension, oxidation rates [106]. For combined $ZrB_2$-SiC oxidation, differences were observed in the temperature-dependent mass change behavior, and were rationalized as limitations in the thermodynamic equilibrium approach.

Although the thermodynamic-driven approach failed to accurately predict the correct temperature dependency for the composite $ZrB_2$-SiC material, thermodynamic constraints alone do not determine the physical limitations of these UHTC materials.

174

Two-dimensional shear flow effects in aerothermal environments [96,104,122–124] and structural failure due to outgassing and thermal expansion [119] were not captured in the model. Nonetheless, the results presented in this chapter provide a baseline to evaluate higher-fidelity modeling approaches, and highlighted areas where future experimental investigations should be focused. In particular, there is a lack of data in nonequilibrium, reaction-limited environments that cannot be modeled from thermodynamics alone.

# CHAPTER 7

# Finite-Rate Surface Oxidation

In this chapter, a finite-rate modeling approach to surface chemistry is described in lieu of the thermodynamic approaches utilized in the preceding chapters. Results from the previous chapters motivate the need for higher-fidelity methods to understand the oxidation-limiting behavior of both SiC and $ZrB_2$-SiC composites. For $ZrB_2$-SiC, the internal oxidation mechanism of SiC may be reaction-limited, rather than diffusion-limited, suggesting the need to investigate nonequilibrium effects. Thus, finite-rate models for both SiC and $ZrB_2$-SiC oxidation are discussed in this chapter.

In addition, the work in this chapter is motivated by ongoing experiments at the University of Vermont (UVM) to investigate SiC and $ZrB_2$-SiC oxidation. The 30 kW ICP torch at UVM was modeled previously in Chapter 3. Anna and Boyd utilized coupled CFD-surface chemistry simulations to validate surface chemistry parameters using relative N-atom profiles measured in the boundary layer of the same facility [30, 43]. The data from the ongoing experiments are not available at the time of this work, but it is anticipated that this data will help inform finite-rate model parameters.

For both SiC and $ZrB_2$ mechanisms, the available and/or expected experimental data are discussed. In particular, the lack of appropriate data in the literature is

emphasized. Next, mechanisms for SiC and ZrB$_2$-SiC oxidation are proposed. Lastly, ZrB$_2$-SiC modeling parameters are discussed in the context of available and anticipated experimental data, laying the foundation for future work.

## 7.1 Proposed SiC Mechanism

### 7.1.1 Experimental and Theoretical Data

Rates of oxidation can be estimated from mass change data in both passive and active oxidation regimes using TGA facilities [69, 78, 81, 84–86, 89, 95]. However, it is difficult to determine *individual* reaction rates from these data alone, since there are too many degrees of freedom from the possible reaction pathways to adequately constrain the system. Panerai et al. performed emission spectroscopy measurements during SiC oxidation in high-enthalpy hypersonic environments, which provide data on the states and relative populations of radiating gas-phase species [73, 93]. Similar measurements are being performed in the ICP facility at the University of Vermont [45].

More recently, researchers have investigated the theoretical oxidation kinetics of SiC crystals using *ab initio* quantum chemistry calculations of SiC crystals [125–128]. This is a promising approach, which may provide an alternative path to determining reaction rate parameters. It is still unclear how well these theoretical calculations can be generalized to the non-ideal microstructures of manufactured SiC materials, so experimental oxidation data is still required.

## 7.1.2 SiC Model Parameters

Since SiC oxidation is largely a surface process, the proposed SiC oxidation mechanism involves only gas-surface and surface-substrate reactions, without any internal oxidation effects. The proposed SiC oxidation mechanism is *surface-coverage* dependent, and borrows elements from the finite-rate surface chemistry model proposed by Marschall and MacLean [129]. The surface-coverage consists of *active sites*, and there are a finite number of surface sites that can be occupied, described by a site *density* (usually expressed in moles/m$^2$).
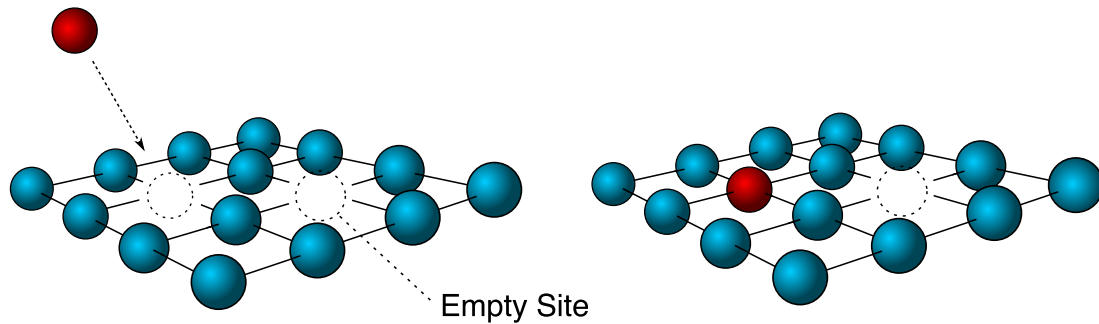


Figure 7.1: Adsorption process onto an empty site.

All reactions must occur at these active sites, and the total number of active sites is conserved. Any number of condensed chemical phases/species can occupy these sites, illustrated in Fig. 7.1, and the surface phases can react with the ambient environment. A single active site can only be occupied by one "particle" of any phase, and vice-versa. Furthermore, active sites may also be "empty," referred to as an *empty site*. These are treated as separate species that participate in reactions, but have no chemical or thermodynamic properties. Physically, the concept of empty

sites relates to the presence of microscopic defects. There exists a lower barrier to reactions at the defect sites, hence surface reactions are more likely to occur at the defects [89].
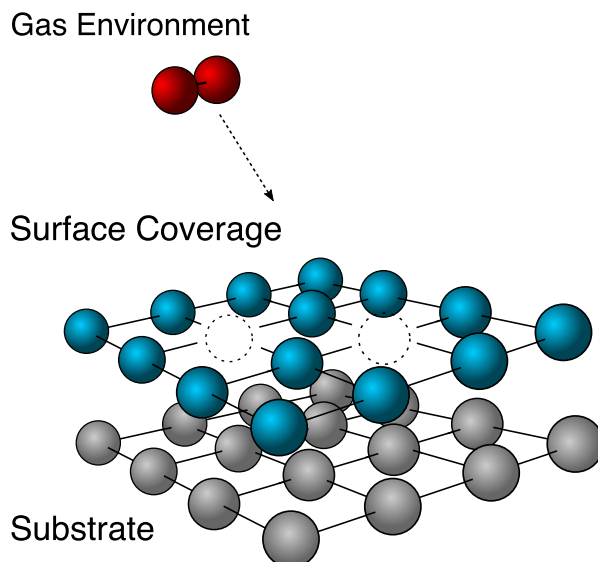


Figure 7.2: Environment, surface, and substrate phases.

Figure 7.1 illustrates a gas-phase adsorption process onto an empty surface site, which is an example of a simple gas-surface reaction. In addition to reactions between the ambient gas and the surface, a distinct feature of this model is that the surface can also react with a separate *substrate* phase, illustrated in Fig. 7.2. The substrate phase is considered a perfect source (no depletion occurs), and acts as a catalyst in gas-surface reactions. For SiC oxidation, the substrate phase is SiC, and the surface coverage consists of condensed SiC, $SiO_2$, Si, or C (graphite). Gaseous chemical species (e.g. $O_2$, SiO, CO) are consumed, exchanged, or produced via surface reactions.

Surface reactions are modeled *explicitly*, without relying on thermodynamic equi-

librium methods as in the previous chapter. This requires *a priori* determination of the "appropriate" reaction mechanisms. In general, the proposed mechanisms for SiC oxidation are more involved than "simple" adsorption/desorption processes, but follow the same general principles. The primary constraint is that all species must have *at least one* formation mechanism.

Table 7.1: Proposed Surface Reaction Mechanisms for SiC Oxidation

| No. | Description | Reaction |
|---|---|---|
| | *Gas–Surface Reactions* | |
| 1 | Exchanges sites | $SiC(s) + 1.5 \ O_2 \leftrightarrow SiO_2(s) + CO$ |
| 2 | Vacate/populate empty site | $SiC(s) + O_2 \leftrightarrow SiO + CO + (s)$ |
| 3 | Vacate/populate empty site | $SiC(s) + 2 \ SiO_2(s) \leftrightarrow 3 \ SiO + CO + 3(s)$ |
| 4 | Vacate/populate empty site | $SiC(s) + SiO_2(s) \leftrightarrow C(s) + 2 \ SiO + (s)$ |
| 5 | Exchanges sites | $2 \ SiC(s) + SiO_2(s) \leftrightarrow 3 \ Si(s) + 2 \ CO$ |
| 6 | Vacate/populate empty site | $SiO_2(s) \leftrightarrow SiO + 0.5 \ O_2 + (s)$ |
| 7 | Vacate/populate empty site | $Si(s) + 0.5 \ O_2 \leftrightarrow SiO + (s)$ |
| 8 | Exchanges sites | $Si(s) + O_2 \leftrightarrow SiO_2(s)$ |
| 9 | Vacate/populate empty site | $C(s) + 0.5 \ O_2 \leftrightarrow CO + (s)$ |
| | *Surface–Substrate Reactions* | |
| 10 | Vacates 2 empty sites | $SiC(b) + 2 \ SiO_2(s) \rightarrow 3 \ SiO + CO + 2(s)$ |
| 11 | Exchanges surface sites | $SiC(b) + SiO_2(s) \rightarrow C(s) + 2 \ SiO$ |
| 12 | Populates 2 empty sites | $2 \ SiC(b) + SiO_2(s) + 2(s) \rightarrow 3 \ Si(s) + 2 \ CO$ |
| | *Gas–Substrate Reactions* | |
| 13 | Populates empty sites | $SiC(b) + 1.5 \ O_2 + (s) \rightarrow SiO_2(s) + CO$ |

Table 7.1 summarizes the proposed reaction set for SiC oxidation between gas environment, surface, and substrate phases. The SiC substrate phase is denoted by SiC(b), and the SiC phase on the surface is SiC(s). Other condensed surface phases are appended with "(s)" in Table 7.1. An empty site is denoted by (s), and other species are gaseous. Reactions #1 to #9 are assumed to be reversible (can proceed in either forward or backward directions). However, reactions (#10 to #13) are

irreversible, since these involve the substrate phase, and the backward reaction would imply formation of additional substrate phase. Instead, reactions #3 to #5 are the "equivalent" reactions that involve only surface phases. The gas-substrate reaction #13 allows the surface to be populated if only empty sites are present, and can only proceed *at* empty sites.

For a complete finite-rate mechanism, rates must also be provided for each reaction in Table 7.1 to describe the chemical kinetics. These rates are typically fit to an Arrhenius form [20] in Eq. (7.1), where coefficients $A$, $b$, and $E_a$ are specified for each reaction in Table 7.1.

$$k_f = AT^b e^{-E_a/RT} \tag{7.1}$$

However, as mentioned previously, there are insufficient high-fidelity data available to make a confident determination of the proper rates for each mechanism.

### 7.1.3 Model Evaluation

Although there is lack of sufficient data at the time of this work to make a determination of the rates, the *equilibrium* behavior can still be investigated, and should be consistent with the prior analyses in Chapter 4. The work in Chapter 4 utilized a *mechanism-independent* approach, which can be used to verify the equilibrium behavior of the set of *mechanism-specific* reactions proposed in Table 7.1. This is sufficient to validate the reaction set in Table 7.1, but not the kinetic rates associated with each reaction.
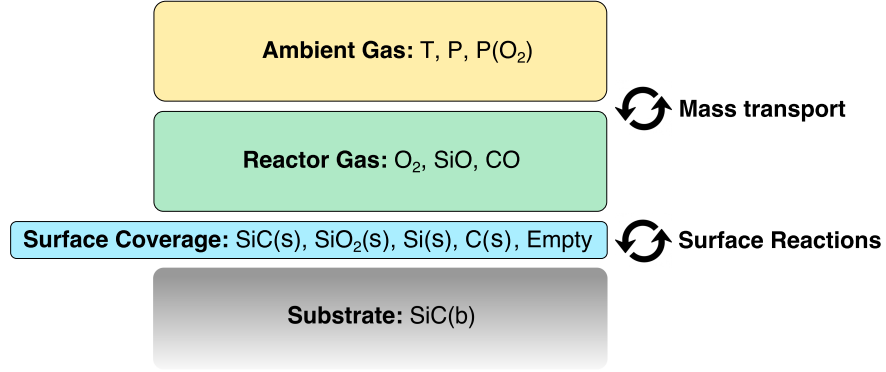
Figure 7.3: Modified zero-dimensional SiC-$O_2$ reactor model.

To evaluate the proposed SiC oxidation mechanism, the modified system illustrated in Fig. 7.3 is evaluated, based on the zero-dimensional ACE model in Fig. 4.4, but utilizing the surface reactions listed in Table 7.1 and the presence of empty sites. The results presented in Chapter 4 demonstrated that SiO and CO are the primary gases produced via surface reactions, and other gaseous species are produced via gas-phase reactions with the ambient environment [106]. The ambient gas environment is considered a perfect source/sink. The gas-surface interface consists of two parts: the reactor gas, and the surface coverage. Gas-phase species exist in the reactor, and diffuse between the ambient environment, while condensed species exist on the surface coverage. Surface reactions occur between the reactor, surface coverage, and substrate, and the ambient gas cannot interact directly with the substrate phase. The surface site density is fixed, but the reactor volume is constrained by the ambient temperature and pressure.

For each species, equations describing the rate of change for gas and surface species from surface reactions are expressed as functions of the kinetic reaction rates in Eqs. (7.2) and (7.3). $X_s$ refers to the generalized concentration of species $s$, which has

units of moles/m$^3$ in the gas phase and moles/m$^2$ on the surface.

$$\frac{\partial X_s}{\partial t} = \dot{\omega}_s \tag{7.2}$$

$$\dot{\omega}_s = \sum_{r=1}^{N_{\text{react}}} \left[ \left( \nu_{sr}'' - \nu_{sr}' \right) \left( k_{f,r} \prod_{i=1}^{N_{\text{species}}} [X_i]^{\nu_i'} - k_{b,r} \prod_{i=1}^{N_{\text{species}}} [X_i]^{\nu_i''} \right) \right] \tag{7.3}$$

The source term $\dot{\omega}_s$ for each species $s$ is computed by summing the contribution over

all reactions, where $\nu$ is the stoichiometric coefficient for species $s$ in reaction $r$. For

gaseous species, an additional term accounts for the diffusion of species between the

ambient and reactor over a unit length $\delta$ in Eqs. (7.4) and (7.5):

$$\frac{\partial X_g}{\partial t} = \dot{\omega}_s - \frac{\partial}{\partial x} J_g \tag{7.4}$$

$$J_g = -D_g \frac{\chi_g^{\text{amb}} - \chi_g^{\text{react}}}{\delta} \frac{P}{RT} \tag{7.5}$$

$\chi_g$ is the mole fraction of gaseous species $g$. To evaluate the spatial derivative of the

gas flux, the gas flux in the ambient is approximated as zero. Constant pressure in

the reactor gas is enforced for gas-phase species by adding the additional constraint

in Eq. (7.6):

$$\sum_{g=1}^{\text{ngs}} \frac{\partial X_g}{\partial t} = 0 \tag{7.6}$$

For reversible reactions, forward and backward rates are related by detailed bal-

ance. Specifically, the backward rates are evaluated from Eq. (7.7), where $\Delta G_r^o$ is the

change in Gibbs free energy between products and reactants for reaction $r$, and n$_{\text{gas}}$

183

is stoichiometric production of gaseous species. $P^o$ is the standard reference pressure, typically 1 bar = 100,000 Pa. Thermodynamic properties for each gaseous and surface species are computed from NASA polynomials [16]. This follows the chemical kinetics methodology described earlier in Chapter 2. For irreversible reactions, the backward rate is zero.

$$k_{b,r}(T) = \frac{k_{f,r}(T)}{K_{c,r}(T)} \tag{7.7}$$

$$K_{c,r}(T) = \left(\frac{P^o}{RT}\right)^{\Delta n_{\text{gas}}} \exp\left(\frac{-\Delta G_r^o}{RT}\right) \tag{7.8}$$

Importantly, the equilibrium state is *independent* of the kinetic rates. The equilibrium behavior can be evaluated by integrating the system of rate equations described by Eq. (7.2) to steady-state, and is equivalent to the free energy minimization approach utilized in Chapters 4 and 5 [129]. The modified reactor model is implemented using Cantera [20], and the reaction mechanisms in Table 7.1 are specified in Cantera along with "representative" kinetic reaction rates. The equilibrium state is then computed by integrating the system of rate equations until steady-state.

This is demonstrated for SiC oxidation in Fig. 7.4 over a range of temperatures and pressures relevant to hypersonic conditions, from $10^2$ to $10^5$ Pa $O_2$ and 1000 to 3000 K [106]. The surface coverage is initialized with a layer of condensed $SiO_2(s)$, representing the passive oxidation regime. The $SiO_2(s)$ coverage is eroded at elevated temperatures, leaving behind empty sites. Note that the tendency to form empty sites at higher temperatures represents the erosion of the surface layer. Passive-to-active transition is determined when the initial $SiO_2(s)$ coverage is *less than 50%*,
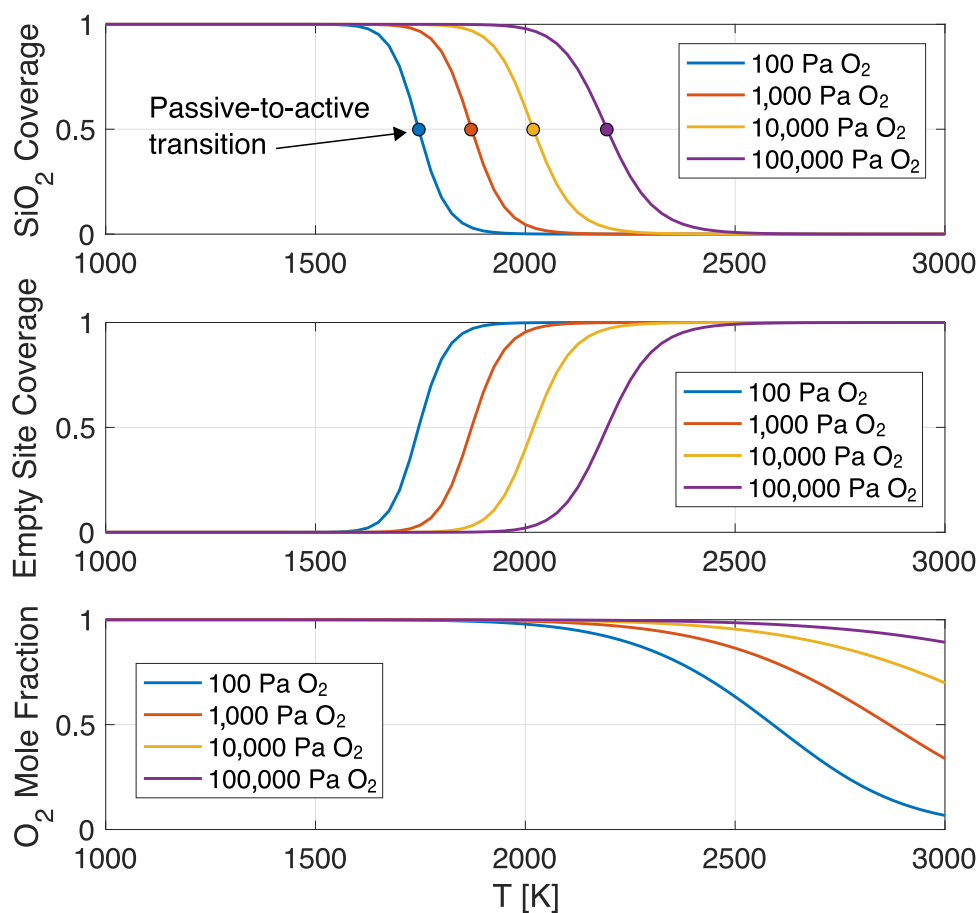
Figure 7.4: Prediction of equilibrium surface coverage for pure SiC oxidation at different ambient oxygen pressures.

and the transition itself occurs over a narrow temperature range. Importantly, these results are independent of the assumed site density, and a representative site density of $1 \times 10^{-12}$ moles/m$^2$ is used for this analysis.

The passive-to-active transition conditions predicted with the mechanism-specific model (Cantera) are compared in Fig. 7.5 with those from the mechanism-independent model (ACE) previously validated in Chapter 4. Excellent agreement is observed with both prior results and experimental data, and the Arrhenius behavior observed in the previous model and in the experiments is accurately recovered. The Cantera predic-

tions are *mechanism-specific* but *rate-independent*. These equilibrium results validate the mechanism set in Table 7.1, but rates are still required for each reaction – these can be derived from a combination of computational modeling and experimental data, but cannot be derived *ab initio* from thermodynamics alone [130].
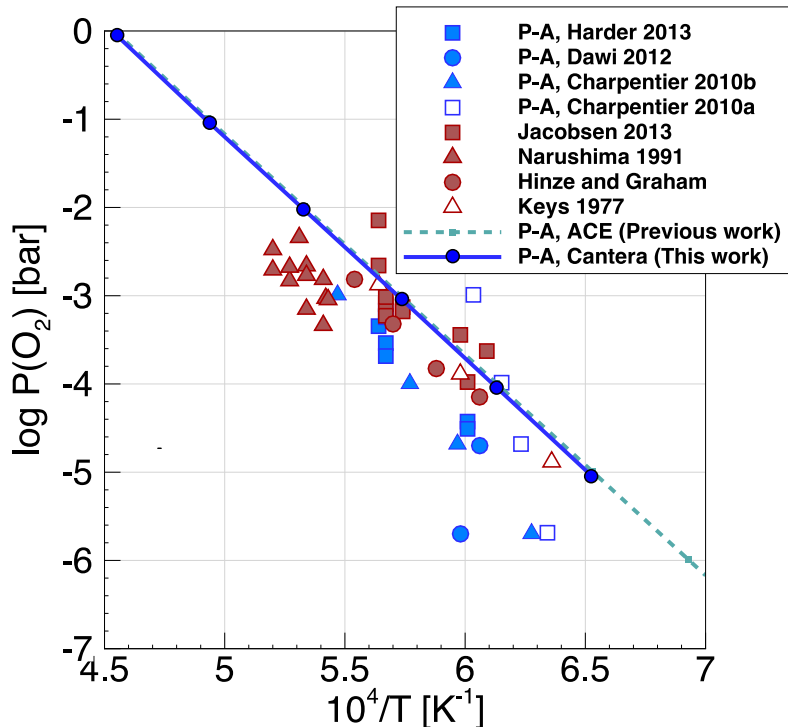


Figure 7.5: Comparison of passive-to-active transition conditions with Cantera, ACE and experiments.

The process of determining rates from experimental data is not trivial. In addition to the bulk oxidation data from TGA experiments [69, 78, 81, 84–86, 89, 95], profiles of O-atom concentrations in the boundary layer can be determined from LIF measurements in UVM's ICP facility, demonstrated by Anna and Boyd for carbon nitridation [43, 45]. The gradient of the O-atom concentration is proportional to the oxygen consumption rate at the surface.

Spectrally-resolved radiative emission measurements also provide information on the relative levels of individual species. Both Si-atoms and SiO emit radiatively, and are characteristic of SiC oxidation. Si-atoms were observed previously in the experimental spectra measured by Panerai et al. [73] (see Fig. 5.14 in Chapter 5). SiO emits in the 210–230 nm band from electronic transitions between the A–X levels [131,132], which was modeled by Johnston et al. [133]. Simulations can be performed by coupling the finite-rate surface chemistry mechanism in Table 7.1 to the CFD calculations performed in previous chapters, incorporating gas-phase chemical kinetics and radiative emission calculations as part of the coupled framework. Although modeling these additional processes introduces uncertainty/error, prior analyses in Chapters 3 and 5 suggest that these mechanisms are relatively well understood compared to SiC surface oxidation.

## 7.2 Proposed ZrB$_2$-SiC Mechanism

### 7.2.1 Experimental Data

Similar to SiC oxidation, there is a lack of sufficient high-fidelity data available in the literature at the time of this work. The measured weight gain data for ZrB$_2$/SiC oxidation across various temperature and pressure conditions provides a good starting point, since this data can be related to bulk oxidation rates [116,118,120,134]. These experiments demonstrate parabolic mass gain behavior in passive oxidation conditions (typically below 2000 K at standard pressure). However, above 2000 K, volatilization

of both the $B_2O_3(l)$ and $SiO_2(s,l)$ phases limits the usefulness of this data. In this case, the surface consumption rate may still be estimated using the measured O-atom profiles in the boundary layer.

More recently, Playez et al. measured the emission spectra during oxidation of $ZrB_2$-SiC composites, and observed emission signatures from boron atoms, BO, and $BO_2$ in the gas-phase [123]. These signatures correspond to the B ($^2S_{1/2}$–$^2P_{1/2,3/2}$), BO (A–X), and $BO_2$ (A–X) electronic transition systems, respectively, and are characteristic of $ZrB_2$ oxidation.

## 7.2.2  $ZrB_2$-SiC Model Parameters

A finite-rate model for $ZrB_2$-SiC oxidation may be treated as an extension of the equilibrium $ZrB_2$-SiC model in the Chapter 6. Since oxidation occurs *in-depth*, a volumetric site density proportional to the volume fraction of each phase is considered, rather than a surface coverage. Recall from Chapter 6 that the matrix is assumed to consist of up to 5 distinct phases: $ZrB_2(s)$, $ZrO_2(s)$, $B_2O_3(l)$, $SiC(s)$, and $SiO_2(s,l)$. Each phase occupies volume fraction $f$, which varies in-depth. A characteristic site density, $n_s$ is also associated with each phase. The total number of sites for each phase is then computed with Eq. (7.9).

$$N_{\text{sites},s} = f_s n_s \tag{7.9}$$

$$N_{\text{sites}} = \sum_{s=1}^{n_{\text{phases}}} N_{\text{sites},s} \tag{7.10}$$

The main internal reaction mechanisms for $ZrB_2$ oxidation can be proposed with

reasonable confidence based on the prior analyses presented in Chapter 6. These are described by reactions #1 and #2 in Table 7.2 below. A reduced set of reactions is considered for the SiC constituent in Table 7.2 compared to Table 7.1, since the one-dimensional formulation presented in Chapter 6 already includes the limiting effects of diffusion through a porous matrix. For internal SiC oxidation, the $Si(l)$ and $C(s)$ phases are generally not involved [109], so reactions describing their chemistry are not needed, simplifying the reaction set.

Table 7.2: Proposed Reaction Mechanisms for $ZrB_2$-SiC Oxidation

| No. | Description | Reaction |
|---|---|---|
| | *$ZrB_2$ Reactions* | |
| 1 | Populate/vacate empty site | $ZrB_2(s) + 2.5\ O_2 + (s) \leftrightarrow ZrO_2(s) + B_2O_3(s)$ |
| 2 | Vacate/populate empty site | $B_2O_3(s) \leftrightarrow B_2O_3 + (s)$ |
| | *SiC Reactions* | |
| 3 | Exchanges sites | $SiC(s) + 1.5\ O_2 \leftrightarrow SiO_2(s) + CO$ |
| 4 | Vacate/populate empty site | $SiC(s) + O_2 \leftrightarrow SiO + CO + (s)$ |
| 5 | Vacate/populate empty site | $SiC(s) + 2\ SiO_2(s) \leftrightarrow 3\ SiO + CO + 3(s)$ |
| 6 | Vacate/populate empty site | $SiO_2(s) \leftrightarrow SiO + 0.5\ O_2 + (s)$ |

Like the SiC oxidation case, rates are still required for each reaction. The proposed finite-rate mechanism can then be evaluated using the methodology detailed in Chapter 6 with only one modification. The chemical source terms, $\dot{\omega}$, are now computed using Eq. (7.3), and the forward and backward rates are related by detailed balance.

Experimental data measuring the transient change in weight of $ZrB_2$ samples during oxidation allow determination of a "bulk" oxidation rate [116, 118, 134], assuming no vaporization of $B_2O_3(l)$ occurs. However, at temperatures above 2000 K when $B_2O_3(l)$ evaporation proceeds rapidly, this method is insufficient unless accompanied

by an accurate estimate of the $B_2O_3(l)$ evaporation rates. Generally, the bulk oxidation data alone are inadequate to make a determination of reaction-specific rates, since any number of rates may be tuned to match the bulk data. Additional constraints are needed from the O-atom profile measurements to make a confident determination of the local, reaction-specific rates.

Now, making the assumption that $ZrB_2$ oxidation is *independent* of SiC oxidation, rates for SiC-specific reactions may be estimated similarly from bulk $ZrB_2$-SiC oxidation data [119, 120] and O-atom profiles, if the $ZrB_2$-specific rates have already been determined. Importantly, the internal rates for reactions #3 to #6 in Table 7.2 may be different from the *surface* rates in Table 7.1.
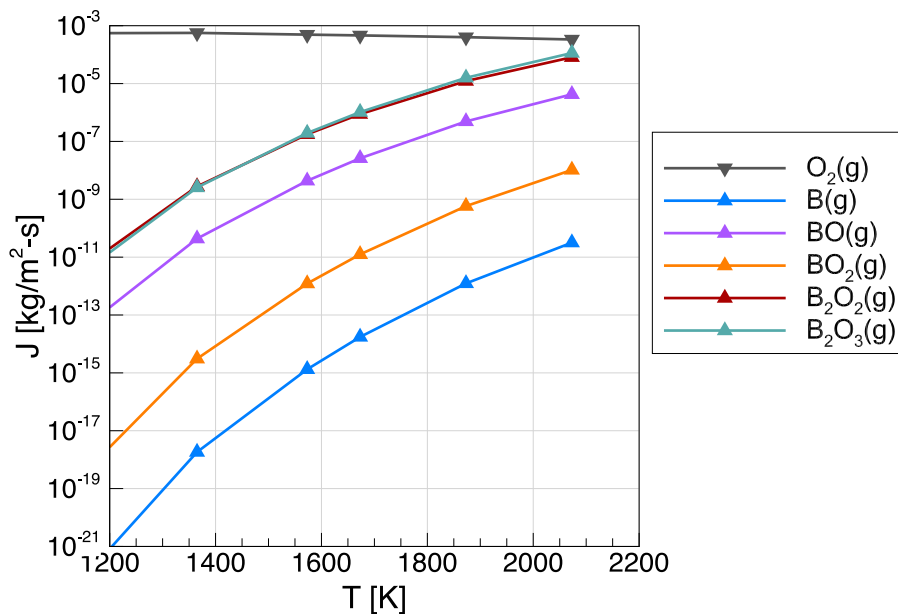


Figure 7.6: Equilibrium gas fluxes at surface for $ZrB_2$ after 2 hrs, 33.3 kPa $O_2$.

Emission spectroscopy provides additional data that is vital to any validation effort for the finite-rate rate mechanisms. A coupled CFD-surface chemistry framework

is needed to evaluate the O-atom profiles and to simulate the radiative emission in the boundary layer. Equilibrium calculations from Chapter 6 are shown in Fig. 7.6, showing the mass fluxes (proportional to the mass fractions) of B, BO, and $BO_2$ species observed in the emission spectra measured by Playez et al. [123]. These calculations suggest that boron atoms are present only in trace amounts at the moderate conditions near the surface, but this fraction likely increases at the elevated temperatures ($T_{tr} > 6000$ K) experienced in the ICP torch. In addition to spectroscopic data for the B ($^2S_{1/2}$–$^2P_{1/2,3/2}$), BO A–X, and $BO_2$ A–X electronic transition systems (see Appendix A.2), additional gas-phase chemical kinetics are needed to describe the formation of B($g$), BO($g$), and $BO_2$($g$) from evaporated $B_2O_3$($g$).

## 7.3   Chapter Summary

This chapter provided an overview of the experimental data currently available for SiC and $ZrB_2$-SiC oxidation kinetics. Ongoing experiments at the University of Vermont to investigate SiC and $ZrB_2$-SiC oxidation were discussed in the context of determining finite-rate reaction parameters. Finite-rate mechanisms were proposed for both SiC and $ZrB_2$ oxidation, and the equilibrium behavior of the proposed SiC oxidation mechanism was evaluated and validated. Overall, this chapter provided a framework to evaluate a finite-rate chemistry model for UHTC oxidation. However, rates for each reaction were not able to be determined at the time of this work. Determination of the rates is left to future work, with the availability of high-fidelity data from ongoing experiments at the University of Vermont.

# CHAPTER 8

# Conclusions and Future Directions

This chapter summarizes the research presented in this dissertation. First, the methodologies and major findings from each of the previous chapters are briefly described. Next, the unique research contributions of this work are stated. Lastly, the overall direction of this research is discussed, and detailed recommendations are made for the future work.

## 8.1 Dissertation Summary

Chapter 2 provided the physical concepts and numerical foundations to model the thermodynamic and chemical processes that occur in material-environment interactions. Principles of thermodynamic equilibrium were discussed, relating thermal and chemical equilibrium to entropy maximization and free energy minimization. The physical models and numerical formulation for CFD and material response calculations were also presented.

Chapter 3 gave a description of a collaborative experiment–simulation effort to investigate the chemical kinetics of pyrolysis gases in representative hypersonic flight

conditions. Experiments performed in an ICP torch facility were modeled using high-fidelity CFD simulations and chemical kinetic mechanisms. Spectrally-resolved radiative emission measurements were simulated by coupling radiation calculations to the CFD framework. The chemical kinetic mechanisms were then evaluated and validated from these comparisons.

Chapter 4 described the development of a thermodynamic model for SiC oxidation and nitridation. The model was validated with several metrics, and found to predict the passive-to-active transition conditions more accurately than existing theories and models in the literature. The importance of modeling both the surface coverage and substrate reactions was demonstrated from these results. In addition, surface energy balance calculations predicted the temperature jump phenomenon during passive-to-active transition, which was validated by experiments. The thermodynamic model accurately described the equilibrium behavior in diffusion-limited environments, but discrepancies were observed in reaction-limited regimes.

Chapter 5 built upon the CFD–radiation approach developed in Chapter 3 by coupling to the SiC material model in Chapter 4. Passive and active oxidation regimes were evaluated for several geometries and freestream conditions, comparing to inert and catalytic wall conditions. Active oxidation resulted in a 20–40% increase in the chemical diffusive heating due to consumption of oxygen and production of SiO and CO. The aerothermal heating coefficient was found to be relatively constant throughout passive and active oxidation regimes. The predicted steady-state radiative equilibrium temperature agreed with experimental temperature measurements within 3%, and simulated emission spectra were in qualitative agreement with available

spectral measurements.

Chapter 6 described the development of a model for $ZrB_2$ and $ZrB_2$-SiC oxidation based on one-dimensional porous flow equations. The model framework can also be extended to other UHTC materials, including binary and tertiary composites. Diffusion-limited equilibrium was approximated using multiphase chemical equilibrium calculations. The internal, transient oxidation behavior was simulated, and reasonable agreement was observed with experimental mass gain data in the passive oxidation regime for $ZrB_2$. However, discrepancies in the temperature-dependent behavior were observed for $ZrB_2$-SiC oxidation, and these were rationalized as deviations from equilibrium SiC volatilization.

In Chapter 7, finite-rate parameters were proposed for SiC and $ZrB_2$-SiC oxidation. The rate-independent equilibrium behaviors of the proposed reaction sets were found to be consistent with prior analyses in Chapters 4 and 6, verifying the reaction sets. Available experimental data in the literature were reviewed, but were ultimately determined to be insufficient for the derivation of reaction-specific rates. Additional experimental data are needed, namely measurements of oxygen profiles in the boundary layer and radiative emission spectra.

Overall, the oxidation behavior and general material-environment interactions of two UHTC materials, SiC and $ZrB_2$, were characterized using first-principle, thermodynamic-based models. Both steady-state surface-level SiC oxidation and transient in-depth $ZrB_2$/SiC oxidation were modeled using this approach. In steady-state equilibrium, results for SiC and $ZrB_2$ showed good agreement with experimental data for a variety of metrics including passive-to-active transition conditions, surface temperatures,

194

gas-phase radiative emission, and mass loss rates. However, limitations of the thermodynamic approach were also identified. For composite $ZrB_2$-SiC oxidation, equilibrium calculations did not predict transient, nor internal SiC oxidation accurately. Although there are certainly other factors that may limit the application of UHTC materials to practical TPS, this work addressed the thermodynamic and chemical limitations in *idealized* environments.

## 8.2   Research Contributions

Within the context of modeling material-environment interactions for hypersonic TPS materials, the major contributions of this research may be summarized as follows:

- **Development of coupled simulation framework:** A coupled CFD–surface chemistry–radiation framework was developed, demonstrated, and validated to model general material-environment interactions for various TPS materials.

- **Radiative emission simulations:** The novel use of radiative emission spectra was demonstrated to validate detailed chemical kinetics and inform chemistry models. This involved coupled CFD-radiation simulations and comparisons to experimentally-measured spectra.

- **Model for SiC oxidation and nitridation:** A model for SiC material-environment interactions in arbitrary gas environments was developed and validated. This model informed detailed surface mass and energy balance calculations in the coupled framework.

- **Model for ZrB$_2$ and ZrB$_2$-SiC oxidation:** A general model was developed and evaluated for ZrB$_2$ and ZrB$_2$-SiC material-environment interactions, and can be extended to other binary and tertiary UHTC composites.

- **Limitations of thermodynamic equilibrium:** Thermodynamic equilibrium analysis techniques were utilized to model material-environment interactions for TPS materials based only on first-principles. The limitations of this approach were explored, highlighting and motivating areas that required additional investigation and higher-fidelity models.

- **Finite-rate surface oxidation parameters:** Finite-rate chemistry parameters were proposed to model nonequilibrium oxidation behavior in SiC, ZrB$_2$, and ZrB$_2$-SiC materials. The simulations inform ongoing and upcoming experiments, which will enable further development of these models.

## 8.3   Recommendations for Future Work

Throughout the work presented in this dissertation, thermodynamic approaches to modeling material-environment interactions were extensively characterized and evaluated. However, thermodynamic stability is not the only consideration when determining the limits of UHTCs and other TPS materials. The models presented in this work relied upon zero and one-dimensional simplifications to investigate the thermochemical limit, and neglected two-dimensional shear effects and possible melt flows. In sharp leading edge applications with strong gradients in velocity and pres-

sure, these effects may detrimentally affect the effective oxidation resistance, and should be investigated. For example, silica ($SiO_2$) and boria ($B_2O_3$) exist as liquid phases on the surface during passive $ZrB_2$-SiC oxidation, limiting oxygen diffusion. A transient/finite-rate approach allows simultaneous determination of the rates of production and loss. Evaporation and melt flow augment the rate of material loss, and likely shifts the equilibrium point to *lower* temperatures and higher oxygen pressures.

More work is also needed in the development of models for new TPS materials. Both SiC and $ZrB_2$-SiC materials are insufficient for more aggressive hypersonic flight trajectories, often requiring TPS materials that have a combined refractory and oxidation limit exceeding 3000 K. There is ongoing interest in alternative binary (e.g. $HfB_2$-SiC) and tertiary (e.g. $ZrB_2$-SiC-ZrC) UHTC composites, and recent experimental efforts have begun characterizing the oxidation behavior of these materials [105, 135, 136]. On the modeling side, the general framework presented in Chapter 6 here should be extended to these new materials. For $HfB_2$, experiments by other researchers have demonstrated that the oxidation mechanisms are similar to $ZrB_2$ and $ZrB_2$/SiC, so the same model may be utilized if thermodynamic and transport data are available for Hf-containing species. For tertiary composites, the model must include additional chemical phases. Experiments have shown qualitatively similar oxidation mechansims, including the formation of a porous microstructure. Importantly, the limiting factor is still the volatilization of passive oxides, but the additional phases likely affect the thermochemistry. Transport mechanisms and thermodynamic data for additional condensed and gaseous species are also required. This work demonstrated that a thermodynamic approach is a good starting point,

197

even for more complex materials.

The chemical equilibrium calculations utilized throughout this work also allow investigation of the oxidation behavior in non-ideal environments. For example, the presence of water vapor in air has been shown in experiments to increase the oxidation rate over dry air [137]. Water vapor ($H_2O$) acts as an oxidant, in addition to $O_2$, and is important for propulsion applications of TPS and UHTC materials.

Beyond thermodynamic models, the results presented in this work demonstrated the need for higher-fidelity finite-rate models and experimental data. Determination of reaction-specific rates for nonequilibrium surface chemistry models relies upon additional data from ongoing experiments, such as passive-to-active transition conditions, radiative emission spectra, and measured oxide-scale thicknesses. A regression-type approach may be utilized to determine the rates, fit to an Arrhenius form. To simulate the experimental emission spectra, additional species and transitions need to be implemented in NEQAIR. For SiC oxidation, characteristic radiative species are Si and SiO (A-X). For $ZrB_2$, characteristic radiative species include B, BO (A-X), and $BO_2$ (A-X). Electronic levels and spectroscopic data for these species are needed, as well as details on the vibrational-electronic transitions for molecules.

In practical TPS applications, the mechanical and structural response of TPS materials is another important limitation that was not modeled in this work. Cracking and spallation are examples of processes that lead to mechanical failure of TPS materials. To evaluate the internal stresses from thermostructural and applied loads, the model developed in Chapter 6 may be extended using a hydrodynamic approach. This requires equations of state to be specified for additional material-specific mass,

momentum, and energy conservation equations.

Finally, fully-coupled CFD–Material Response–Surface Chemistry–Radiation simulations are possible with the framework demonstrated throughout this dissertation, although were not performed. More development effort is required to strongly couple the various modeling domains together (flowfield, material response, surface chemistry). Time-accurate CFD–material response simulations with surface chemistry allow the thermal and chemical response of hypersonic vehicles to be analyzed along an entire flight trajectory. This is a critical step in the development of truly predictive simulation capabilities.

## 8.4   List of Publications

### Journal Publications

1. Chen, S.Y. and Boyd, I.D., "Boundary-Layer Thermochemical Analysis During Passive and Active Oxidation of Silicon Carbide", *Journal of Thermophysics and Heat Transfer*, 2020. (Accepted)

2. Chen, S.Y., Boyd, I.D., Martin, N.C., and Fletcher, D.G., "Modeling of Emission Spectra in Nonequilibrium Plasmas for Testing Pyrolyzing Ablators", *Journal of Thermophysics and Heat Transfer*, Vol. 33, No. 4, 2019, pp. 907–916.

3. Chen, S.Y. and Boyd, I.D., "Chemical equilibrium analysis of silicon carbide oxidation in oxygen and air", *Journal of the American Ceramic Society*, Vol. 102, 2019, pp. 4272–4284.

## Conference Proceedings

1. Chen, S.Y. and Boyd, I.D., "A thermodynamic meso-scale model for oxidation of $ZrB_2$-SiC", *AIAA SciTech Forum*, 6-10 January 2020, Orlando, FL, AIAA 2020-0399.

2. Chen, S.Y. and Boyd, I.D., "Analysis of the Silicon Carbide Boundary Layer under Passive and Active Oxidation", *AIAA Aviation Forum*, 17-21 June 2019, Dallas, TX, AIAA 2019-3261.

3. Chen, S.Y. and Boyd, I.D., "A Chemical Equilibrium Analysis Approach to Oxidation and Nitridation of Silicon Carbide", *AIAA SciTech Forum*, 7-11 January 2019, San Diego, CA, AIAA 2019-0243.

4. Chen, S.Y., Boyd, I.D., Martin, N.C., and Fletcher, D.G., "Modeling of Gas-Phase Chemical Kinetics for Pyrolyzing Ablators", *AIAA Aviation Forum*, 25-29 June 2018, Atlanta, GA, AIAA 2018-3274.

5. Palmer, G.E., Coughlin, S., Chen, S.Y., and McGuire, K., "The Effect of Surface Catalycity on the Predicted Recession of TPS Materials", *AIAA SciTech Forum*, 8-12 January 2018, Kissimmee, FL, AIAA 2018-0496.

# APPENDIX A

# Chemical Kinetic Mechanisms

The finite-rate chemistry model in LeMANS uses a modified Arrhenius rate co-efficient in Eq. (A.1). The forward reaction parameters $C_f$, $\eta_f$, and $\Theta$ are provided by the chemical kinetics mechanisms. The backward rates are calculated using an equilibrium constant computed with Gibb's free energy, similar to Eq. (2.27).

$$k_f(T) = C_f T^{\eta_f} \exp\left(-\frac{\Theta}{T}\right) \tag{A.1}$$

## A.1  Johnston-Brandis Mechanism

This mechanism is taken from Johnston and Brandis [57], and is reproduced below in Table A.1. It involves 18 species and 34 reactions, describing $CO_2$-air chemistry at hypersonic-relevant conditions. This mechanism was validated against data from the Electric Arc Shock Tube (EAST) at NASA Ames [57].

Table A.1: Johnston-Brandis Chemical Kinetic Mechanism.

| No. | Reaction | $C_f$ $[\frac{cm^3}{mol\text{-}s}]$ | $\eta_f$ | $\Theta$ [K] | $T_c$ |
|---|---|---|---|---|---|
| 1 | $CO_2 + M \leftrightarrow CO + O + M$ | 6.90E+21 | -1.5 | 6.33E+04 | $\sqrt{T_{tr}T_{ve}}$ |
| | M = N, C, O | 1.38E+22 | -1.5 | 6.33E+04 | $\sqrt{T_{tr}T_{ve}}$ |
| | M = Ar | 6.90E+20 | -1.5 | 6.33E+04 | $\sqrt{T_{tr}T_{ve}}$ |
| 2 | $CO + M \leftrightarrow C + O + M$ | 1.20E+21 | -1 | 1.29E+05 | $\sqrt{T_{tr}T_{ve}}$ |
| | M = N, C, O | 1.80E+21 | -1 | 1.29E+05 | $\sqrt{T_{tr}T_{ve}}$ |
| | M = Ar | 1.20E+20 | -1 | 1.29E+05 | $\sqrt{T_{tr}T_{ve}}$ |
| 3 | $C_2 + M \leftrightarrow C + C + M$ | 4.50E+18 | -1 | 7.15E+04 | $\sqrt{T_{tr}T_{ve}}$ |
| 4 | $CN + M \leftrightarrow C + N + M$ | 6.00E+15 | -0.4 | 7.10E+04 | $\sqrt{T_{tr}T_{ve}}$ |
| 5 | $N_2 + M \leftrightarrow N + N + M$ | 7.00E+21 | -1.6 | 1.13E+05 | $\sqrt{T_{tr}T_{ve}}$ |
| | M = N, C, O | 3.00E+22 | -1.6 | 1.13E+05 | $\sqrt{T_{tr}T_{ve}}$ |
| | M = e | 6.00E+03 | 2.6 | 1.13E+05 | $T_{ve}$ |
| 6 | $NO + M \leftrightarrow N + O + M$ | 2.00E+15 | 0 | 7.55E+04 | $\sqrt{T_{tr}T_{ve}}$ |
| | M = N, C, O, NO, $CO_2$ | 4.40E+16 | 0 | 7.55E+04 | $\sqrt{T_{tr}T_{ve}}$ |
| 7 | $O_2 + M \leftrightarrow O + O + M$ | 2.00E+21 | -1.5 | 5.94E+04 | $\sqrt{T_{tr}T_{ve}}$ |
| | M = N, C, O | 1.00E+22 | -1.5 | 5.94E+04 | $\sqrt{T_{tr}T_{ve}}$ |
| 8 | $CO_2 + O \leftrightarrow O2 + CO$ | 2.71E+14 | 0 | 3.38E+04 | $T_{tr}$ |
| 9 | $CO + C \leftrightarrow C_2 + O$ | 2.40E+17 | -1 | 5.80E+04 | $T_{tr}$ |
| 10 | $CO + N \leftrightarrow CN + O$ | 1.00E+15 | 0 | 3.86E+04 | $T_{tr}$ |
| 11 | $CO + NO \leftrightarrow CO_2 + N$ | 3.00E+06 | 0.88 | 1.33E+04 | $T_{tr}$ |
| 12 | $CO + O \leftrightarrow O_2 + C$ | 3.90E+13 | -0.18 | 6.92E+04 | $T_{tr}$ |
| 13 | $C_2 + N_2 \leftrightarrow CN + CN$ | 1.50E+13 | 0 | 2.10E+04 | $T_{tr}$ |
| 14 | $CN + C \leftrightarrow C_2 + N$ | 3.00E+14 | 0 | 1.81E+04 | $T_{tr}$ |
| 15 | $CN + O \leftrightarrow NO + C$ | 1.60E+12 | 0.1 | 1.46E+04 | $T_{tr}$ |
| 16 | $N + CO \leftrightarrow NO + C$ | 1.10E+14 | 0.07 | 5.35E+04 | $T_{tr}$ |
| 17 | $N_2 + C \leftrightarrow CN + N$ | 1.10E+14 | -0.11 | 2.32E+04 | $T_{tr}$ |
| 18 | $N_2 + CO \leftrightarrow CN + NO$ | 1.20E+16 | -1.23 | 7.70E+04 | $T_{tr}$ |
| 19 | $N_2 + O \leftrightarrow NO + N$ | 6.00E+13 | 0.1 | 3.80E+04 | $T_{tr}$ |
| 20 | $O_2 + N \leftrightarrow NO + O$ | 2.49E+09 | 1.18 | 4.01E+03 | $T_{tr}$ |
| 21 | $C + O \leftrightarrow CO^+ + e$ | 8.80E+08 | 1 | 3.31E+04 | $T_{tr}$ |
| 22 | $C + e \leftrightarrow C^+ + e + e$ | 3.90E+33 | -3.78 | 1.31E+05 | $T_{ve}$ |
| 23 | $C^+ + CO \leftrightarrow CO^+ + C$ | 1.00E+13 | 0 | 3.14E+04 | $T_{tr}$ |
| 24 | $CO + e \leftrightarrow CO^+ + e + e$ | 4.50E+14 | 0.275 | 1.16E+05 | $T_{ve}$ |
| 25 | $N + O \leftrightarrow NO^+ + e$ | 5.30E+12 | 0 | 3.19E+04 | $T_{tr}$ |
| 26 | $NO^+ + C \leftrightarrow C^+ + NO$ | 1.00E+13 | 0 | 2.32E+04 | $T_{tr}$ |
| 27 | $NO^+ + N \leftrightarrow O^+ + N_2$ | 3.40E+13 | -1.08 | 1.28E+04 | $T_{tr}$ |
| 28 | $NO^+ + O \leftrightarrow O_2^+ + N$ | 7.20E+12 | 0.29 | 4.86E+04 | $T_{tr}$ |
| 29 | $NO^+ + O_2 \leftrightarrow NO + O_2^+$ | 2.40E+13 | 0.41 | 3.26E+04 | $T_{tr}$ |
| 30 | $O + O \leftrightarrow O_2^+ + e$ | 7.10E+02 | 2.7 | 8.06E+04 | $T_{tr}$ |
| 31 | $O + e \leftrightarrow O^+ + e + e$ | 3.90E+33 | -3.78 | 1.59E+05 | $T_{ve}$ |
| 32 | $O_2 + C^+ \leftrightarrow O_2^+ + C$ | 1.00E+13 | 0 | 9.40E+03 | $T_{tr}$ |
| 33 | $O_2^+ + O \leftrightarrow O^+ + O_2$ | 4.00E+12 | -0.09 | 1.80E+04 | $T_{tr}$ |
| 34 | $O_2 + e \leftrightarrow O_2^+ + e + e$ | 2.19E+10 | 1.16 | 1.30E+05 | $T_{ve}$ |

## A.2   SiC Oxidation Mechanism

Rates for reactions between SiC oxidation products and air are summarized in Table A.2. These are aggregated from a variety of sources listed in the Table. Rates (38) - (41) are obtained from experiments performed between 1000 K and 3000 K, so are relevant for this work. However, (42) is obtained from experiments performed at *very low* temperatures ($< 300$ K), so its validity at higher temperatures is questionable.

Table A.2: Chemical Kinetic Rates for Ar, Si, SiO, and SiN

| No. | Reaction | $C_f \ [\frac{cm^3}{mol\text{-}s}]$ | $\eta_f$ | $\Theta$ [K] | $T_c$ | Ref. |
|---|---|---|---|---|---|---|
| 35 | Ar + e $\leftrightarrow$ Ar$^+$+ e + e | $2.30{\times}10^{34}$ | -3.60 | 182,900 | $T_{ve}$ | Park [58] |
| 36 | Si + e $\leftrightarrow$ Si$^+$+ e + e | $2.50{\times}10^{34}$ | -3.82 | 94,600 | $T_{ve}$ | Johnston [133] |
| 37 | SiO + M $\leftrightarrow$ Si+ O + M | $4.40{\times}10^{14}$ | 0.0 | 95,600 | $T_{tr}$ | Johnston [133] |
| 38 | Si + CO $\leftrightarrow$ SiO + C | $7.80{\times}10^{14}$ | 0.0 | 34,510 | $T_{tr}$ | Mick [138] |
| 39 | Si + CO$_2$ $\leftrightarrow$ SiO + CO | $6.00{\times}10^{14}$ | 0.0 | 9420 | $T_{tr}$ | Mick [138] |
| 40 | SiN + O $\leftrightarrow$ SiO + N | $4.00{\times}10^{13}$ | 0.0 | 0.0 | $T_{tr}$ | Mick [139] |
| 41 | Si + NO $\leftrightarrow$ SiO + N | $3.20{\times}10^{13}$ | 0.0 | 1775 | $T_{tr}$ | Mick [139] |
| 42 | Si + O$_2$ $\leftrightarrow$ SiO + O | $1.04{\times}10^{14}$ | -0.53 | 17.0 | $T_{tr}$ | Le Picard [140] |

# APPENDIX B

# NH Radiative Emission Models

The development and validation of a radiative emission model for the NH A-X $(A^3\Pi_i - X^3\Pi^-)$ band in NEQAIR [40] is described here, which is relevant between 300–400 nm.

## B.1 Boltzmann Model

The molecular constants in Table B.1 come from a combination of NIST [98], Owono [141], and Ram and Bernath [142]. The data from NIST [98] was updated with values from Owono [141] and/or Bernath [142] where available. Some parameters were manually fit from the vibrationally-resolved data in the Ram and Bernath paper [142], and these resulted in the most accurate line shapes for the NH A-X band.

The Franck-Condon factors and transition moments in Table B.2 were taken from Owono [143]. With the *r-centroid* approximation, the transition moments $R_e(r)$ can be fit to a linear form with $k = 0.62$ and $\rho = 0.60$ $\mathring{A}^{-1}$ [143]:

$$R_e(r) = k(1 - \rho r) \tag{B.1}$$

Table B.1: Diatomic Constants for NH

| Symbol | g | $T_e$ | $r_e$ [Å] | $D_0$ | $A$ (spin-orbit) | $\lambda$ |
|--------|---|-------|-----------|-------|------------------|-----------|
| $X^3\Sigma^-$ | 3 | 0 | 1.04 | 2.80E+04 | 0 | 0 |
| $a^1\Delta$ | 2 | 1.26E+04 | 1.03 | 3.10E+04 | 0 | 2.00 |
| $b^1\Sigma^+$ | 1 | 2.12E+04 | 1.04 | 3.21E+04 | 0 | 0 |
| $A^3\Pi_i$ | 6 | 2.98E+04 | 1.04 | 1.51E+04 | -3.47E+01 | 1.00 |
| $c^1\Pi$ | 2 | 4.37E+04 | 1.11 | 4.08E+03 | 0 | 1.00 |
| | $\omega_e$ | $\omega_e x_e$ | $\omega_e y_e$ | $B_e$ | $\alpha_e$ | $D_e$ |
| | 3.28E+03 | 78.4 | 0 | 16.7 | 6.58E-01 | 1.71E-03 |
| | 3.19E+03 | 68.0 | 0 | 16.4 | 6.60E-01 | 1.62E-03 |
| | 3.35E+03 | 74.2 | 0.7 | 16.7 | 5.91E-01 | 1.60E-03 |
| | 3.23E+03 | 98.6 | 0 | 16.7 | 7.61E-01 | 1.78E-03 |
| | 2.12E+03 | 5.00 | 0 | 14.5 | 5.93E-01 | 2.20E-03 |

$^*$ All units in $cm^{-1}$ unless noted.

In Table B.2, the Franck-Condon factors are set to unity for convenience while preserving the overall quantity $q_{v'v''}^{1/2} R_e(\bar{r}_{v'v''})$ needed in the Einstein coefficient calculation in Eq. 3.4.

Table B.2: Franck-Condon Factors and Transition Moments for NH $A^3\Pi_i$–$X^3\Pi^-$

| $v'$ | $v''$ | $q_{v'v''}$ | $R_e(\bar{r}_{v'v'})$ |
|------|-------|-------------|-----------------------|
| 0.0 | 0.0 | 1.000E+00 | 2.223E-01 |
| 1.0 | 0.0 | 1.000E+00 | 1.578E-02 |
| 1.0 | 1.0 | 1.000E+00 | 2.082E-01 |
| 2.0 | 0.0 | 1.000E+00 | 2.304E-03 |
| 2.0 | 1.0 | 1.000E+00 | 2.077E-02 |
| 2.0 | 2.0 | 1.000E+00 | 1.926E-01 |

## B.1.1 Validation

Simulations are performed using the CFD-radiation framework with LeMANS and NEQAIR [40] following the procedure described in Chapter 3. The experimental conditions in Fig. B.1 utilize the Dilute $N_2$ plasma composition with 282 sccm $H_2$

injection, and spectra measured 2.0 mm from the probe.

Table B.3: Experimental ICP Exit Conditions (Freestream)

| Plasma | Gas [SLPM] | $T_{exit}$ [K] | $T_{90mm}$ [K] | $h_{exit}$ [MJ/kg] | $Y_{Ar}$ | $Y_{N_2}$ | $Y_{O_2}$ |
|--------|-----------|----------------|----------------|--------------------|----------|-----------|-----------|
| Dilute $N_2$ | 40 Ar + 2 $N_2$ | 6625 | 6584 | 4.96 | 95.3% | 4.3% | 0.4% |



(a) Overall spectra

(b) NH A-X band
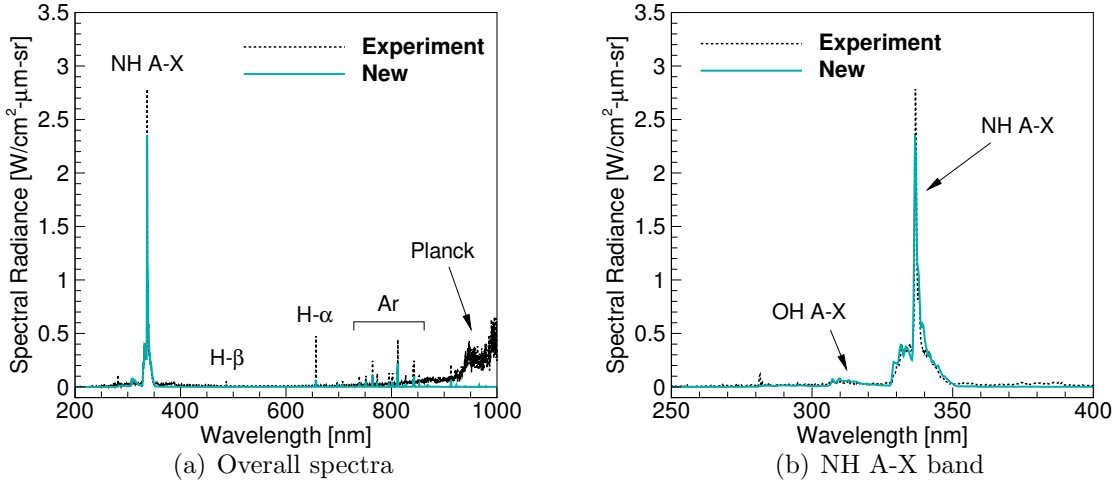
Figure B.1: Validation of NH A-X Boltzmann model in NEQAIR [40].

## B.2    Non-Boltzmann Model

Similar to the Boltzmann model, Franck-Condon factors come from Owono [143] in Table B.2. Electron-impact excitation and dissociation cross-sections (used to compute effective rates) for the A-X transition were estimated from Gupta et al. [144]. The NH dissociation rate from Gokcen was used [145]. Predissociation rates were averaged from Patel-Misra [146], and this rate was tuned to match data from the Electric Arc Shock Tube (EAST) facility at NASA Ames.

# BIBLIOGRAPHY

[1] Anderson Jr, J. D., *Hypersonic and high-temperature gas dynamics*, American Institute of Aeronautics and Astronautics, 2006.

[2] NASA Glenn Research Center, "Speed Regimes: Hypersonic Re-Entry," 2020, https://www.grc.nasa.gov/WWW/BGH/hihyper.html, Last accessed on 2020-03-31.

[3] Fay, J. A. and Riddell, F. R., "Theory of stagnation point heat transfer in dissociated air," *Journal of the Aerospace Sciences*, Vol. 25, No. 2, 1958, pp. 73–85.

[4] Sutton, K. and Graves Jr, R. A., *A General Stagnation-Point Convective-Heating Equation for Arbitrary Gas Mixtures*, NASA TR R-376, NASA Langley Research Center, Hampton, VA, 1971.

[5] Wright, M., "Aerothermodynamic and Thermal Protection System Aspects of Entry System Design," Presented at Thermal and Fluids Analysis Workshop, Pasadena, CA, 2012.

[6] Seiferth, R. W., *Ablative Heat Shield Design for Space Shuttle*, NASA CR-132282, Martin Marietta Corporation, Denver, CO, 1973.

[7] Johnson, S. M., "Thermal Protection Materials: Development, Characterization and Evaluation," Presented at HiTemp2012, Munich, Germany, 2012.

[8] Martin, A. and Boyd, I. D., "Modeling of Heat Transfer Attenuation by Ablative Gases During the Stardust Reentry," *Journal of Thermophysics and Heat Transfer*, Vol. 29, No. 3, 2015, pp. 450–466.

[9] Park, C., Jaffe, R. L., and Partridge, H., "Chemical-Kinetic Parameters of Hyperbolic Earth Entry," *Journal of Thermophysics and Heat Transfer*, Vol. 15, No. 1, 2001, pp. 76–90.

[10] Poerschke, D. L., Novak, M. D., Abdul-Jabbar, N., Krämer, S., and Levi, C. G., "Selective active oxidation in hafnium boride-silicon carbide composites above 2000°C," *Journal of the European Ceramic Society*, Vol. 36, No. 15, 2016, pp. 3697–3707.

[11] Fahrenholtz, W. G., Wuchina, E. J., Lee, W. E., and Zhou, Y., *Ultra-high temperature ceramics: materials for extreme environment applications*, John Wiley & Sons, 2014.

[12] Boyd, I. D. and Schwartzentruber, T. E., *Nonequilibrium Gas Dynamics and Molecular Simulation*, Cambridge University Press, Cambridge, United Kingdom, 2017.

[13] Park, C., "Assessment of Two-Temperature Kinetic Model for Dissociation and Weakly Ionizing Nitrogen," *Journal of Thermophysics and Heat Transfer*, Vol. 3, No. 3, 1989, pp. 233–244.

[14] Bard, A. J., "Calculation of Equilibrium Constants from Free Energy Data," *Chemical Equilibrium*, edited by S. A. Rice, Harper & Row, New York, NY, 1966, pp. 182–185.

[15] Chase Jr, M. W., *NIST-JANAF Thermochemical Tables*, American Institute of Physics, New York, NY, 4th ed., 1998.

[16] McBride, B. J., Zehe, M. J., and Gordon, S., *NASA Glenn Coefficients for Calculating Thermodynamic Properties of Individual Species*, NASA TP-2002-211556, NASA Glenn Research Center, Cleveland, Ohio, 2002.

[17] Powars, C. A. and Kendall, R. M., *Aerotherm Chemical Equilibrium (ACE) Computer Program*, User Manual, Aerotherm Corporation, Mountain View, CA, 1969.

[18] Gordon, S. and McBride, B., *Computer Program for Calculation of Complex Chemical Equilibrium Compositions and Applications I. Analysis*, NASA RP-1311, NASA Glenn Research Center, Cleveland, OH, 1994.

[19] McBride, B. and Gordon, S., *Computer Program for Calculation of Complex Chemical Equilibrium Compositions and Applications II. User Manual and Program Description*, NASA RP-1311, NASA Glenn Research Center, Cleveland, OH, 1996.

[20] Goodwin, D. G., Speth, R. L., Moffat, H. K., and Weber, B. W., "Cantera: An Object-oriented Software Toolkit for Chemical Kinetics, Thermodynamics, and Transport Processes," https://www.cantera.org, 2018, Version 2.4.0.

[21] Scalabrin, L. C. and Boyd, I. D., "Numerical Simulations of the FIRE-II Convective and Radiative Heating Rates," AIAA Paper 2007-4044, 2007.

[22] Martin, A., Scalabrin, L. C., and Boyd, I. D., "High Performance Modeling of Atmospheric Re-entry Vehicles," *Journal of Physics: Conference Series*, Vol. 341, No. 1, 2012, pp. 1–12.

[23] Farbar, E., Boyd, I. D., and Martin, A., "Numerical Prediction of Hypersonic Flowfields Including Effects of Electron Translational Nonequilibrium," *Journal of Thermophysics and Heat Transfer*, Vol. 27, No. 4, 2013, pp. 593–606.

[24] Scalabrin, L. C., *Numerical Simulation of Weakly Ionized Hypersonic Flow Over Reentry Capsules*, Ph.D. thesis, University of Michigan, Ann Arbor, MI, 2007.

[25] Karypis, G. and Kumar, V., "METIS: A Software Package for Partition- ing Unstructured Graphs, Partitioning Meshes, and Computing Fill-Reducing Orderings of Sparse Matrices," University of Minnesota, MN, 1998.

[26] Millikan, R. C. and White, D. R., "Systematics of vibrational relaxation," *The Journal of Chemical Physics*, Vol. 39, No. 12, 1963, pp. 3209–3213.

[27] Chaudhry, R. S., Bender, J. D., Schwartzentruber, T. E., and Candler, G. V., "Quasiclassical Trajectory Analysis of Nitrogen for High-Temperature Chemical Kinetics," *Journal of Thermophysics and Heat Transfer*, Vol. 32, No. 4, 2018, pp. 833–845.

[28] Alkandry, H., Boyd, I. D., and Martin, A., "Comparison of Transport Properties Models for Flowfield Simulations of Ablative Heat Shields," *Journal of Thermophysics and Heat Transfer*, Vol. 28, No. 4, 2014, pp. 569–582.

[29] Bartlett, E. P., Kendall, R. M., and Rindal, R. A., *An Analysis of the Coupled Chemically Reacting Boundary Layer and Charring Ablator. Part IV; a Unified Approximation for Mixture Transport Properties for Multicomponent Boundary Layer Applications*, NASA CR-1063, Itek Corporation, Vidya Division, 1968.

[30] Anna, A. and Boyd, I. D., "Numerical Analysis of Surface Chemistry in High-Enthalpy Flows," *Journal of Thermophysics and Heat Transfer*, Vol. 29, No. 4, 2015, pp. 653–670.

[31] Martin, A. and Boyd, I. D., "Simulation of Pyrolysis Gas Within a Thermal Protection System," AIAA Paper 2008-3805, 2008.

[32] Cross, P. G., *Conjugate Analysis of Two-Dimensional Ablation and Pyrolysis in Rocket Nozzles*, Ph.D. thesis, University of Michigan, Ann Arbor, MI, 2017.

[33] Martin, A., Zhang, H., and Tagavi, K. A., "An introduction to the derivation of surface balance equations without the excruciating pain," *International Journal of Heat and Mass Transfer*, Vol. 115, 2017, pp. 992–999.

[34] Kays, W. M., Crawford, M. E., and Weigand, B., *Convective Heat and Mass Transfer*, McGraw-Hill, New York, NY, 4th ed., 2005.

[35] Chen, S. Y., Boyd, I. D., Martin, N. C., and Fletcher, D. G., "Modeling of Gas-Phase Chemical Kinetics for Pyrolyzing Ablators," AIAA Paper 2018-3274, 2018.

[36] Chen, S. Y., Boyd, I. D., Martin, N. C., and Fletcher, D. G., "Modeling of Emission Spectra in Nonequilibrium Plasmas for Testing Pyrolyzing Ablators," *Journal of Thermophysics and Heat Transfer*, Vol. 33, No. 4, 2019, pp. 907–916.

[37] Helber, B., Turchi, A., Scoggins, J. B., Hubin, A., and Magin, T. E., "Experimental investigation of ablation and pyrolysis processes of carbon-phenolic ablators in atmospheric entry plasmas," *International Journal of Heat and Mass Transfer*, Vol. 100, 2016, pp. 810–824.

[38] Owano, T. G., Gordon, M. H., and Kruger, C. H., "Measurements of the radiation source strength in argon at temperatures between 5,000 and 10,000 K," *Physics of Fluids B*, Vol. 2, No. 12, 1990, pp. 3184–3190.

[39] Brandis, A. M., Morgan, R. G., and McIntyre, T. J., "Analysis of Nonequilibrium CN Radiation Encountered During Titan Atmospheric Entry," *Journal of Thermophysics and Heat Transfer*, Vol. 25, No. 4, 2011, pp. 493–499.

[40] Brandis, A. M. and Cruden, B. A., *Nonequilibrium and Equilibrium Radiative Transport Spectra Program*, NASA TR-20150000832, NASA Ames Research Center, Moffett Field, CA, 2014.

[41] Martin, N. C., Meyers, J. M., Fletcher, D. G., Dang, D., and Boyd, I. D., "Investigation of Pyrolyzing Ablators Using a Gas Injection Probe," AIAA Paper 2017-0437, 2017.

[42] Kolesnikov, A. F., "The concept of local simulation for stagnation point heat transfer in hypersonic flows - Applications and validation," AIAA Paper 2000-2515, 2000.

[43] Anna, A., *Numerical Modeling of Surface Chemistry Processes for Hypersonic Entry Environments*, Ph.D. thesis, University of Michigan, Ann Arbor, MI, 2013.

[44] Tillson, C. C., Uhl, J., Meyers, J. M., and Fletcher, D. G., "Investigation of Pyrolysis Gas Chemistry in an Inductively Coupled Plasma Facility," AIAA Paper 2016-3235, 2016.

[45] Tillson, C. C., *Investigation of Pyrolysis Gas Chemistry in an Inductively Coupled Plasma Facility*, Graduate College Dissertations and Theses 692, University of Vermont, Burlington, VT, 2017, pp. 46–62.

[46] Kruger, C. H., Owano, T., Gordon, M., and Laux, C., "Nonequilibrium effects in thermal plasmas," *Pure and Applied Chemistry*, Vol. 64, No. 5, 1992, pp. 607–613.

[47] Gordon, M. H. and Kruger, C. H., "Temperature and Density Measurements in a Recombining Argon Plasma with Diluent," *Plasma Chemistry and Plasma Processing*, Vol. 13, No. 3, 1993, pp. 365–378.

[48] Gordon, M. H. and Kruger, C. H., "Nonequilibrium effects of diluent addition in a recombining argon plasma effects of diluent addition in a recombining argon plasma," *Physics of Fluids B*, Vol. 5, No. 3, 1993, pp. 1014–1023.

[49] Park, C., "Rate Parameters for Electronic Excitation of Diatomic Molecules I. Electron-Impact Processes," AIAA Paper 2008-1206, 2008.

[50] Park, C., "Rate Parameters for Electronic Excitation of Diatomic Molecules II. Heavy Particle-Impact Processes," AIAA Paper 2008-1446, 2008.

[51] Laux, C. O., *Optical diagnostics and radiative emission of air plasmas*, Ph.D. thesis, Stanford University, Stanford, CA, 1993.

[52] Gilmore, F. R., Laher, R. R., and Espy, P. J., "Franck–Condon factors, r-centroids, electronic transition moments, and Einstein coefficients for many nitrogen and oxygen band systems," *Journal of Physical and Chemical Reference Data*, Vol. 21, No. 5, 1992, pp. 1005–1107.

[53] Whiting, E. E., Park, C., Liu, Y., Arnold, J. O., and Paterson, J. A., *NEQAIR96, Nonequilibrium and Equilibrium Radiative Transport Spectra Program: User Manual*, NASA RP-1389, NASA Ames Research Center, Moffett Field, CA, 1996.

[54] Brandis, A. M., "Investigation of Nonequilibrium Radiation for Mars Entry," AIAA Paper 2013-1055, 2013.

[55] Hyun, S.-Y., Park, C., and Chang, K.-S., "Rate parameters for electronic excitation of diatomic molecules: CN radiation," *Journal of thermophysics and heat transfer*, Vol. 23, No. 2, 2009, pp. 226–235.

[56] Tillson, C. C., Meyers, J. M., and Fletcher, D. G., "Spectrally Resolved Emission Measurements from Pyrolyzing Ablators in an Inductively Coupled Plasma Facility," AIAA Paper 2017-0435, 2017.

[57] Johnston, C. O. and Brandis, A. M., "Modeling of nonequilibrium CO Fourth-Positive and CN Violet emission in $CO_2$-$N_2$ gases," *Journal of Quantitative Spectroscopy and Radiative Transfer*, Vol. 149, 2014, pp. 303–317.

[58] Park, C. and Lee, S. H., "Validation of Multi-Temperature Nozzle Flow Code," *Journal of Thermophysics and Heat Transfer*, Vol. 9, No. 1, 1995, pp. 9–16.

[59] Martin, A., Cozmuta, I., Wright, M. J., and Boyd, I. D., "Kinetic Rates of Gas-Phase Chemistry of Phenolic-Based Carbon Ablator in Atmospheric Air," *Journal of Thermophysics and Heat Transfer*, Vol. 29, No. 2, 2015, pp. 222–240.

[60] Suzuki, K., Kubota, H., Fujita, K., and Abe, T., "Chemical Non-Equilibrium Ablation Analysis of MUSES-C Super-Orbital Reentry Capsule," AIAA Paper 1997-2481, 1997.

[61] Olynick, D. R., Chen, Y. K., and Tauber, M. E., "Aerothermodynamics of the Stardust Sample Return Capsule," *Journal of Spacecraft and Rockets*, 1999, pp. 442–462.

[62] Bonnie J. McBride and Sanford Gordon, "NASA Chemical Equilibrium with Applications (CEA)," 2020, https://cearun.grc.nasa.gov/, Last accessed on 2020-01-21.

[63] Thompson, R. A. and Gnoffo, P. A., "Implementation of a Blowing Boundary Condition in the LAURA Code," AIAA Paper 2008-1243, 2008.

[64] Park, C., Howe, J. T., Jaffe, R. L., and Candler, G. V., "A Review of Chemical-Kinetic Problems of Future NASA Missions, II: Mars Entries," *Journal of Thermophysics and Heat Transfer*, Vol. 8, No. 1, 1994, pp. 9–23.

[65] Cruden, B. A. and Brandis, A. M., "Characterization of CO Thermochemistry in Incident Shockwaves," AIAA Paper 2018-3768, 2018.

[66] Hanson, R. K., "Shock-tube study of carbon monoxide dissociation kinetics," *Journal of Chemical Physics*, Vol. 60, No. 12, 1974, pp. 4970–4976.

[67] Jaffe, R. L., "Vibrational and Rotational Excitation and Dissociation of $CO_2$ Reexamined," AIAA Paper 2011-447, 2011.

[68] Jacobson, N. S. and Myers, D. L., "Active oxidation of SiC," *Oxidation of Metals*, Vol. 75, 2011, pp. 1–25.

[69] Hinze, J. W. and Graham, H. C., "The Active Oxidation of Si and SiC in the Viscous Gas-Flow Regime," *Journal of the Electrochemical Society*, Vol. 123, No. 7, 1976, pp. 1066–1073.

[70] Gasch, M., Ellerby, D., Irby, E., Beckman, S., Gusman, M., and Johnson, S., "Processing, properties and arc jet oxidation of hafnium diboride/silicon carbide ultra high temperature ceramics," *Journal of Materials Science*, Vol. 39, No. 19, 2007, pp. 5925–5937.

[71] Heuer, A. H. and Lou, V. L. K., "Volatility Diagrams for Silica, Silicon Nitride, and Silicon Carbide and Their Application to High Temperature Decomposition and Oxidation," *Journal of the American Ceramic Society*, Vol. 73, No. 10, 1990, pp. 2789–2803.

[72] Wang, J., Zhang, L., Zeng, Q., Vignoles, G. L., and Guette, A., "Theoretical investigation for the active-to-passive transition in the oxidation of silicon carbide," *Journal of the American Ceramic Society*, Vol. 91, No. 5, 2008, pp. 1665–1673.

[73] Panerai, F., Helber, B., Chazot, O., and Balat-Pichelin, M., "Surface temperature jump beyond active oxidation of carbon/silicon carbide composites in extreme aerothermal conditions," *Carbon*, Vol. 71, 2014, pp. 102–119.

[74] Hald, H., "Operational limits for reusable space transportation systems due to physical boundaries of C/SiC materials," *Aerospace Science and Technology*, Vol. 7, No. 7, 2003, pp. 551–559.

[75] Chen, S. Y. and Boyd, I. D., "A Chemical Equilibrium Analysis Approach to Oxidation and Nitridation of Silicon Carbide," AIAA Paper 2019-0243, 2019.

[76] Chen, S. Y. and Boyd, I. D., "Chemical equilibrium analysis of silicon carbide oxidation in oxygen and air," *Journal of the American Ceramic Society*, Vol. 102, 2019, pp. 4272–4284.

[77] Wagner, C., "Passivity during the oxidation of silicon at elevated temperatures," *Journal of Applied Physics*, Vol. 29, No. 9, 1958, pp. 1295–1297.

[78] Jacobson, N., Harder, B., and Myers, D., "Oxidation transitions for SiC part I. Active-to-passive transitions," *Journal of the American Ceramic Society*, Vol. 96, No. 3, 2013, pp. 838–844.

[79] Balat, M. J., "Determination of the Active-to-Passive Transition in the Oxidation of Silicon Carbide in Standard and Microwave-Excited Air," *Journal of the European Ceramic Society*, Vol. 16, No. 1, 1996, pp. 55–62.

[80] Gulbransen, E. A., Andrew, K. F., and Brassart, F. A., "The Oxidation of Silicon Carbide at 1150° C to 1400° C and at $9 \times 10^{-3}$ to $5 \times 10^{-1}$ Torr Oxygen Pressure," *Journal of the Electrochemical Society*, Vol. 113, No. 12, 1966, pp. 1311–1314.

[81] Harder, B., Jacobson, N., and Myers, D., "Oxidation transitions for SiC part II. Passive-to-active transitions," *Journal of the American Ceramic Society*, Vol. 96, No. 2, 2013, pp. 606–612.

[82] Ogura, Y. and Morimoto, T., "Mass Spectrometric Study of Oxidation of SiC in Low-Pressure Oxygen," *Journal of The Electrochemical Society*, Vol. 149, No. 4, 2002, pp. 47–52.

[83] Raj, R. and Terauds, K., "Bubble nucleation during oxidation of SiC," *Journal of the American Ceramic Society*, Vol. 98, No. 8, 2015, pp. 2579–2586.

[84] Charpentier, L., Balat-Pichelin, M., and Audubert, F., "High temperature oxidation of SiC under helium with low-pressure oxygen-Part 1: Sintered $\alpha$-SiC," *Journal of the European Ceramic Society*, Vol. 30, No. 12, 2010, pp. 2653–2660.

[85] Charpentier, L., Balat-Pichelin, M., Glenat, H., Beche, E., Laborde, E., and Audubert, F., "High temperature oxidation of SiC under helium with low-pressure oxygen. Part 2: CVD $\beta$-SiC," *Journal of the European Ceramic Society*, Vol. 30, No. 12, 2010, pp. 2661–2670.

[86] Dawi, K., Balat-Pichelin, M., Charpentier, L., and Audubert, F., "High temperature oxidation of SiC under helium with low-pressure oxygen. Part 3: $\beta$-SiC-SiC/PyC/SiC," *Journal of the European Ceramic Society*, Vol. 32, No. 2, 2012, pp. 485–494.

[87] Narushima, T., Iguchi, Y., and Hirai, T., "High-Temperature Active Oxidation of Chemically Vapor-Deposited Silicon Carbide in an Ar-$O_2$ Atmosphere," *Journal of the American Ceramic Society*, Vol. 74, No. 10, 1991, pp. 2583–2586.

[88] Keys, L. H., "The Oxidation of Silicon Carbide," *Properties of High Temperature Alloys With an Emphasis on Environmental Effects*, edited by Z. A. Foroulis and F. S. Pettit, Electrochemical Society, Princeton, NJ, 1977, pp. 681–697.

[89] Rosner, D. E. and Allendorf, H. D., "High temperature kinetics of the oxidation and nitridation of pyrolytic silicon carbide in dissociated gases," *Journal of Physical Chemistry*, Vol. 74, No. 9, 1970, pp. 1829–1839.

[90] Jacobson, N. S., Harder, B. J., and Myers, D. L., "Hysteresis in the Active Oxidation of SiC," *ECS Transactions*, Vol. 41, No. 42, 2012, pp. 105–114.

[91] Vaughn, W. L. and Maahs, H. G., "Active-to-Passive Transition in the Oxidation of Silicon Carbide and Silicon Nitride in Air," *Journal of the American Ceramic Society*, Vol. 73, No. 6, 1990, pp. 1540–1543.

[92] Nickel, K. G., Hoffmann, M. J., Greil, P., and Petzow, G., "Thermodynamic calculations for the formation of SiC-whisker-reinforced $Si_3N_4$ ceramics," *Advanced Ceramic Materials*, Vol. 3, No. 6, 1988, pp. 557–562.

[93] Panerai, F., Helber, B., Chazot, O., Nickel, K. G., and Balat-Pichelin, M., "Aerothermal response of ceramic matrix composites to nitrogen plasma at temperatures above 2000 K," *Aerospace Science and Technology*, Vol. 39, 2014, pp. 1–5.

[94] Muehlhoff, L., Choyke, W. J., Bozack, M. J., and Yates, J. T., "Comparative electron spectroscopic studies of surface segregation on SiC(0001) and SiC(000$\bar{1}$," *Journal of Applied Physics*, Vol. 60, No. 8, 1986, pp. 2842–2853.

[95] Rosner, D. E. and Allendorf, H. D., "Nitrogen as an Ablative Reactant in Dissociated Air," *AIAA Journal*, Vol. 8, No. 1, 1970, pp. 166–168.

[96] Marschall, J., Pejakovic, D., Fahrenholtz, W. G., Hilmas, G. E., Panerai, F., and Chazot, O., "Temperature jump phenomenon during plasmatron testing of $ZrB_2$-SiC ultrahigh-temperature ceramics," *Journal of Thermophysics and Heat Transfer*, Vol. 26, No. 4, 2012, pp. 559–572.

[97] Chen, S. Y. and Boyd, I. D., "Analysis of the Silicon Carbide Boundary Layer under Passive and Active Oxidation," AIAA Paper 2019-3261, 2019.

[98] NIST, "NIST Chemistry WebBook," 2020, https://webbook.nist.gov/, Last accessed on 2020-01-21.

[99] Hash, D., Olejniczak, J., Wright, M., Prabhu, D., Pulsonetti, M., Hollis, B., Gnoffo, P., Barnhardt, M., Nompelis, I., and Candler, G., "FIRE II Calculations for Hypersonic Nonequilibrium Aerothermodynamics Code Verification: DPLR, LAURA, and US3D," AIAA Paper 2007-605, 2007.

[100] Panerai, F. and Chazot, O., "Characterization of gas/surface interactions for ceramic matrix composites in high enthalpy, low pressure air flow," *Materials Chemistry and Physics*, Vol. 134, No. 2-3, 2012, pp. 597–607.

[101] Davide, A., L. S. S. C. and Balat-Pichelin, M., "Emissivity and Catalycity Measurements on SiC-coated Carbon Fiber Reinforced Silicon Carbide Composite [J]," *Journal of the European Ceramic Society*, Vol. 29, No. 10, 2009, pp. 2045–2051.

[102] Purić, J., Djeniže, S., Labat, J., and Ćirković, L., "Stark broadening parameters of Si I, Si II and Si III lines," *Zeitschrift für Physik*, Vol. 267, No. 1, 1974, pp. 71–75.

[103] Shugart, K. and Opila, E., "SiC depletion in $ZrB_2$-30 vol% SiC at ultrahigh temperatures," *Journal of the American Ceramic Society*, Vol. 98, No. 5, 2015, pp. 1673–1683.

[104] Marschall, J., Pejakovic, D. A., Fahrenholtz, W. G., Hilmas, G. E., Zhu, S., Ridge, J., Fletcher, D. G., Asma, C. O., and Thoemel, J., "Oxidation of $ZrB_2$-SiC Ultrahigh-Temperature Ceramic Composites in Dissociated Air," *Journal of Thermophysics and Heat Transfer*, Vol. 23, No. 2, 2009, pp. 267–278.

[105] Kubota, Y., Tanaka, H., Arai, Y., Inoue, R., Kogo, Y., and Goto, K., "Oxidation behavior of $ZrB_2$-SiC-ZrC at 1700 °C," *Journal of the European Ceramic Society*, Vol. 37, No. 4, 2017, pp. 1187–1194.

[106] Chen, S. Y. and Boyd, I. D., "A thermodynamic meso-scale model for oxidation of $ZrB_2$-SiC," AIAA Paper 2020-0399, 2020.

[107] Parthasarathy, T. A., Rapp, R. A., Opeka, M., and Kerans, R. J., "A model for the oxidation of $ZrB_2$, $HfB_2$ and $TiB_2$," *Acta Materialia*, Vol. 55, No. 17, 2007, pp. 5999–6010.

[108] Parthasarathy, T. A., Rapp, R. A., Opeka, M., and Kerans, R. J., "Effects of phase change and oxygen permeability in oxide scales on oxidation kinetics of $ZrB_2$ and $HfB_2$," *Journal of the American Ceramic Society*, Vol. 92, No. 5, 2009, pp. 1079–1086.

[109] Parthasarathy, T. A., Rapp, R. A., Opeka, M., and Cinibulk, M. K., "Modeling oxidation kinetics of SiC-containing refractory diborides," *Journal of the American Ceramic Society*, Vol. 95, No. 1, 2012, pp. 338–349.

[110] Fahrenholtz, W. G., "Thermodynamic analysis of $ZrB_2$–SiC oxidation: formation of a SiC-depleted region," *Journal of the American Ceramic Society*, Vol. 90, No. 1, 2007, pp. 143–148.

[111] Gasch, M. and Johnson, S., "Physical characterization and arcjet oxidation of hafnium-based ultra high temperature ceramics fabricated by hot pressing and field-assisted sintering," *Journal of the European Ceramic Society*, Vol. 30, No. 11, 2010, pp. 2337–2344.

[112] Fahrenholtz, W. G., "The $ZrB_2$ volatility diagram," *Journal of the American Ceramic Society*, Vol. 88, No. 12, 2005, pp. 3509–3512.

[113] Amar, A. J., *Modeling of one-dimensional ablation with porous flow using finite control volume procedure*, Master's thesis, North Carolina State University, Raleigh, NC, 2006.

[114] Wiebenga, J. E., *High-Fidelity Material Response Modeling as Part of an Aerothermoelastic Framework for Hypersonic Flows*, Ph.D. thesis, University of Michigan, Ann Arbor, MI, 2014.

[115] Taylor, D., "Thermal expansion data. II: Binary oxides with the fluorite and rutile structures, $MO_2$, and the antifluorite structure, $M_2O$," *Transactions and journal of the British Ceramic Society*, Vol. 83, No. 2, 1984, pp. 32–37.

[116] Tripp, W. C. and Graham, H. C., "Thermogravimetric Study of the Oxidation of $ZrB_2$ in the Temperature Range of 800 to 1500 C," *Journal of the Electrochemical Society*, Vol. 118, No. 7, 1971, pp. 1195–1199.

[117] Mallik, M., Ray, K. K., and Mitra, R., "Oxidation behavior of hot pressed $ZrB_2$-SiC and $HfB_2$-SiC composites," *Journal of the European Ceramic Society*, Vol. 31, No. 1-2, 2011, pp. 199–215.

[118] Berkowitz-Mattuck, J. B., "High-Temperature Oxidation III. Zirconium and Hafnium Diborides," *Journal of the Electrochemical Society*, Vol. 113, No. 9, 1966, pp. 908–914.

[119] Levine, S. R., Opila, E. J., Halbig, M. C., Kiser, J. D., Singh, M., and Salem, J. A., "Evaluation of Ultra-High Temperature Ceramics for Aeropropulsion Use," *Journal of the European Ceramic Society*, Vol. 22, 2002, pp. 2757–2767.

[120] Wang, M., Wang, C. A., Yu, L., Huang, Y., and Zhang, Z., "Oxidation Behavior of SiC Platelet-Reinforced $ZrB_2$ Ceramic Matrix Composites," *International Journal of Applied Ceramic Technology*, 2011, pp. 908–914.

[121] Tripp, W. C., Davis, H. H., and Graham, H. C., "Effect of an SiC addition on the oxidation of $ZrB_2$," *American Ceramic Society Bulletin*, Vol. 52, No. 8, 1973, pp. 612–616.

[122] Monteverde, F., Savino, R., and De Stefano Fumo, M., "Dynamic oxidation of ultra-high temperature $ZrB_2$-SiC under high enthalpy supersonic flows," *Corrosion Science*, Vol. 53, No. 3, 2011, pp. 922–929.

[123] Playez, M., Fletcher, D. G., Marschall, J., Fahrenholtz, W. G., Hilmas, G. E., and Zhu, S. M., "Optical Emission Spectroscopy During Plasmatron Testing of $ZrB_2$-SiC Ultrahigh-Temperature Ceramic Composites," *Journal Of Thermophysics and Heat Transfer*, Vol. 23, No. 2, 2009, pp. 279–285.

[124] Monteverde, F., Savino, R., Fumo, M. D. S., and Di Maso, A., "Plasma wind tunnel testing of ultra-high temperature $ZrB_2$-SiC composites under hypersonic re-entry conditions," *Journal of the European Ceramic Society*, Vol. 30, No. 11, 2010, pp. 2313–2321.

[125] Yu, S., Yi-Jun, L., and Fei, X., "ReaxFF molecular dynamics study on oxidation behavior of 3C-SiC: Polar face effects," *Chinese Physics B*, Vol. 24, No. 9, 2015, pp. 096203.

[126] Simonka, V., Hossinger, A., Weinbub, J., and Selberherr, S., "ReaxFF reactive molecular dynamics study of orientation dependence of initial silicon carbide oxidation," *The Journal of Physical Chemistry A*, Vol. 121, No. 46, 2017, pp. 8791–8798.

[127] Gamallo, P., Prats, H., and Sayós, R., "ReaxFF molecular dynamics simulations of CO collisions on an O-preadsorbed silica surface," *Journal of molecular modeling*, Vol. 20, No. 4, 2014, pp. 2160.

[128] Newsome, D. A., Sengupta, D., and van Duin, A. C., "High-temperature oxidation of SiC-based composite: rate constant calculation from ReaxFF MD simulations, Part II," *The Journal of Physical Chemistry C*, Vol. 117, No. 10, 2013, pp. 5014–5027.

[129] Marschall, J. and MacLean, M., "Finite-rate surface chemistry model, I: Formulation and reaction system examples," AIAA Paper 2011-3783, 2011.

[130] Poovathingal, S., Schwartzentruber, T. E., Murray, V. J., Minton, T. K., and Candler, G. V., "Finite-rate oxidation model for carbon surfaces from molecular beam experiments," *AIAA Journal*, Vol. 55, No. 5, 2017, pp. 1644–1658.

[131] Deutsch, J., Deutsch, E., Elander, N., and Lagerqvist, A., "The Emission Spectrum of SiO: The AX System in the 2 100-2 300 Å Region," *Physica Scripta*, Vol. 12, No. 4, 1975, pp. 248.

[132] Field, R., Lagerqvist, A., and Renhorn, I., "The low lying electronic states of SiO," *Physica Scripta*, Vol. 14, No. 6, 1976, pp. 298.

[133] Johnston, C. O., Stern, E. C., and Wheeler, L. F., "Radiative heating of large meteoroids during atmospheric entry," *Icarus*, Vol. 309, 2018, pp. 25–44.

[134] Opeka, M. M., Talmy, I. G., Wuchina, E. J., Zaykoski, J. A., and Causey, S. J., "Mechanical, thermal, and oxidation properties of refractory hafnium and zirconium compounds," *Journal of the European Ceramic Society*, Vol. 19, 1999, pp. 2405–2414.

[135] Inoue, R., Arai, Y., Kubota, Y., Kogo, Y., and Goto, K., "Initial oxidation behaviors of ZrB2-SiC-ZrC ternary composites above 2000 C," *Journal of Alloys and Compounds*, Vol. 731, 2018, pp. 310–317.

[136] Zhuang, L., Fu, Q. G., and Liu, T. Y., "Ablation resistance of wedge-shaped C/C-ZrB2-ZrC-SiC composites exposed to an oxyacetylene torch," *Corrosion Science*, Vol. 112, 2016, pp. 462–470.

[137] Nguyen, Q. N., Opila, E. J., and Robinson, R. C., "Oxidation of ultrahigh temperature ceramics in water vapor," *Journal of the Electrochemical Society*, Vol. 151, No. 10, 2004, pp. B558–B562.

[138] Mick, H. J. and Roth, P., "Shock tube study of silicon atom oxidation by CO and $CO_2$," *Journal of Physical Chemistry*, Vol. 98, No. 32, 1994, pp. 7844–7847.

[139] Mick, H. J. and Roth, P., "High-temperature kinetics of Si + $N_2O$," *Journal of Physical Chemistry*, Vol. 98, No. 20, 1994, pp. 5310–5313.

[140] Le Picard, S. D., Canosa, A., Reignier, D., and Stoecklin, T., "A comparative study of the reactivity of the silicon atom $Si(^3P_j)$ towards $O_2$ and NO molecules at very low temperature," *Physical Chemistry Chemical Physics*, Vol. 4, No. 15, 2002, pp. 3659–3664.

[141] Owono Owono, L., Jaidane, N., Kwato Njock, M., and Ben Lakhdar, Z., "Theoretical investigation of excited and Rydberg states of imidogen radical NH: Potential energy curves, spectroscopic constants, and dipole moment functions," *The Journal of Chemical Physics*, Vol. 126, No. 24, 2007, pp. 244302.

[142] Ram, R. and Bernath, P., "Revised molecular constants and term values for the $X^3\Sigma^-$ and $A^3\Pi$ states of NH," *Journal of Molecular Spectroscopy*, Vol. 260, No. 2, 2010, pp. 115–119.

[143] Owono Owono, L., Ben Abdallah, D., Jaidane, N., and Ben Lakhdar, Z., "Theoretical radiative properties between states of the triplet manifold of NH radical," *The Journal of Chemical Physics*, Vol. 128, No. 8, 2008, pp. 084309.

[144] Gupta, D., Baluja, K., and Song, M.-Y., "Vibrationally resolved excitation, dissociation, and rotational cross sections of NH radical by electron-impact using the R-matrix method," *Physics of Plasmas*, Vol. 26, No. 6, 2019, pp. 063503.

[145] Gokcen, T., "$N_2$-$CH_4$-Ar chemical kinetic model for simulations of atmospheric entry to Titan," *Journal of Thermophysics and Heat Transfer*, Vol. 21, No. 1, 2007, pp. 9–18.

[146] Patel-Misra, D., Parlant, G., Sauder, D. G., Yarkony, D. R., and Dagdigian, P. J., "Radiative and nonradiative decay of the NH (ND) A$^3\Pi$ electronic state: Predissociation induced by the $^5\Sigma^-$ state," *The Journal of Chemical Physics*, Vol. 94, No. 3, 1991, pp. 1913–1922.